Rheological measurement of biological fluids by a portable differential dynamic microscopy-based device

Ungkarn Jarujareet

Submitted in fulfilment of the requirements for the Degree of Doctor of Philosophy

James Watt School of Engineering

College of Science and Engineering

University of Glasgow

May 2021

Abstract

Elementary function of fluids in being able to flow and deform continuously is an important field of study variously known as rheology. Understanding of such characteristics provides benefits for not only being able to control and understand fluid dynamics following an exposure to force. In a simple fluid, a shear stress exposed on a small fluid element causes the fluid to deform. The rate of the deformation that is proportional to the shear stress is referred to as Newtonian fluid. This rheological response reflects the intrinsic structure of the fluid from internal friction amongst the fluid. Unlike simple fluid, mechanical responses of many biological fluids are more complex due to their heterogeneity in structure. In addition, these mechanical behaviours are often relevant to the biological functionality of the fluids. For example, human whole blood exhibits a shear-thinning characteristic in which its viscosity decreases according to a progressive rate of change in velocity or shear rate. When the blood is at rest, viscosity dramatically increases due to ongoing coagulation processes to prevent and stop bleeding injuries. Several methodologies have previously been developed and demonstrated in measuring of such rheological characteristics.

This thesis exploits the emerging technique of differential dynamic microscopy (DDM) for quantitative rheological assessment of biological fluids using simple implementation of passive microrheological measurements. Improvements have been carried out to achieve and quantify reliable results. Firstly, time-stamps of every acquiring images associated more accurate dynamic (time-based) information for the typical DDM to analyse. In addition, the use of a near-infrared illumination source allowed human whole blood experiment (overcoming visible light absorbance of the blood.)

Finally, the thesis implemented a direct conversion approach to eliminate high frequency artefacts of the obtained viscoelastic moduli from using generalised Stokes-Einstein relation. In order to determine the fluid viscosity the Cox-Merz relationship

was adopted. Apart from rheological measurement, the developed device was successfully use to also determine particle size distribution of both colloidal particles and cells from the measurement data, applying a numerical inversion which was a non-negative least square approach.

Table of contents

Chapter 3

Chapter 4

Chapter 5

List of tables

List of figures

Acknowledgement

I would like to express my appreciation to both of my supervisors, Prof. Jon Cooper and Dr. Julien Reboud, for their support, guidance, and contribution in this work that will become a memorable part of my life for the past four years. I must also thank Dr. Manlio Tassieri for his invaluable advice and suggestions in this work. Without their scientific expertise, I could not accomplish this work. I would like to also acknowledge Dr. Rab Wilson for his suggestion in time-stamping in image acquisition which I implemented in this thesis. Many thanks to Dr. Andriejus Demcenko for helping me out from his comments and suggestions.

I also sincerely thankful to my parents Aroon and Charatsri, my sister Aruncharat, and my brother-in-law Kriangkrai. I appreciate them for the help and moral support that I received during my studies.

Author's Declaration

I declare that the work described in this thesis has been carried out by me unless otherwise cited or acknowledged. It is entirely of my own composition and has not, in whole or in part, been submitted for any other degree.

Ungkarn Jarujareet

May 2021

Abbreviations

- 3D — Three dimension
- aPPT — Activated Partial Thromboplastin Time
- BSA — Bovine serum albumin
- cP — Centipoise
- DDA — Differential dynamic algorithm
- DDM — Differential dynamic microscopy
- DI water — Deionised water
- DLS — Dynamic light scattering
- DNA — Deoxyribonucleic Acid
- DWS — Diffusing wave spectroscopy
- EDTA — Ethylenediaminetetraacetate
- EMS — Electro-magnetic spinning
- FOV — Field of view
- GSER — Generalised Stokes-Einstein relation
- Hct — Haematocrit
- HNFS — Heterodyne near-field scattering
- LED — Light emitting diode
- mPa.s — Millipascal-second
- MSD — Mean square displacement
- NaCl — Sodium chloride
- NNLS — Non-negative least square
- PEO — Poly(ethylene oxide)
- pH — Power of hydrogen
- PMT — Photon multiplier tube
- PT — Prothrombin time
- RBCs — Red blood cells

- SD Standard deviation
- VPT Video particle tracking
- WBCs White blood cells

Chapter 1

Introduction

The complexity of biological systems is extraordinary. Many biological fluids are highly heterogeneous and the dynamics of the fluids is an important biological parameter [1]. For instance, human whole blood contains several components such as red blood cells (RBCs), white blood cells (WBCs), plasma, and platelets. When the blood is at rest, RBCs are aggregated and form complex 3D structures called a rouleaux [2]. However, the rouleaux can be broken apart by imposing a shear force. This prominent behaviour of the RBCs play an important role in the flow behaviour of the whole blood as the RBCs are the main cellular component, representing approximately 40-45% by volume.

The study in flow behaviour of the blood and its formed elements, known as haemorheology, has been found to associate with many haematological disorders in many studies [3]–[6]. For example, the RBCs are rigid and lose their deformability in sickle cell disease, [7] increasing the whole blood viscosity in comparison to normal blood by up to fifty times [8] as illustrated in Figure 1.1.

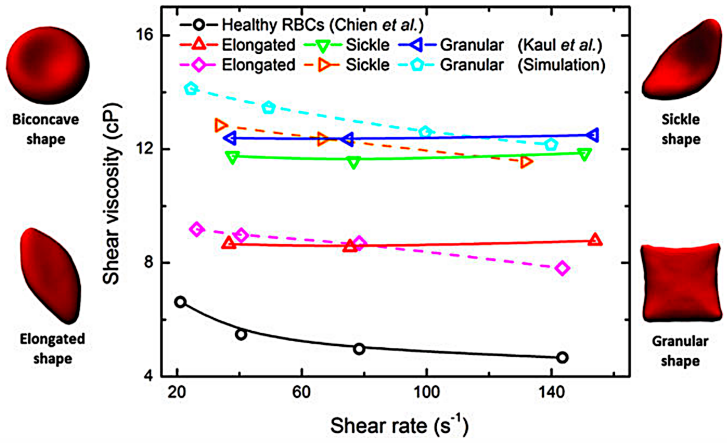

Figure 1.1. Shear viscosity obtained by simulation (dash lines) and experiment (solid lines) of whole blood samples with different cell shapes (Image taken from [9]).

The increase of blood viscosity, or hyper-viscosity, can also be used as an indicator of inflammatory activity [10] as shown in Figure 1.2.

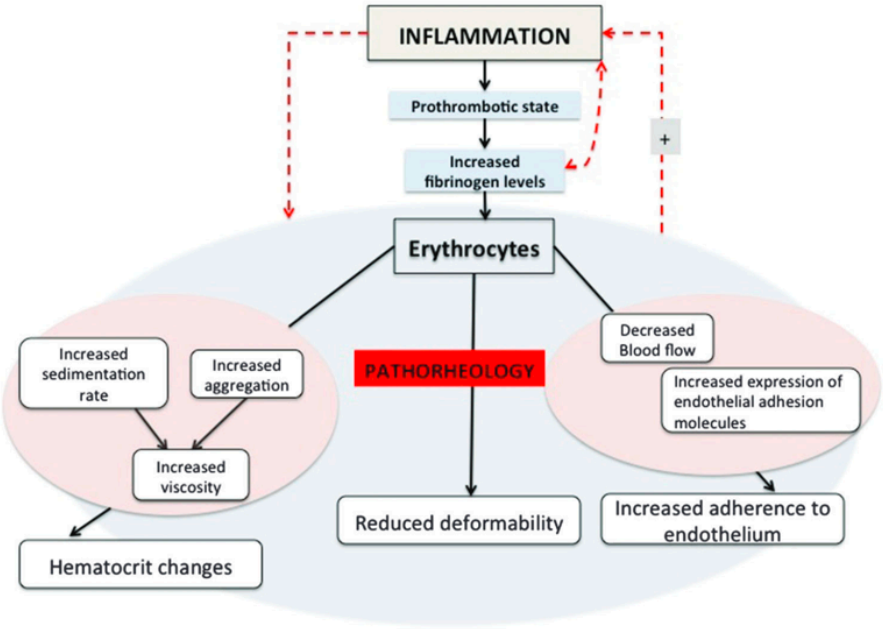

Figure 1.2. Pathorheology (rheological pathology) due to inflammatory (Image taken from [11]).

Haemorheology is also broadly related to blood coagulation process or haemostasis. Typically, the process is relevant not only to RBC behaviuors but also to those for plasma proteins and platelets. When a blood vessel is injured, muscle in the vessel wall contracts near the injury point. Chemicals released from the injured cells activate

nearby platelets to an aggregation called platelet plug [12]. This process lets the activated platelets become "spikey" and stick to each other at the injury point. Subsequently, fibrinogen in the blood plasma is converted to fibrin that forms a mesh to trap the platelet plug and the RBCs, producing a clot as illustrated in Figure 1.3. Furthermore, the study of haemostasis helps to understand many diseases, especially vascular disturbances in the chronically or critically ill [13].

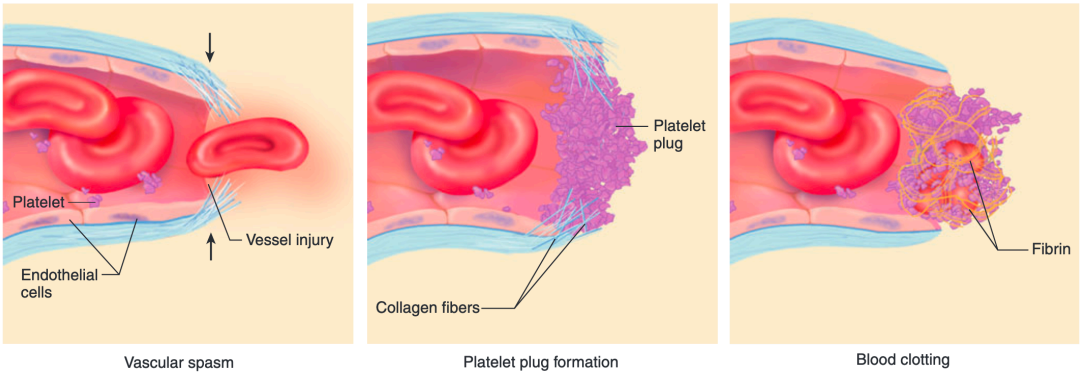

Figure 1.3. Haemostasis and the process of blood clotting (Image taken from [12]).

Rather than haemostasis, accessing the rheological properties of the cell membrane can also allow quantitative descriptions of various pathologies. The viscoelastic membrane plays an important role in holding the biconcave shape of RBCs [14]. Hence, diseases such as spherocytosis, malaria, and sickle cell anaemia affect the RBCs morphology and their dynamic properties [15]. In addition, the mechanical responses of cells allows the identification of cell phenotype (including for example cell differentiation).

Generally populations of cells are highly heterogeneous in both their biophysical and biochemical make-up. The study of single cells brings about important information that can be hidden in population-level values when many cells, with different properties are present. For instance, cancer cells are more flexible than other regular cells, and can migrate and invade to other tissues, with each cell having very varied properties [16], [17]. Thus, the characterisation of single cell properties [18] is

extremely time and data-intensive, and coupled with the characterisation of rheological properties of biological fluids provides highly relevant understanding of changes in physiology and the mechanism of disease. As a result, the development of robust measurement methods would provide further improvements in disease diagnostic and treatment.

In rheological characterisation, conventional mechanical rheometry provides an average measurement of a large amount of sample [19]. By applying a force to a sample, the resistance to the force can be monitored and inferred to the corresponding rheological responses. In biotechnology and clinical analysis, biological specimens are often difficult to extract and synthesize in large quantities [20]. In addition, their performance can vary under different laboratory conditions [20]. Moreover, assembling of these small biological components is difficult as they can interact with one another and affect their physical mechanisms [21]. This limitation has led to the development of the field of microrheology, which holds a key benefit from sampling only microliters sample volumes. In microrheology, microparticles are often added to the sample in order to monitor and record their movements. These movements are numerically converted to yield the rheological responses of the sample.

Microrheology can be divided into two broad fields, namely active and passive implementations. In active microrheology, the rheological responses are measured from an applied external force to the probe particles. As a result, this approach extends the measurable range to materials with higher modulus compared to passive rheology [22]. However, this ability leads to costly and complex systems as it needs a dedicated system to control the exerted force. In contrast to active microrheology, passive rheology relies only on thermal motion ($K_B \cdot T$) of colloidal particles resulting in a much more simple configuration. By tracking particle motion [23] or light scattering analysis [24], [25], the mean square displacement can provide the mechanical properties of the surrounding medium. In addition, the result of this method is always within

linear viscoelastic regime because of no external stress is applied. This will be discussed in more details in the following paragraphs.

Innovative microrheology assessment has been exploited and demonstrated in various devices such as dynamic light scattering (DLS) [26]–[28], diffusive wave spectroscopy (DWS) [28]–[30], and video particle tracking (VPT) [28], [31]. These devices rely on passive microrheology from having probe microparticles embedded in a fluid sample. The probe experiences Brownian motion such that a time-dependent mean square displacement (MSD) of the probe can be evaluated. In particular, the MSD is described by $\langle \Delta r^2(t) \rangle \equiv \langle |r(\delta + t) - r(\delta)|^2 \rangle$ [32], [33], where t is the fixed lag time, and $r(\delta)$ is the position of a particle at specified time δ. A generalised Stokes-Einstein relationship (GSER) [34] is then employed to convert the MSD to viscoelastic property, which is a measure of mechanical property lies between elastic (storage modulus G') and viscous (loss modulus G'') responses, as detailed in Chapter 2. A more recent approach combines scattering and microscopy in a single device called differential dynamic microscopy (DDM) [35]–[38]. This approach analyses microscopic images to perform light scattering experiment without the need for a microscope. In addition, a further development of the DDM allows for manipulating passive microrheology measurement to evaluate viscoelastic behaviours of sample fluids [39], [40]. These behaviours can be converted to a steady-shear viscosity which is comparable to the measurement done in a mechanical rheometer [41].

1.1. Conventional techniques in microrheology

1.1.1. Video particle tracking

Video particle tracking employs a digital video-microscopy to record the movement of probe particles embedded in a fluid as illustrated in Fig 1.4.

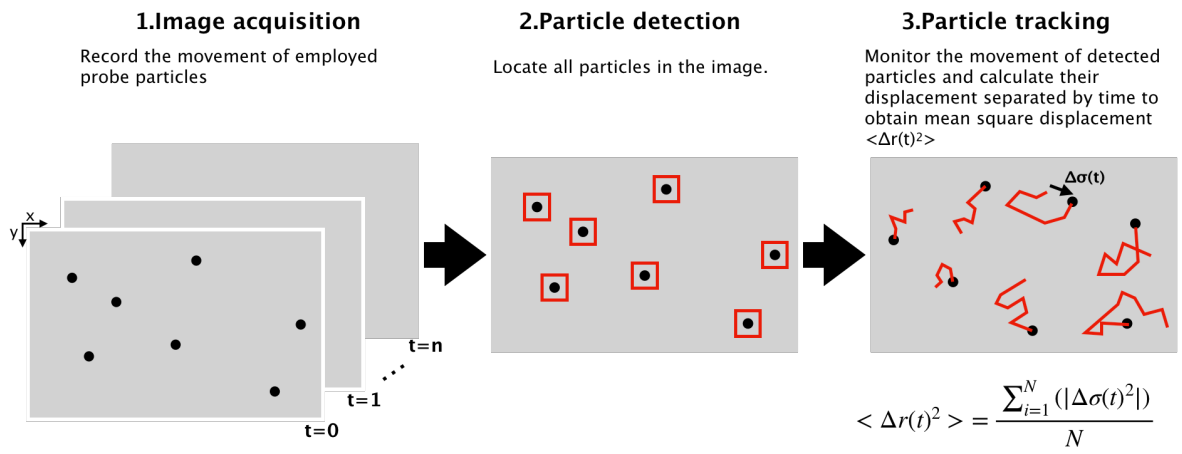

Figure 1.4. A schematic diagram of video particle tracking procedure. Probe particles are used in a sample fluid, then, images of their movement according to Brownian motion are recorded by using a light microscope. This system locates all the particles from the recorded images and monitors the movements to obtain mean square displacement $<\Delta r^2(t)>$ for estimating viscoelastic properties.

In general, digital image analysis is applied to the recorded video to obtain the trajectory of the particles as a function of time, as their mean square displacement. This statistic parameter can be converted to viscoelastic properties using GSER [23]. Nevertheless, the accurate recording of time and motion are crucial during the particles movements [42]. Time and image resolution depend on the capturing hardware and tracking algorithm used. For the time resolution, image acquisition should be fast enough to be able to track movements of multiple particles. In addition, image resolution needs to be high so that the micron-size particles can be seen and located with precise position. Besides, the optical resolution relies on the magnification of the microscopy used in the study. Thus, the particles smaller than the resolving power of the microscope are undetectable and become untraceable by this technique.

An example of video particle tracking was for studying lubricin protein in synovial fluid, also known as a joint fluid. Individual genetic deficiency of lubricin production may result in the development of precocious joint failure. In the study, fluorescent particles size of 200 nm were added and used as probe particles in normal and lubricin-deficient synovial fluid samples. The mean square displacement and viscoelastic

behaviour were investigated as shown in Figure 1.5. This study found that the lubricin contributed to the elastic absorption as it provide lubrication functionality to the synovial fluid. The obtained viscoelastic modulus was reported in good agreement with mechanical rheometer as shown in Figure 1.5 (b).

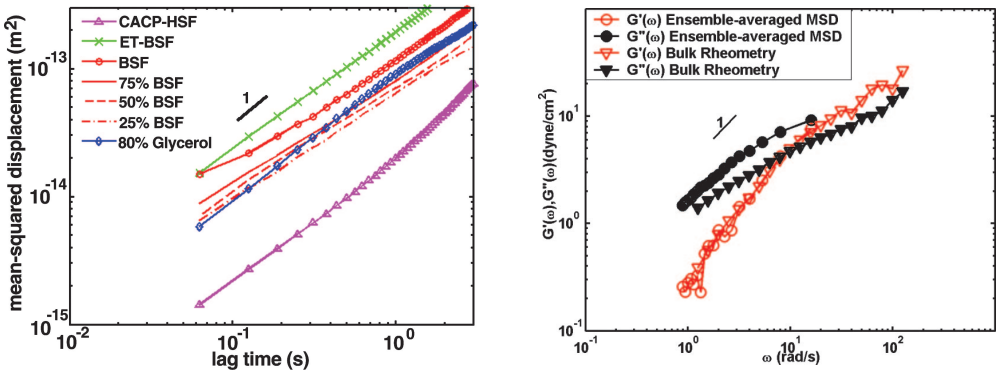

Figure 1.5. The role of lubricin in synovial fluid rheology investigated using particle tracking microrheology [43]. (a, left) the obtained mean square displacement of normal synovial fluid (bovine synovial fluid;BSF) and lubricin-deficient synovial fluids (enzyme (trypsin)-treated BS;ET-BSF,and patient-derived camptodactyly-arthropathy-coxavara-pericarditis synovial fluid;CACP-HSF). (b, right) Comparison of particle tracking microrheology and rheometry of storage (G'(ω)) and loss moduli (G''(ω)) for the BSF.

1.1.1. Dynamic light scattering

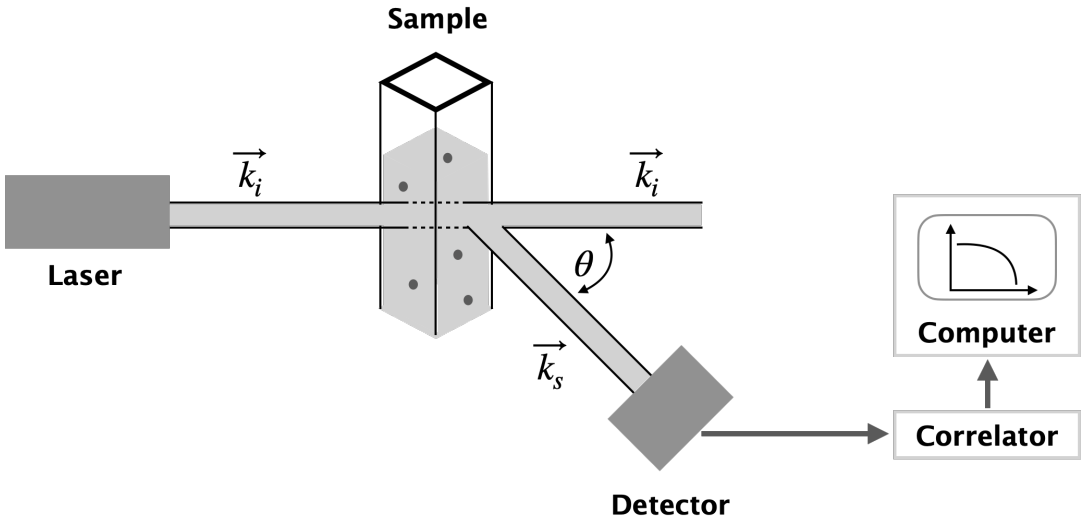

Figure 1.6. A typical dynamic light scattering configuration (images inspired by [9]).

Dynamic light scattering (DLS) is a light scattering method for recording and analysing the scattered light of the particles suspended in a fluid. As illustrated in Fig 1.6, a monochromatic laser beam is shone onto a sample fluid in which the probe particles are. The beam is scattered in all direction when it hits the particles. However, only the beam scattered at a specific range of angles is collected via a photon multiplier tube (PMT) [44]. Similarly to particle tracking microscopy, DLS makes use of the passive microrheology principle in which the particles move due to the thermal force $K_B T$.

Time-correlation analysis is performed on the collected light scattering intensity as $g^2(\tau) = \frac{\langle I(t)I(t+\tau)\rangle}{\langle I(t)\rangle^2}$ with $\langle . \rangle$ is the averaging over time t, τ represents a lag time, and $I(.)$ is the collected light intensity. Then, this intensity-correlation can be related to establishing electric-field correlation $g(\tau)$ by Siegert relation in which $g^2(\tau) = 1 + |g(\tau)|$ [45], [46]. As a result, the MSD can be evaluated by $g(\tau) = e^{-\frac{q}{6}\langle \Delta r^2(\tau)\rangle}$, where $\mathbf{q} = \frac{4\pi n}{\lambda} \sin\left(\frac{\theta}{2}\right)$ is a wave vector with refractive index n, laser wavelength λ, and scatting angle θ [45], [46]. Following this, viscoelastic property of the suspension can be determined using GSER numerical conversion. However, this approach requires high sensitivity light collector to capture weak scattered light as it relies on homodyne configuration [47].

DLS has been employed to investigate molecular relaxation of DNA solutions where conventional mechanical rheology is impractical [48], as the technique is accessible to angular frequency up to 10^6 s^{-1}, whereas mechanical rheology provides access only to 10^2 s^{-1} [48]. In the measurement, probe particles size of 500 nm were added to the unentangled linear solutions of DNA. Then, MSD of the probes was obtained from the intensity autocorrelation. To determine the viscoelastic moduli, generalised Stokes-Einstein relation was performed on the mean square displacement. The workflow of the calculation was shown in Figure 1.7(a). From the calculation, the obtained

viscoelastic modulus matched the theoretical predictions as shown in Figure 1.7(b). The study also related the transition of a hierarchy of molecular relaxation regimes as shown in Figure 1.7(b).

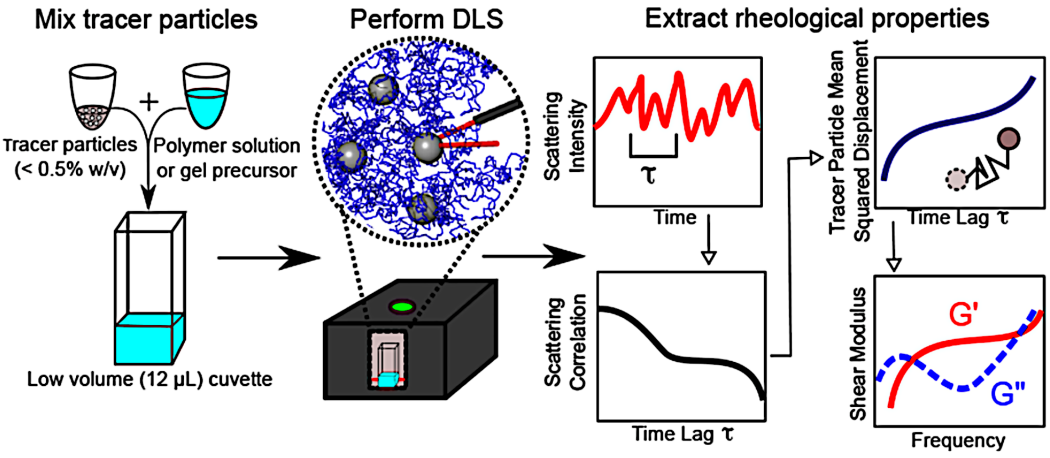

(a)

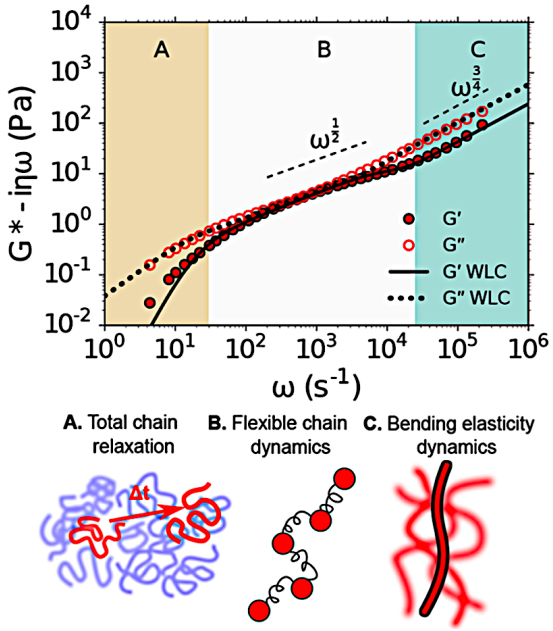

(b)

Figure 1.7. A DLS system for studying molecular relaxations of unentangled solutions of DNA [48]. (a) The study workflow using a commercial DLS system. Brownian motion of the tracer particles produced fluctuations in scattering intensity. The autocorrelation of the intensity is analysed by the custom software to extract the mean squared displacement of particles, which was used to determine the frequency-dependent linear viscoelastic shear modulus G*(ω). (b) The result storage G′ and loss G″ moduli with approximation of internal chain relaxation regimes A, B, and C. The dotted and solid lines indicate the theoretical predictions for G′ and G″, respectively.

1.1.2. Diffusive wave scattering

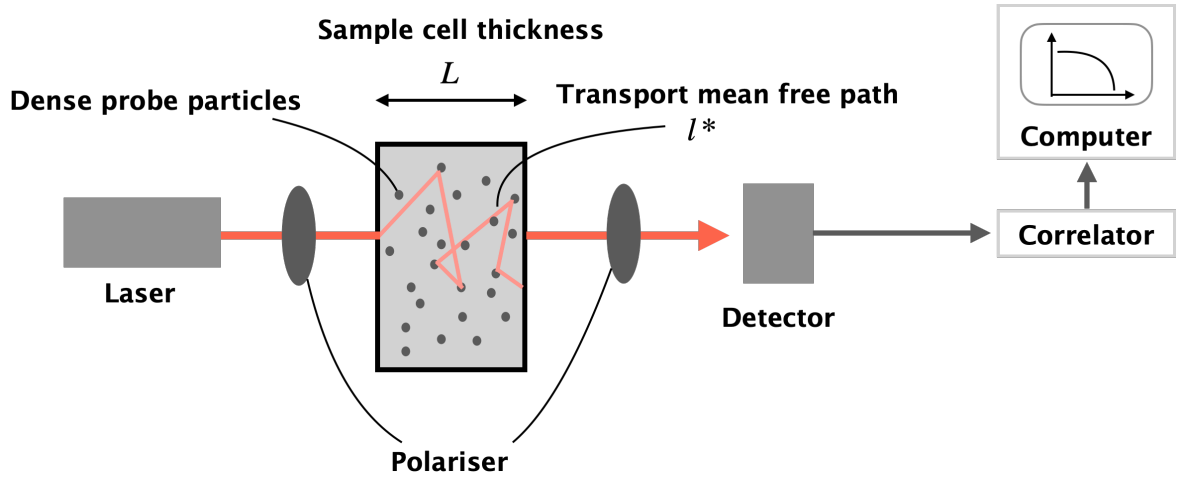

Figure 1.8. A diffusing wave spectroscopy configuration (inspired by [22]).

Diffusive wave scattering (DWS) is a new development adapted from DLS to solve strong multiple scattering of light in a turbid media. A laser beam is shone through a sample which contains probe particles. This system collects multiple scattering light from dense probe particles [49]. As a result, the optical configuration is complex due to it has many optical elements as shown in Figure 1.8. In addition, knowledge of path length distribution is crucial to calculate the correlation function of DWS [50]–[52]. This is because, the correlation function is depended on the sample thickness L and the mean free path of light l^*as $g^2(\tau) = 1 + \frac{L/l^*+4/3}{\alpha^*+2/3}\left(\sinh[a^*x]+\frac{2}{3}x\cosh[a^*x]\right)$ $\left(1+\frac{4}{9}x^2\right)\sinh\left[\frac{L}{l^*}x\right]+\frac{4}{3}x\cosh\left[\frac{L}{l^*}x\right]$,

where $x = [\mathbf{k}_0^2\langle\Delta r^2(t)\rangle]^{1/2}$, $\alpha^* = \frac{z_0}{l^*}$, z_0 is the distance into the sample from the incident surface to the place where diffuse source is located, and k_0 is the incident wave vector [53], [54]. In addition, the criteria of $L \gg l^*$ of the DWS configuration must be fulfilled for the correlation to be valid [49].

In a rheological study, DWS has been demonstrated for investigating rheological properties in human synovial fluid from patients suffering from joint diseases of osteoarthritis (OA), rheumatoid arthritis (RA), and gouty arthritis (GA) [55]. The

study also observed the obtained viscoelastic modulus with the white blood cell count from the patients. From the results, the study found that the white blood cell count exhibited an inversely proportional to both loss G'' and storage G' moduli. In addition, the average value of G'' and G' followed an order of OA > RA > GA as illustrated in Figure 1.9.

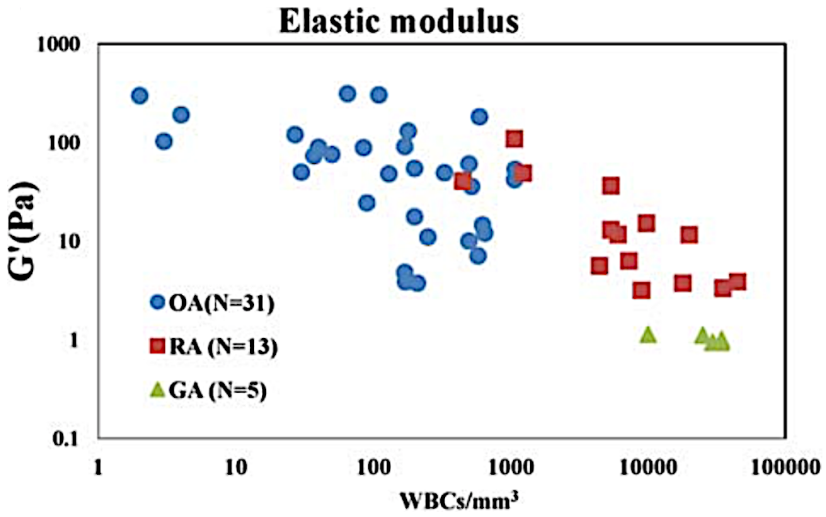

(a)

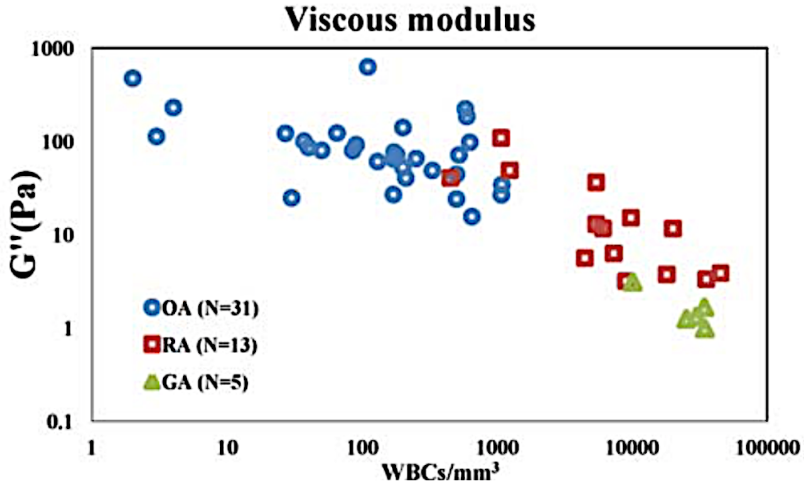

(b)

Figure 1.9. (a) Storage (Elastic) modulus. (b) loss (viscous) modulus (both at 1 Hz) of synovial fluids (at 27 ^{o}C) from 49 arthritis patients versus their white blood cell (WBC) count [55].

1.1.3. Laser speckle rheology

Laser speckle is an intensity pattern arising from coherent light interference between the light source and the light scattered by a specimen. Laser speckle rheology expands the applicability of DWS to study elasticity and viscosity in tissues by analysing the speckle pattern [16], with sensitivity to Brownian motion [56]. As a result, passive microrheology can be studied by this approach. In a demonstration, a laser speckle rheology system can evaluate a patient's coagulation status [57]. The device illuminated a blood sample with 690 nm laser spot, creating temporal speckle intensity fluctuation, backscattered on a high-speed camera as illustrated in Figure 1.10.

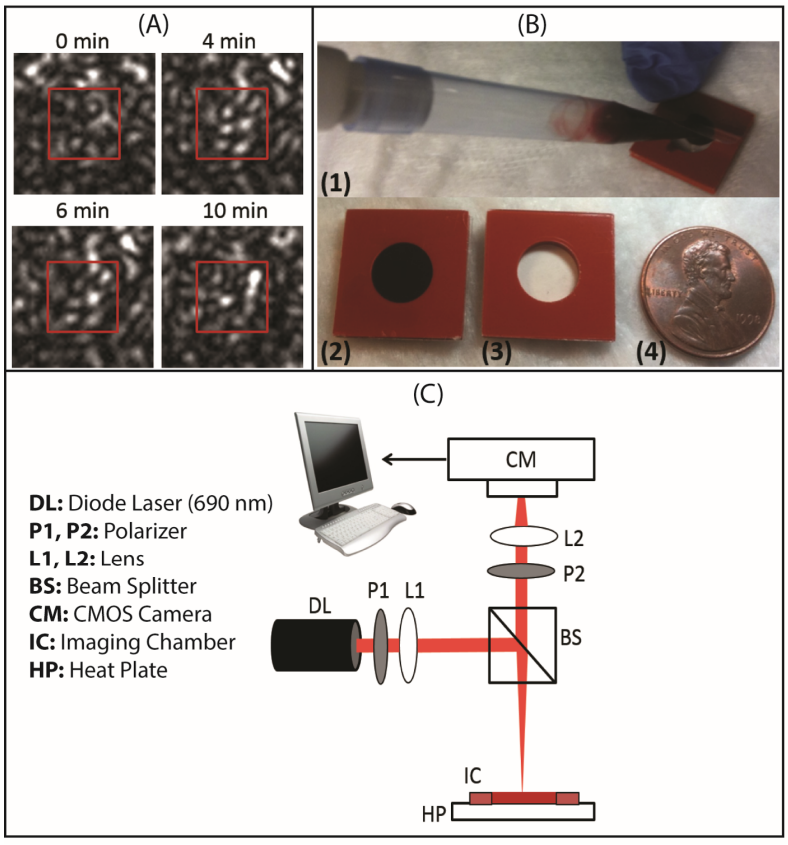

Figure 1.10. A Laser speckle rheology configuration (Image taken from [58]).

Time series of fluctuations were captured, and the autocorrelation calculated. The speckle patterns were analysed to infer blood clotting time and maximum clot stiffness in real-time. In this measurement, the result reflected a close correlation with reference standard (aPPT and PT). However, the proposed system was complex due to it

consisting of many optical elements. A speckle autocorrelation time constant, τ (primary y-axis), and the viscoelastic modulus |G*(ω)| of ω = 1 Hz (secondary y-axis) were plotted as a function of coagulation time for a human blood sample. Similar trends were observed for both the τ, and |G*| curves during coagulation. In each case, the average value of the three LSR τ-measurements is plotted and the error bars depict standard deviations.

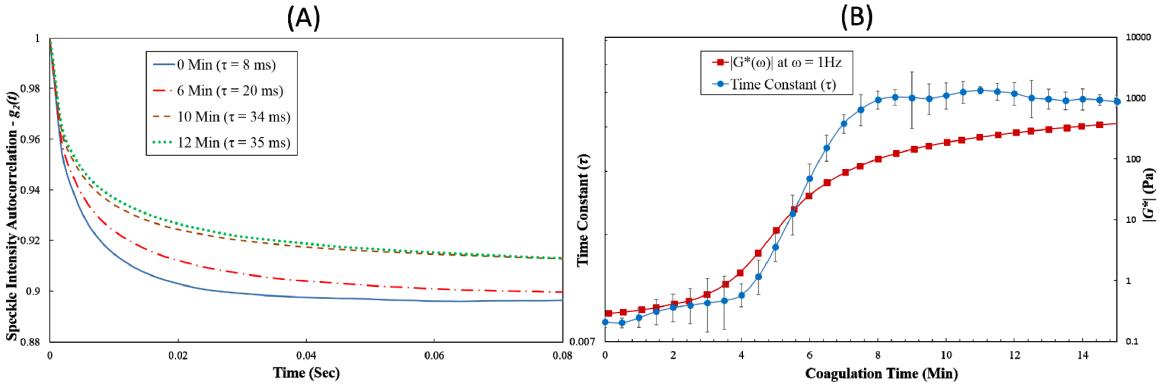

Figure 1.11. (A) intensity correlation $g^2(\tau)$ measured at 0, 6, 10, and 12 minutes during coagulation process from a Human blood sample. It was observed that $g^2(\tau)$ decay slowed down as blood coagulation progressed. Slower $g^2(\tau)$ decay and the corresponding increase in autocorrelation time constant (τ) indicated an increase in clot viscoelastic modulus during coagulation process. (B) Autocorrelation time constant, (τ) (primary y-axis), and the viscoelastic modulus $|G^*(\omega)|$ at $\omega = 1$ Hz (secondary y-axis) plotted as a function of coagulation time for a human blood sample. Similar trends were observed for both the τ, and $|G^*|$ curves during coagulation. In each case, the average value of the three LSR τ-measurements is plotted and the error bars depict standard deviations [57].

1.2. Differential Dynamic microscopy

In microrheological study, scattering and microscopy have become two well-known and distinct tools to investigate and analyse colloidal dynamics. Microscopy, such as video particle tracking, provides direct access to the motion of individual heterogeneous particles from visualised images in two-dimensional manner. Alternatively, scattering monitors average intensity fluctuations and can approach larger sample quantities in a scattering volume [59].

Integration of microscopy and dynamic light scattering (DLS) have been developed, in particular in biological experiments i.e. red blood cell membranes [15], and a living cell system [62]. In the membrane study [15], the red blood cells were immobilised on a glass slide using polylysine hydrobromide with conjugated micro-particles on their membranes. Rheological properties of the membrane were obtained using DLS principle with the Brownian particles that conjugated on the membrane. In the same manner, the integrated microscope with DLS was used for investigating of motility in living macrophage cells [62]. The device imaged the cell at a few thousand frame per second and created a motility map of the cell regarding to the intensity correlation calculated by the DLS principle. The result of this study found that most of motion occurred in the outer region than its centre interior of the cell. However, difficulty of modifications and optical alignments has restricted to capability to build instruments outside of the laboratory.

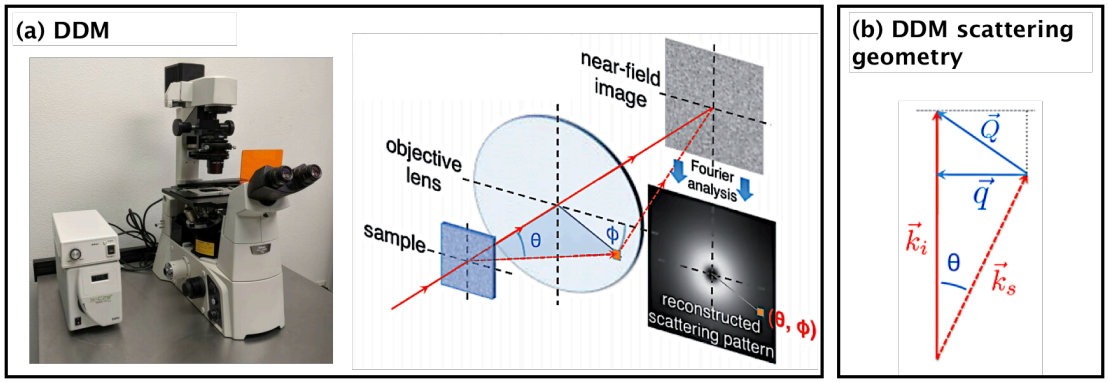

Figure 1.12. A DDM configuration used in [38]. (a) Light passthrough a sample is scattered at various angles and is collected by objective lens. Two-dimensional microscope images of the sample are Fourier analysed and information equivalent to Dynamic light scattering (DLS) is recovered. (b) DDM scattering geometry. $\vec{\mathbf{k}}_\mathbf{i}$ is an incident light, $\vec{\mathbf{k}}_\mathbf{s}$ is a scattered light at scattering angle of θ. In DDM, scattering wave vector $\vec{\mathbf{Q}}$ is approximated using $\vec{\mathbf{q}} \approx \vec{\mathbf{Q}}$ for small scattering angle [36]. [61]

DDM is a relatively new approach to study the dynamics. It has equivalent result of both VPT and DLS combined [38], [62]. The DDM set-up consists of a standard light microscope equipped with a digital video camera with a high frame rate as shown in

Figure 1.12. Close proximity of detector-to-sample is a requirement in which correlation properties of the scattered light are free from the distance to sample. Although the partially coherent illumination source and out-of-focus image acquisition bring difficulties to the system, the result strongly agrees with gold standard methods [36]. For this reason, DDM is a flexible and reliable tool for the investigation of dynamic phenomena.

Current DDM techniques are based on a bench-top microscope resulting bulky imaging system. These systems use costly lenses and costly high-speed video acquisition systems for data acquisition. In addition, preinstalled light sources and optical filters inevitably limit available wavelengths for rheological measurement in some biological samples i.e. human whole blood. This would lead to additional costs to the system and bring more difficulty of implementation to developing countries. In this thesis, a portable DDM-based system is proposed for quantitative measuring of rheological behaviour in biological fluids.

1.3. Aims

The main aim of this thesis is to develop a portable microscopy-based system to measure viscoelastic behaviours of biological fluids particularly in Human whole blood samples in small volumes. In addition, the device should be able to evaluate steady-shear viscosity of the biological samples to provide valuable information for rheological study.

1.4. Objectives

In this thesis, a portable differential dynamic microscopy prototype is proposed for measuring viscoelastic properties of biological fluids. The objectives of the PhD are as follows:

1. To design and build a portable differential dynamic microscopy prototype;
2. To develop an image-based algorithm for quantitatively estimating viscoelastic modulus of biological fluids;
3. To validate the approach in a range of biofluids of interest, benchmarked with established rheometers.

1.5. Thesis outline

This thesis is organised in seven chapters as followed:

Chapter 2: shows fundamental principle of rheology, differential dynamic algorithm (DDA), and how to obtain rheological properties from the DDA. In addition, this thesis extends capability of the DDM to estimate particle size distribution of colloidal particles using non-negative least square (NNLS) method which is also described in this chapter.

Chapter 3: provides information of material and methods used in this thesis. Furthermore, the chapter describes a development of proposed DDM-based device for obtaining rheological properties of biological samples. This includes the development of in-house microchamber which can hold small sample volumes and prevents sample evaporation.

Chapter 4: presents rheological parameters obtained by proposed device from measuring standard materials.

Chapter 5: demonstrates particle size distribution of mono and polydisperse colloidal particles obtained by proposed device.

Chapter 6: shows rheological assessments of biological samples including human whole blood, blood plasma, and saliva.

Chapter 7: summarises and discusses the main findings and provides a perspective for advancement of proposed device for the future work.

Chapter 2

Background

Optical microrheological approaches in both of light scattering and imaging based have gained increasing attention over the last decades [63]. These rheological characterisation tools have been demonstrated for a wide range of fluids such as investigation of molecular relaxation of DNA solutions [48] and study of the role of lubricin in synovial fluid rheology [43]. A notable advantage of these approaches is that they requires small sample volume which allow for rheological investigation in biological samples [22], [64]. Optical microrheology uses probe particles to measure their movements and infer the corresponding rheological behaviour of materials of interest. In the imaging approach, video particle tracking is an example of a device for monitoring the movements of these particles as discussed in Chapter 1. This approach relies upon the resolving power of the microscope used in the experiment for monitoring micron-sized probe particles. In addition, the speed of the tracking algorithm should be fast enough to track multiple moving particles leading to a need of high power computer.

In contrast, Light scattering obtains thermally-driven displacement of probe particles by calculation of intensity autocorrelation which consumes less computing power. DLS is an example of most commonly used light scattering instrument that can reveal rheological responses of the fluid of interest from determining of the displacement [65]. In DLS, autocorrelation of scattered light intensities at a certain angle is calculated

to recover intermediate scattering function which is related to displacement of the probe particles. In analogous to the DLS, differential dynamic microscopy (DDM) is a relatively new approach that can obtain the intermediate light scattering function [36]. However, the DDM Fourier analyses microscopic images in order to obtain scattering information [36], [66]. This Chapter starts by exploring and highlighting analytical methods to evaluate steady-shear viscosity of a fluid using our developed DDM-based device. This includes an implemented technique for estimating particle size distribution of colloidal particles in an interesting colloidal suspension.

In brief, our developed device implements DDM method that can perform light scattering experiment with Fourier analysis of a collection of microscopic images. The DDM can recover the intermediate light scattering function to obtain the displacement of probe particles that employed in the fluid of interest [67], [68]. This displacement can reveal rheological behaviours of a fluid of interest using passive rheology.

In passive rheology, microparticles are in a micro volume of the fluid as a probe particle. These particles are randomly relocated by collision with surrounding molecules called Brownian motion. When the particle is in Brownian equilibrium, the motions of these particles are monitored and recorded. To determine rheological responses of the suspension, the motion is performed by the Generalised Stokes-Einstein Relation (GSER). However, performing the GSER calculation can introduce numerical artefacts at high frequencies of the measurement [69], [70]. Thus, a direct numerical conversion can instead be implemented to eliminate such artefacts in the obtained rheological measurement. This resulting rheological measurement can then be used to evaluate complex viscosity of the fluid.

Notwithstanding this, steady-shear viscosity is the most-commonly used viscosity measurement in most of rheological studies. To comply with this observation, the Cox-Merz rule [71] was performed on the obtained complex viscosity to estimate the

corresponding steady-shear viscosity of the fluid. Thus, the rheological measurement evaluated by our device can be compared directly with the result from previous complementary studies [72], [73].

2.1 Rheology

Rheology is the study of how material flow and deform in response to the applied forces or stresses to the material [74]. The change in the material properties that are caused by the applied forces are called rheological properties [75]. When a stress is applied to a fluid element, the responding deformation is illustrated in Figure 2.1.

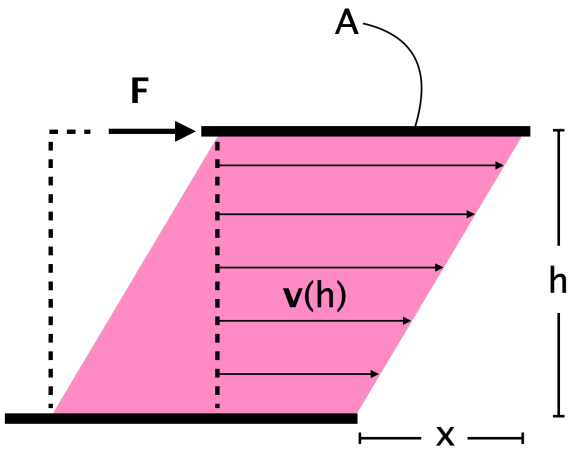

Figure 2.1. A fluid element representation of simple shear flow.

An applied force, $\mathbf{F}$, causes to the fluid moved at velocity, $\mathbf{v}$, results in a displacement, x, within the top plate to the fluid. The force, $\mathbf{F}$, transmitted to cross-sectional area A that parallel to the force is defined by a stress, $\boldsymbol{\tau}$, which is shown in Equation (2.1).

$$\boldsymbol{\tau} = \frac{\mathbf{F}}{A} \tag{2.1}$$

The deformation, or shear strain, γ, is defined as a ratio of the displacement, x, to the thickness of the fluid, h. Rate of deformation, $\dot{\gamma} = \frac{\partial \gamma}{\partial t}$, or shear rate, is related to the resistance to the flow, or viscosity, η, which is described by $\boldsymbol{\tau} = \eta\dot{\gamma}$ [76].

In static experiments, performing strain measurements as a function of time is not easy to implement, as the unit step function of the applied stress must be precisely controlled [77]. In addition, the strain measurement within a short time regime is not reliable if the unit step function is not exact [77]. In contrast to static experiments, oscillatory shear stimulation are easier to generate [77]. The corresponding shear harmonic motion to the applied small amplitude oscillatory shear is shown in Equation (2.2), [32], [33], [78]:

$$\gamma(t) = \gamma_0(\omega)\sin(\omega t) \tag{2.2}$$

where $\gamma(t)$ is the strain at time, t, $\gamma_0(\omega)$ represents the amplitude of the strain, and ω is the angular frequency.

2.1.1 Hookean solid

For metals and elastic materials, the stress is proportionally related to the deformation described by Hooke's law of elasticity as shown Equation (2.3), [32], [33], [78]:

$$\tau(t) = G\gamma(t) \tag{2.3}$$

where G is a time-independent elastic constant proportional to the Young's modulus of the material [32], [33].

For oscillatory shear, the Equation (2.3) can be represented by Equation (2.4), [32], [33], [78]:

$$\tau(t) = G\gamma_0(\omega)\sin(\omega t) \tag{2.4}$$

2.1.2 Newtonian fluid

Newtonian fluids obey the Newton's law of viscosity [79]. When applied a shear stress to a Newtonian fluid, the corresponding deviation, or strain, of the fluid is characterised by a linear relationship as shown by the Equation (2.5), [78]:

$$\tau(t) = \eta \frac{\partial \gamma}{\partial t} \tag{2.5}$$

When substituting the strain from Equation (2.2) into Equation (2.5), Equation (2.5) becomes

$$\tau(t) = \eta \frac{\partial \gamma_0 \sin(\omega t)}{\partial t} = \eta \omega \gamma_0(\omega) \cos(\omega t) \tag{2.6}$$

Using trigonometry, $\cos(\omega t)$ is equivalent to $\sin\left(\omega t + \frac{\pi}{2}\right)$, thus, the oscillatory shear of Newtonian fluid is described by Equation (2.7), [78]:

$$\tau(t) = \eta \omega \gamma_0(\omega) \sin\left(\omega t + \frac{\pi}{2}\right) \tag{2.7}$$

Accordingly, the stress oscillates at the same frequency of applied strain. However, the stress lags the strain by $\frac{\pi}{2}$ for Newtonian fluid as indicated in Equation (2.7).

2.1.3 Viscoelastic material

Mechanical responses of viscoelastic material lie in between those of a Hookean solid and Newtonian fluid [74], [78]. A harmonic stress imposes to the viscoelastic material that can be generalised by Equation (2.8)[74], [78].

$$\tau(t) = \tau_0 \sin(\omega t + \theta) \tag{2.8}$$

Where θ represents phase angle in which $\theta = 0$ for Hookean solid and $\theta = \frac{\pi}{2}$ for Newtonian fluid. For the sine angle addition $\sin(\omega t + \theta)$, the Equation (2.8) becomes

$$\tau(t) = \tau_0 \cos(\theta) \sin(\omega t) + \tau_0 \sin(\theta) \cos(\omega t) \tag{2.9}$$

Dividing stress of Equation (2.9) [78] by strain of Equation (2.2) yields the storage and loss modulus noted by G' and G'', respectively, each defined by Equation (2.10) and (2.11) respectively [32], [33], [74], [78].

$$G' = \frac{\tau_0}{\gamma_0(\omega)} \cos(\theta) \tag{2.10}$$

$$G'' = \frac{\tau_0}{\gamma_0(\omega)} \sin(\theta) \tag{2.11}$$

Thus, Equation (2.9) can be rewritten as shown in Equation (2.12) [74], [78].

$$\tau(t) = \gamma_0(\omega)(G' \sin(\omega t) + G'' \cos(\omega t)) \tag{2.12}$$

It is usually convenient to express the sinusoidally varying stress as a complex quantity as shown in Equation (2.13), [80]:

$$G^* = G' + iG'' \tag{2.13}$$

Where G^* is complex modulus.

An alternative representation is as the complex viscosity $\eta^* = \eta' + i\eta''$ where η' and η'' represent elastic and viscous components, respectively [76], [79]. The complex

viscosity η^* as a function of angular frequency is related to the complex modulus G^* via $\eta^*(\omega) = \frac{G^*(\omega)}{i\omega}$.

2.2 Differential Dynamic Analysis (DDA)

DDM, as recently proposed by Cerbino and Trappe [35] has been used to quantify dynamics of colloidal particles. It is a class of Fourier microscopy that analyses light scattering fluctuation of the particles. Typically, monodisperse spherical particles are added to a sample fluid. Light scattering of these particles, where thermal energy generate random movements, can be observed under a microscope. A DDA is performed to access dynamic of these particles.

In DDA principle, a sequence of light fluctuated images are acquired from a microscope to analyse dynamical measurements. It has been noted that if the average of the sequence does not change in time, and that the fluctuation can be determined by averaging many frames and subtracted to an individual frame [36]. The individual image of the sequence is described by its intensity $I(x, y, \delta)$ of the position (x, y) at acquired time δ. From this description, the image fluctuation can be calculated at time delay or lag time t by image difference Equation (2.14), [36].

$$\Delta I(x, y, \delta, t) = I(x, y, \delta + t) - I(x, y, \delta) \tag{2.14}$$

where t is a fixed lag time, and $I(x, y, \delta)$ is the intensity at pixel position (x, y) from acquired time δ.

From Equation (2.14), the subtraction of two adjacency lag time images eliminates time-independent artefacts such as contamination/dust on the slide or the microscope lenses, or any static objects in the imaging plane. As a result, intensity signals are

entirely a consequence of the movement of particles, in which dynamic properties depend only upon the lag time, t, with the expectation value, $\langle I(x, y, \delta)\rangle$, being equal to zero [36].

Acquiring a time sequence of images allows analysis of image correlation function, $G(\mathbf{q}, t)$, as the product between conjugate of the image in Fourier space at time δ, $I^*(\mathbf{q}, t)$, and the image in Fourier space at time $\delta + t$, $I(\mathbf{q}, \delta + t)$. The image correlation function is shown in Equation (2.15), [36].

$$G(\mathbf{q}, t) = \langle I^*(\mathbf{q}, t) \cdot I(\mathbf{q}, \delta + t)\rangle \tag{2.15}$$

where $I(\mathbf{q}, t)$ is the Fourier transform of the image $I(x, y)$ at acquired time t, and $I^*(\mathbf{q}, t)$ is the conjugate of $I(\mathbf{q}, t)$

From Equation (2.15), the function can be normalised (as an autocorrelation function) by division with the square norm of $I(\mathbf{q}, t)$, as presented in Equation (2.16), [81].

$$g_{2D} = \frac{G(\mathbf{q}, t)}{\langle |I(\mathbf{q}, \delta)|^2\rangle} \tag{2.16}$$

where $G(\mathbf{q}, t)$ is the image correlation function at acquired time, t.

Statistical analysis of the stationary differences of intensity fluctuations describes dynamic of the sample [82]. According to previous research works [13], [36], [38], [83], the expected value of two-dimensional Fourier power spectrum yield an image structuring functions $S(\mathbf{q}, t)$. Such a statistical estimator of the Fourier power spectrum are defined in equation (2.17), [81].

$$S(\mathbf{q},t) \equiv \langle|\Delta I(\mathbf{q},t)|^2\rangle = \langle\left|I_{\mathbf{q},\delta+t} - I_{\mathbf{q},\delta}\right|^2\rangle = \langle\left|I^2_{\mathbf{q},\delta+t} - 2\cdot I_{\mathbf{q},\delta+t}\cdot I_{\mathbf{q},\delta} + I^2_{\mathbf{q},\delta}\right|\rangle \tag{2.17}$$

Using cross-correlation theorem [84], convolution in Fourier space $(I_{\mathbf{q},\delta+t}\cdot I_{\mathbf{q},\delta})$ is identical to $I_{\mathbf{q},\delta+}\cdot I^*_{\mathbf{q},\delta}$. Thus, the image structuring function $S(\mathbf{q},t)$ becomes Equation (2.18), [81].

$$S(\mathbf{q},t) = \langle\left|I^2_{q,\delta+t} - 2\cdot I_{q,\delta+t}\cdot I^*_{q,\delta} + I^2_{q,\delta}\right|\rangle = 2\langle\left|I_{q,\delta}\right|^2\rangle\left(1 - \frac{\langle I^*_{q,\delta}\cdot I_{q,\delta+t}\rangle}{\langle\left|I_{q,\delta}\right|^2\rangle}\right) \tag{2.18}$$

From Equation (2.18), the image structuring function $S(\mathbf{q},t)$ is expressed in simple form as shown in Equation (2.19) [35], [36], [38], which also contains an expression for added noise contributions from the camera, $B(\mathbf{q})$, e.g. camera read-out noise.

$$S(\mathbf{q},t) = A(\mathbf{q})[1 - g_{2D}] + B(\mathbf{q}) \tag{2.19}$$

where $A(\mathbf{q}) = 2\langle\left|I_{q,\delta}\right|^2\rangle$ which depends on imaging system [35], [66], $B(\mathbf{q})$ accounts for noise of the imaging system, and g_{2D} is the autocorrelation function.

The image structuring function does not directly obtain autocorrelation function. Instead, it needs to evaluate $A(\mathbf{q})$ and $B(\mathbf{q})$ to yield the autocorrelation.

Thus there are two different scheme to estimate $A(\mathbf{q})$ and $B(\mathbf{q})$ [38], accordingly. In scheme 1, $A(\mathbf{q})$ and $B(\mathbf{q})$ can be treated as adjusting parameters, whilst in scheme 2, $A(\mathbf{q})$ and $B(\mathbf{q})$ are measured independently. At short time intervals, in which $g_{2D} = 1$ and $S(\mathbf{q},t\to 0) = B(\mathbf{q})$. Similarly, at long time intervals, $g_{2D} = 0$, $S(\mathbf{q},t\to\infty) =$

$A(\mathbf{q}) + B(\mathbf{q})$. Accordingly, the autocorrelation g_{2D} is evaluated by substituting $A(\mathbf{q})$ and $B(\mathbf{q})$ which can be obtained from either scheme. At this point, it should be stated that only scheme 1 was implemented in this thesis, due to the difficultly in measuring long enough lag times t for $g_{2D} = 0$ in the scheme 2. The DDA scheme can be visualised in Figure 2.2.

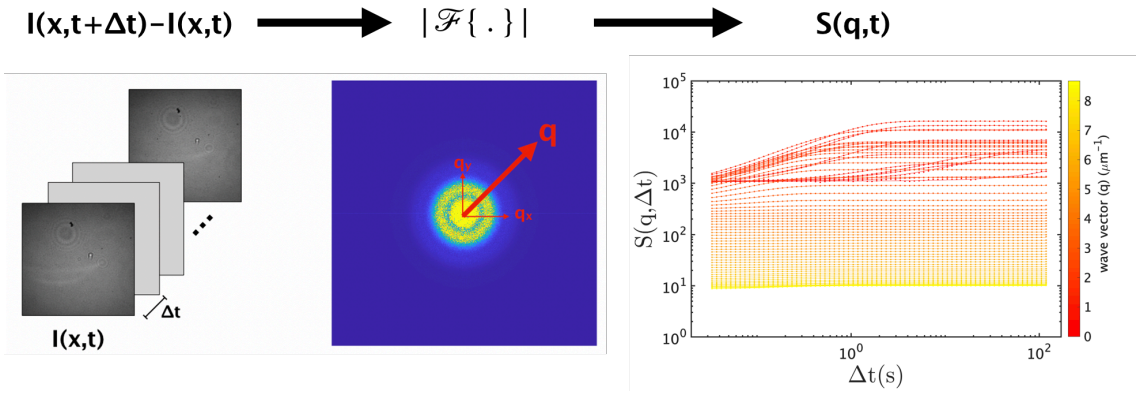

Figure 2.2. Schematic showing the work flow of Differential Dynamic Analysis (DDA).

2.3 Passive Rheology

Conventional rheometry measures samples with large quantities, > 1 mL of sample using mechanical measurements [22], [64]. In contrast, DDM can characterise the dynamics of colloidal suspension using microliters sample volume via passive rheology [22], [64]. This small sample volume requirement is of particular benefit to rheological inspection of rare or costly materials in which it is hard to synthesize and obtain the necessary volumes for traditional analysis. In addition, the low inertia of probe particles allows measurement of a high frequency response of materials [22], [64].

Typically, passive rheology usually refers to Brownian motion of particles [85]. It is based on entirely thermal energy $k_B T$ to create dynamic measurements, where particles experience forces which arise from molecules surrounding them. Changes in the position/location of these particles due to these forces can be monitored. The GSER [86] provides a method to quantify particle displacement, thermal energy and

the viscoelastic behaviour of the fluid. This Section now provides a fundamental understanding of rheological measurement which depends upon the fluid properties, which can be either Newtonian and non-Newtonian fluids. In addition, the method to quantify dynamics of colloidal particles using DDM is also described.

2.3.1 Brownian motion

Brownian motion is explained by the random thermal collision of suspending medium molecules that act onto a particle [87]. As a consequence, the particle moves diffusively. In macroscopic view, this suspension is at an equilibrium state, where the medium does not move. For this reason, time-averaging of the total force applied to the particles will be zero. However, the average distance from any initial position of a particle increases with time.

Gravity also pays a negligible contribution to the motion of particle [38] (when gravitation forces dominate the Brownian motion, the particle will rapidly sediment). To ensure that such a particle is in Brownian motion, thermal energies (k_BT) must dominate gravity force in which $K_BT > \frac{4}{3}\pi a^3 \Delta\rho \mathbf{g} h$ [88]. This circumstance can also be characterised by Péclet number (Pe) where $Pe = \frac{4}{3}\pi a^3 \Delta\rho \mathbf{g} h / K_BT$ [89], a dimensionless value relating the ratio of convective to diffusive movement. For non-interacting particles, a high concentration of the colloidal particles setting leads to collision among the suspended particles. That is, the particles are likely to move in a confined area resulting underestimate diffusion coefficient and lead to overestimate the fluid viscosity. However, this problem can be simply tackled by diluting the particles. In addition, hydrodynamic interaction with the wall and surface also shows a decreasing diffusion coefficient as the particles moving in a confined geometries [90] and small sample volume [91], [92]. The motion of particles proximity to a wall is slow down caused by so-called wall drag effect [93]. To minimise this contribution, field-of-view of the device should be away from the surfaces of sample container.

In detail, the analysis of particle motions will rely upon their MSD instead of their average distance [94], as the diffusion effect of Brownian motion is related to probability distribution of the movements [95]. Einstein and Smoluchowski independently related the MSD $\langle \Delta r^2(t) \rangle$ of the colloidal particles to the time, t [87]. The result relationship leads to diffusion coefficient in Equation (2.20), [96].

$$\lim_{t \to \infty} \langle \Delta r^2(t) \rangle = 2dDt \tag{2.20}$$

where d is the dimension of displacement, D is a Einstein-Smoluchowski diffusivity, and $\Delta r^2(t)$ is the mean square displacement at specified time, t.

Sutherland [28] later related the diffusion coefficient to thermal energy and frictional coefficient as shown in Equation (2.21).

$$D = \frac{k_B T}{f_{drag}} \tag{2.21}$$

where k_B is the Boltzmann's constant, T is the absolute temperature, and f_{drag} is the drag force of particles.

When a colloidal probe particle is a perfect sphere, the frictional coefficient is given by $f_{drag} = 6\pi\eta r$ which also known as Stokes drag [76], where r is the average radius of colloidal particles. As a result, the diffusion coefficient is defined by equation (2.22) [35], [36].

$$D = \frac{k_B T}{6\pi\eta r} \tag{2.22}$$

2.3.2 DDM and Stokes-Einstein relation

Intensity fluctuations of suspended particles during Brownian motion are represented by a dynamic. For quantitative characterisation of DDM, these fluctuations are themselves related to exponential decay of the autocorrelation function, g_{2D}. Regarding to image structuring function (2.19), the autocorrelation g_{2D} of spherical Brownian particles is given by Equation (2.23) [35], [38], [97].

$$g_{2D} = e^{\left(\frac{-t}{\tau_c}\right)} \tag{2.23}$$

where $\tau_c = \frac{1}{D \cdot \mathbf{q}^2}$ is the characteristic diffusion time [35], and $\mathbf{q}$ is the wave vector

The average Fourier spectrum from Equation (2.21) represents the autocorrelation function of Brownian motion. However, the resulting averaging value also includes the terms $A(\mathbf{q})$ and $B(\mathbf{q})$, see Equation (2.19). To achieve the autocorrelation function, $A(\mathbf{q})$ and $B(\mathbf{q})$ are required and they can be evaluated from the two schemes, as described above, Section 2.2.

Another representation of the characteristic diffusion time, τ_c can be given by applying a logarithm to both side of the above equation, where $\tau_c = \frac{1}{D \cdot \mathbf{q}^2}$ is shown in Equation (2.24).

$$\log \tau_c = -2 \log q - \log D \tag{2.24}$$

From the Equation (2.24), the diffusion coefficient of suspended particles can be obtained by determining y-intercept of the plot between $\log \tau_c$ and $\log q$.

2.4 Measurement of viscoelastic moduli

Evaluation of the mean square displacement of Brownian motion is necessary for obtaining fluid viscoelasticity. Given that the GSER relates displacement to the viscoelasticity, as indicated in Equation (2.27), the mean square displacement for a typical DDM system can be readily obtained by [25], [98]. Due to modification of the autocorrelation function, the calculation of mean square displacement can be determined by the following procedure:

1. substitute $\tau_c = \frac{1}{D \cdot \mathbf{q}^2}$ and the autocorrelation function g_{2D} can be rearranged in the form as shown in the Equation (2.25) [25], [98].

$$g_{2D} = e^{\frac{-\langle \Delta r^2(t) \rangle \cdot \mathbf{q}^2}{4}} \tag{2.25}$$

2. To obtain the mean square displacement, Equation (2.25) is substituted into Equation (2.19). Thus, the formation of the mean square displacement becomes (2.26) [25], [98].

$$\langle \Delta r^2(t) \rangle = \frac{-4}{\mathbf{q}^2}\left(\ln\left(1 - \frac{\mathcal{D}(\mathbf{q},\tau) - B(\mathbf{q})}{A(\mathbf{q})}\right)\right) \tag{2.26}$$

3. Viscoelasticity can thus be determined using Mason method, as shown in the Equation (2.27), [86].

2.4.1 Generalised Stokes-Einstein Relation (GSER)

The Stokes component of the Stokes-Einstein relation is valid only for Newtonian fluids. However, Mason and Weitz [51] used the Langevin Equation to theoretically and experimentally generalise Stokes-Einstein Relation, to describe non-Newtonian fluids. By establishing the relationship between ensemble-average displacement of

particles they described the macroscopic viscoelastic response of such a fluid. Nevertheless, this equation is based under the assumption that a complex fluid is considered as a continuum around particles. This relation provides accessibility to viscoelastic modulus $G^*(\omega)$ of the fluid and lead to modern rheology study [28].

Typically, the GSER has several advantages when compared to conventional method. First, there is no external forces applied. The thermal energy $k_B T$ of Brownian motion is embedded as colloidal or tracer probes randomly move. Furthermore, as the mass of probe particles are very small, their inertia can be negligible [28], [99], such that the viscoelasticity of the fluid can be measured [100] at high frequencies, up to 100 kHz (measurements which would require large force and torques in conventional methods [101]). A further advantage is that the results can be correlated with conventional bulk measurement approaches whilst only requiring microlitres of sample volume. Last but not least, this technique has the advantage that it can also be applied to living cells whereas there no current, similar approaches available [102].

Viscoelasticity is a property of material which comprises both elasticity and viscosity. When stresses have been applied to viscoelastic material, the material deformed, although, it returns to its original state when the stresses are released. In the GSER, the complex viscoelastic modulus $G^*(\omega)$ can be obtained by Equation (2.27), [86].

$$G^*(\omega) = \frac{k_B \cdot T}{\pi \cdot a \cdot \langle \Delta r\left({}^{1}/_{\omega}\right)\rangle \cdot \Gamma\left(1 + \alpha\left({}^{1}/_{\omega}\right)\right)} \tag{2.27}$$

where $\alpha\left({}^{1}/_{\omega}\right)$ is the log-log slope of MSD at $t = {}^{1}/_{\omega}$, a is the average radius of colloidal particles, $\Gamma(.)$ is the gamma function [86] and ω is the measuring angular frequency.

Typically, the viscoelastic modulus exhibits both of storage modulus $G'(\omega)$ and loss modulus $G''(\omega)$. The real $\left(G'(\omega)\right)$ and imaginary $\left(G''(\omega)\right)$ parts of viscoelastic modulus $G^*(\omega)$ represent the solid-like and liquid-like behaviour of the medium respectively [76]. When a material is purely solid, its loss modulus $G''(\omega) = 0$. In the same manner, the storage modulus of a material $G'(\omega) = 0$, if such material is purely liquid. These two moduli can be defined as Equations (2.28) and (2.29) respectively, [86].

$$G'(\omega) = G^*(\omega) \cdot cos\left(\frac{\pi \cdot \alpha(\omega)}{2}\right) \tag{2.28}$$

$$G''(\omega) = G^*(\omega) \cdot sin\left(\frac{\pi \cdot \alpha(\omega)}{2}\right) \tag{2.29}$$

2.4.2 A direct conversion method

Viscoelastic behaviour conversion using the GSER has been reported for numerical artefacts at high frequencies [103] as it has a two-step numerical conversion [69], [70]. This method is however reported to underestimate loss modulus [77]. A direct conversion method proposed by Evans et al [69], [70] provides an alternative approach to eliminate such numerical artefacts at high frequencies. This approach directly converts creep compliance $J(t)$ into viscoelastic modulus $G^*(\omega)$ but data interpolation and extrapolation of the mean square displacement $\langle \Delta r^2(t) \rangle$ is necessary. The approach is defined by Equation (2.30), [40].

$$\frac{i\omega}{G^*(\omega)} = i\omega J(0) + \left(1 - e^{-i\omega t_1}\right) \cdot \frac{\left(J_1 - J(0)\right)}{t_1} + \frac{e^{-i\omega t_n}}{\eta} + \sum_{k=2}^{N} \left(\frac{J_k - J_{k-1}}{t_k - t_{k-1}}\right) \cdot \left(e^{-i\omega t_{k-1}} - e^{-i\omega t_k}\right) \tag{2.30}$$

Where $J(t) = \langle \Delta r^2(t) \rangle \cdot \frac{\pi a}{K_b T}$, [104].

2.5 Evaluation of steady-shear viscosity

Viscosity is an important physical property of fluids to characterise its resistance to deformation in flow. In oscillatory shear experiment, complex viscosity can be obtained via $\eta^*(\omega) = \frac{G^*(\omega)}{i\omega}$. To compare oscillatory and shear flow measurements, the complex viscosity can be converted to steady-shear viscosity using Cox-Merz rule [71], as an empirical relationship which relates the steady state shear viscosity of shear rate, $\eta(\dot{\gamma})$, and the complex viscosity of angular frequency, $|\eta^*(\omega)|$, as shown in Equation (2.31) [105].

$$\eta(\dot{\gamma}) = |\eta^*(\omega)| \text{ for } \dot{\gamma} = \omega \tag{2.31}$$

2.6 Particle size distribution

In addition to viscoelasticity measurements, particle size distribution can be obtained using the developed device, see later. According to Equation (2.19), the autocorrelation of monodisperse particle suspended in a liquid can be modelled by a single exponential decay. When two or more particle populations are mixed, the resulting decay is an average form of each decays of the populations composition.

Thus, the typical analysis of single decay by DDA Equation (2.19) cannot be decomposed. Although, analytical methods have been developed to decompose the composite decay and then convert to particle size distribution information, these are time-consuming. In this research, we propose to use the nonnegativity least square (NNLS) method [106] to obtain the particle size distribution. The particle size cannot be negative from the constrained treatment in the NNLS, providing a method with reduced computational time to retrieve the particle size distribution [107], [108].

In short, monodisperse solutions generate a single exponential decay which is described by $e^{\frac{-t}{\tau}}$. A summation of single exponential decays can be represented in polydisperse solution. If, weights, w, are subsequently added to the decays to represent amount of particles. The final form of polydisperse particle is represented in Equation (2.32), [109].

$$g_{2D} = w_0 e^{\frac{-t}{\tau_0}} + w_1 e^{\frac{-t}{\tau_1}} + \cdots w_n e^{\frac{-t}{\tau_n}} = \sum_{i=0}^{n} w_i e^{\frac{-t}{\tau_i}} \tag{2.32}$$

Unlike DLS system, the multi scattering wave vector $\mathbf{q}$ is recorded by our proposed DDM system. These wave vectors can be regarded as angle parameters which are shown in the Equation (2.33). To achieve optimal value of Y, iterative calculation is required under $\min|Y - \phi X|^2$ criteria, where $X \geq 0$ [110], [111].

$$\begin{bmatrix} Y_1 \\ Y_2 \\ \vdots \\ Y_3 \end{bmatrix} = \begin{bmatrix} \phi_{11} & \cdots & \phi_{1n} \\ \phi_{21} & \cdots & \phi_{2n} \\ \vdots & \ddots & \vdots \\ \phi_{m1} & \cdots & \phi_{mn} \end{bmatrix} \begin{bmatrix} X_1 \\ X_2 \\ \vdots \\ X_m \end{bmatrix} \tag{2.33}$$

Where $\phi_{mn} = e^{\frac{-t_m}{\tau_n}}$, m is the total number of measurements, n is the total characteristic time collected from DDM device , and Y is the result distribution

Chapter 3

Material and Methods

Rheological properties provide insights to mechanical behaviours and responses following an applied stress to the material [112]. In this thesis, a DDM-based device was developed and realised as a portable microscale rheological device to characterise rheological behaviour of the fluids. This approach probes the movement of microparticles to infer the fluids' rheological behaviours. Thus, both size and concentration of the probe particles are crucial for the device to perform the rheological measurement. To determine this limitation, sizes and concentration of the probe particles that can be used with the device are studied in this Chapter. In addition, material and methods used in the experiments throughout this thesis are also given. This includes the development and characterisation of the developed portable device for evaluation of viscoelastic behaviour of biological materials e.g. human whole blood and human saliva (described in detail in Chapter 6).

3.1 Materials

3.1.1 Newtonian fluids

Deionised water and stock solution of Glycerol (G9012-500ML, >= 99.5%, Sigma-Aldrich Corp.) were used for preparation of glycerol-water mixtures from glycerol content of 0, 10, 20, 30, 40, 50, 60, 70, 80, 90 and 100 percent by weight. A Bovine

Serum Albumin (BSA) solution was prepared by diluting 80 mg of BSA powder (A9085-25G, Sigma-Aldrich Corp.) with 1 mL of deionised water. For blood plasma preparation, whole blood sample (Cambridge Bioscience) was centrifuged at 1.5 g for 10 min. For purification, the supernatant was transferred to an Eppendorf tube. The tube was re-centrifuged at the same configuration and the supernatant was kept in a 4°C fridge, prior to measurement.

3.1.2 Viscoelastic liquid

Polyethylene oxide (PEO) solutions of 1%, 2%, and 5% by weight were prepared by diluting PEO powder (181994-250G, Mw 200,000, Aldrich) with deionised water. Whole blood samples were obtained from commercially source (Cambridge Bioscience, screened samples) and Queen Elizabeth University Hospital, Glasgow (Strokes patients, Unscreened samples). Human whole saliva was obtained from a commercially available source (Bio IVT Inc.). Both whole blood and saliva sample were stored in 4 °C fridge.

3.1.3 Probe particles

Stock solutions of polystyrene microparticle (Bangs laboratories and Polysciences Inc.) sizes of 0.15, 0.21, 0.29, 0.35, 0.52, 1.00, 1.54, and 2.10 μm were diluted by 10^3 times with a sample fluid prior to measurement. The specification of stock solutions of the polystyrene microparticles in the experiment are indicated in Table 3.1.

Table 3.1 Specification of probe particles used in the experiment

Diameter (μm)	**Weight (g/ml)**	**Density (g/cm^3)**	**Original concentration ($\times 10^{10}$ particles/ml)**	**Company**
0.15	0.01	1.05	538.93	Bangs Laboratories, Inc.
0.21	0.01		202.41	
0.29	0.01		1.05	
0.35	0.01		43.16	Polysciences, Inc.
1.00	0.03		4.73	
1.54	0.03		1.39	
2.10	0.03		0.53	

3.2 Sample container

In this work, Brownian motion of embedded microparticles were monitored via passive rheology approach. Sample evaporation, which is affected to equilibrium of the motion, inevitably influenced the measurement result. To prevent this , the sample were tested in an enclosed container which was produced using a glass slide as indicated in Section 3.2.1.

3.2.1 In-house microchamber

An in-house microchamber was made of double-sided tape (260 μm thickness) and a glass slide. For the glass slide, a cleaning process was necessary to remove dust particles, impurities and contamination on the glass surface, involving sonication of the slide filled with acetone for 5 minutes. Then, the slide was washed using methanol and blow-dry with nitrogen. Finally, the slide is put in oxygen plasma asher to remove organic contamination on the glass surface for one minute. Following this, the tape was punched to form a diameter of 6.0 mm hole, and placed on a glass slide to create

a microwell of the microchamber. For a rheological measurement, a sample approximately of 6.0 µL was dispensed in the microwell before a coverslip was placed on top of it. Nail vanish was applied to seal around the edges of the coverslip to prevent sample evaporation as illustrated in Fig 3.1.

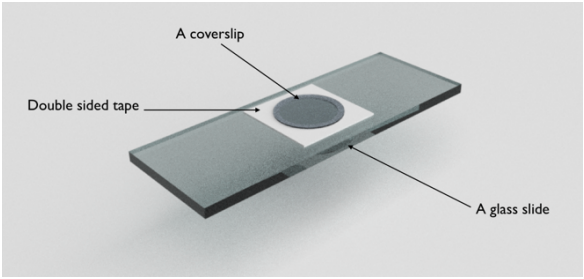

Figure 3.1 A 3D model of an in-house microchamber.

3.3 Developed device

The development of a device for use in DDM was extension of previous work using an optical heterodyne near-field scattering (HNFS) [113]–[115]. This optical detection scheme collects the modulation of transmitted light and scattered light of a sample fluid in a focused plane [114]. As a result, the developed device is simply implemented using light transmission configuration which allows for the heterodyne detection scheme as illustrated in Figure 3.2.

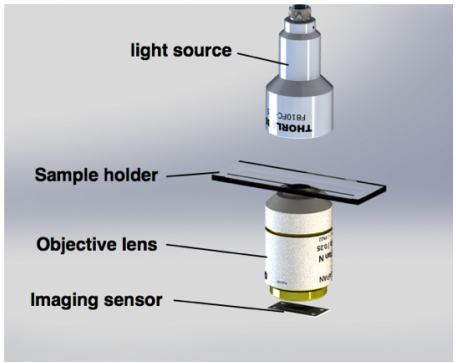

(a)

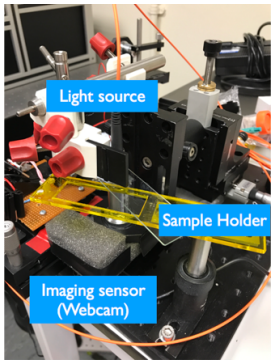

(b)

Figure 3.2. (a) 3D schematic of our developed system. (b) Hardware implementation from (a) comprising a light source, sample holder, objective lens, and an imaging sensor.

A monochromatic LED light source ($\lambda = 532$ nm), which was coupled with an optical fibre, creates spatial coherence at the end of an optical fibre [116]. When the light passed through a sample fluid, it was diffracted and enlarged by an objective lens [117]. Diffracted light was collected by an imaging sensor for further processing. The ray diagram of the developed device is shown in Figure 3.3(a) whereas the Figure 3.3(b) illustrated a typical DLS system for comparison.

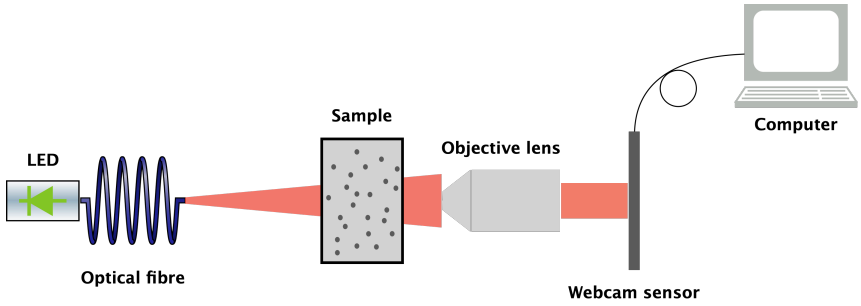

(a)

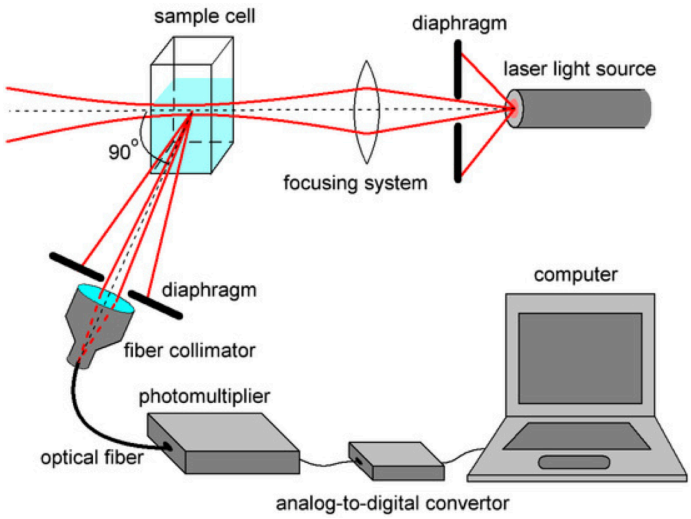

(b)

Figure 3.3. Ray diagrams of (a) the developed device and (b) a typical DLS system (Image taken from [118]) .

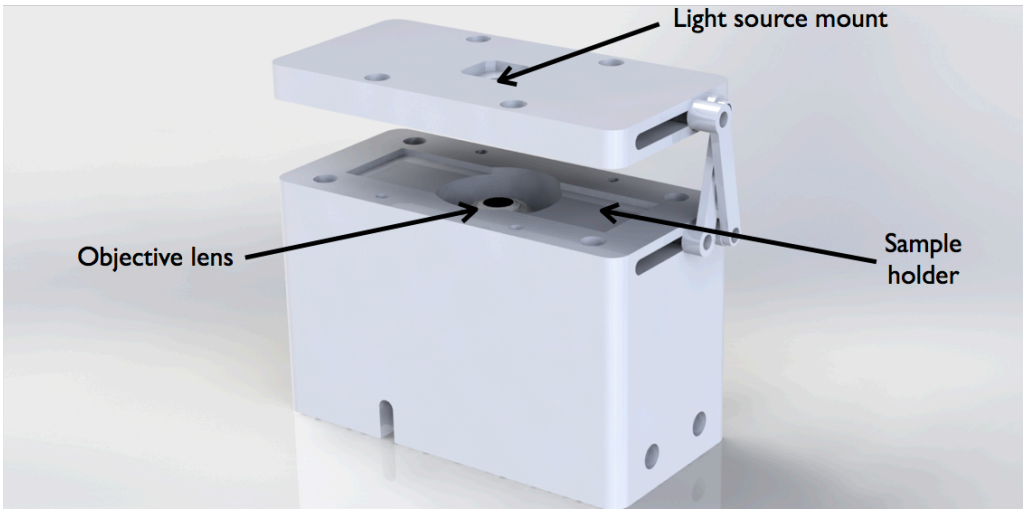

(a)

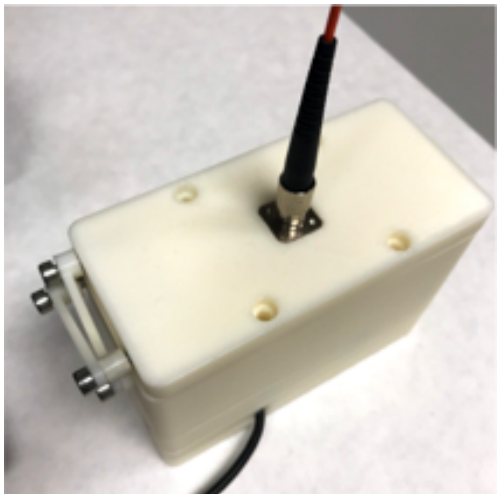

(b)

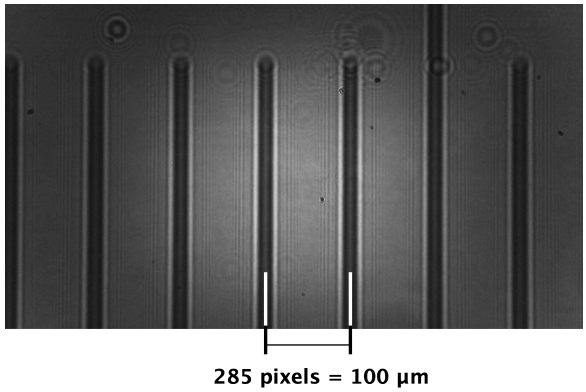

(c)

Figure 3.4. 3D model and resolving power of our developed system. (a) is the 3D model, (b) is the developed device, and (c) indicates resolving power of the device (a 1920x1080 pixels image with scale bar obtained from the device without cropping)

The sample holder and component support were made using a 3D printer. These printed parts were connected by screw fittings as illustrated in the Figure 3.4(a). The pixel size of the image was obtained by taking an image of microscope slide with a known reference scale, such that the pixel size can be calculated by dividing the known scale with measuring pixels distance which is 0.35 µm. This measurement is illustrated in Figure 3.4(b).

Figure 3.4(b) depicts that the width of the captured image is 800 pixels, giving a total field-of-view is 0.08 mm^2. To operate the device, sample was pipetted (6.0 µL) into the sample container. Next, the sample was covered with a coverslip to prevent sample evaporation. Then, the slide was placed on the sample holder as indicated in Figure 3.4(a). To capture the signal, the device was connected to the computer by a USB interface to enable our in-house developed software to acquire the image data. An image sequence is collected for further processing on a computer.

3.3.1 Image time-stamp

Typically, the DDM has been demonstrated using laboratory-grade optical microscope equipped with a camera [47], [119]. This sort of camera has ability to transfer imaging data at real-time from its dedicated connector. In contrast to our developed DDM device, a low-cost webcam (Advent AWCAMHD15,~£20) was employed to collect the data. This system can acquire data and transfer it to the computer in real-time. However, the system may discard some frames that are not able to processed by the camera in time as shown in Figure 3.5.

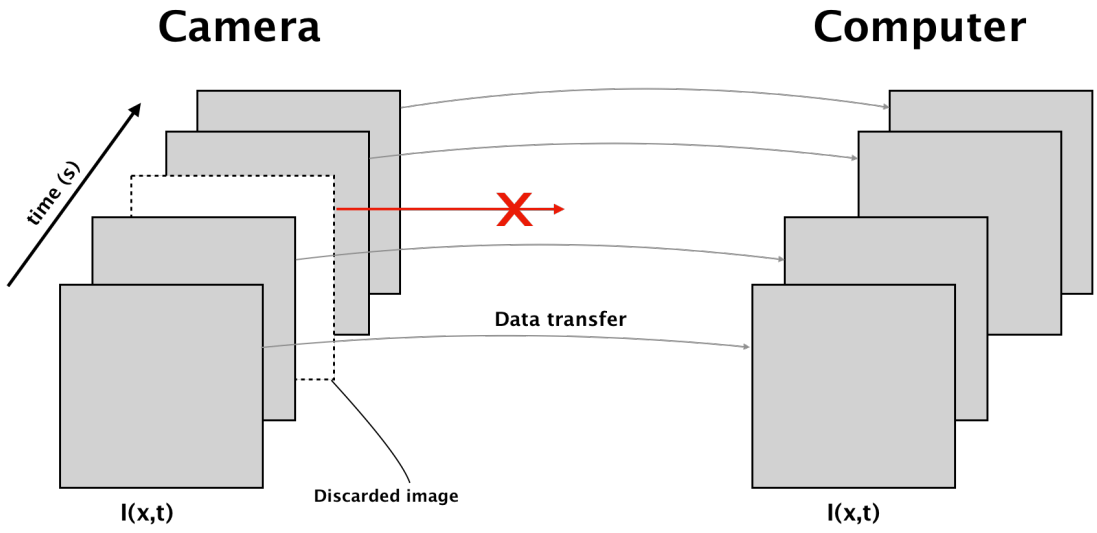

Figure 3.5. An image discarded during data transmission (Video frame drop event). The red arrow with red cross symbol indicates the image is not transfer to the computer.

In fact, DDA calculates correlation of an image series separated by a fixed lag-time. Thus, a problem arises when some images in the series are discarded as shown in Fig 3.6.

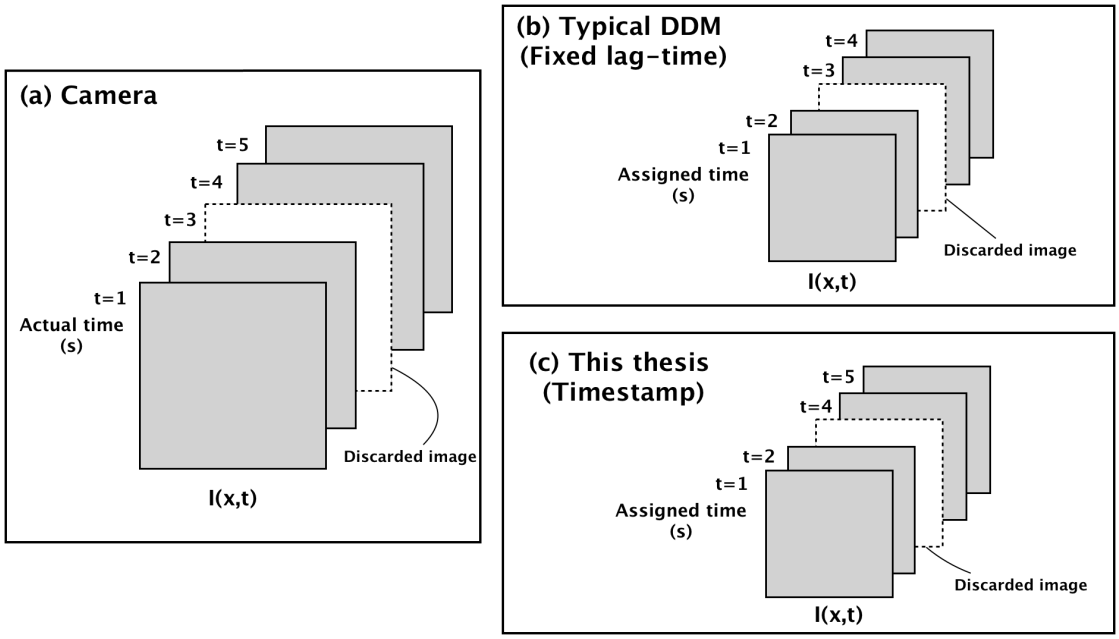

Figure 3.6. Image time-stamped: (a) a camera transfer images to the computer in real-time manner. In the case where some images discarded, the typical DDM assigned these images with a fixed lag-time. Thus, incorrect time information is assigned which is the image at the time t=3 should be t=4 (shown in (b)). This thesis implements image time-stamp to copy actual time information from (a) and assign the time to individual image shown in (c).

In this case, the time of the next coming image is mismatched if using a fixed-lag time for the calculation. To tackle this problem, an image time-stamp was introduced to avoid such effect. Accordingly, the time of a every image received by the acquisition system, is recorded. This modification allows DDA calculates autocorrelation at accurate measurement times, τ.

In order to illustrate the value of this simple manipulation, an image series of 0.52 μm polystyrene particles in deionised water was acquired for 15 minutes at environmental temperature of 20°C. Then, typical and time-stamped DDA were performed on an identical image series collected by the developed device. A characteristic time τ_c was

obtained by linear fitting of the autocorrelation function $\left(g_{2D} = e^{\frac{-\tau}{\tau_c}}\right)$ in logarithm scale. As discussed in Chapter 2, the result characteristic time τ_c is $\frac{1}{D\mathbf{q}^2}$. Then, the diffusion coefficient D was obtained by determining of slope between the linear equation of $\frac{1}{\tau_c} = D\mathbf{q}^2$. In this experiment, the slope was determined by fitting the equation resulting the diffusion coefficient D as shown in Figure 3.7.

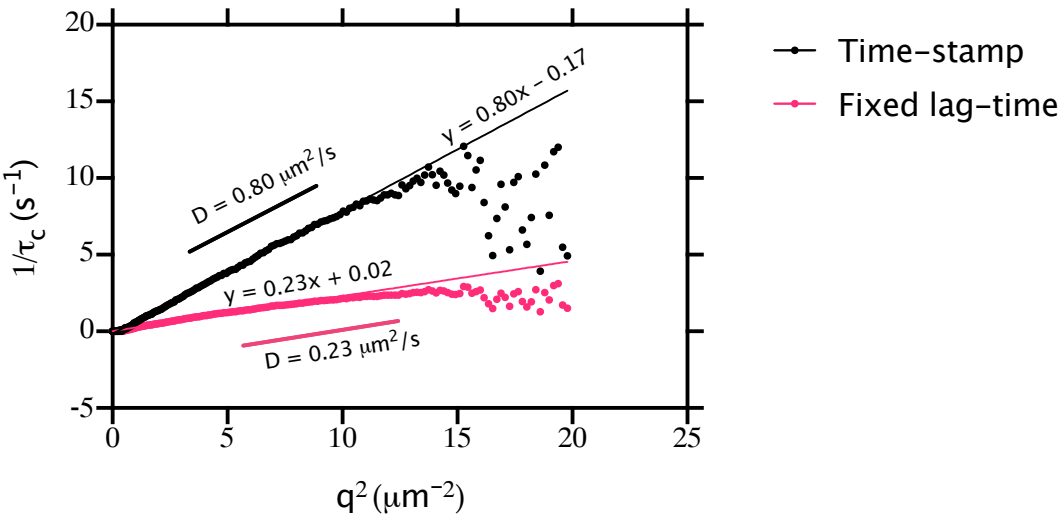

Figure 3.7. A plot of $1/\tau_c$ and q^2 in deionised water at 20°C from using 0.52 μm polystyrene probe microparticles. Black dots represent the data plots when the time-stamp (this thesis) approach is used while the pink dots are the result of using fixed lag-time (typical DDM). The black and red lines denote the fitted line of slope 0.80 and 0.23 $\mu m^2/s$ respectively. The resulting viscosity of deionised water from the fixed lag-time and the time-stamp are 3.61 mPa.s and 1.03 mPa.s respectively.

In Figure 3.7, the $\frac{1}{\tau_c}$ as a function of wave vector $\mathbf{q}$ using a fixed lag-time and time-stamp were plotted. Regarding to the data plot, the diffusion coefficients of using a fixed lag-time was considerably different than that was obtained from using time-stamp. In the fixed lag-time, the obtained diffusion coefficient was 0.23 $\mu m^2/s$ which corresponded to the viscosity of 3.61 mPa.s by Stokes-Einstein equation as $\eta = \frac{K_B T}{4\pi D a}$. In contrast to the time-stamp approach, the obtained diffusion coefficient was 0.80 $\mu m^2/s$ which corresponded to viscosity of 1.03 mPa.s. In comparison with the reference [120], absolute errors of using fixed lag-time (typical DDM) and time-stamp (this

thesis) were 206.54% and 2.72% respectively. Thus, the time-stamp approach was able to tackle unstable image transfer problems in which there were some discarded images and, despite this, produce a reliable result.

3.3.2 Probe particle selection and performance evaluation of the developed device

This section characterises the probe particle selection for rheological investigation with the developed device. By determining sizes of the probe particles in various concentrations, the range of probe sizes that can be used as probe particles is revealed. The result is also compared to a commercial DLS system (Malvern Zetasizer Nano ZS90) to evaluate performance of the device.

A Microbeads size estimation

A verification step is essential to ensure that the autocorrelation function g_{2D} is also applicable to other bead sizes. Accordingly, variation of bead sizes and dilutions were prepared and performed the DDM analysis. In this experiment, the bead sizes of 0.29, 0.52, 1.00 and 1.54 μm were diluted by 10^2, 10^3, 10^4, and 10^5 times their original concentrations. These bead solutions were measured at room temperature using the developed device.

Each sample was pipetted and dispensed in a microchamber then was placed in the sample holder of the device. Accordingly, an image sequence was acquired and analysed by DDA in which their autocorrelation function was evaluated. For monodisperse non-interacting particles [121], the autocorrelation function g_{2D} was related to diffusion coefficient D by $g_{2D} = e^{\frac{t}{\tau_c}}$ where $\tau_c = \frac{1}{D\mathbf{q}^2}$. The diffusion coefficient was either determined by calculating y-intercept between characteristic diffusion time

τ_c and wave vector $\mathbf{q}$ [62], or slope between $\frac{1}{\tau_c}$ and $\mathbf{q}^2$ [122]. The evaluated diffusion coefficient allowed for calculation of diameter of the Brownian particles which were the beads in this case. By perform Stokes-Einstein relation [62], the average diameter of the beads was determined. The outcome beads diameter determined by the approach is illustrated in Fig 3.8.

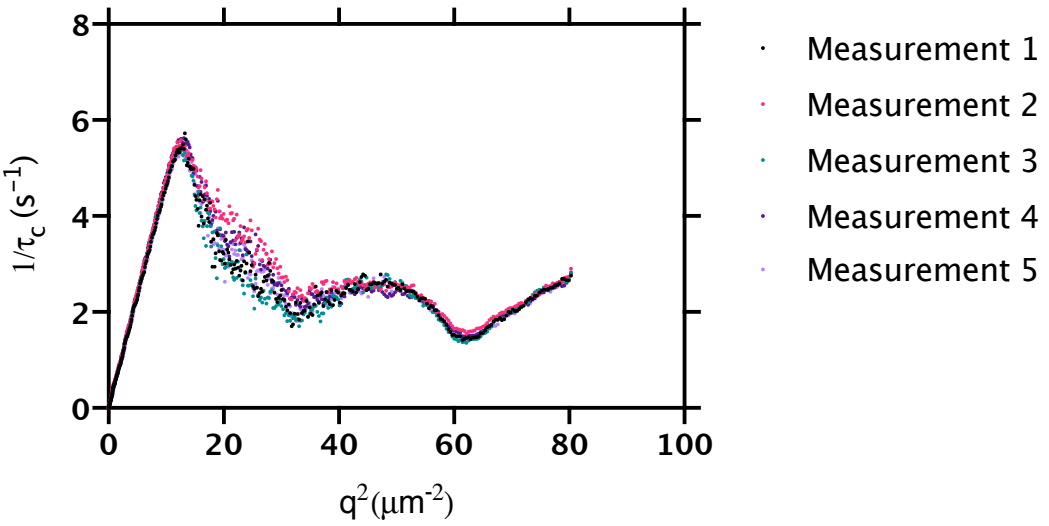

Figure 3.8. A plot between $1/\tau_c$ and q^2 of 1.00μm polystyrene beads diluted 10^2 fold by deionised water. The measurement was performed at room temperature (25°C) and is five-fold replicated. The measurement shows strong linear relationship from $0 \leq q^2 \leq 15$ μm^{-2}. However, Brownian particles crossing image boundary cause significant artefacts at high wave vector q ($q^2 > 15$ μm^{-2}) in DDM experiment [123].

As shown in Fig 3.8, the plot between $\frac{1}{\tau_c}$ and $\mathbf{q}^2$ of 1.00 μm polystyrene beads, diluted by 10^2 fold using deionised water is illustrated. The diffusion coefficient, D, was obtained by calculating the slope between $\frac{1}{\tau_c}$ and $\mathbf{q}^2$ as $\frac{1}{\tau_c} = D\mathbf{q}^2$. Following this, linear regression was performed to the plot of $\frac{1}{\tau_c}$ and $\mathbf{q}^2$ to determine diffusion coefficient D.

Brownian particles crossing image boundary caused significant artefacts at high wave vector $\mathbf{q}$ in DDM experiment [123]. As a result, the linear fitting regime was limited to the maximum $\mathbf{q}^2$ which was 15 μm^{-2} ($\mathbf{q} = 3.87$ μm^{-1}) for the experiment in Fig 3.8.

Accordingly, the linear regression fitting was performed for all replications of experiment to determine average diffusion coefficient D which was summarised in Table 3.2.

Table 3.2. The corresponding goodness of fit obtained by performing linear regression to the measurement of Figure 3.8 for wave vector range of $0 \leq q^2 \leq 15$ μm^{-2}. Data was collected using 1.00 μm polystyrene beads, diluted by 10^2 fold using deionised water.

Measurement	Slope	Y-intercept	R-Squared
1	0.46	0.01	1.00
2	0.48	0.02	1.00
3	0.48	-0.03	1.00
4	0.49	0.01	1.00
5	0.46	-0.01	1.00
Mean	0.47		
SD	0.01		

From Table 3.2, the average diffusion coefficient D obtaining from five-fold replication of 1.00 μm polystyrene beads diluted by 10^2 fold in deionised water was 0.47 μm^2/s with SD of 0.01. For measurement validation, the obtained diffusion coefficient was substituted in Stokes-Einstein relation for evaluation of average particle size as $a = \frac{K_B T}{4\pi D \eta}$. Thus, the average size of beads in deionised water was 1.04 μm which was close to the factory stated nominal value. By analogy to the above process, diffusion coefficient of various bead sizes are measured which is shown in Table 3.3 and the corresponding bead sizes are illustrated in Figure 3.9.

Table 3.3. Diffusion coefficients of various bead sizes diluted with deionised water by measurements using developed device. Data was collected using 1.00 µm polystyrene beads, diluted by 10^2 fold using deionised water.

Nominal (µm)	Dilutions			
	Diffusion coefficient (at times dilution, mean ± SD ,$\times 10^{-12}$ µm^2/s)			
	10^2	10^3	10^4	10^5
0.29	0.84 ± 0.13	1.01 ± 0.08	*	*
0.52	0.60 ± 0.02	0.59 ± 0.02	*	*
1.00	0.31 ± 0.01	0.32 ± 0.02	0.29 ± 0.02	0.34 ± 0.12
1.54	0.21 ± 0.01	0.20 ± 0.01	0.22 ± 0.03	*

*** indicates linear regression fails to fit due to the unexpected nonlinear relationship between $\frac{1}{\tau_c}$ and q^2 in the fitting regime of $0 \leq q^2 \leq 15$ µm^{-2}.**

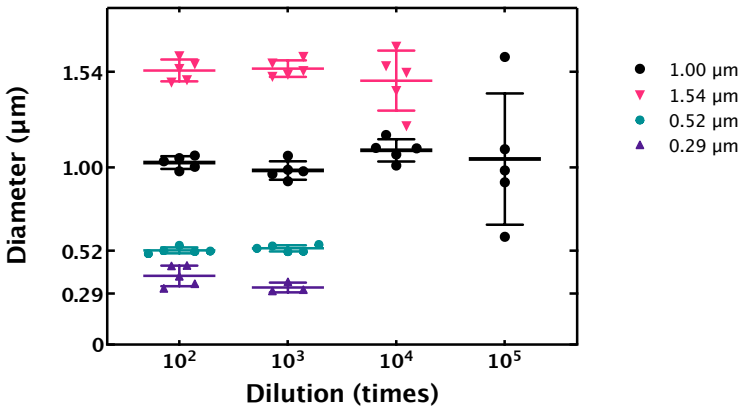

Nominal (µm)	Concentration (mean ± SD , µm)			
	Estimated diameter (at times dilution)			
	10^2	10^3	10^4	10^5
0.29	0.39 ± 0.06	0.32 ± 0.03	*	*
0.52	0.53 ± 0.02	0.54 ± 0.02	*	*
1.00	1.03 ± 0.04	0.98 ± 0.05	1.09 ± 0.06	1.05 ± 0.37
1.54	1.55 ± 0.06	1.56 ± 0.05	1.49 ± 0.17	*

*** indicates undefined value due to unable to obtain the diffusion coefficient regarding to Table 3.3**

Figure 3.9. A plot of estimated particle sizes which are diluted in deionised water at 298.15K. Data was collected using 1.00 µm polystyrene beads, diluted by 10^2 fold using deionised water. The symbols show the nominal sizes which are 0.29, 0.52, 1.00 and 1.54 µm. Each data plot represents the estimated value along the indicated size by the symbols. The mean and SD are represented by a bar where the middle line shows the average value. The top and bottom lines indicate +SD and -SD respectively.

From Figure 3.9, the result showed estimated bead sizes in the diluted solutions. At low concentration, the estimated value had a higher SD compared to the lower concentration, as there was not a sufficient number of beads represented in the image in the FOV of the device (0.08 mm^2). By analogous at high concentrations, the beads easily hit adjacency beads and motion was not in Brownian equilibrium.

B Particles dilution limit

In this Section, particle dilution limit of the developed device is investigated. The maximum dilution was determined to indicate the lowest concentration of particles that can be used as a probe particle. This number refers to a minimum number of probe particles that can be used for measuring of the fluid of interest and still achieve a "reliable" result. In the measurement, again polystyrene microparticles with diameters of 1.00 and 1.54 μm were diluted by 10^2, 10^3, 10^4, and 10^5 times of original concentrations. Then, their sizes were measured by both the developed device and the DLS system as shown in Figure 3.1.

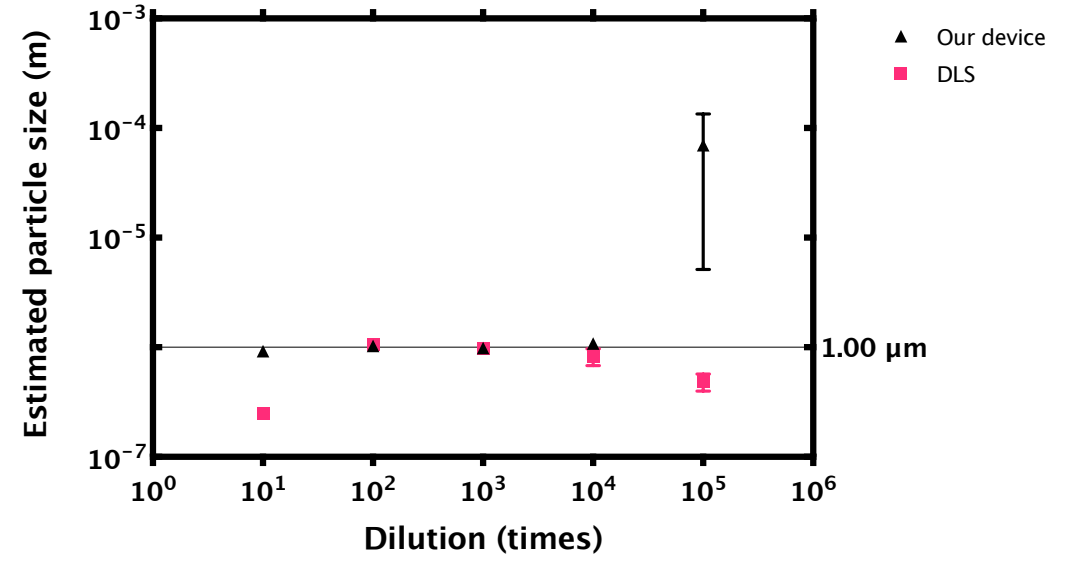

(a)

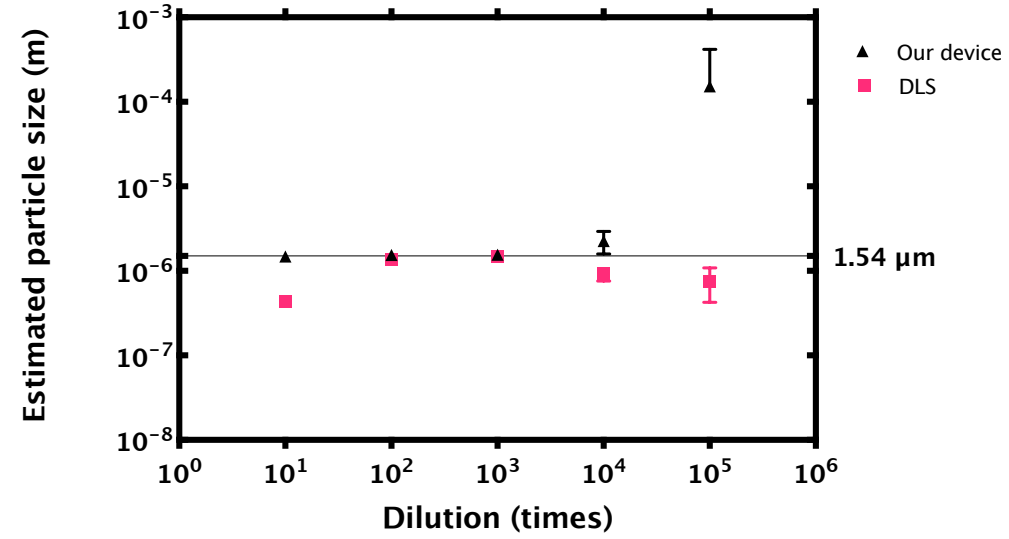

(b)

Figure 3.10. The particle size dilution limit of 10-folded serial dilution of polystyrene bead. The symbols represent the average value of the size estimation of (a) 1.00 µm and (b) 1.54 µm. The error bars in the plot indicate SD from five measurements in each dilution (no display if the SD is very small compared to the size of the symbol).

Regarding the result from Figure 3.10, our device has ability to detect high concentrations of beads (x 10 times) compared to the reference DLS system (Malvern Zetasizer Nano ZS90). In experiments involving 10^2 and 10^3 fold dilutions, both systems can estimate the beads sizes accurately. In contrast to low concentrations (10^4 and 10^5 fold), our device cannot achieve accurate result with the absolute errors are more than

8% as shown in Table 3.4 and Table 3.5 for particle size estimation of 1.00 and 1.54 μm respectively. The reason for this is the FOV of the developed device is quite small (280 x 280 μm^2). This is lead to small amount of the probe particles are presented in the acquired image.

Table 3.4. Particle size estimation of 1.00 μm polystyrene microparticles with various dilutions by developed device and dynamic light scattering (Malvern Zetasizer Nano ZS90)

Dilutions (times)	**Estimated average particle size (μm)**		**Absolute error (%)**	
	Developed device	**DLS**	**Developed device**	**DLS**
10	0.92	0.25	**8.00**	**75.09**
10^2	1.03	1.05	**2.76**	**5.02**
10^3	0.98	0.98	**1.67**	**1.60**
10^4	1.08	0.82	**8.38**	**17.76**
10^5	0.07	0.48	**6,893.00**	**51.55**

Table 3.5. Particle size estimation of 1.54 μm polystyrene microparticles with various dilutions by developed device and dynamic light scattering (Malvern Zetasizer Nano ZS90)

Dilutions (times)	**Estimated average particle size (μm)**		**Absolute error (%)**	
	Developed device	**DLS**	**Developed device**	**DLS**
10	1.48	0.43	**4.17**	**71.84**
10^2	1.55	1.38	**0.51**	**10.35**
10^3	1.56	1.49	**1.15**	**3.33**
10^4	2.26	0.92	**46.67**	**40.37**
10^5	0.002	0.75	**9840.18**	**51.05**

In summary, our device can estimate the concentration of 1.00 µm and 1.54 µm polystyrene particles between 10 – 10^3 fold dilutions of original concentrations which are 4.55 x 10^{10} and 1.51 x 10^{10} particles/mL respectively. However, the reference DLS system can accurately estimate the bead sizes in the range of 10^2 – 10^3 times of original concentration. In contrast to the DLS, the developed device is able to measure concentrated microparticles with diameters of 1.00 and 1.54 µm up to 4.55x10^9 and 1.51x10^9 particles/mL (10 times dilution) respectively.

C Performance evaluation

This section measured the agreement of particle size estimation between the developed device and the DLS system. Particle solutions with diameters of 0.29, 0.35, 0.52, 1.00, and 1.54 µm are diluted by 10^2 times of their original concentration. The particle sizes obtained by both devices are plotted as shown in Figure 3.1.

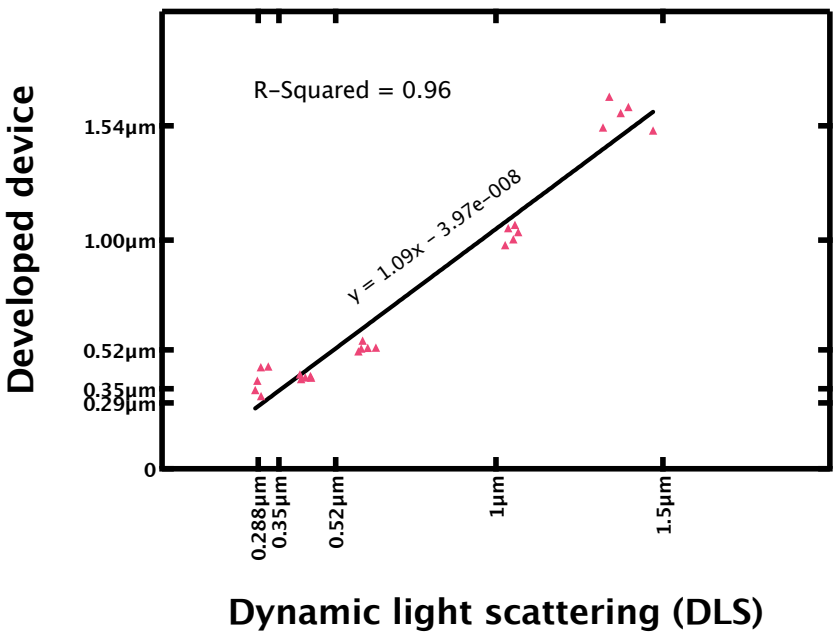

Figure 3.11. A correlation plot between our device and the reference DLS system.

According to Figure 3.11, this experiment shows the correlation between our device and the reference DLS system. Each data plot represents the estimated bead size from

our device and the reference DLS system. The bead sizes used in this experiment are 0.29, 0.52, 1.00 and 1.54 μm. The result shows that bead size estimation of our device has highly correlated with the reference DLS system which is indicated by r-squared value (0.96).

3.4 Conclusions

In this chapter, a DDM based device was developed for rheological investigation of fluids. In contrast to typical DDM device, this device employs a low-cost webcam as a sensor which allows for resource limiting countries. However, the webcam may discard some images in order to transfer them to a computer in real-time. This problem is considerable in a typical DDM calculation, which assumes every image has a fixed lag-time. As a result, time information that associated with each image is inaccurate if there are some images discarded. In this chapter, a time-stamp image is implemented to associate actual time information to the image captured by the webcam. Thus, the developed device produces more reliable result.

Microparticles were then added to a fluid of interest and their motions were obtained by the developed device to infer the corresponding rheological response fluid using passive rheology principle. However, the size and concentration of the probe particle were found to be crucial, as the probe must be visible to the device and concentrated enough to contribute the motion signals. This chapter characterised the probe sizes and concentration that can be used for the developed device to measure. The results were compared with a commercial dynamic light scattering system (Malvern Zetasizer Nano ZS90) for verification.

In 10^2 and 10^3 fold dilutions from factory prepared samples, both systems can estimate the beads sizes accurately. In contrast to low concentration (10^4 and 10^5 times), both systems cannot achieve accurate result with the absolute errors are more than 8%.

However, our developed system provides more reliable result than the DLS system at 10 times dilution. From the experiments, the particle size estimation of 0.52 μm probe particle shows the lowest mean absolute error of 1.92% in 10^2 dilution. In addition, its SD is also the lowest at 0.02 μm in 10^2 dilution.

Particle size estimation of 1.00 μm probe particle also shows a comparable mean absolute error with the 0.52 μm at 2% in 10^3 dilution with SD of 0.05. As a result, the probe with diameter of 0.52 μm and 1.00 μm can be used as probe particles for measuring rheological property of a fluid with the developed device.

Chapter 4

Newtonian and non-Newtonian fluids

A fluid actuated by a shear force results in a deformation as the fluid cannot resist the applied force. Unlike ideal fluids, the real fluid has a resistance to the act of force against the deformation, known as its viscosity [78]. In Newtonian fluids, the fluid obeys the Newton's law of friction for which the viscosity is independent to the applied shear [76], [78]. In contrast to non-Newtonian fluid, alteration of viscosity relies on the applied shear [76], [78]. Such reversible shear-dependent behaviours are important physical properties of materials in occurrence of flow situation as many materials exhibit non-Newtonian characteristic. Thus, the study these physical properties allow for understanding the nature of how the materials flow and why they do not flow as normal.

In fact, knowledge of the material properties important as it enables us to predict variable practical parameters of interest in the real-world. For instance, toothpaste needs to be viscous enough to sit on the brush. At the same time, it should be easy to squeeze out from the tube [76] and must stop flowing immediately after it has been applied to the brush [124]. Thus, the toothpaste viscosity is altered due to the applied shear force which affect to the material behaviour where the shear-dependent viscosity can be described within the flow of material [79]. Similar realisations can be seen in tomato ketchup, being squeezed from a bottle, or in humans, in the evolution of the tear drop (shear thinning) or the mucus in the throat (shear thickening).

In general, viscosity of fluids can be characterised by a viscometer. However, only fluid that obeys Newton's viscosity law, known as Newtonian fluids, can be measured [125]. On the contrary, rheometers [126], [127] are mainly used to measure the viscosity of all type of liquids which are both Newtonian and non-Newtonian [125]. Such a device typically requires a volume of fluid sample to fill in its sample container and a rotating part, which is submerged in or contacted to the fluid, which is rotated during a rheological measurement. Subsequently, the resistance to the flow of the fluid is observed from the applied force to the rotating part. However, large quantities of at least a millilitre of sample is necessary for evaluating of the bulk rheological parameters [128].

In contrast in microrheology [28], [64], [70], [129], rheological parameters can be observed within microlitre sample volumes. By employing tracer microparticles, movement of the particles is either manipulated (active microrheology) [130] or solely influenced by Brownian motion (passive microrheology) [64]. Accordingly, displacement upon Brownian movement of the microparticles is monitored. For rheological assessment, the tracer displacement is analysed using the GSER [64], [86], [130]. Both microrheological assessment approaches are founded to meet excellent agreement with mechanical rheometry [130], although system complexity of passive approaches is relatively simple to implement because it does not need a system to control the probe motion.

Characterisation of fluids via passive microrheology has been visualised by two most common approaches, namely those involving microscopy and light scattering [24], [131]. In microscopy, trajectories of the tracer particles are monitored and tracked by video particle tracking algorithm. The obtained trajectories of the particles can directly yield average mean square displacement $\langle \Delta r^2(t) \rangle$ respected to time t which can be converted to rheological measurement of the fluid. However, inevitably,

occurrence of noise by image acquisition system causes positioning error to the algorithm. To tackle this problem, spatial resolution of the acquisition system is increased [132] or improvement of tracking algorithms [133] to allow for more precision in particle localisation.

In contrast, light scattering approaches can extract rheological information of the fluid without requirement of time-consuming tracking algorithm. In this methodology, light shines through a sample fluid which is embedded with tracer particles, and the scattered light is recorded by a high-sensitive light detector to calculate time-correlation function of the tracer at a certain angle [64], [134].

Recent development for characterising the fluid has been proposed as a DDM [135], [136]. This relatively new approach analyses microscopic images for conducting light scattering experiments [35]. More recently, a further development of this approach allows for evaluation of viscoelastic behaviours of fluids [24].

In this Chapter, the main aim was to study rheological behaviour of Newtonian and non-Newtonian fluids using a passive microrheology. To achieve this, a passive microrheology was developed and validated. This device was based on a differential dynamic microscopy which was able to perform light scattering experiment by means of microscopic images. However, the pre-installed light configuration of microscope is inadequate for some (opaque and highly scattering) biological samples such as human whole blood, as the light detector of the device collects relatively weak signal (and image noise becomes a major presence).

To tackle this problem, light sources wavelength of 532 and 860 nm can be manually selected for illuminating the samples in order to record strong scattering signal which improves the signal-to-noise ratio. For rheological measurement, a small quantity of microparticles was added to the fluid sample as a tracer. To investigate rheological

property, the movements are monitored and recorded by the developed DDM-based device. Next, DDA was performed to the recorded data to evaluate mean square displacement of the particles. Accordingly, viscoelastic behaviours of the fluid are obtained by a numerical conversion of the mean square displacement using a direct conversion approach [70]. The Cox-Merz rule is applied to the viscoelastic behaviours for a steady-shear viscosity conversion [71], see Chapter 2.

4.1. Material and Method

Stock solutions of glycerol (purity ≥ 99.5%, Sigma Aldrich, part no. G9012) and poly(ethylene oxide) (PEO, $M_w = 2 \times 10^5\ Da$, Sigma Aldrich, part no. 181994) were used as fluid samples of Newtonian and non-Newtonian fluids, respectively. In fact, these solutions are standard material for rheological study and viscosity data are widely available.

Polystyrene microparticles are employed in both fluids to trace their motion by the developed device to measure fluid viscosity. The viscosity measurements were compared with reported data [137], [138]. To obtain fluid viscosity, diffusion coefficient D can be obtained from a relationship between characteristic time τ_c and wave vector $\mathbf{q}$ as $D = 1/\tau_c \mathbf{q}^2$ [35], [36]. Then, the diffusion coefficient D was inserted in Stokes-Einstein equation for calculating viscosity of the fluid with prior knowledge of tracer size and measurement temperature [35], [36], [38].

This analytical procedure is only valid for the Newtonian fluid which its viscosity does not change upon applied shear. To enable shear-dependent viscosity measurement, the GSER was performed on mean square displacement of the tracer particle [24], [67], and the Cox-Merz rule is applied to retrieved steady-shear viscosity measurements [71], [139]. It is important to note that all measurements are conducted in a temperature controlled room at 20°C.

4.1.1. Newtonian fluids

A. Deionised water

Validation of viscosity measurement is essential for evaluating performance of the developed device. The viscosity of deionised water obtained by the device was compared with a reference viscosity measured using a viscometer [120]. In the measurement, a monodisperse microparticle size of 0.52 μm was added to deionised water at mixing ratio of 1: 1000 to probe the viscosity. Furthermore, various sizes of microparticles (0.52, 1.00, and 1.54 μm) were added to the water to investigate viscosity of the water.

B. Glycerol-water mixtures

Viscosity spectrum was performed by measurement of developed device by experiments of wide range viscosity of Newtonian fluids. In general, glycerol-water mixtures are usually used as a standard test fluid, providing a broad viscosity range from 1.005 to 1412 mPa.s at 20 °C[140]. For mixture preparation, various viscosities are obtained by adding different quantities of glycerol stock solution to deionised water where the total weight is restricted to one gram. Vortex mixing was used to incorporate glycerol and water mixture. In this work, the glycerol-water mixtures ranging from glycerol content of 0, 10, 20, 30, 40, 50, 60, 70, 80, 90 and 100 percent by weight were prepared.

4.1.2. Non-Newtonian fluid

A. Aqueous PEO solutions

In viscoelastic fluids, PEO solutions are typically used as an example of viscoelastic material [139]. In preparation, PEO powder molecular weight of 200,000 g/mol

(Aldrich, 181994-250G) was dissolved by deionised water at PEO content of 1, 2, and 5 %wt. Then, the solutions were incubated for 2 days to allow them to completely dissolve [139]. For rheological measurements, the solutions were prepared by dispensing polystyrene microparticles sizes of 0.52 and 1.54 μm in each solution with the identical percentage volume of 0.1.

4.1.3. Examination of viscosity by a developed device

The developed device, which is presented in Chapter 3, acquired measurement data of prepared Newtonian and non-Newtonian fluids. To perform a measurement, these fluids used polystyrene microparticles as a tracers. Next, an approximately 6.0 μL of sample was dispensed in an in-house microchamber. Then, the microchamber was placed in the sample holder of the device. In data acquisition, a sequence of images was recorded by an image sensor of the device. Following this, the DDA was performed on the recorded data to retrieve intermediate scattering function

A. Intermediate scattering function

Collision of solvent molecules with embedded microparticles causes the microparticles to move randomly while the whole fluid is at rest (i.e. through Brownian motion). These movements cause intensity fluctuations which were recorded by the developed device. In DDM principle, the intensity fluctuation can be defined by equation [35], [36], [38]:

$$S(\mathbf{q}, t) = A(\mathbf{q})[1 - f] + B(\mathbf{q}) \tag{4.1}$$

where $S(\mathbf{q}, t)$ represents the signal at wavevector q and time t, $A(\mathbf{q})$ is the related to scattering properties of particles and optical setup [36], $B(\mathbf{q})$ accounts the noise term of the system, and f is the normalised intermediate structuring function.

For Brownian motion, the intermediate scattering function was characterised as exponential decay of $e^{\left(-\frac{t}{\tau_c}\right)}$, where t is the lag time, and $\tau_c = 1/D\mathbf{q}^2$ is a characteristic time which indicates the time taken by a particle to move a distance $\mathbf{q}^{-1}$ µm [141]. Accordingly, diffusion coefficient D can be obtained which benefits for further analysis of particle size and viscosity of solvent solution.

B. Stokes-Einstein equation

According to Stokes-Einstein equation [28], diffusion coefficient of the particles in Brownian equilibrium is defined by equation:

$$D = \frac{k_B T}{\gamma}$$

$$D = \frac{k_B T}{3\pi\eta a} \tag{4.2}$$

Where D represents the diffusion coefficient, k_B is the Boltzmann constant, T is the absolute temperature, γ is frictional coefficient, η is the viscosity of the solution, and a is the diameter of the colloidal particle.

In fact, analysing Brownian motion using the Stokes-Einstein equation is valid only to a spherical particle, as stated in Chapter 2, the friction coefficient derived by Stokes is only applicable for spheres. For non-spherical particles, the frictional coefficient γ can be expressed through the diameter of sphere with equal projected and surface area that move parallel and normal to the observed plane, as derived in [142]. Moreover, the equation is only restricted for Newtonian fluid analysis, as Stokes law is not valid for viscoelastic medium [141].

C. Generalised Stokes-Einstein relation and Cox-Merz rule

A further analysis extends the Stokes-Einstein equation enabling investigation of viscoelastic materials as known as GSER, [26]. The GSER employs Langevin equation establishing a relationship between ensemble-average mean square displacement of such particles and viscoelastic properties of the suspending fluid in Fourier frequency domain [26]. For this relationship, the mean square displacement of tracer particles is essential to obtain viscoelastic modulus of the material.

In DDM principle, the mean square displacement can be obtained via the intermediate scattering function in which $f = e^{-\frac{\mathbf{q}^2}{4}\langle \Delta r^2(t) \rangle}$ [24]. In general, performing GSER to the mean square displacement introduced numerical artefact at high frequency. Nevertheless, a direct conversion of mean square displacement is an alternative approach to evaluate artefact-free viscoelastic moduli [143].

The majority of rheological characterisation investigates Newtonian and non-Newtonian fluids in steady-shear viscosity particularly in human blood sample [73]. In contrast to oscillatory shear experiment, complex viscosity can be obtained by $\eta^*(\omega) = G^*/\omega$ where G^* is the viscoelastic modulus, and ω represents the angular frequency. However, the complex viscosity can be converted to steady-shear viscosity via empirical Cox-Merz rule [71]. In summary, the calculation scheme to obtain steady-shear viscosity by the developed device is shown in Figure 4.1.

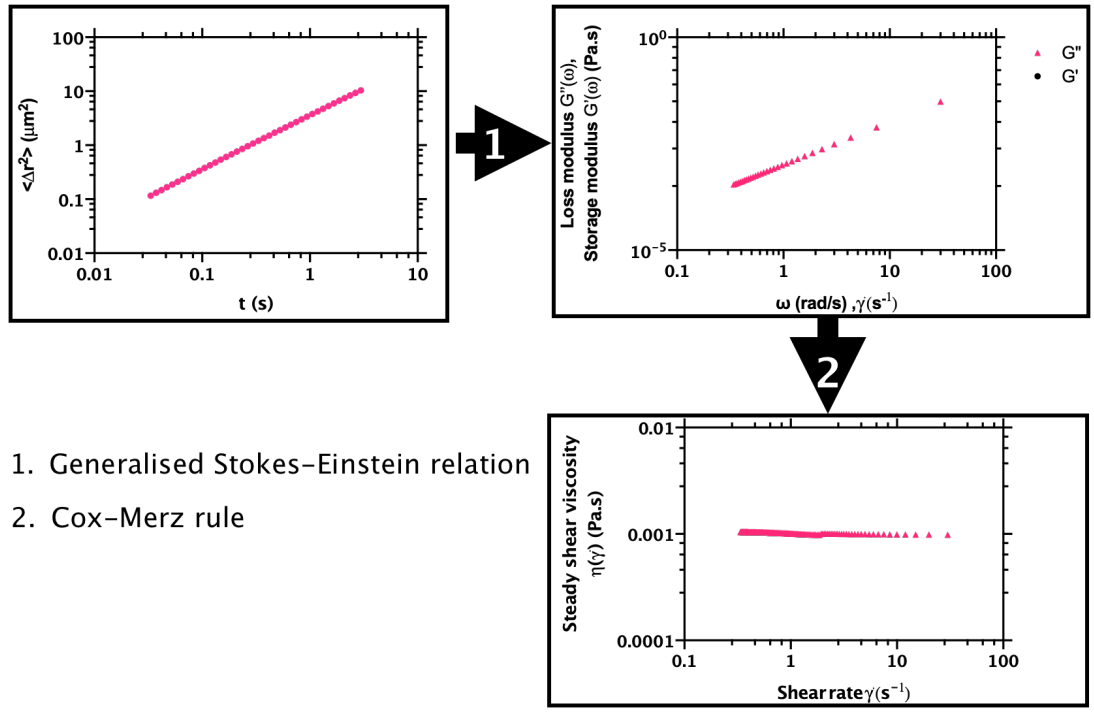

Figure 4.1. Calculation scheme for preforming steady-shear viscosity by passive microrheology, involving 1. The GSER and 2. The Cox-Merz rule.

4.2. Experimental results

4.2.1. Stokes-Einstein equation analysis

A. Deionised water

Viscosity measurement of deionised water is an essential procedure for validation of the developed device. To obtain viscosity of the water, polystyrene microparticles were employed to a volume of the water at mixing ratio of 1:1000. The sample was gently mixed to incorporate the microparticles. An image sequence was acquired by the developed device. Following this, DDA was performed on the image sequence to retrieve intermediate scattering function. For Brownian particles, the intermediate scattering function corresponds to exponential of decay of $e^{\left(-\frac{t}{\tau_c}\right)}$. As $\tau_c = 1/Dq^2$, diffusion coefficient of the particles was obtained by determining the slope between $\frac{1}{\tau_c}$ and q^2 as shown in Figure 4.2.

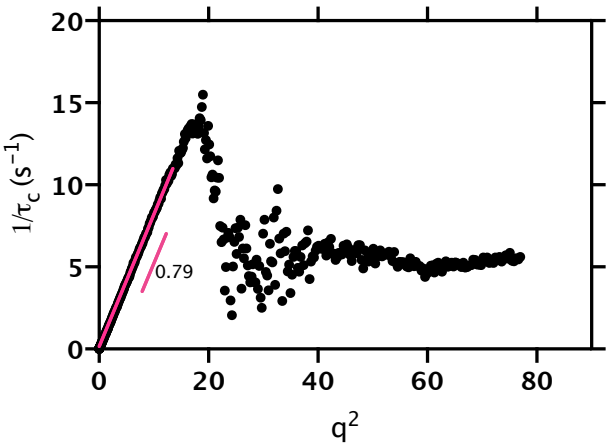

Figure 4.2. A plot of $1/\tau_c$ and q^2 of suspended polystyrene microparticles of 0.52 μm in 20°C deionised water. The pink line represents a linear fitting of the plot data from the wave vector range of 0 to 3.87 μm^{-1}. Slope of the fitted line indicates the diffusion coefficient of the microparticles which is 0.79 $\mu m^2/s$.

From Figure 4.2. the result diffusion coefficient was 0.79 $\mu m^2/s$ from added polystyrene microparticles sized at 0.52 μm in 20°C deionised water. To achieve the standard deviation of the developed device, a three-fold replicated was collected and analysed which yielded average diffusion coefficient of 0.80 ± 0.01 $\mu m^2/s$ as shown in Figure 4.3.

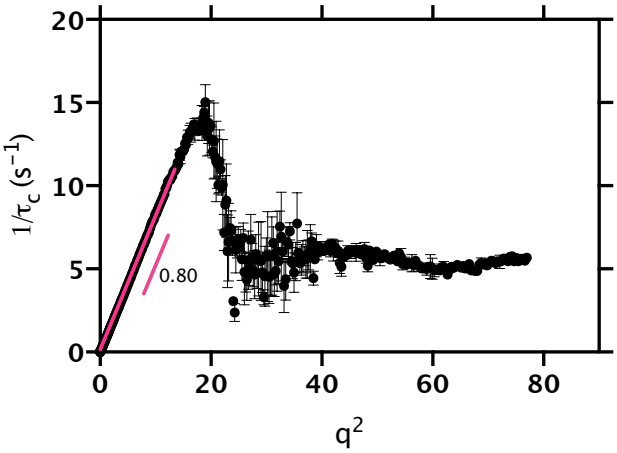

Figure 4.3. A plot of $1/\tau_c$ and q^2 of suspended polystyrene microparticles of 0.52 μm in 20°C deionised water from three-fold replication. The pink line represents a linear fitting of the plot data from the wave vector range of 0 to 3.87 μm^{-1}. Slope of the fitted line indicates the diffusion coefficient of the microparticles which is 0.80 $\mu m^2/s$.

Regarding to Equation (4.2), the viscosity of the water was calculated from the obtained diffusion coefficient. From the calculation, the resulting mean and standard deviation of viscosity was 1.03 ± 0.01 mPa.s. For comparison with reference values in [120], mean absolute percentage error [144] was calculated to determine measurement accuracy as a percentage by $\frac{1}{n}\sum_{i=1}^{n}\left|\frac{a_i - r_i}{r_i}\right|$, where n is the total data points, a_i refers to a measurement at data point i, and r_i is a reference value at data point i. In this measurement, the mean absolute percentage error was estimated as 3.03 %.

Various sizes of tracer particle can be used for investigation of diffusion coefficient of fluid of interest. To demonstrate this, polystyrene microparticles with diameters of 1.00 and 1.54 μm were used to the deionised water for the viscosity investigation. These suspensions were measured by the device at room temperature of 20°C then compared against the result obtained among such tracer particles. For clearly illustration, the result plot of $\frac{1}{\tau_c}$ and $\mathbf{q}^2$ was fitted from $\mathbf{q}^2$ between 0 and 15 μm^{-2} where $\frac{1}{\tau_c}$ had linear relationship with q^2. The result diffusion coefficients of the tracer particle size of 0.52, 1.00 and 1.54 μm are shown in Figure 4.4.

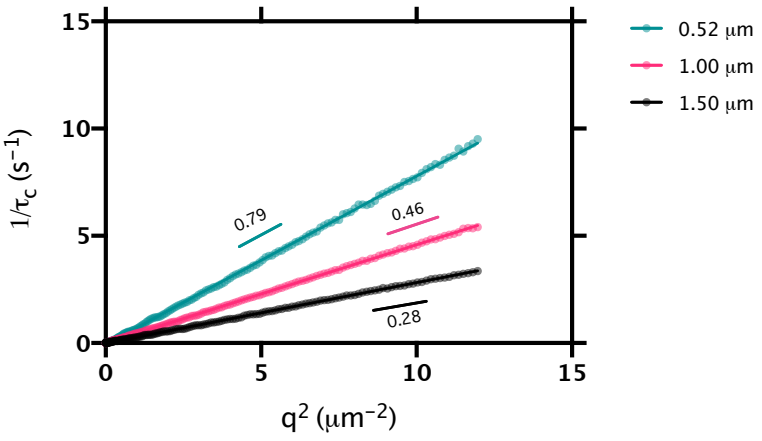

Figure 4.4. A plot of $1/\tau_c$ and q^2 of suspended polystyrene microparticles of 0.52, 1.00, and 1.54 μm in 20°C deionised water. The green, pink, and black dots represent the microparticles size of 0.52, 1.00, and 1.54 μm. Colour lines represent a linear fitting of the plot data from the wave vector range of 0.00 to 3.87 μm^{-1}. Slope of the fitted line of the microparticles size of 0.52, 1.00, and 1.54 μm are 0.79, 0.46, and 0.28 $\mu m^2/s$.

As in Figure 4.4, diffusion coefficients of the particles sizes of 0.52, 1.00, and 1.54 μm diluted in deionised water at 20°C were illustrated. The fitted lines between $\frac{1}{\tau_c}$ and $\mathbf{q}^2$ indicated diffusion coefficients of such particles which experience Brownian motion. The obtained diffusion coefficients revealed that small particle provided results with lower values than larger particles, as small particles moved more in a unit of time than the larger particle. The experiment was performed as a three-fold replicatate enabling calculation of a mean and SD of the measurement. To obtain viscosity, the measurement diffusion coefficient were substituted in Stokes-Einstein equation. Accordingly, the viscosity of deionised water at 20°C by three sizes of probe particles are represented in Table 4.1.

Table 4.1. Diffusion coefficient and viscosity measurement of the 20°C deionised water using various tracer size.

Tracer size (μm)	**Diffusion coefficient (μm²/s)**	**Measured viscosity (mPa.s)**
0.52	0.80 ± 0.01	1.03 ± 0.01
1.00	0.43 ± 0.01	1.03 ± 0.01
1.50	0.28 ± 0.01	1.03 ± 0.03

According to Table 4.1, the viscosity measurements of deionised water at 20°C was obtained using various tracer sizes by three-fold replication of experiment conducted by the developed device. Diffusion coefficients of tracer particles sizes of 0.52, 1.00, and 1.54 μm were added to the water for viscosity examination. As represented in Table 4.1, diffusion coefficient depended on sizes of the tracer particles, although the diffusion coefficients yielded, gave the viscosity of water with no significant difference.

B. Glycerol-water mixtures

In sample preparation, glycerol was diluted by a deionised water ranging from 0 to 100 %wt by glycerol content. Then, polystyrene microparticles size of 0.52 μm were added to these glycerol-water mixtures, as a tracer particles. Each mixture was pipetted approximately 6.0 μL and dispensed in an in-house microchamber. Then, a cover slip was placed on and sealed with nail vanish to prevent sample evaporation. Following this, the microchamber was put on a sample holder of the developed device. Accordingly, a sequence of images was acquired by the developed device, which was processed by DDA to retrieve intermediate scattering function. The diffusion coefficient of the tracer particles was obtained by determine the slope between $\frac{1}{\tau_c}$ and $\mathbf{q}^2$ as illustration in Figure 4.2. Then, viscosity of the mixture was obtained by using Stokes-Einstein equation (4.2). Following this, result viscosities of the glycerol-water mixtures were listed and depicted in Table 4.2 and Figure 4.5, respectively.

Table 4.2. Viscosities of glycerol-water mixtures at 20 °C indicated by glycerol content using developed device in comparison with reference capillary viscometer measurement.

	Glycerol content (%wt)										
	0	**10**	**20**	**30**	**40**	**50**	**60**	**70**	**80**	**90**	**100**
Obtained viscosity (mPa.s)	1.02	1.31	1.79	2.64	3.87	5.56	9.08	17.90	44.10	117.80	209.60
Reference [137] (mPa.s)	1.01	1.31	1.76	2.50	3.72	6.00	10.80	22.50	60.10	219.00	1412.00

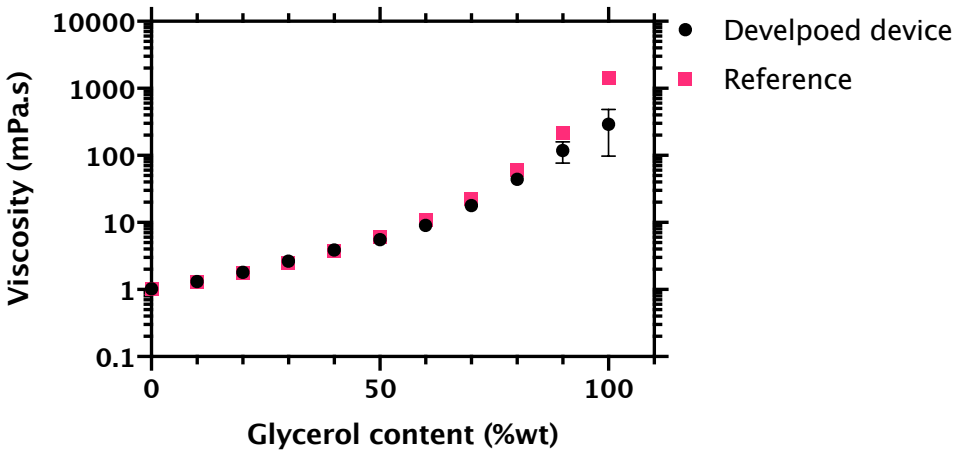

Figure 4.5 Viscosity as a function of glycerol weight fraction at 20 °C using the developed device in comparison of a reference capillary viscometer. Black solid circles are the obtained mean viscosity by three-folded replication using the developed device whereas the error bar was the standard deviation. The pink solid rectangles are results from the reference capillary viscometer measurement [137].

From Figure 4.5, it can be seen that the result was in agreement with reference measurement. However, the measurement diverged from reference values with increasing glycerol mass fraction in the mixture as the embedded tracer particles were hindered from movement in highly viscous material. As a consequence, the result of image difference was close to zero. Thus, the DDA collected gave a low signal. From this experiment, relative absolute error of the measurement indicated by glycerol mass fraction are represented in Figure 4.6.

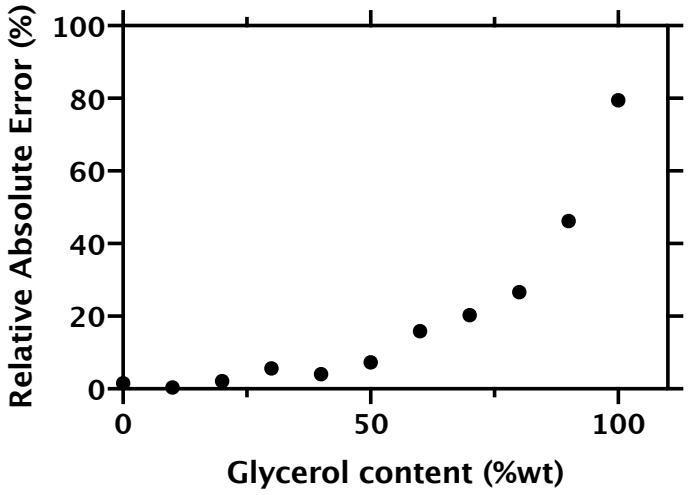

Figure 4.6 Corresponding relative absolute error obtained from Figure 4.5.

4.2.2. Shear-dependent viscosity

A. Deionised water

Unlike analysis with Stokes-Einstein equation, a shear dependent viscosity was obtained using the analysis of GSER as described in Chapter 2.4. In brief, the mean square displacement of the employed probe tracer was retrieved by the DDA. Then, a numerical conversion was performed on the mean square displacement to extract the viscoelastic properties of the sample. Finally, shear-dependent viscosity is obtained by a conversion of the obtained viscoelastic properties using the Cox-Merz rule.

For demonstration, an experiment was conducted to examine viscosity of deionised water by using 0.52 μm polystyrene microparticles as tracer particles. A volume of the water was added to an in-house microchamber and a slide added to secure and enclose the fluid in place. Then, the microchamber was placed in the sample holder of the device to secure the sample in place. Next, the movement of the particles was recorded for 2 minutes. Accordingly, the recorded data was analysed using a procedure detailed in Chapter 2.4 to obtain viscoelasticity of the water, see Figure 4.7.

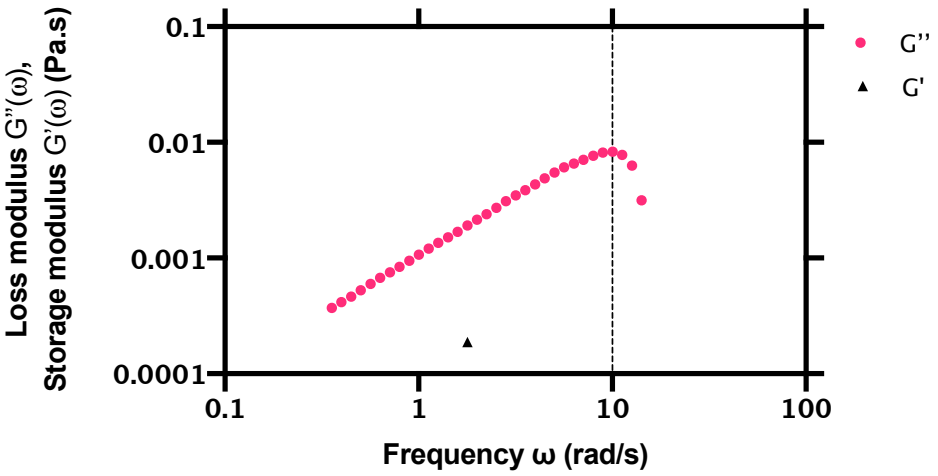

Figure 4.7. Viscoelastic propoerties as a function of angular frequency ω of deionised water at 20 °C using polystyrene microparticle size of 0.52 μm. It is important to mention that negative value of loss and storage moduli cannot be plotted in log-log plot.

From Figure 4.7, the obtained viscoelasticity exhibited mostly the loss modulus (G'') part due to the deionised water is purely Newtonian fluid [78]. However, this conversion algorithm generated artefacts from frequencies at 10.0 rad/s due to the two-step numerical conversion [69], [70]. Furthermore, this method reported that its conversion underestimated loss modulus [77]. In contrast to direct conversion method [69], [70], this alternative approach can eliminate numerical artefacts at high frequency by a single conversion step. Creep compliance $J(t)$ is directly converted into viscoelastic modulus $G^*(\omega)$. However, data interpolation and extrapolation of the Creep compliance $J(t)$ is necessary [70].

To demonstrate these numerical conversions further, a solution of 0.52 μm polystyrene particles was diluted in deionised water as a test sample. Following this, the signal was acquired by our DDM device then analysed using the DDA. The next procedure was to calculate the mean square displacement of tracer particles regarding to Section 2.4.

The obtained mean square displacement was then converted to viscoelastic moduli using GSER. The mean square displacement was converted to creep compliance by $J(t) = \langle \Delta r^2(t) \rangle \cdot \frac{\pi a}{K_b T}$ for performing with the direct conversion method. The result of both conversions revealed viscoelastic moduli of the deionised water at 20 °C in the Figure 4.8.

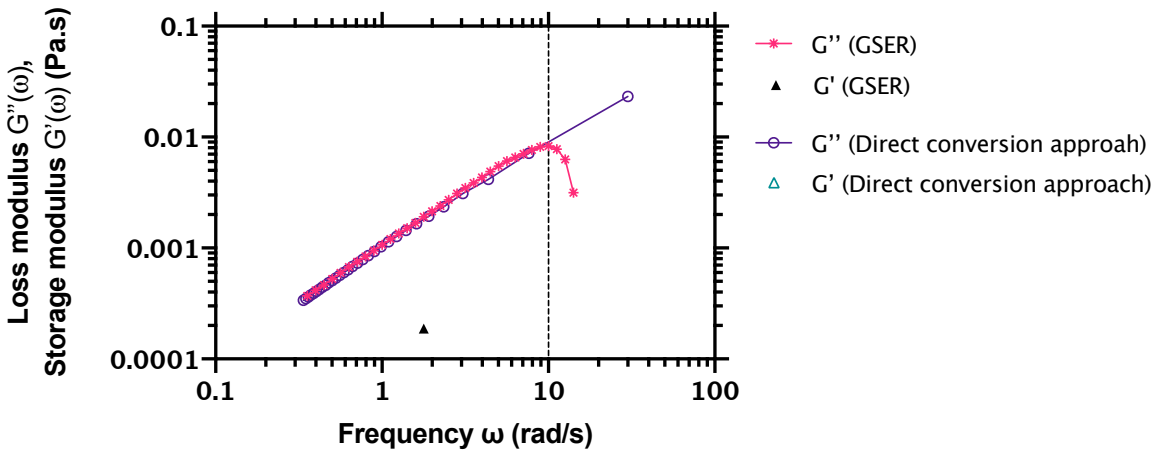

Figure 4.8. Experimental result of viscoelastic properties of deionised water at 20°C using GSER and [26], [86], and direct conversion approach [69], [70]. Pink stars and black upward triangles represent loss and storage modulus of GSER conversion approach respectively. For direct conversion approach, purple opened circles and opened green upward triangles are loss and storage modulus respectively. It is important to mention that negative value of loss and storage moduli cannot be plotted in log-log plot.

From Figure 4.8, two numerical conversions using the same measurement data were compared using data obtained by adding 0.52 μm tracer particles to deionised water. The measurements were performed by the developed device to probe viscoelastic properties of deionised water at 20 °C. Both numerical conversions revealed loss moduli G'' parts since the deionised water was a Newtonian fluid. The loss moduli G'' was obtained from both numerical conversions and were in the same trend where the frequency response ω below 10.0 rad/s. However, the loss modulus G'' obtained from GSER has a numerical artefact at frequency >10.0 rad/s. In addition, the storage modulus G' obtained from GSER was appeared at some frequency responses. In contrast to direct conversion approach, numerical artefact from frequency response, ω > 10.0 rad/s vanished. Nevertheless, storage modulus G' from both conversion approach were unable to be displayed in the log-log plot (as they had negative values).

To evaluate shear-dependent viscosity, the Cox-Merz rule was applied to the retrieved viscoelastic moduli. By determining of complex viscosity $\eta^*(\omega) = \frac{G'(\omega)+iG''(\omega)}{i\omega}$, the absolute value of the complex viscosity $|\eta^*(\omega)|$ was used to estimate its shear-dependent viscosity, and was in good agreement to mechanical rheometry experiments [139]. The result shear-dependent viscosity are shown in Fig 4.9.

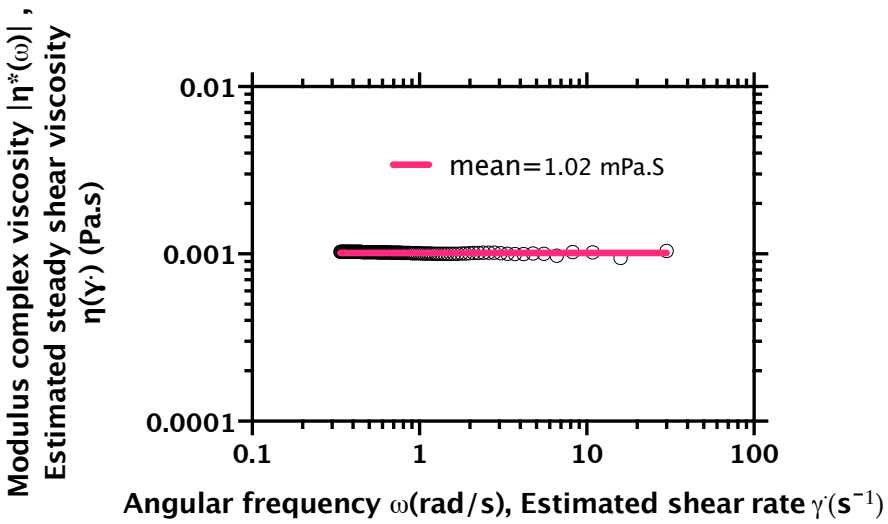

Figure 4.9. The corresponding shear-dependent viscosity of using Cox-Merz rule with the viscoelastic moduli obtained by the direct conversion approach in Figure 4.8. Black opened circles are the result shear-dependent estimation using Cox-Merz rule. The pink line represents mean value of the viscosity for all measuring shear rate which is 1.02 mPa.s

From Figure 4.9, the results showed viscosity as a function of shear rate of deionized water at 20°C using 0.52 µm as tracer particles. Apparently, there was no significant alteration of the result viscosity upon the measuring shear rate because the water was a Newtonian fluid. For verification, the measurement was replicated by employing various sizes of tracer particle in which the result steady-shear viscosity were illustrated in Figure 4.10 and 4.11 respectively.

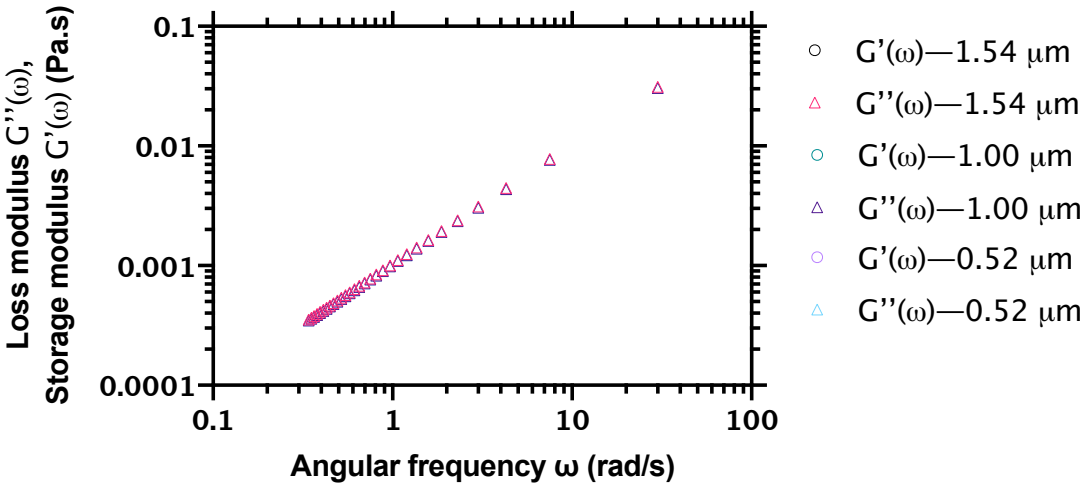

Figure 4.10. Viscoelastic properties of deionised water at room temperature of 20°C probed using Polystyrene microparticle sizes of 0.52, 1.00, and 1.54 μm.

Regarding to Figure 4.10, viscoelastic properties of deionised water at 20°C by tracer size of 0.52, 1.00, and 1.54 μm were displayed. The result indicated the loss moduli $G''(\omega)$ were independent from size of the tracer. The storage moduli $G'(\omega)$ were negatives.

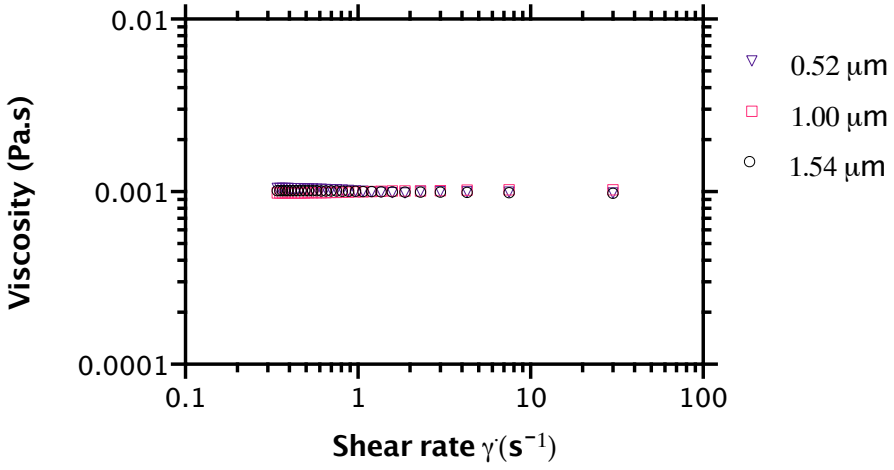

Figure 4.11. The corresponding viscosities of deionised water at 20°C obtained by 0.52 (Purple downward opened triangles), 1.00 (Pink squares), and 1.54 (Black opened circle) μm sizes of tracer microparticles. The result steady-shear viscosities are revealed by performing Cox-Merz rule to Figure 4.10.

From Figure 4.11, shear-dependent viscosities of deionised water at 20°C were measured using polystyrene microparticle sizes of 0.52, 1.00, and 1.54 μm. The resulting viscosities remained remarkably stable along the measuring shear rates because the deionised water was Newtonian fluid. However, these viscosities were slightly different which might be caused by the variations of the sample temperature and uniformability of the employed tracer particle.

B. Glycerol-water mixtures

In these experiments, a shear-dependent viscosities of glycerol-water mixtures were obtained by performing calculation according to Section 4.1.3.C with experiment data in 4.2.1.B. Viscosities of the mixtures relied upon a ratio of glycerol content rather than water viscosity of pure glycerol was relatively high in comparison with deionised water (measuring at the same temperature). For a measurement, a stock solution of 0.52 μm polystyrene microparticles were added to the prepared glycerol-water mixtures at dilution ratio of 1: 1000. The mixtures were dispersed and secured in in-house microchamber. Then, their viscoelastic properties were evaluated using the direct conversion approach. Finally, the obtained viscso-elastic properties were converted shear-dependent viscosities using Cox-Merz rule as illustrated in Figure 4.12.

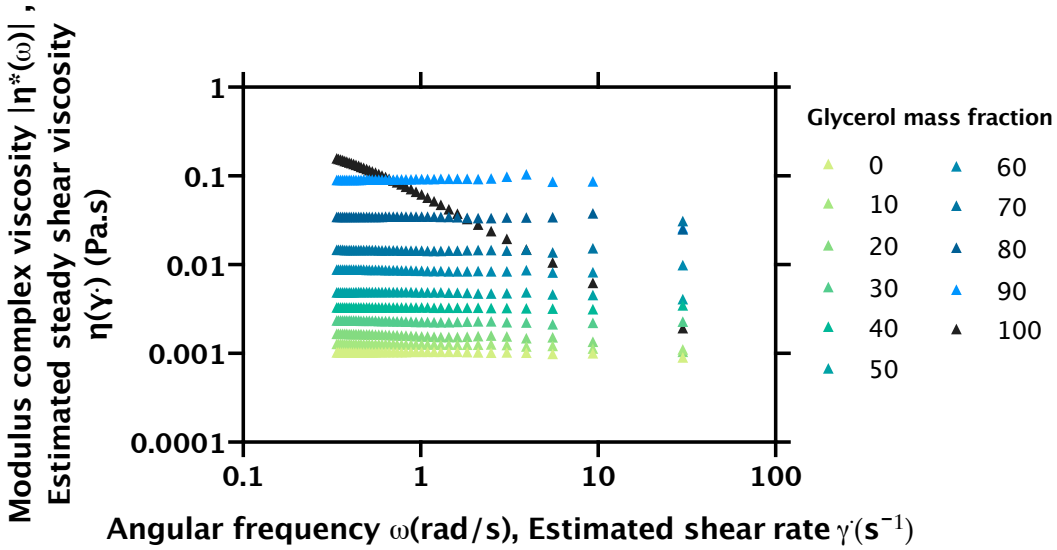

Figure 4.12. The corresponding Shear-dependent viscosities of glycerol-water mixtures according to the measurement described in section 4.2.1.B.

From Figure 4.12, the result indicated that shear-dependent viscosities of glycerol ontent of 0 to 50 %wt were not significantly different as a function of the shear rate. In contrast to glycerol content of 60 to 100 %wt, their viscosities depended on shear rate which were inaccurate. These incorrect results were the limit of the measurement due to the employed tracer particles were barely move in high viscosity fluid (from glycerol content of 60 %wt). As a result, DDM collected relatively low movement signal since the difference of images are calculated.

C. Non-Newtonian fluid : PEO-water solutions

In this section, shear dependent viscosity of a viscoelastic material was examined using the developed device for the viscoelasctic measurement. In general, PEO-water solutions are usually used for examining of viscoelastic behavior [41]. To evaluate the viscosity, polystyrene particles size of 0.52 μm were added as tracer particles by diluting the particles 1,000 times using the PEO-water solution. A 6.0 μL of sample was dispensed in an in-house microchamber and put in the developed device to hold the sample in place. Next, motion of the tracer was recorded for DDA to analyse.

Viscoelastic properties of the PEO-water solution were obtained using the direct conversion approach. The result viscoelastic properties were plotted in the Figure 4.13.

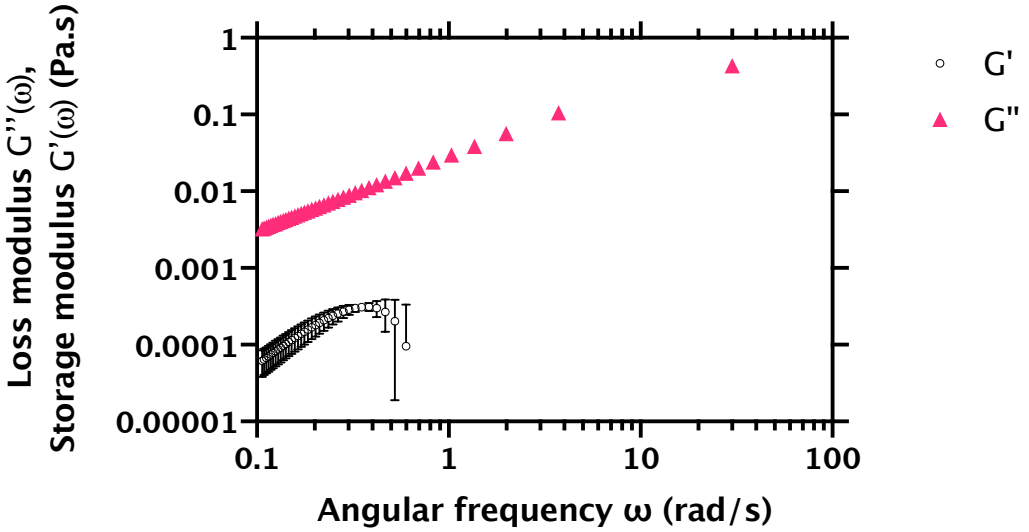

Figure 4.13. Viscoelastic properties of 5%wt PEO in deionised water measuring at 20°C by three-folded replication. Pink upward triangles and black open circles are average loss and storage moduli respectively. The error bars represent standard deviation of the measurement. It is important to note that error bars shorter than symbol size cannot be plotted by the software (Prism 8).

From Figure 4.13, the evaluated viscoelastic properties of 5%wt PEO-water solution exhibited both of loss and storage moduli from a three-folded replication of the measurement. The result loss modulus dominated the storage modulus in all range of measuring frequencies. The appearance of storage modulus in the PEO-water solution is due to the polymer chain entanglement particularly in high concentration and high molecular weight [145], [146]. As a result, the viscosity shows shear-dependent behaviour as it relies on both of loss and storage moduli according to the viscosity calculation from Cox-Merz rule [71]. The corresponding steady-shear viscosity of 5%wt PEO-water solution is illustrated in Figure 4.14

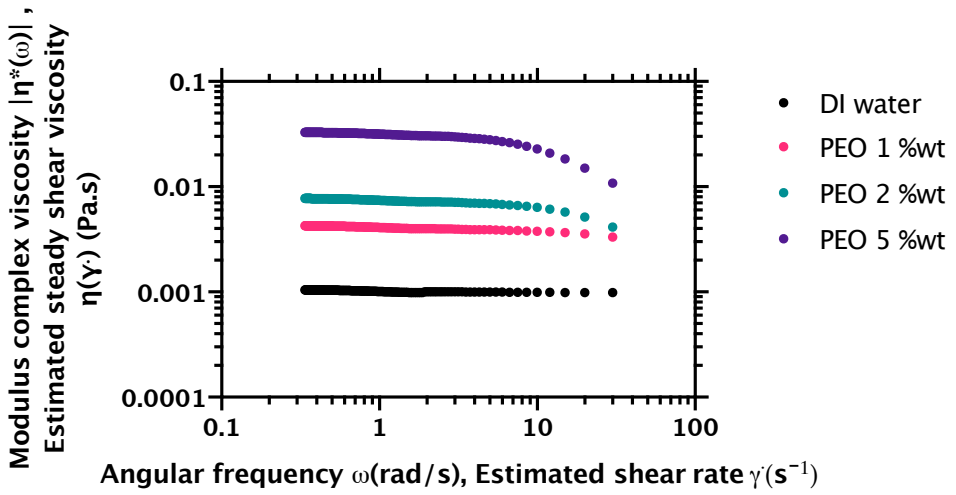

Figure 4.14. Steady-shear viscosities of deionised water and PEO-water solutions measured at 20°C using 0.52 μm tracer particles. Red, green, and purple dots represent average viscosities of 1%, 2%, and 5% PEO by weight content in the solution respectively. Black dots are steady-shear viscosity of deionised water which represents a reference Newtonian fluid. Error bars indicate standard deviation of three-folded replication of the measurement. The error bars shorter than symbol size are unable to displayed.

From Figure 4.14, result steady-shear viscosities of PEO-water solutions were plotted. Increment of PEO content elevated viscosity of the solution for all shear rates. In addition, the viscosity profile had a dependence on shear rate for 1%wt and 2%wt PEO-water solutions. However, the obtained viscosity indicates the PEO-water solution behaved a shear-thinning fluid which is analogous to the reported work [41], [145]. This behaviour indicates non-Newtonian behaviour since the viscosity is dependent on the shear rate.

4.3. Conclusions

In this chapter, steady-shear viscosity was demonstrated using the developed device based on differential dynamic microscopy (DDM). The device characterises viscosity of the fluid of interest by passive microrheology principle. By adding probe particles to the fluid, the mean square displacement of the probe was evaluated. This probe displacement was an essential parameter to retrieved the viscoelastic moduli of the

fluid using the GSER. Form the obtained moduli, the corresponding steady-shear viscosity was calculated using the Cox-Merz relationship. However, this conversion introduces numerical artefacts at high frequencies. As a result, the artefact produced inaccurate result viscosity at low shear rate as $\omega = \frac{1}{shear\ rate}$ according to the Cox-Merz relationship. In contrast, a direct conversion method can eliminate the artefact by using direct conversion of mean square displacement. Thus, this thesis implements the direct conversion method to obtain viscoelastic moduli of the fluid to achieve more reliable result.

For validation, steady-shear viscosities of Newtonian and non-Newtonian fluids were examined using the developed device. In Newtonian fluid, viscosity of deionised water and glycerol-water was investigated by the device and verified with reference value. For the water measurement, the obtained viscosity was in close agreement with the reference value although the probe size for the investigation was varied. However, there were slight deviation of the obtained viscosities in each measurement due to the lack of sample temperature control.

To determine measuring viscosity spectrum, glycerol-water mixtures were examined using the device (as viscosity variations was depended on glycerol content dissolved in the water). In the measurements, the mixtures were prepared by dissolving glycerol content from 0 to 100 % wt in deionised water. From the measurement, glycerol-water mixtures of 0 to 50 % wt of glycerol content were in good agreement with the reference value. However, the relative absolute error was increased along with glycerol content. For non-Newtonian fluid, aqueous polyethylene oxide (PEO-water) solutions were used for demonstrating shear-dependent viscosity measurement. The result viscosity of PEO-water solutions exhibited a shear-thinning behaviour especially in high polymer content (5 % wt) of PEO. This behaviour is found to be in analogous to previously reported work [41], [145].

Chapter 5

Particle sizing

Examining particle size distribution is an essential procedure to obtain physical parameter of colloidal micro and nanoparticles. A wide range of applications including molecular biology, biomedical engineering, and chemical and physical property studies are broadly associated to size of the particles [113], [147], including for example, investigation of homogeneity of particles suspended in a fluid, aggregation of recombinant proteins, and protein-protein interaction [148]. In general, dynamic light scattering (DLS) is a well-established optical approach for particles size distribution of micro-nanoparticles [149], [150]. In DLS device, a laser light shines through dispersed particles and the incident light is scattered in all direction. Simultaneously, these particles are in Brownian motion caused by collision of smaller surrounding molecules of the solution. The scattered light is either constructive-phase or destructive-phase and its intensity is recorded by a light detector. A correlator registers such intensity fluctuations as a function of time and relates this fluctuation to a diffusion coefficient. The average size of the particles can be evaluated by Stokes-Einstein relation from the obtained diffusion coefficient [108]. However, this approach is applicable only for monodisperse particles. Hence, there is a demand for a measurement system that efficiently determines particle size distribution in a polydisperse system.

A cumulant [151] is a most common approach for analysing DLS data of polydisperse suspensions [152], [153]. It provides information about average and standard deviation

of the decay rate, Γ, [152], [154] which can be related to particle size via Stokes-Einstein relation. Obviously, differential dynamic microscopy (DDM) has a strong connection to DLS via intermediate scattering function [35], [155].

A modified cumulant fit [37] can thus be used for DDM data analysis of the polydisperse populations as $S(q,t) = A(q)\left[1 - e^{(-\Gamma t)\cdot\left(1+\frac{\mu t^2}{2}\right)}\right] + B(q)$, where μ is responsible for variance of the decay rate $(\Gamma = \tau_c^{-1})$ [152]. This method works well for monodisperse solution with a polydisperse index $\mu/\bar{\Gamma} \leq 0.3$ [156], where $\bar{\Gamma}$ represents the average value of the decay rate. The polydisperse index is dimensionless and it indicates uniformity of the sample. That is, the less polydisperse index reveals that the dispersed particles have more consistency of their size. In fact, this method does not give information about particle size distribution of the dispersed particles in the fluid. However, mean and variance of diluted particles can be reconstructed using Schulz distribution [157].

Recently developed brightfield differential dynamic microscopy (BDDM) has shown its ability to quantify particle size distribution of polydisperse particles [37]. In this approach, the detectable particle size is ranged from nanometres to micrometres. However, it requires and relies upon the magnification power of optical microscope. The BDDM technique was demonstrated to characterise weakly scattering and polydisperse nanoscale biological samples, with haemoglobin A and lysozyme, which contain polydisperse clusters of radius 70-250 nm, analysed in this work. Mie scattering intensities were calculated as a function of scattering angle and weighted by a Gaussian function to estimate particle size distribution. This approach is restricted only for the Gaussian distribution and it cannot estimate particle size distribution of two or more populations of colloidal particles.

In this Chapter, a portable DDM for estimating particle size distribution of polydisperse population is developed. This device is composed of a LED light source coupled with an optical fibre. The light from the optical fibre illuminated a sample and due to the particles light was scattered in all directions. This scattered light was then collected by a webcam to process and analyse using DDA. Finally, particle size distribution was obtained by performing non-negative linear least square method (NNLS) with the measurement data.

The benefits of this approach is that it requires remarkably less in computational time without the need for complicated calibration [108]. To demonstrate particle size distribution, monodisperse and polydisperse microbeads in solutions were studied and verified with a gold standard method DLS (Zetasizer ZS90, Malvern Panalytical Ltd).

5.1. Conventional method

5.1.1. Dynamic light scattering method

DLS is a well-established method for evaluating particle size distribution of particles in a sample fluid [149]. It analyses light fluctuations of dispersed particles which are caused by Brownian motion of the particles. These size-dependent fluctuations are detected by a light detector. Conventional DLS relies upon homodyne detection [37], [158], as only weak scattered light are recorded by the system. Thus, a high sensitivity light detector is necessary to the system in order to capture the weak scattered light. Usually a photon multiplier tube (PMT) is used for registration of small fraction of scattered light. This light detector is often located at 90 degree angle to avoid influence of strong light scattered from the sample cell at around 0 degree angle [159]. In particle size analysis, the monitored intensities are analysed by self-correlation, also known as time auto-correlation function. Then, the autocorrelation function is analysed by

constrained regularization method (CONTIN) [160] software package to obtain particle size distribution.

5.1.2. Diffusing wave spectroscopy

A major problem of DLS system is the measurement cannot be done for turbid media [161], as the increasing particle content in a solution leads to multiple scattering of light before reaching a detector [54]. That is, the incident light scattered from a certain particle encounters another particle before it reaches a detector. In fact, the easiest way to tackle this problem for DLS system is to dilute and repeat the measurement [162]. However, diffusive-wave spectroscopy (DWS) addressed this problem by considering the multiple scattered light that is contributed to the correlation function [54]. As a result, particle size distribution of turbid media can be obtained by DWS [163] using an analytical method used in DLS [164].

5.1.3. Differential dynamic microscopy

DDM is a method to quantify dynamics of micro-nanoparticles in a fluid [113]. These particles are moving randomly due to collisions of smaller molecules in the fluid, and motions are analysed by the Fourier processing to access light scattering information that is equivalent to the scattering information obtained by DLS experiment [35], [165].

By analysing the recorded motion as mentioned in Chapter 2 and 3, a diffusion coefficient of the particles can be evaluated [35], [36]. Finally, this parameter can be related to average diameter of colloidal particles by Stokes-Einstein relation. A further development of DDM yields particle size distribution of dispersed particles in a fluid [37]. However, this analytical methodology is restricted to single Gaussian distribution

of the particle size. This is because, the Gaussian function is used to model the particle size.

5.2. Particle size analysis by the developed device

Particle size characterisation of various dispersed microparticles in deionized water was performed by the developed device. This device relied upon the DDM principle in that it analyses an image sequence in Fourier space to perform light scattering experiment similarly to the DLS [155]. In addition, a low-cost webcam was used as an image sensor unlike traditional DDM that is based on a camera-equipped optical microscope [36]. A main drawback of the employed webcam is the inconsistence of image transfer. As a result, some images are discarded which causes incorrect time information associated to the recorded image as mentioned in Chapter 3. To tackle this problem, time-stamp image was implemented for recording actual time information to the DDM calculation which produces more reliable result.

To characterise the particle size, solution of mono and polydisperse microparticles were investigated by both of Stokes-Einstein relation and NNLS which were implemented in this Chapter. In Stoke-Einstein relation, only the average particle size can be obtained as $a = \frac{K_B T}{4\pi D \eta}$, see Chapter 3. In contrast, NNLS can recover particle size distribution which is also implemented in this thesis. For validation, the obtained particle size distributions are compared with a gold standard method (DLS system).

5.2.1. Particle sizing using Stokes-Einstein relation

A. Monodisperse particles

Samples containing monodisperse population of colloidal particles are identical in size and shape [166]. A simple model of the DDM signal to non-interacting monodisperse particles in Brownian is given by [35], [36], [38] :

$$S(\mathbf{q},t) = A(\mathbf{q})[1-f] + B(\mathbf{q}) \tag{5.1}$$

where $S(\mathbf{q},t)$ represents the signal at wavevector q and time t, $A(\mathbf{q})$ is related to scattering properties of particles and optical setup, [35], [66], $B(\mathbf{q})$ accounts the noise term of the system, $f = e^{\left(-\frac{t}{\tau_c}\right)}$ is the normalised intermediate structuring function, [35], [36], [66], $\tau_c = \frac{\mathbf{q}^2}{D}$ is the characteristic time, and D is the diffusion coefficient.

A particle size distribution in a sample fluid was measured through the diffusion coefficient which is dependent on the particle size. The quantitative description of the diffusion coefficient is [35], [36], [38]:

$$D = \frac{k_B T}{3\pi\eta a} \tag{5.2}$$

where k_B is Boltzmann constant, T is the absolute temperature (K), η is the viscosity of the solution, and a is the diameter of the colloidal particle.

To estimate the particle size distribution, a sample solution was prepared by diluting 0.52 μm polystyrene microparticles with deionised water by 1000 times. Then, an image sequence of the sample was recorded using the developed device. Subsequently,

the image sequence was analysed by the DDA to obtain the intermediate scattering function f.

At this point, characteristic time τ_c was calculated by solving $f = e^{\left(-\frac{t}{\tau_c}\right)}$ from known values of f and time t. For noninteracting particles in Brownian motion, the characteristic time represents a linear relationship of τ_c and $\mathbf{q}^2$ which is $\tau_c = \mathbf{q}^2/D$ [35]. Thus, the diffusion coefficient is evaluated by determining slope between $1/\tau_c$ and $\mathbf{q}^2$ as it is shown in Figure 5.1.

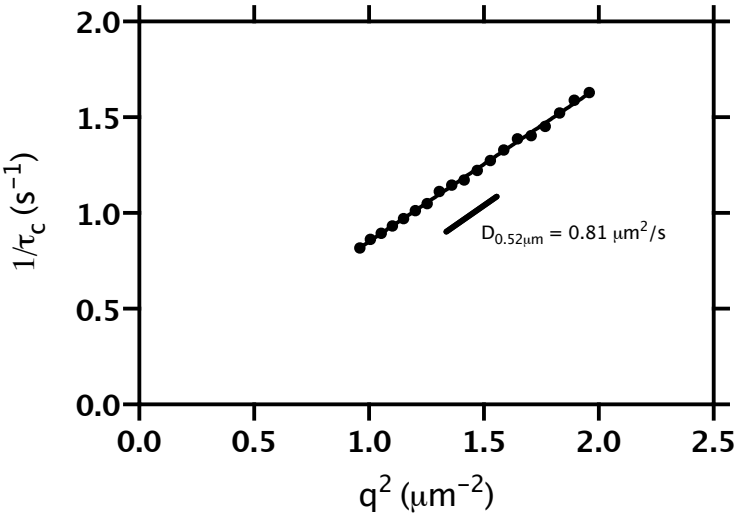

Figure 5.1. Illustration of $1/\tau_c$ and q^2 of 0.52 μm polystyrene microparticles in 20 °C deionised water. The black line represents the linear fit to the data points (from q^2 of 0.95 to 1.95 μm^{-2}) where its gradient indicated the diffusion coefficient which is 0.81 $\mu m^2/s$.

The illustration, see Fig, showed $1/\tau_c$ versus $\mathbf{q}^2$ of monodisperse particles from a three-fold replication. The linear fitting was described by the equation $1/\tau_c = 0.81\mathbf{q}^2+0.04$ with R^2=1.00. The gradient corresponded to the diffusion coefficient which was 0.81 $\mu m^2/s$, see Figure 5.1

To validate the result, the obtained diffusion coefficient was inserted into Equation (4.2) with a prior knowledge of measurement temperature and viscosity of the

deionised water. Accordingly, the particle size distribution of the dispersed microparticles was obtained. From these parameters, the estimated average particle size was 0.53 μm which was ~2% as a difference to the nominal factory calibrated value (0.52 μm).

B. Polydisperse particles

In polydisperse particles, non-uniform of several distinct size particle populations of varying size are dispersed in a solution of interest [167]. All of these particles contribute to the intermediate scattering function regarding to their size. Thus, the intermediate structuring function is generalised by summation of exponential functions as shown [152].

$$f = \int F(\Gamma) e^{-\Gamma t}\, d\Gamma \tag{5.3}$$

where $F(\Gamma)$ is a normalised weight function in which $\int F(\Gamma)\, d\Gamma = 1$ and $\Gamma = -1/\tau_c$.

From Equation (5.1), analysing the DDM signal of polydisperse particles using the developed device evaluates the average intermediate scattering function as shown in Equation (5.3). As a result, analysis using Stokes-Einstein relation yielded only average diffusion coefficient of suspended microparticles as $f = e^{\left(-\frac{t}{\tau_c}\right)}$ and $\tau_c = \mathbf{q}^2/D$.

To demonstrate this, a mixture of 0.52 μm and 1.54 μm polystyrene microparticles were put in an in-house microchamber. Then, the microchamber was placed in the developed device to acquire a sequence of images. The DDA was performed on the sequence to obtain the intermediate scattering function. Subsequently, $1/\tau_c$ and wave vector squared $\mathbf{q}^2$ of the intermediate scattering function was fitted as illustrated in Figure 5.2. The diffusion coefficient is calculated from the slope of the fitting shown in Figure 5.2.

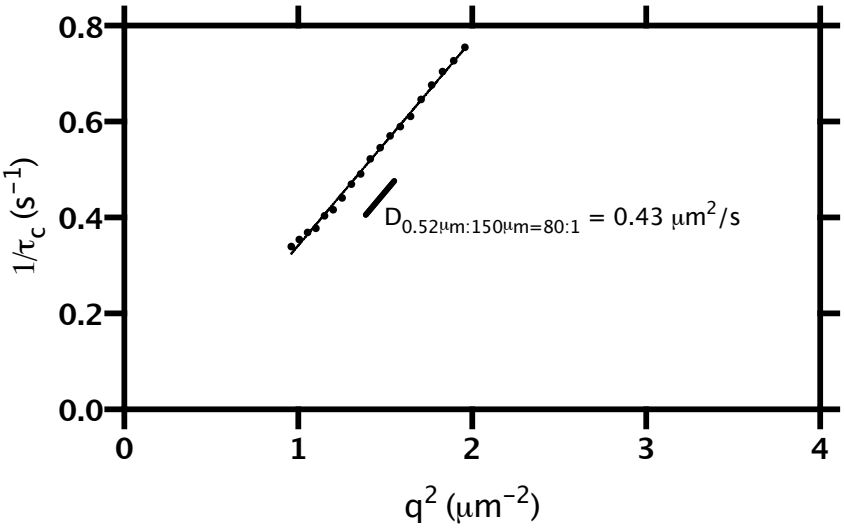

Figure 5.2 Illustration of $1/\tau_c$ and q^2 of a mixture with 0.52 μm and 1.54 μm polystyrene microparticles with mixing ratio of 80:1 suspended in deionised water at room temperature of 20 °C. The black line represents linear fitting to the data points (from q^2 = 0.95 to 1.95 μm^{-2}) where its gradient indicated the diffusion coefficient which is 0.43 $\mu m^2/s$.

From the results shown in Figure 5.2, the diffusion coefficient was estimated 0.43 $\mu m^2/s$. Then, by Equation (4.2) the estimated particle size was 1.00 μm, and it was incorrect. Thus, the particle size evaluation was not possible using the presented analytical method as demonstrated in Section 5.2.1C.

C. Particle sizing of mono and polydisperse microparticles

Solutions of monodisperse microparticles were mixed to prepare polydisperse microparticles solutions for size investigation of the suspended particles. To obtain the particle size, the intermediate scattering function of these solutions were determined by the developed device from fitting the signal with Equation (5.1).

Subsequently, the diffusion coefficient was obtained by $f = e^{\left(-\frac{t}{\tau_c}\right)}$ where $\tau_c = \mathbf{q}^2/D$ with known values of f, t and $\mathbf{q}$. Regarding to Stokes-Einstein relation (Equation (4.2)), particle size was obtained by $a = \frac{k_B T}{3\pi\eta D}$.

In this experiment, mixtures of two microparticle populations were prepared and measured with the developed device using stock solutions of both polystyrene microparticle sizes of 0.52 μm and 1.00 μm at 0.1×10^9 particles/mL by using Equation (5.6). Following this, these samples were pipetted out 6.0 μL then dispensed in an in-house microchambers. Next, data acquisition was performed to these microchambers to obtain their diffusion coefficients.

Table 5.1 Properties of stock solutions of polystyrene microparticle used in the experiment

Diameter (μm)	**x (g/mL)**	**y (g/cm^3)**	**a (μm)**	**Particle density ($\times 10^{12}$ particles/mL)**
0.35	0.01	1.05	0.35	0.43
0.52	0.03	1.05	0.52	0.39
1.00	0.03	1.05	1.00	0.05
1.54	0.03	1.05	1.54	0.01
2.10	0.03	1.05	2.10	0.01

For polydispersity measurement, the equalised particle concentration of 0.52 μm and 1.00 μm solutions were mixed with mixing ratio of 80:1 and 160:1 by volume. Then, diffusion coefficients of these samples were evaluated by performing DDA to the recorded data. The diffusion coefficients of the mixed particles and monodisperse particles are shown in Figure 5.3.

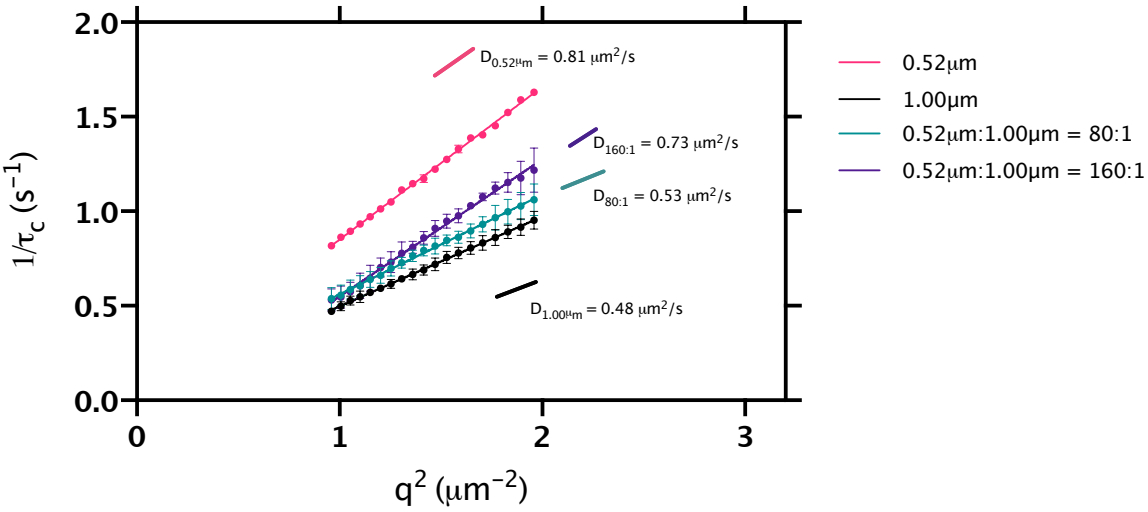

Figure 5.3. Illustration of $1/\tau_c$ versus q^2 of monodisperse of 0.52 μm and 1.00 μm which are indicated by pink and black dots respectively. In polydisperse solutions, mixtures of 0.52 μm and 1.00 μm are mixed at ratio of 80:1 and 160:1 which are indicated by green and purple dots respectively. The pink, purple, green, and black lines are obtained by performing linear fitting to the data points. These points present average and the error bars are standard deviations of three-fold replication of the measurement. The error bars smaller than symbols cannot be shown in the plot.

Figure 5.3 showed a linear dependence between $\mathbf{1/\tau_c}$ and wave vector squared $\mathbf{q^2}$ of monodisperse and polydisperse microparticle solutions. The slopes of lines revealed diffusion coefficients for 0.52 μm and 1.00 μm particles as 0.81 and 0.48 μm²/s respectively. The mixtures of 0.52 μm and 1.00 μm at mixing ratio of 80:1 and 160:1 indicated their diffusion coefficients within the diffusion coefficient of 0.52 μm and 1.00 μm.

From these results, it can be seen that the size of particle influenced to their diffusion coefficients. The smaller microparticles move faster thus the diffusion coefficient was higher than for larger microparticles. In case of mixed microparticle, the diffusion coefficient of large particles dominated small particles for the same amount. That was, the diffusion coefficient of 80 parts of 0.52 μm microparticles in the mixture (0.53 μm²/s) was still closer to the diffusion coefficient of 1.00 μm microparticles (0.48 μm²/s) than the diffusion coefficient of 0.52 μm microparticles (0.81 μm²/s).

5.2.2. Particle size distribution

Measurement of particles size distribution is an important application of DLS. Various analytical approaches of particle size distribution have been studied for this system . In analogous to DLS, DDM has ability to perform light scattering experiments. Thus, such analytical approaches can also be implemented on DDM platform.

A. Non-negative least square (NNLS)

Analytical methods have been developed to decompose the intermediate scattering function to particle size distribution of microparticles in a sample fluid. However, nonnegativity least square (NNLS) method [106], [171] was performed in the developed device to access particle size distribution. This method ensures that there is no negative particle size in the result distribution to reflect real-world information [172]. In addition, the NNLS has benefit of spending less in computational time while it provides a good particle size estimation result [108], [109].

The first and widely used NNLS [173] was developed an active set algorithm [174]. This algorithm partitions the set of measurement variable into active and passive sets. The active set contained the variables that violate the constraints whereas the passive set does not. The algorithm computes the solution and verify the constrain of each element in the active set. Then, the element is moved to the passive set and this process is repeated util there is no further update. The details of NNLS algorithm was described in [175] and [176].

For typical DLS system, intensity fluctuations are monitored by a PMT which is located at a certain scattering angle. Intensity autocorrelation was performed on such fluctuations resulting a single exponential decay. Following this, an analytical method

such as CONTIN or NNLS were applied to the decay to recover the particle size distribution. However, the particle size retrieval at a single angle does not providing a reliable results [107]. In contrast to the DLS, the developed device employed a webcam to record intensity fluctuations. The webcam accommodates arrays of micron-sized photo detectors to measure the scattering intensities at various angles. Due to this advantage, a resolution of particle size distribution was enhanced by performing multi-angle NNLS calculation [109], [177].

In general, the intermediate scattering function of monodisperse microparticles was calculated as a single exponential decay which is $f = e^{-t/\tau_c}$. A summation of single exponential decays represents a polydisperse solution. Then, weights w were added to the decays to represent fractions contribution by the particles [178]. The discrete form of polydisperse particles is written in this form [179]:

$$f = \sum_{i=0}^{n} w_i e^{\frac{-t}{\tau_{ci}}} \tag{5.4}$$

Unlike typical DLS system, scattering angles are accessed through Fourier analysis using the DDA [36]. This analysis provides accessibility to Fourier components or wave vectors $\mathbf{q}$ which were associated with scattering angles $\theta = 2sin^{-1}(\frac{\mathbf{q}\lambda}{4\pi n})$ where λ is wavelength of the light source, and n is reflective index of solution [35]–[38], [165].

In principle, the accessible range of wave vectors by the DDM are between $\frac{2\pi}{L}$ to $\frac{2\pi}{2dL}$ where L represents the size of image and dL is pixel correspond to distance [36], [38]. For aqueous sample, the developed device accessed the wave vector $\mathbf{q}$ from 0.02 to 8.68 μm^{-1} which corresponded to a scattering angle of 0.36° to 32.07°.

For Brownian equilibrium, random motions of microparticles cause intensity fluctuations in experimental data. The analyses of the fluctuations allows calculations

of the intermediate scattering function of the microparticles as a function of wave vectors. That is, exponential decays along the wave vectors are retrieved which are represented by $e^{-t/\tau_{ci}}$ where i is the index of the characteristic time τ_c. For multi-angle NNLS analysis, these decays are arranged in the form as represented in a system of equations [109]:

$$\begin{bmatrix} Y_1 \\ Y_2 \\ \vdots \\ Y_n \end{bmatrix} = \begin{bmatrix} \phi_{11} & \cdots & \phi_{1n} \\ \phi_{21} & \cdots & \phi_{2n} \\ \vdots & \ddots & \vdots \\ \phi_{m1} & \cdots & \phi_{mn} \end{bmatrix} \begin{bmatrix} X_1 \\ X_2 \\ \vdots \\ X_n \end{bmatrix} \tag{5.5}$$

where $\phi_{mn} = e^{\frac{-t_m}{\tau_{cn}}}$, m is the total number of measurement time, n is the total characteristic time collected from DDM device, $\mathbf{X}$ represents the weight function, and $\mathbf{Y}$ is the result distribution.

The aim of NNLS is to obtain coefficient or weight function $\mathbf{X}$ which represents particle size distribution of the measurement. The optimal value of weight function $\mathbf{X}$ can be found by $\mathbf{X} = (\boldsymbol{\phi}^T\boldsymbol{\phi})^{-1}\boldsymbol{\phi}^T\mathbf{Y}$ under criteria of $\min|\mathbf{Y} - \boldsymbol{\phi}\mathbf{X}|^2$, where $\mathbf{X} \geq 0$, [110], [111], [180], [181].

5.3. Material and methods

In sample preparation, sample solutions were divided into two groups which were monodisperse and polydisperse microparticles. For monodisperse microparticles, stock solutions of 0.348 μm, 0.52 μm, 1.00 μm, and 1.54 μm polystyrene microparticles were diluted by 100 times with deionised water. Then, each of diluted solution was pipetted a 6.0 μL and dispensed into an in-house microchamber. Next, a cover slip was placed on the sample and sealed the edge of the cover slip using nail vanish to prevent sample evaporation. In data acquisition, the motion of particles in the microchamber was recorded by the developed device. Following this, the recorded data were analysed

using the DDA to obtain intermediate scattering function. Accordingly, the NNLS was performed on the function to evaluate particle size distribution of the sample.

For validation, a DLS (Zetasizer ZS90 Malvern Panalytical Ltd) measured and analysed the identical samples that were measured using the developed device. Particle size distribution of the samples were obtained using the DLS software which also analysed by NNLS algorithm according to the device information [182]. In the measurement, 50.0 μL of sample was prepared in a disposable cuvette for a measurement. To obtain a reliable result, the sample was rest in the device for 2 minutes prior to the measurement. Each sample measurement was replicated three-fold.

In sample preparation, the concentration of the stock solutions of monodisperse microparticles were equalised to 0.1×10^9 particles/mL, each sample of which was pipetted according to the calculation in Equation (5.6) [183]. Then, the unit of volume was dispensed in an Eppendorf with 1.0 mL of deionised water.

$$total\ Particles\ per\ mL = \frac{6x \cdot 10^{12}}{y \cdot \pi \cdot a^3} \tag{5.6}$$

where, x is the particle weight per mL (g/mL), y is the density (g/mL) , and a represents the diameter (μm).

5.4. Experimental results

5.4.1. Monodisperse particles

In monodisperse particles, 0.35 μm, 0.52 μm, 1.00 μm, and 1.54 μm of stock polystyrene microparticles solutions were used in experiments. The particle size

selection was based on a resolving power of the developed DDM system (0.35 μm). In sample preparation, each particle population was diluted with deionised water by 1000 times. Following this, these samples were pipetted approximately 6.0 μL and dispensed into in-house microchambers.

Coverslips were placed on the samples with nail vanish around the edges of the coverslips to seal them. Then, the developed device acquired the light fluctuations due to motion of microparticles which were in the microchambers. Afterwards, DDA analysed the fluctuation to obtain their intermediate scattering functions. Then, NNLS was performed on rearranged the intermediate scattering functions as indicated in Equation (5.5). As a result, the population distributions were inversed and they are shown in Figure 5.4.

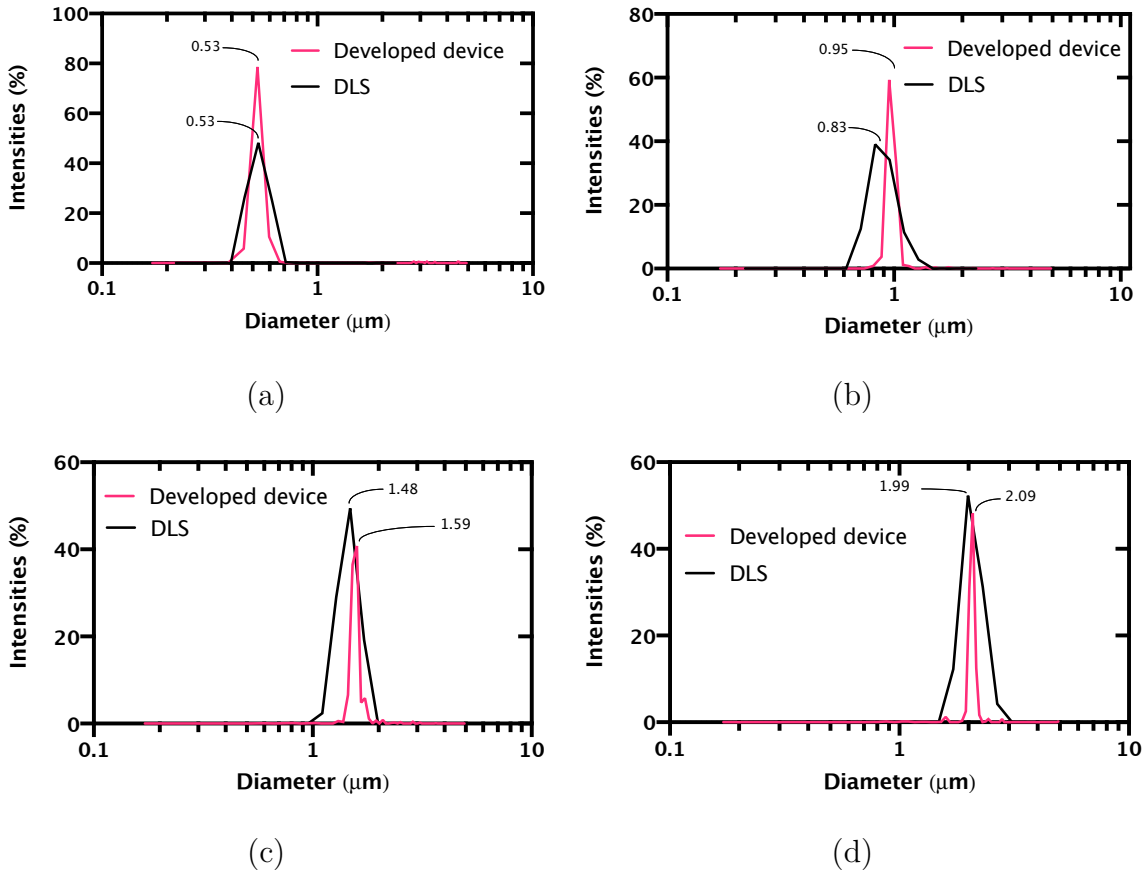

Figure 5.4. Particle size distributions of polystyrene microparticles dispersed in 20°C deionised water. (a) 0.52 μm, (b) 1.00 μm, (c) 1.54 μm, and (d) 2.10 μm. The red and black lines represent particles size distributions obtained by the developed device and a DLS system respectively.

Regarding to Figure 5.4(a)-(d), the red lines represented particle size distribution obtained by the developed device while the black lines indicated the distributions measured by a DLS system. In the developed device, the peak intensities were 78.63%, 59.29%, 40.78%, and 48.17% at diameters of 0.53, 0.95, 1.59, and 2.09 μm respectively.

Similarity, the particle size distributions obtained by the reference DLS system show the peak intensities of 48.20%, 39.00%, 49.43%, and 52.27% at diameters of 0.53, 0.83, 1.48, and 1.99 μm respectively. However, the particle size distributions retrieved by the developed device show narrow distributions compared to the DLS system, as the resolution of particle size distribution was enhanced by more information available from multi-angle NNLS approach [177], [184]. Comparison of the retrieved diameters

at the peak intensities of the developed device and DLS system to the nominal diameters are listed in Table 5.2.

Table 5.2. Particle sizes at the peak intensities.

Nominal diameter (µm)	**Developed device**		**DLS**	
	Peak intensity at diameter (µm)	**Absolute error (%)**	**Peak intensity at diameter (µm)**	**Absolute error (%)**
0.52	0.53	1.92	0.53	1.92
1.00	0.95	5.00	0.83	17.00
1.54	1.59	6.00	1.48	1.33
2.10	2.09	0.48	1.99	5.24

Results in Table 5.2 shows that the absolute error of the developed device was comparable to DLS system. When compared with nominal diameters, the absolute error of peak diameters produced by multi-angle NNLS were <10%. That is, the result measurement was within ±5% from the nominal value.

A. Particle size distribution beyond limit of resolution

In this context, limit of resolution restricts an imaging device to perceive of microparticles by mean of discrete pixels in an image at a wavelength emitted by the device. Two adjacent particles can be resolved as only one particle by the system from the limit. In addition, a particle which its size much smaller than the limit, or the physical size of 1 pixel, is invisible. This parameter indicates sizes selection of microparticles that are suitable for a measurement by the device. Accordingly, the size of microparticles should be above the resolution limit therefore the device could detect weak scattered signal. For the developed device, the resolution limit of the developed

device was evaluated by imaging a prior known length of scalebar as illustration in Fig 5.5.

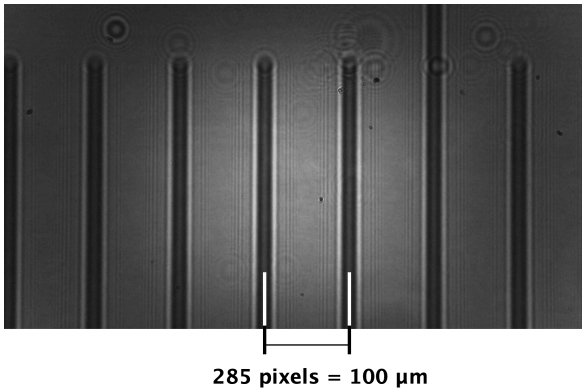

Figure 5.5. Resolution limit of the developed device. The scale bar indicates the actual length is 100 µm and the middle-to-middle distance of the bar measured by the device is 285 pixels.

Figure 5.5 shows that the length of the scale bar of 100 µm was approximately 285 pixels when measured by the device. Thus, the resolution limit of the developed device was 0.35 µm. However, DDM has been reported for measuring the particle below the resolution limit [37], [62]. From this reason, particle size distribution beyond the resolution limit was also investigated by the developed device. For sample preparation, polystyrene particles size of 150, 208, 288, and 348 nm were diluted by 1,000 times with deionised water.

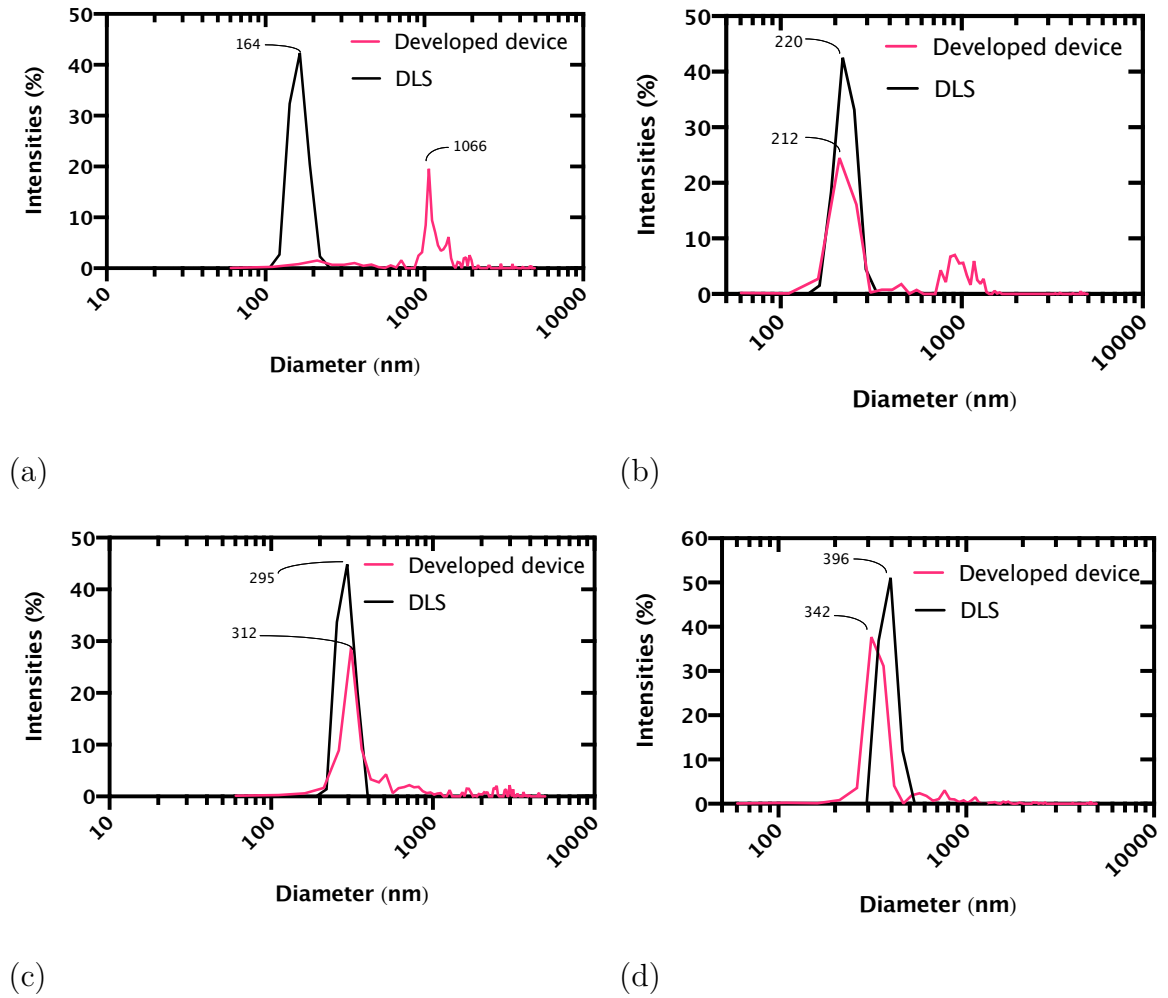

Figure 5.6. Particle size distributions of polystyrene microparticles dispersed in 20°C deionised water: (a) 150 nm, (b) 208 nm, (c) 288 nm, and (d) 348 nm. The red and black lines represent particles size distributions obtained by the developed device and a DLS system respectively.

These sample solutions were then pipetted and dispersed into in-house microchambers for data acquisitions. Following this, DDA was performed on the data to evaluate intermediate scattering functions of the solutions. To retrieve particle size distributions, multi-angle NNLS was applied to the intermediate scattering functions. The inversed particle size distributions of polystyrene particles sizes of 150, 207.9, 288, and 348 nm were shown in Figure 5.6(a) to (d) respectively.

According to Figure 5.6, particle sizes distributions of polystyrene particles sizes of 150, 208, 288, and 348 nm were plotted in Figure 5.6 (a) to (d) respectively. This figure illustrated the measurement of microparticles whose sizes are below the

resolution limit of the developed device (1 pixel ≈ 0.35 μm). Red colour indicated the particle size distributions measured by the developed device. The measured particle size distributions had peak intensities of 19.57%, 24.48%, 28.18%, and 36.90% at diameters of 1066, 212, 312, and 342 nm, respectively. In comparison with DLS, the particle size distributions show peak intensity of 42.30%, 42.53%, 44.83%, and 51.07% at diameters of 164, 220, 295, and 396 nm, respectively. These results with the nominal values were listed in Table 5.3.

Table 5.3. Experimental particle sizes beyond the resolution limit of the developed device in comparison to the DLS system.

Nominal diameter (nm)	**Developed device**		**DLS**	
	Peak intensity at diameter (nm)	**Absolute error (%)**	**Peak intensity at diameter (nm)**	**Absolute error (%)**
150	1066	610.67	164	9.33
208	212	1.97	220	5.82
288	312	8.33	295	2.43
348	342	1.72	396	13.79

Results listed in Table 5.3 show that the particle size distribution beyond resolution limit of the developed device was determined. From the measurements, peaks of the distribution of 208, 288, and 348 nm were in agreement with the DLS measurements. The results showed that the developed device could not measure the actual size of 150 nm solution. Unlike the result from the DLS system, unexpected peaks were presented when size of detecting particles becomes smaller as the DLS collects scattered light using high sensitivity light detector.

5.4.2. Polydisperse particles

In polydisperse particles, stock solution of polystyrene microparticles were normalised to the same concentration as it was presented in Section 5.6.1. Following this, mixtures were produced by combining two or more normalised monodispersed particles. From Figure 5.3, mixing ratio affects diffusion coefficient obtained by Stokes-Einstein relation analysis. In addition, larger particles contributed considerably to the diffusion coefficient than smaller particles. However, only an average size of particles could be obtained using the Stokes-Einstein relation analysis. In this section, an inversion of particle size distribution using multi-angle NNLS for polydisperse particles solution was demonstrated. Then, the result was compared and validated with the reference DLS system.

A. Binary mixture

For binary mixture, three mixtures of polystyrene microparticles with diameter of 1.00 and 2.10 μm were mixed at mixing ratio of 2:1, 10:1, and 40:1. Then, in-house microchambers were filled by these mixtures, and they were placed on the sample holder of the device. Following this, developed device recorded light scattering due to the motion microparticles motion in the microchambers. Next, the recorded data were analysed by the DDA to obtain intermediate scattering function. Accordingly, the multi-angle NNLS was performed on the obtained intermediate scattering function to achieve particle size distribution, see Figure 5.7.

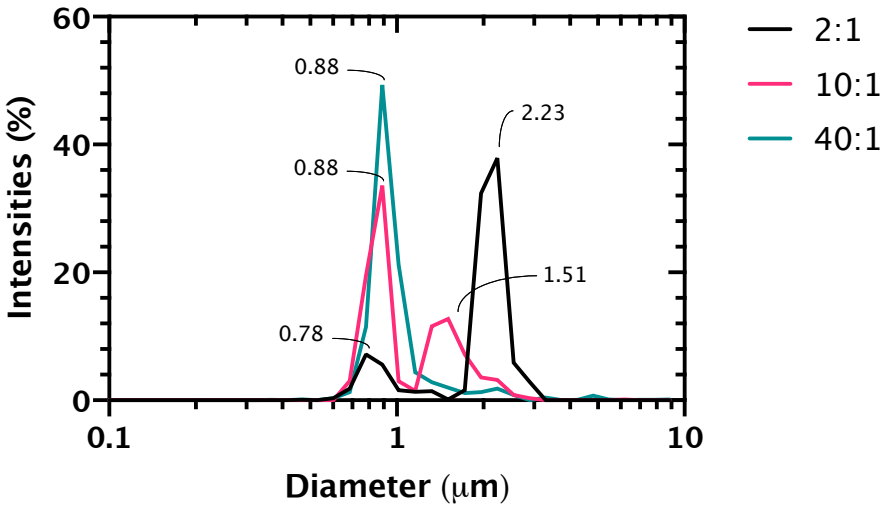

Figure 5.7. Particle size distribution of the polystyrene microparticles mixture with diameters of 1.00 μm and 2.10 μm at three mixing ratios. All of the distributions are evaluated by performing the NNLS to the measurement data obtained by the developed device. The black, pink, and green lines represent particle size distributions of 1.00 μm:2.10 μm at mixing ratio of 2:1, 10:1, and 40:1, respectively.

Figure 5.7 showed the particle size distributions of polystyrene microparticles mixtures with diameter of 1.00 and 2.10 μm. At mixing ratio of 2:1, the peak intensities were 7.18% and 37.89% at diameter of 0.78 μm and 2.23 μm, respectively, although the particle concentration of 1.00 μm was two-folded compared to 2.10 μm. For the mixing ratio of 10:1, the peak intensities were 33.56% and 12.72% at diameter 8.89 μm and 1.51 μm, respectively. Nevertheless, there was only one peak of 49.33% at diameter 8.89 μm for the mixing ratio of 40:1.

In summary, both of proportion and size of microparticles was seen to significantly influence to the particle size distribution by the NNLS approach. The increasing portion of particles will increase percent intensity of the particle. By analogy to the size of particle, larger particles contributed more intensity in the particle size distribution, as the larger particle accommodated more pixels in an acquired image than the smaller ones.

For validation, particle size distributions measured by the developed devices were compared with the result measured using DLS system. In sample preparation, particle density of the mixing particle were equalised. Then, mixtures of two particles populations were prepared by limiting the mixing ratio to 80:1. In this experiment, the mixtures were prepared according to gap size different of two particle populations. For two-folded size different, particle sizes of 0.52 and 1.00 μm were used in the experiment. These particles were mixed, then, put 6.0 μL of the mixture into an in-house microchamber. Next, light scattering due to the movement of particles in the microchamber was recorded by the developed device. Following this, the recorded data were analysed by the DDA to obtain its intermediate scattering function. This function was later analysed by the NNLS to evaluate particle size distribution of the mixture. The measured particle size distribution is shown in Figure 5.8.

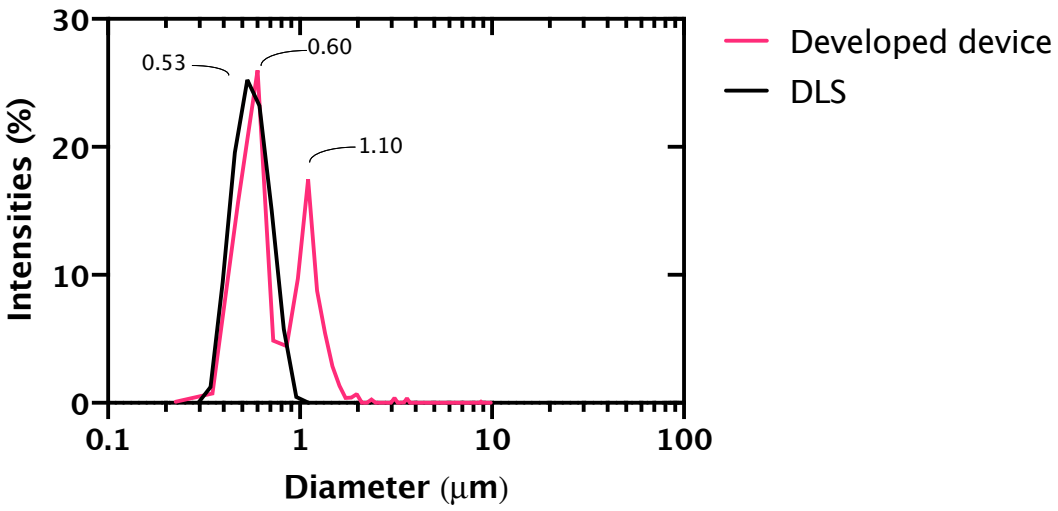

Figure 5.8. Particle size distribution of the polystyrene microparticles mixture with diameters of 0.52 μm and 1.00 μm and mixing ratio of 80:1. The black colour indicates the size distribution measured by the DLS system. The pink colour represents the size distribution measured by the developed device. The peak intensity by the DLS system is 25.23% at diameter of 0.53 μm while the developed device shows two peak intensities of 25.98% and 17.48% at diameters of 0.60 μm and 1.10 μm, respectively.

Figure 5.8 showed particle size distribution of a mixture with diameters of 0.52 and 1.00 µm and mixing ratio of 80:1. Two peak intensities were obtained at diameter of 0.60 and 1.10 µm by the developed device. On the contrary, DLS detected only one particle population which was represented at diameter of 0.53 µm. However, the result populations obtained by the developed device were overlapping between 0.60 - 0.80 µm, as the gap between two sizes of microparticles were small for the NNLS conversion. Therefore, a three-fold gap size was investigated, see Figure 5.9.

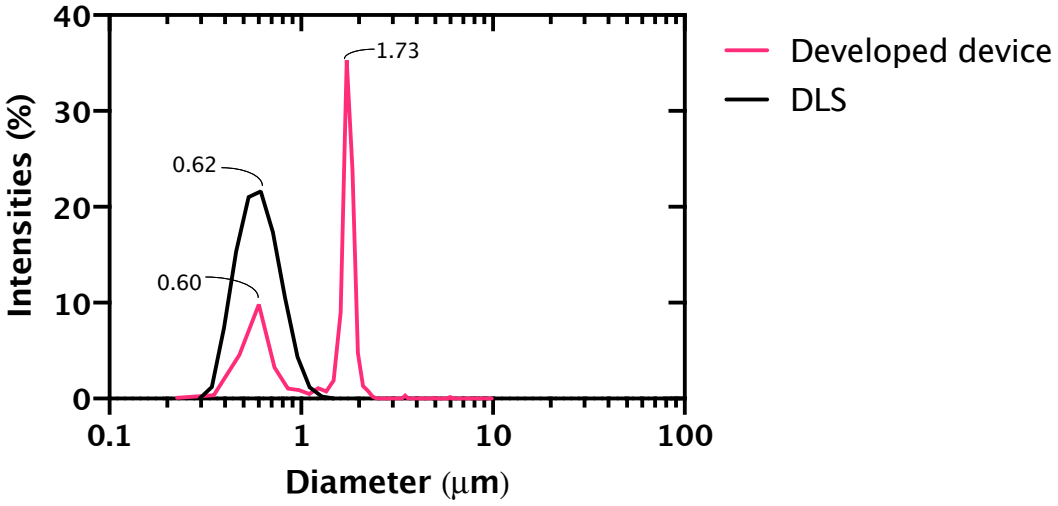

Figure 5.9. Particle size distribution of a polystyrene microparticles mixture with diameters of 0.52 µm and 1.54 µm and mixing ratio of 80:1. The black colour indicates the size distribution obtained by the DLS system. The pink colour represents the size distribution obtained by the developed device. The peak intensity by the DLS system is 21.60% at diameter of 0.62 µm while the developed device shows two peaks intensities of 9.81% and 35.27% at diameter of 0.60 µm and 1.73 µm, respectively.

Figure 5.9 depicted particle size distribution of three-fold gap size in a mixture. The normalised monodisperse particles with sizes of 0.52 and 1.54 µm were mixed at mixing ratio of 80:1. Following this, the mixture was analysed by the DDA and the NNLS was performed on the analysed data afterwards to achieve the particle size distribution. For DLS system, the particle size distribution indicated only one peak at diameter of 0.62 µm.

In contrast to the developed device, two peaks were seen at diameters of 0.60 and 1.73 µm. When compared to the twice gap size, the three-fold gap size differentiated the mixed population better, see Figure 5.8 and Figure 5.9. The particle size distributions of twice and three-fold gap sizes were shown in Fig 5.10. It is important to note that the four-fold gap size of 0.52 and 2.10 µm was also shown in Figure 5.10.

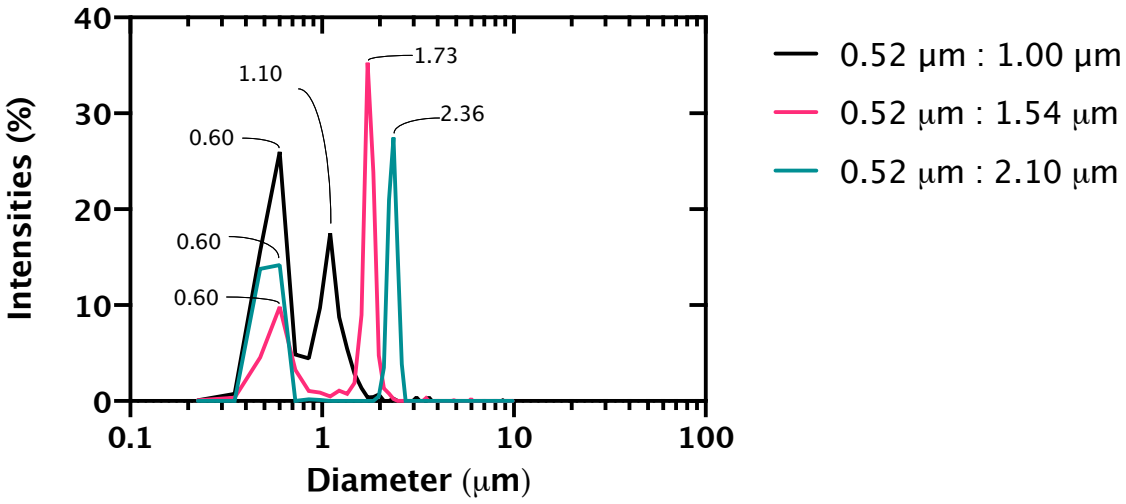

Figure 5.10. Particle size distributions measured by the developed device of three polydisperse mixtures at mixing ratio of 80:1. The black colour shows the size distribution of 0.52 and 1.00 µm where two peaks intensities are detected at 0.60 and 1.10 µm. The pink colour represents the size distribution of 0.52 and 1.54 µm where two peaks intensities are detected at 0.60 and 1.73 µm. The green colour indicates the size distribution of 0.52 and 2.10 µm where two peaks intensities are detected at 0.60 and 2.36 µm

Figure 5.10 depicted particle size distributions of three gap sizes. The results showed that twice gap size indicates an overlap of two mixed populations which were 0.52 and 1.00 µm. When the gap size increased, the mixed population was better differentiated. In addition, the developed device was able to differentiate two mixed populations with a good approximation compared to the nominal values. In contrast, DLS can only determine single population distributions as this technique collects scattered light at a certain angle while the developed device detected the scattered light at the multiple angles in a single measurement.

5.5. Conclusions

DLS is an established method for measuring size distribution of colloidal particles [185]. Inversion methods such as CONTIN [160] and NNLS [174] has been successfully analyse the DLS measurement to obtain the particle size distribution. In fact, DDM can perform light scattering experiment similar to DLS from Fourier analysis of images. As a result, DDM should be able to measure particle size distribution of colloidal particles. However, the particle size distribution that can differentiate two or more particles populations in a suspension is still not implemented in DDM measurement yet.

In this chapter, NNLS was implemented to estimate particle size distribution from the data obtained by the DDM-based device that developed in this thesis. This method has benefited for obtaining non-negative distribution from the calculation constraint. In addition, it spends considerably less in computational time and provide a reliable result without complicated calibration [108]. For validation, the obtained distribution was compared with the result of NNLS algorithm that implemented in a reference DLS system (Zetasizer ZS90 Malvern Panalytical Ltd) [182].

In the experiment, size analysis with Stokes-Einstein relation obtained only average particle size in a particle suspension, as expected. As a result, particle size of polydisperse microparticles calculated using this relation did not yield a reliable result. However, intermediate scattering function of monodisperse microparticles was modelled by single exponential decay. Thus, an intermediate scattering function of polydisperse microparticles is composed of multi exponential decays. From this reason, the intermediate scattering function of can be decomposed into the decays from using a numerical analysis.

In this work, NNLS was used to obtain particle size distribution of mono and polydisperse microparticles from the intermediate scattering function obtained using the developed device. In monodisperse particles, the develop device was able to obtain particle size distributions of 0.52, 1.00, 1.54, and 2.10 μm colloidal particles. In verification, the peak value of the distributions were compared with the nominal values. From the result, the absolute error of the measurement done by the developed device was approximately within 6% in comparison to the nominal values.

When compared with the reference DLS system, the result distribution was in good agreement. However, the distributions obtained using the developed device shown the narrower distribution. As expected, this was the developed device measured multiple angles at a single measurement. Thus, the multi angles NNLS improved the resolution according to the prior studies [109], [177].

For the particle sizes beyond limit of resolution (0.35 μm) of the developed device, the obtained particle size distributions were comparable to the nominal values. In 208, 288, and 348 nm colloidal nanoparticles, the device was able to determine reliable results. The diameters at their peak intensities were selected for calculating absolute error of the measurement compared with the nominal values. It turned out that the absolute error was within 9% from the measurement done by the developed device. However, the 150 nm colloidal particles did not provide a reliable result. Unlike the result from the reference DLS system, unexpected peaks were presented when size of detecting particles becomes smaller. This was because, the DLS collects scattered light using high sensitivity light detector.

In polydisperse particles, the developed device was successfully differentiated two particle populations in a colloidal solution. In sample preparation, the particle solutions were equalised by total number to 0.1×10^{9} particles/mL from using the calculation provided by the technical data from the microparticle commercial source

(Polysciences Inc) [183]. The reason for this was to investigate size influence to obtained particle distribution. It turned out that larger particles were influenced more to the intensity in the distribution as the larger particles accommodated more in pixels representation in an image than smaller ones. In addition, the gap size between both populations was a major parameter that the developed device was able to differentiate. Furthermore, the differentiation is also governed by size uniformity of the particles used in the experiment. For single fold gap size, there was a crossover region between two population in the obtained particle size distribution. However, there was a negligible crossover region from more than twice gap size difference. When compared with the reference DLS system, the DLS was unable to differentiate two mixed particles populations in a solution.

Chapter 6

Haemorheology and rheology of biological fluids

Haemorheology is the study of rheological properties in blood [186]–[188]. This study includes the investigation of deformation and flow of its corpuscles or formed cellular elements i.e. RBCs (erythrocytes), WBCs (leukocytes), and platelets (thrombocytes) [186], [187]. In general, blood is considered as a two-phase liquid [189] of those elements suspended in a light pale yellow solution of water, salt, proteins and enzymes called plasma. However, the most remarkable influence to the mechanical properties of the blood are the RBCs.

RBCs constitute about 40 to 45 % of the volume of the blood in healthy individual. This high volume percentage of RBCs (% known as the haematocrit) causes the rheological properties to be significantly dependent on deformation and aggregation of the RBCs. Despite the fact that RBCs dominate in the blood rheology, WBCs also have an influence on the blood rheology in disease because they maintain adhesion to the endothelium in fighting infections [190]. However, their effect to the blood rheology is negligible due to it has small population in healthy individuals.

Individual RBCs collides and adhere other RBCs can form an aggregate. The probability of the contact between RBCs increases due to Brownian motion [191]–[193]. However, aggregation of RBCs is not sufficiently understood. At least two types of aggregation formations are reported which are bridging and depletion models [191],

[194]. In bridging model, chemical bonds to the surface of RBCs occurs between the collision. As opposed to depletion model, the RBCs could be aggregated by depletion force.

In very low or no flow setting, adhesive interaction between RBCs leads to a formation of RBCs aggregate (Rouleaux) [195]. The primary aggregate formation consists of aggregation between two RBCs called RBCs doublet which allows for large rouleaux formation [196]. In the RBCs doublet formation, two non-interacting RBCs are very close with inter-central distance in ranges between 7.0 to 9.0 μm for normal RBCs [197]. Then, these RBCs slowly overlap each other with a mean time of 100 s [198] to resemble a stack of coins. As the aggregation proceeds, size of the RBCs aggregate increases in which sedimentation of the RBCs dominates the Brownian diffusion [119]. Therefore, the viscosity measurement obtained using passive rheology approach (by the developed device) is invalid and unreliable as the measurement relies on the Brownian diffusion of individual RBCs. To minimise this influence, the blood sample was gently shake and measured immediately. In addition, light scattering signal of the RBCs movement were collected only 10 s for obtaining blood viscosity.

Whole blood behaves as a non-Newtonian fluid, that is, viscosity of the blood is considerably depended on shear rate [101], [186], [198]. This behaviour occurs due to the ability of RBCs to aggregate, stack, and form 3D structures (known as a rouleaux) [101]. When the blood is at rest, its viscosity increases exponentially due to the RBCs undergo rouleaux formation. In contrast, this formation can be broken apart by an action of blood flow particularly at high shear rate. As a result, viscosity is decreased which then continues to reach steady state as no more RBCs are aggregated. This prominent reversible behaviour is called shear-thinning (or pseudoplastic) system [2], [199]. Altogether, the viscosity of the blood is dependent upon RBCs rigidity and their formation.

An increase in haemorheology interests arises from clinical studies of cardiovascular diseases, where it may be a primary cause in blood flow pathologies [190]. In reality, alteration of haemorheological parameters is also related to various other diseases such as diabetes mellitus [200], sickle cell anaemia [7], and stroke [2], [201], [202]. Thus, rheological properties of the blood are important to maintain biological function in microcirculation. As a result, measurement of blood rheology could provide useful clinical information and to advance investigation for developing new accurate and rapid evaluation methodologies related to these diseases.

A vast majority of heamorheological studies measure and characterise viscosity as a function of shear rate , usually obtained using a mechanical rheometer. By imposing a shear force, the result response is measured according to the applied shear. However, the main drawback of this instrument is it requires large sample volumes (>1 mL) to operate. In addition, the instrument is bulky and time-consuming to process in general because it is necessary to calibrate prior to measurement [205]. Furthermore, complications of blood interaction with the sample container may lead to misinterpretation of the obtained responses. For example, cleaning is a vital process for the indisposable container in order to clear out previous blood clots [205]. Apart from that, thin film occurrence at blood interfaces exposed to the air leads to the inaccurate of the measurement at low shear rate [206]. Evaluation of haemorheology at the microscale remains a field where study is needed [202], [204].

In this chapter, rheological assessment of biological fluids such as human whole blood, blood plasma, and human whole saliva were measured by the developed device. In addition, alteration of blood viscosity underwent storage was examined. Moreover, preliminary investigation of viscosity between healthy individuals and stroke patients were observed by the developed device.

The developed device was based on DDM which investigates dynamical properties of a fluid. The DDM device analyses a sequence of images by Fourier analysis allow for performing light scattering experiment i.e. DLS. It is important to note that a few modifications were applied to the typical DDM. The first step is miniaturisation of the device. This system was built up from 3D printer equipped with an objective lens and a webcam for data acquisition.

In addition, performing data acquisition by a webcam has limitation in real-time image transfer. Loss of images may occurred if that image cannot be transmitted to a computer in time. However, time associated with the image is assumed in typical DDA, which exploits a fixed lag time associated with each acquired image. For this reason, a time stamp was introduced in this work to tackle this issue in the typical DDA.

Secondly, an infrared light emitting diode of 860 nm was used for specimen illumination in our developed device. At this wavelength, there is a remarkably less of light absorbance by human whole blood which is almost 2 to 3 fold less compared to visible light.

The last modification is an in-house microchamber to accommodate a tiny volume of sample fluid. This sample container is simply made of a glass slide with double-sided tape and coverslip. Then, the sample was sealed and enclosed by nail vanish around edges to prevent evaporation. This microchamber occupies approximately 6.0 μL. As opposed to macro-scale bulk rheometry, the microchamber consumes less sample and is inexpensive and disposable.

In viscoelastic assessment, the DDA calculates mean square displacement from movement of tracer particles in a measuring fluid. Then, the GSER converts this mean square displacement to viscoelastic moduli of the fluid. Nevertheless, numerical

artefacts are present at high frequency response obtained by the GSER conversion. Accordingly, a direct numerical conversion [70] was implemented and performed to obtain the viscoelastic moduli throughout this work. Then, these moduli can be converted to complex viscosity $\eta(\omega)$ of the fluid which is $\sqrt{G'(\omega)^2 + G''(\omega)^2}/\omega$.

A vast majority of rheological studies of biological fluids evaluate the steady-shear viscosity $\eta(\dot{\gamma})$ of the fluid. From this reason, Cox-Merz rule was applied to the complex viscosity to estimate steady-shear viscosity. It was noted that viscosity conversion using the Cox-Merz rule shows high deviation at low shear rate [202].

6.1. Blood components

Blood is a complex fluid contain living cells suspended in a water-based solution as known as plasma [101], [207]. In blood composition, plasma represents roughly 55% of the blood volume whereas the remaining part are the cells [207]. Blood plasma is made of 92% water while the remaining parts are mainly proteins which are fibrinogen, globulins, albumin, beta lipoprotein and lipalbumin [208]. The majority of suspended proteins are albumin, globulins, and fibrinogen which are approximately 50%, 45% and 5% of the total proteins respectively [208].

In fact, plasma behaves as a Newtonian fluid [2], [209], [210] whose viscosity is directly correlated with concentration of proteins and lipids [206]. However, recent studies [211], [212] found that the plasma behaves like a slightly non-Newtonian fluid in pure extensional flow, as macro-mechanical rheometers cannot stretch proteins in plasma effectively [211], [212]. As a result, elasticity of the plasma is not present in the viscoelasticity from these measurements.

In the matter of cells composition, RBCs constitute approximately 95% of the total cells volume [101]. In general, a RBC is a biconcave discoid shape with approximately 8 μm in diameter and 2 μm of thickness [213], [214]. The total volume of a RBC is roughly 85 μm^3 [214]. RBCs consist of very flexible membrane surround within a solution of haemoglobin [2], [209]. The flexibility of the membrane makes the RBCs easy to bend and deform with the flow direction. In contrast to RBCs, WBCs represent quite fewer roughly 1 to 500 RBCs [1], [215]. Thus, WBCs are only slightly influential to the rheological responses of the blood in healthy individuals.

Platelets are a blood component whose individual sizes are approximately 2-3 μm [214], [216]. They constitute approximately 4% of the total blood cells [214]. The key function of platelets is to maintain haemostasis by binding to together to form a thrombus (clot) to stop bleeding [101], [217].

6.2. Rheological characteristics of the blood

Rheological investigation of blood has been studied for many decades [218]. The majority of the study has been found the blood exhibits a non-Newtonian characteristic, specifically shear thinning, in healthy individual [101], [186], [198]. At low shear rate, the RBCs aggregate, stack, and form a rouleaux structures. This behaviour leads to a remarkably rise to the blood viscosity. In contrast to high shear rate flow, these rouleaux break apart. Thus, the relative viscosity is almost constant as shown in Fig 6.1.

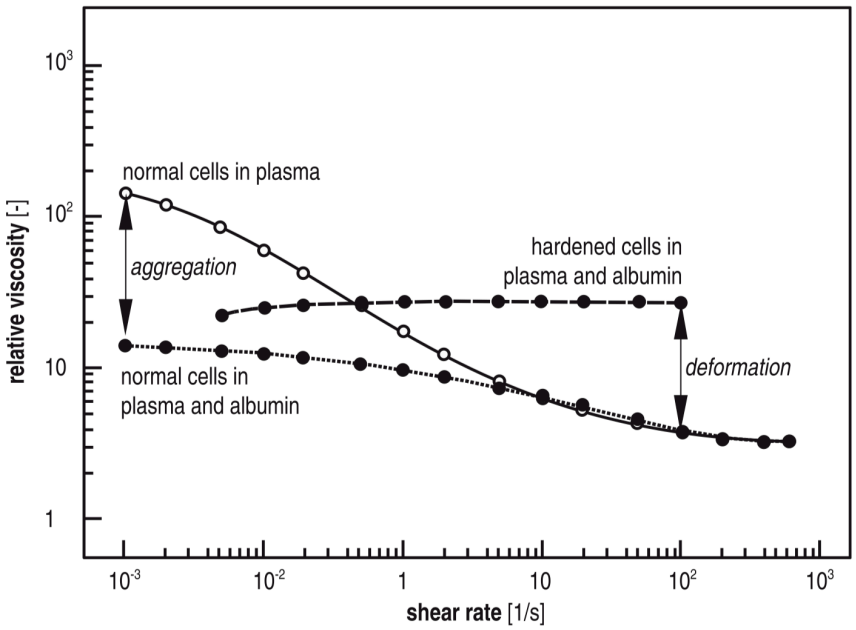

Figure 6.1 Relation between relative viscosity (normalised by plasma viscosity) and shear rate of human whole blood (45% haematocrit and normalised with plasma viscosity of 1.20 mPa.s) The circle represents whole blood viscosity while the solid circle is the result viscosity when adding albumin to reduce RBCs aggregation [219]. The solid circle dashed line responsible for viscosity of hardened RBCs in whole blood (Image is taken from [31]).

In addition, elasticity of the RBCs also plays a vital role to the blood viscosity and its ability to flow as shown in Figure 6.1. Whole blood viscosity is also influenced by plasma viscosity, haematocrit, and platelet aggregation [220]. These important determinants to blood viscosity can be summarised in an illustration in Figure 6.2.

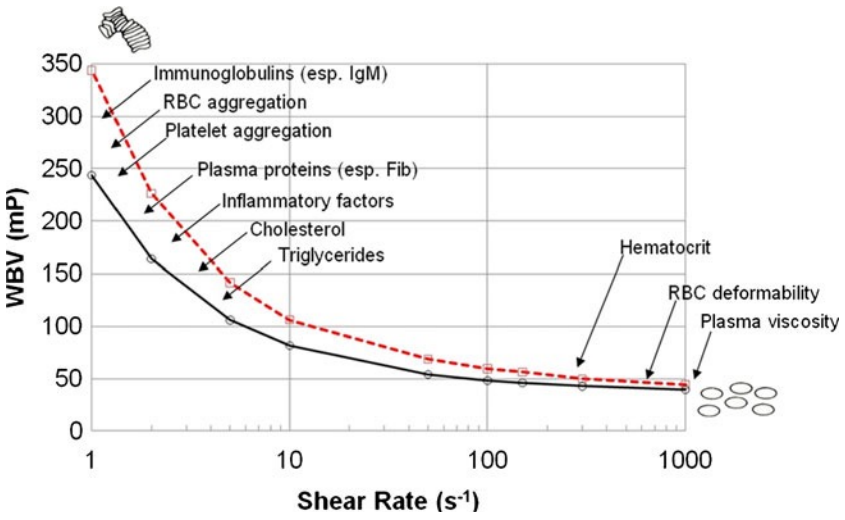

Figure 6.2. Important determinants of whole blood viscosity (image taken from [220]).

For rheological study of the blood, anticoagulant is added to the blood sample in general. This additional chemical helps to prevent blood becomes clotted, as a consequence, it allows for longer time to measure. In practice, common anticoagulants used in the blood measurement are heparin and ethylenediaminetetraacetate (EDTA) [221], as they have a negligible effect on the blood viscosity in a wide range of shear rate (0.0009 – 1000 s^{-1}) [2], [206], [222]. However, whole blood with heparin influences haemorheological parameters to greater extent than EDTA [206], [223].

Abundant over-use of such anticoagulant can cause erroneous of the measurement [204], [224]. As a result, International Society for Clinical Haemorheology recommends EDTA as an anticoagulant for haemorheological studies which maximum concentration of 1.8 mg/mL [206]. Such that, the anticoagulant does not influence to the measurement.

6.3. Conventional techniques for measuring blood viscosity

Numerous of the study emphasis in steady shear flow experiment to achieve steady-shear viscosity [225]. However, blood is a Non-Newtonian fluid. Thus oscillatory shear experiment is best suited for the blood study since it is in-between solid and liquid [202]. In this section, conventional techniques used for rheological assessment of the blood are introduced and discussed.

6.3.1. Small-amplitude oscillatory shear flow (SAOS) rheometry

SAOS rheometry is a gold standard approach to measure viscoelastic properties of a fluid. This technique applies a small oscillatory shear amplitude to limit small strain

of a fluid for linear viscoelastic investigation [226]. For a measurement, a volume of sample fluid is dispensed in a fixed position container. A sinusoidal stress exposes the sample by moving a rotating rod or a plate which is submerged in the sample [101]. From having co-concentric between the fixed container and the rotating part, a corresponding resistance to the deformation is measured and interpreted as rheological properties as known as material functions [227].

In principle, a basic assumption of mechanical rheometer is that sample is homogenous [2], [228]. Indeed, blood is genuinely regarded as a two-phase liquid in which cells are diluted in plasma [73], [218]. Therefore, the cells migration around boundaries, which lead to non-homogeneous distribution, must be taken in consideration. In addition, blood cells sedimentation is directly influence to heterogeneity of the blood sample. Although individual RBC sedimentation rate is relatively slow at 0.13 μm/min [229], aggregation of RBCs sharply accelerates sedimentation rate [230], [231]. As a consequence, cells are relatively highly concentrated at the bottom of the sample container. Following this, the rheometer reads lower viscosity than the actual value if the torque is sensed by the upper rotating element [221]. Altogether, homogeneity of the blood must be ensured prior the measurement which would increases complexity in experiment to achieve reliable result.

Apart from cells migration, blood surface that is exposed to air creates thin film layers [221], [232]. These protein layers cause the nonuniformity of the blood sample. This protein layers pay a considerably contribution and cause artefacts to the rheological responses. As a result, this would lead to misinterpretation of the obtained responses. To tackle this problem, a guard ring [2], [206] or a small amount of surfactant [202], [233] are essential additions to prevent thin film occurrence at the interfaces. Thus, complexity of such configurations requires a skilled technician in order to achieve accurate and reliable result.

A. Length scale and volume of SAOS

A large amount of fluid sample (> 1 mL) is required to evaluate viscoelastic responses. Thus, the rheometer provides an average measurement of the bulk responses and do not allow for local measurement [234]. To enable the rheometer to measure a small volume, the concentric surfaces must be aligned perfectly which is difficult to achieve [235]. This is a main drawback of this system because biological sample is not easy to obtain or synthesize a large quantity. Furthermore, the length scale of mechanical rheometer is large compared to the largest scale of RBCs (micrometer) [236]. That is, the precision of moving a rotating part is in the order of millimeters [236]. As a result, large length scale of measurement can be obtained by the rheometer [225], [234], [236]. This question arises when validating microscale measurement (microrheology) with macroscale measurement (mechanical rheometer).

B. Safety issues of SAOS

In a measurement, a sample is filled in the sample container, and the rotating element is submerged in the sample to expose a sinusoidal shear. As a result, both of container and rotating element surfaces are directly contact with the sample. Cleaning procedure must be applied throughout these surfaces to ensure that the sample is not cross-contaminated particularly biological fluids in disease settings [237].

6.3.2. Capillary-based viscometer

Capillary-based viscometers are frequently used to measure viscosity of the blood [2]. This approach relies upon a pressure difference between the capillary tube ends to initiate fluid flow. This pressure drop is related to viscosity of the fluid by the Hagen-Poiseuille law [238]. However, this approach cannot evaluates viscoelastic moduli.

A. 3D-printed capillary circuit

A low-cost hand-powered operation device was developed for measurements of haemorheological properties [239]. This device relies on a parallel capillary network which allows a comparison of reference and sample fluid with naked-eye readout. The device operated by pulling and pushing the plunger of a syringe, then, a vacuum and a pressure were generated to both of the reference and blood capillaries. Then, the plunger was depressed to release the pressure until the fluids reach a low level. Following this, volumetric flow rates Q of both capillaries were determined from the pressure drops of reference and blood according to Hagen-Poiseuille law [238]. However, shear rate $(\dot{\gamma})$ can be calculated via $\dot{\gamma} = 4Q/\pi r^3$, where r represents the capillary radius. To evaluate a reliable result, approximately 150 μL of blood volume was required to evaluate its steady-shear viscosity.

B. Microfluidic based viscometer

A microfluidic device was developed and demonstrated as a blood viscometer [240]. The device consisted of 10 sets of microchannel arrays with different width ranges from 25 to 100 μm. From having 10 sample sets, the device achieved 10 shear rates in single a measurement. Each array consisted of 100 identical microchannels which had 500 μm length in parallel with the flow. To perform viscosity estimation, the microfluidic was placed in the sample holder of microscope. Following this, a blood sample and a reference fluid were simultaneously fed in the inlet of the device via a syringe pump. Sample-filled microchannels in each array were counted by a camera of a microscope. Accordingly, hydraulic resistances with the reference were obtained, and these resistances were related to the viscosity of the blood sample upon shear rates as described in [240], [241].

The accuracy of blood viscosity estimation was verified by a rheometer and it showed a relative error of 5.3%. However, this approach has some drawbacks from having complicated design and fabrication. In addition, external devices such as a syringe pump and tubing is necessary for operating the device. Moreover, diameter selection of microfluidic device and tubing must be in consideration to avoid the Fåhræus–Lindqvist effect [242].

6.3.3. Electro-magnetic spinning method

A study explored rheological behaviour of a blood sample by using an electro-magnetic spinning method (EMS) [243]–[245]. This method relied upon rotational speeds from both of a pair of magnets and a 2 mm ball submerged in a sample fluid. In general, the EMS spined the permanent magnets via a controllable-speed motor. Whereas, the aluminium ball was indirectly rotated by a Lorentz force introduced by the spinning magnets. However, rotational speed of the ball required an image analysis system to obtain. Viscosity of the blood was calculated by difference of rotational speeds of these two spinning elements as presented in [245].

In EMS demonstration, viscosity of bovine blood [245] and human whole blood [244] were examined by the system. It was necessary to calibrate the measurement system with silicone oil prior to the experiments. This system required a minimum volume of 300 μL to fill in a test tube where a 2 mm ball was in. The rotational speed of the ball and the spinning magnets were measured to calculate the blood viscosity. In human whole blood experiment, measurement viscosities of 100 healthy individuals were performed. The study shows blood viscosity exhibited a stronger correlation with total count of RBCs and platelets. However, this system did not provide performance information with gold standard method.

6.3.4. Particle tracking micro-rheology

Particle tracking micro-rheology is a well-established approach for measuring material properties of complex fluids [23] and biological samples [246]. A study [201] demonstrated a potential application to measure viscosity of a human whole blood. Monodisperse tracer particles were employed to a blood with hematocrit of 44%. Following this, the sample was dispersed in a quartz cuvette. These particles (diameter of 2.8 μm) were tracked and recorded their motion using a high speed camera at 90 fps for 45 s. Then, the trajectories were converted to viscoelastic properties via the GSER [34]. The blood steady-shear viscosity was estimated by applied the Cox-Merz rule [247] to the obtained viscoelastic properties. Although the viscoelastic moduli were evaluated at 27°C, rescaling of the measurement to obtain the corresponding result at 37°C was done using temperature shift factor [248]. The main benefit to this approach that no external force was applied to the system. As a result, the whole system was easy to implement. However, probe selection was a vital. The probe must not interact with the sample (i.e. no aggregation with sample) [249], [250], easy to differentiate from the other elements in the blood (by size or fluorescent-labelled) [250], and uniform in size and shape [250]. Besides, computational time of particle tracking depended on complexity of algorithm which was a time consuming process in general. Thus, the high speed computation system was essential to monitor the location of the probe in time by this approach.

6.4. Developed and implemented approach

In our developed and implemented approach, a DDM based device was employed for evaluating steady-shear viscosity of human whole blood. A visible light, which shined through a sample in a typical DDM configuration, was mostly absorbed by the whole blood sample. As a result, the typical DDM was negligibly collected the light signal from the blood sample. As opposed to the typical DDM, a near infrared light

wavelength of 860 nm was used as a light source in our developed device. In comparison with the visible light, the infrared light absorbance by blood is remarkably lower, see Fig 6.3.

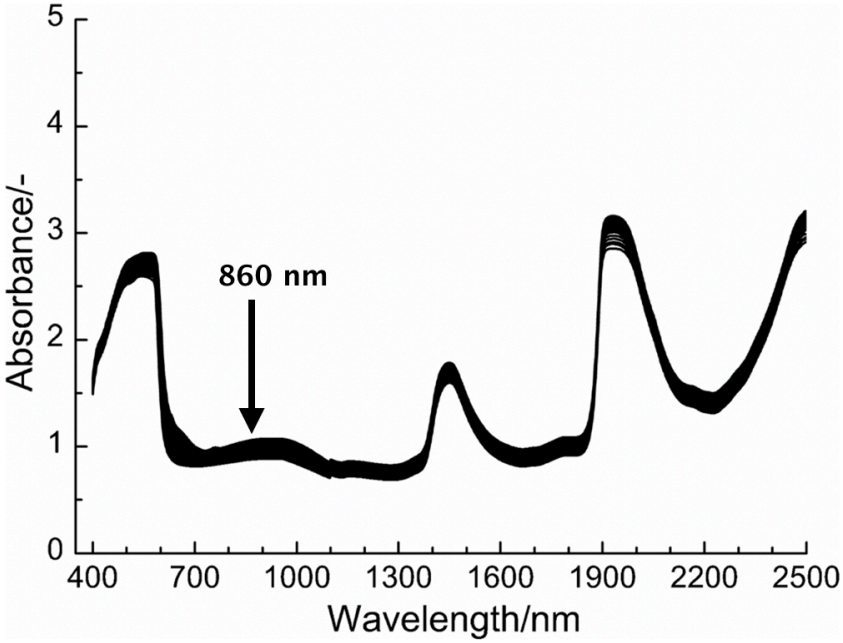

Figure 6.3. Wavelength absorbance of 450 human blood samples (Modified from the image in [251]).

In analogues, both of DDM and DLS have been employed for light scattering experiment [252]. Unlike DLS, DDM is an optical heterodyne detection which records interference pattern from both of transmitted light and weak scattered light of the sample by a detector [37]. As a consequence, the DDM is applicable for turbid media [37], [253] which may measures the whole blood sample.

To operate the device, the sample is inserted into an in-house microchamber made from double-sided tape as depicted in Figure 6.4. Next, a cover slip is put on top of the sample and using nail vanish to seal it. Following this, the microchamber is placed in the sample holder for data acquisition, see Figure 6.4.

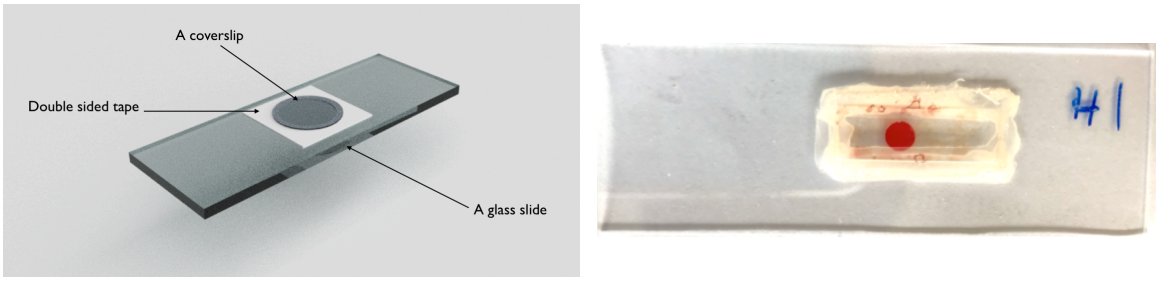

(a) (b)

Figure 6.4. An in-house microchamber. (a) a 3D model and (b) realisation with a blood sample.

This in-house microchamber is easy-to-reproduce and disposable for a rheological measurement. As a result, cleaning procedure is negligible because the sample is not directly in a contact with the device. In other techniques, a disinfection is usually essential to prevent cross-contamination after each measurement. In addition, this procedure ensures the surfaces which is in direct contact with sample were clean. Otherwise, remaining clots around surfaces and corner could influence mechanical responses and lead to misinterpretation of the obtained responses [205]. Thus, this procedure further increases complexity and time to operate the rheometer. Furthermore, unenclosed sample container of the rheometer allowed for direct contact between sample and air. As a result, mechanical responses obtained using the rheometer were interfered by film occurrence at blood-air interfaces [206]. Furthermore, at least 1 mL of sample volume is required to obtain reliable result using the rheometer. This bring challenge in measuring expensive and difficult to obtain or synthesis materials. Moreover, mechanical movement to rotate and sense the responses consumes much time to cover a wide range of frequencies. As a result, RBCs sedimentation affects the mechanical responses due to inhomogeneous of the blood sample particularly at low shear flow.

In our developed device, the sample was accommodated in an enclosed in-house microchamber, where the sample has no contact with air. Moreover, sample volume approximately 6.0 µL was needed for our developed device (i.e. a finger-prick drop).

Furthermore, only ten seconds of data acquisition covered the frequency response from 0.1 to 30.0 rad/s. Thus, sedimentation of the RBCs was negligibly influenced to the low-shear-rate responses obtained by our developed device.

Finally, our system provided a simple configuration, as there was no external equipment required i.e. bulky microscope, syringes, and syringe pump to operate. The rheological properties of the blood sample could be collected without having a reference fluid (contrast to capillary devices, where Fåhræus–Lindqvist effects were not relevant to our developed system because there was no tubing and pump in the configuration of our device).

6.4.1. Viscoelastic measurement

In viscoelastic measurement, the direct conversion is performed on acquired data for obtaining viscoelastic moduli (detailed in Chapter 2). For human whole saliva and blood plasma, polystyrene microparticles are employed as a tracer particle. In contrast to whole blood, the RBCs can be used as a tracer, and there is no requirement for additional tracer particles to evaluate viscoelastic moduli of the blood.

6.4.2. A note to Cox-Merz rule in blood measurement

In a majority of studies, human whole blood viscosity is usually performed in steady-shear experiment [202]–[204]. This lack of oscillatory shear investigation of the blood is a constrain of this study. However, a complex viscosity $\eta^*(\omega)$ obtained by the developed device can be converted to steady-shear viscosity $\eta(\dot{\gamma})$ using the Cox-Merz rule according to Chapter 2. In addition, a study found the conversion aimed at good approximation from the experiment using a SAOS rheometer [202]. From this reason, the Cox-Merx rule was applied to the complex viscosity obtained using the developed device to aim steady-shear viscosity for verification with previous studies.

6.4.3. Temperature variation influence on blood viscosity

The majority of blood rheological studies are conducted at the temperature approximately 37°C [202], as the rheological changes of blood happen at body temperature. However, rheological investigations at lower temperatures are also important in various medical procedures such as Raynaud's syndrome and cardio-pulmonary bypass surgery [204], [210].

In general, like other fluids, blood viscosity is considerably dependent upon the temperature. However, variation of measuring temperature of blood can be rescaled for $T \in [10,40]\,℃$ and $\dot{\gamma} \in [1,100]\,s^{-1}$ based on Arrhenius relationship [2], [210]:

$$\eta(\dot{\gamma}, T) = \eta(\dot{\gamma}, T_0) e^{-\frac{E_a}{R}\left(\frac{1}{T}-\frac{1}{T_0}\right)} \tag{6.1}$$

where R is the gas constant, T is the temperature, T_0 is the reference temperature, η is the blood viscosity, E_a is activation energy (cal/mol), and $\frac{E_a}{R}$ for blood is $2.01 \pm 0.03 \times 10^3$ °K.

6.5. Material and Method

6.5.1. Whole blood sample

In this work, whole blood samples were obtained from two sources. For healthy individuals, experiments were based on a commercially available source (Cambridge Biosciences Inc.). Blood samples were also taken from individuals as follow-up stroke patients from the Queen Elizabeth University hospital, Glasgow, United Kingdom.

A. Blood sample from a healthy individual

Human whole blood (Cambridge Biosciences) was taken from a single donor and had haematocrit of 36.2%. A volume of whole blood was dispersed in an in-house microchamber which is made from plastic double-sided tape as shown in Figure 6.4. Thickness of the chamber was 260 μm with a roughly 5 mm circular hole which accommodates approximately 6.0 μL of sample. After dispensed the sample, a coverslip is placed on top and sealed with nail polish to prevent sample evaporation. Finally, the chamber was placed on the sample holder of our device for a measurement.

B. Blood samples from stroke patients

The patient whole blood samples were freshly drawn and contained in EDTA anticoagulant. These blood samples were measured using their steady-shear viscosities on the date of arrival. Our developed device was used to examine the blood viscosities and verified with a reference stain-controlled rheometer (MCR302, Anton Paar GmbH) in the identical environment at 20°C. However, an additional temperature control for sample container was also provided in the rheometer. Therefore, the temperature of sample was more reliable in the rheometer than in our developed device. In a measurement, a blood sample was gently shaken and drawn off approximately 6.0 μL for our device. At least 800 μL of blood was used for the rheometer measurement.

6.5.2. Blood plasma

A whole blood in EDTA was centrifuged at 1.5 g for 5 mins to separate cells from the blood. The supernatant, or plasma, was removed and recentrifuged for purification. After that, a volume of 1.5 μm polystyrene microparticles was diluted 1000 times by

the purified blood plasma. Following this, a 6.0 μL of the diluted solution was filled in an in-house microchamber for viscoelastic measurement.

6.5.3. Human saliva

One of natural function of saliva is to lubricate and protection of oral surfaces [254], [255]. However, rheological characterisation of saliva is not easy to perform in clinical setting. This is because, the conventional rheometer is large sized and mostly experimental techniques developed for research purposes [256]. The aim of this study is to characterise rheological behaviour of human saliva using our portable device.

In sample preparation, a female saliva sample was obtained from a commercial available source (BioIVT). The donor was fasted for minimum of 4 hours, drug free, without smoking, and with no alcohol consumption before saliva collection. In sample preparation, the sample was centrifuged at 10,000 rpm for 15 minutes to remove particulates in the saliva. Then, the supernatant was drawn up and dispensed in an Eppendorf tube. Following this, 0.52 μm monodisperse probe particles were 100 fold diluted by the prepared saliva. Next, the sample with probe particles was filled in an in-house microchamber to acquire data for a viscosity measurement.

6.6. Experimental results

6.6.1. Whole blood

A human whole blood was collected in EDTA tube with 36.2% Hct and stored in a fridge at 4°C for a blood ageing study. The measurement was performed at the arrival date of the blood in a controlled room temperature at 20°C. For measuring viscoelastic behaviour, the tube was gently shaken to avoid cell lysis and maintain homogeneity of the blood sample. Following this, 6.0 μL of the blood was pipetted and dispensed

into an in-house microchamber which left in the room temperature. Then, a cover slip was placed on top and seal with nail polish around its edges to prevent sample evaporation.

In data acquisition, an image sequence of moving cells was recorded without using probe particles. Following this, differential dynamic analysis (see Chapter 2) was applied to the recorded data, and a mean square displacement of the cells was calculated. Then, viscoelastic moduli of the blood sample were calculated by performing the direct numerical conversion from the mean square displacement. The measurement was three-folded replicated to achieve mean and standard deviation of the moduli as shown in Figure 6.5.

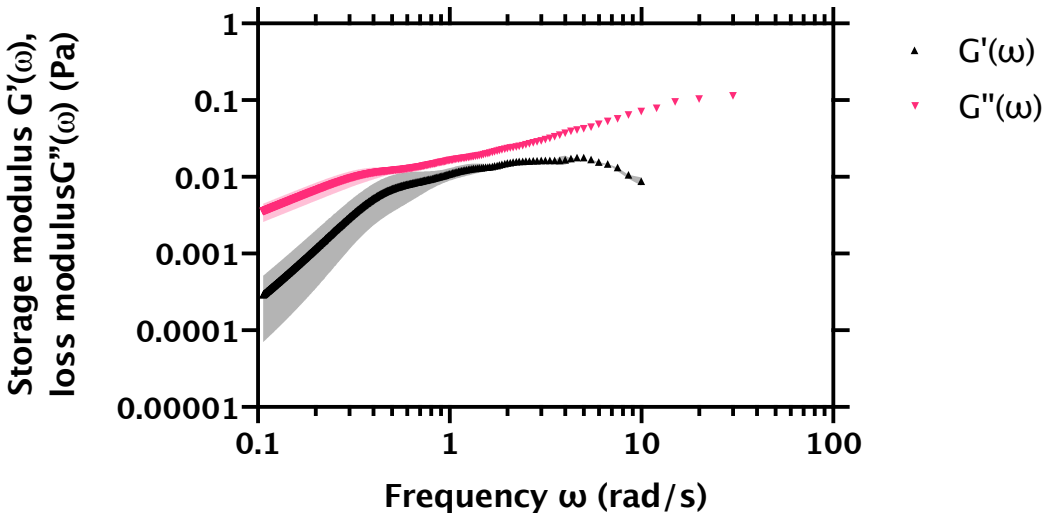

Figure 6.5. Viscoelasticity of human whole blood of 35.5% Hct in ETDA at 20°C. The measurement was done without sample dilution and probe particles employed. The acquisition time was 10 seconds which corresponds to frequency range from 0.1 to 30.0 rad/s. The mean storage and loss moduli were the black and pink triangles respectively. The black and pink colour bands were the error of storage and loss modulus from three-fold replication. It should be noted that log of negative value is undefined thus, it cannot be displayed in the plot.

Figure 6.5 shows that the viscoelastic moduli as a function of angular frequency of the human whole blood was revealed. For the analyzed frequency range, the loss moduli dominated the storage moduli. This dominant characteristic indicated the blood sample was more like liquid than solid along the testing angular frequencies of 0.1 to 30.0 rad/s. At angular frequency above 10.0 rad/s, the storage modulus was negative while the loss modulus continued to rise and saturated from the angular frequency above 20.0 rad/s.

In fact, viscosity of the blood is mainly determined by steady-shear experiments [73]. To compare with previous studies, the obtained viscoelastic moduli were converted to the corresponding steady-shear viscosity with the Cox-Merx rule applied. Accordingly, the estimated steady-shear of the blood sample is shown in Figure 6.6.

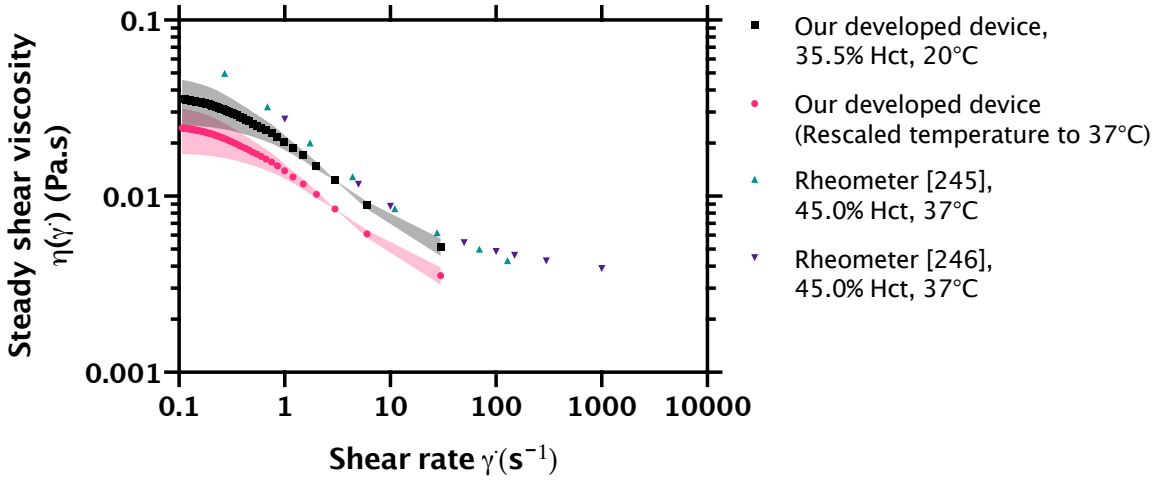

Figure 6.6. An apparent viscosity of a human whole blood in EDTA with 35.5% Hct measured at 20°C. The solid black rectangles represented the viscosity obtained from our developed device. The pink dots showed the rescaled temperature (from 20°C to 37°C) of the viscosity obtained from our developed device using Equation (6.1). The upward green triangles and purple rectangles illustrated the viscosity from reference studies [257] and [258] accordingly.

Figure 6.6 shows that the viscosity tended to remain steady at shear rate below 0.3 s^{-1} , and then it was considerably declined at shear rate from 1.0 s^{-1} to 30.0 s^{-1}. In comparison with those obtained by rheometers [257] and [258], the viscosities of both

devices were in the same characteristic. Nevertheless, our developed device reached its limit of measurement at shear rate 30.0 s^{-1} due to the maximum frame rate of the employed webcam. From three-folded replication of the measurement, the result viscosity at low shear rate aimed more deviation than high shear rate (Displayed by colour bands). As expected, this characteristic of the deviation was due to the use of the Cox-Merz rule according to a study [202].

A. Ageing of the blood

Several studies [239], [259]–[261] reported human whole blood viscosity is elevated during storage. The cause of the gradually increase is related to alteration of physiology and morphology of the red blood cells [261]. For example, shape of RBCs is progressively changed during storage. This behaviour related to the loss of their membrane in which they evolve from flexible biconcave shape to more rigid spheres [262]. Furthermore, enzymes released from broken down of stored WBCs damage RBCs surface as the RBCs become lysed [263]. From these natural processes, viscosity of the blood are remarkably influenced when the blood undergo storage as in literatures [239], [259]. However, these studies investigated blood viscosity at high shear rate [239] and short storage duration [259]. Thus, human whole blood up to 29 days of storage for both of high and low shear rates were measured using our developed device.

In the measurement, a whole blood sample of 36.2% Hct was obtained from a commercially available source with EDTA anticoagulant. The measurement was conducted at room temperature (20 °C). The sample was gently shaken before drawn up approximately of 1 mL, dispensed in a sterilised Eppendorf tube, and kept in a 4 °C fridge. For daily measurement, viscosity from measuring a 6.0 µL of blood volume was obtained by the developed device. To achieve a reliable result, this daily measurement was triplicated to obtain mean and standard deviation, see Figure 6.7.

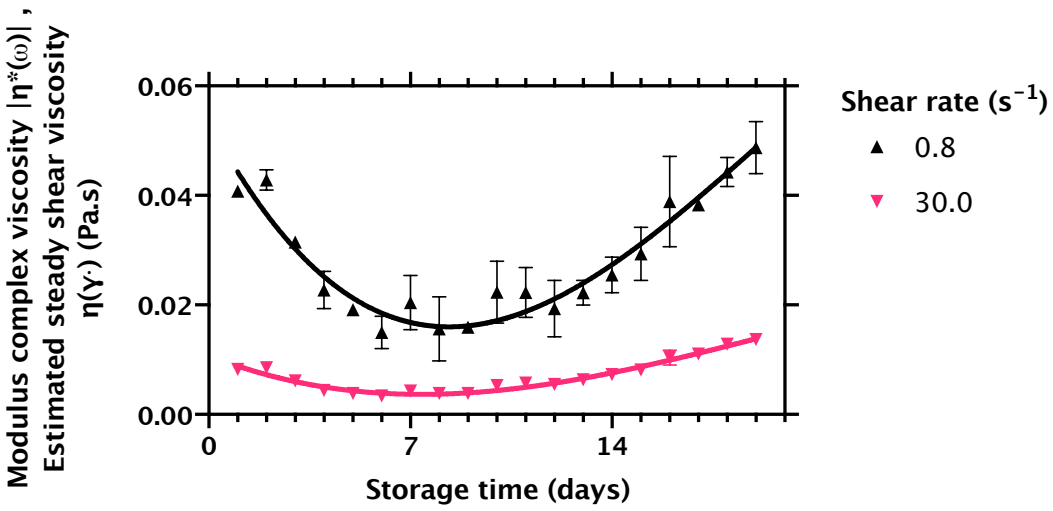

Figure 6.7. Viscosity of human whole blood of 36.2% Hct underwent storage measured using the developed device. Black triangles were the viscosity at shear rate = 0.8 s^{-1} whereas the pink downward triangles indicated the viscosity at shear rate = 30.0 s^{-1}. Black and pink curves indicated cubic fitting for the viscosity of shear rate 0.8 s^{-1} and 30.0 s^{-1}, respectively.

Figure 6.7 showed how the viscosity of 36.2% Hct human whole blood underwent storage. The shear-dependent viscosity at two shear rates were observed. To simplify, the viscosity investigation at shear rate of 0.8 s^{-1} and 30.0 s^{-1} were represented as the low and high shear rate. For the low shear rate, the viscosity was rapidly declined more than half on day 6. Afterwards, the viscosity was considerably risen and reached the maximum value on day 19. It is seen that the low shear viscosity was raised more than twice compared to viscosity at high shear rate. In analogous to the low shear rate, viscosity of high shear rate was in the same trend. However, the high shear viscosity was prone to achieve small variation. One assumption was the blood experienced external environment and forces while drawing blood out of the Eppendorf tube. As a result, degradation of the blood was occurred at faster rate. This further degraded the blood when it was drawn out from the single tube throughout the experiment. Therefore, investigation of blood viscosity during storage was repeated. Instead, blood sample was divided into five sterilised Eppendorf tubes to minimise such effect.

In the measurement, a new human whole blood of 35.5% Hct with EDTA anticoagulant was obtained for blood ageing investigation. The blood was pipetted and dispensed into five tubes which were labelled from 1 to 5 respectively. These tubes were kept in a fridge at 4°C and used by ascending order according to the label. In daily measurement, 6.0 μL of the blood was drawn up from the tube and dispensed in three in-house microchambers.

Average of the blood viscosity was evaluated as described in previous experiment, after which, the tube was kept in the fridge again for storage. On the next day, the measurement was repeated and then for seven day consecutively. Thereafter, it was discarded. This procedure was repeated for the remaining tubes to record alteration of blood viscosity for 30 days. From the experiment, the result viscosity as a function of storage time is depicted in Figure 6.8.

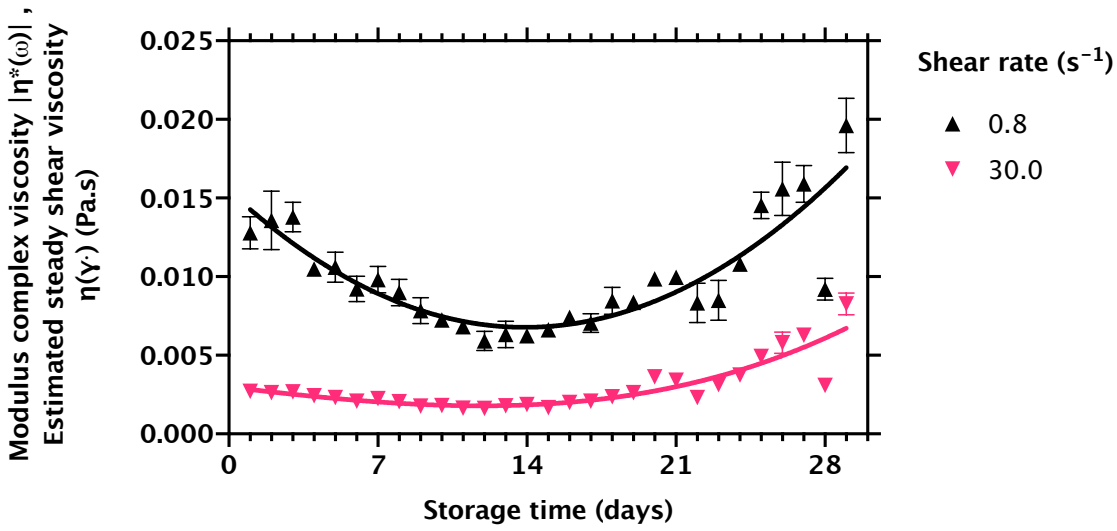

Figure 6.8. Viscosity of human whole blood of 35.5% Hct under storage measured using the developed device. Black triangles were the viscosity at shear rate of 0.8 s^{-1} whereas the pink downward triangles indicated the viscosity at shear rate = 30.0 s^{-1}. Black and pink curves indicated cubic fitting for the viscosity of shear rate 0.8 s^{-1} and 30.0 s^{-1}, respectively.

Results clearly show that viscosity of the blood altered during storage time, see Figure 6.8. At shear rate of 0.8 s^{-1}, the whole blood viscosity was rapidly reduced and reached the lowest point at approximately 7 mPa.s on 12 days of storage. Then, it was remarkably increased to almost 20 mPa.s on day 29. At shear rate of 30.0 s^{-1}, the blood viscosity was slightly decreased day by day. Afterwards, the viscosity was considerably increased for more than twice after two weeks of storage.

From Figure 6.1, it can be seen that alteration in morphology of the RBCs is also influenced the viscosity of the blood. At high shear rate, blood viscosity tended to rise when the RBCs lost their deformability. That was, viscosity of the blood was leveraged as RBCs become more rigid. In addition, the RBCs also lost their deformability compared to fresh RBCs during storage [264]. As expected, the high-shear viscosity was elevated particularly on day 29 as illustrated in Figure 6.8. In low shear viscosity, a study [265] found aggregability of RBCs was significantly decreased at the first week of storage. After which, the viscosity recovered for the following weeks. This characteristic was in analogous to the measurement results depicted in Fig 6.7 and 6.8. However, the declined of viscosity was approximately two weeks from the first date of measurement which could be from the subdividing blood procedure as mentioned earlier.

B. Performance evaluation of blood viscosity measurement

Validation of our developed device is necessary to ensure that the measurement result is comparable to a gold standard method, or a Rheometer (MCR 302, Anton Paar GmbH). In this step, steady-shear viscosities of unknown human blood donors were measured by both devices. In addition, the blood experiment of both devices were conducted simultaneously with the same sample, as the blood degraded by time, as described in previous Section.

In addition, temperature variation also influenced the blood viscosity. Both devices were in the identical environment where temperature was controlled at 20°C to minimise the temperature difference between the devices. However, the rheometer had more precisely temperature controlled since it had a dedicated system to control temperature of its sample container.

In the rheometer, a calibration procedure was necessary for maintaining accuracy of a measurement. This crucial procedure was done prior to the blood measurement which took approximately 1.30 hour. To evaluate viscosity response, ~0.8 mL of blood sample was put into a sample container of the rheometer. After the measurement was performed, the container was cleaned and disinfected in order to measure the next sample.

In contrast to rheometry, calibration process was unnecessary for our developed device. Only 6.0 μL of the blood was required to fill in an in-house microchamber for the measurement. A coverslip was placed on the sample and its edges were sealed using nail vanish to prevent sample evaporation. After that, the microchamber was placed on the sample holder of the device. In data acquisition, a sequence of images was recorded for 3 seconds which corresponded to shear rate of 0.3 s^{-1} to 30.0 s^{-1}.

The sequence was then analysed by DDA to evaluate a mean square displacement. Subsequently, numerical conversion of the mean square displacement was performed to obtain viscoelastic properties of the blood sample. Then, complex viscosity of the blood sample was converted to steady-shear viscosity using the Cox-Merz rule. Subsequently, the microchamber was removed from the device. Then, the microchamber was put in a sterile solution and discarded properly in a sharp bin. At this point, the measurement was continued without interruption by cleaning the device.

Unscreened human whole blood samples, which were collected from fourteen donors, were used in this experiment. These blood samples were provided by the Queen Elizabeth University Hospital, Glasgow, UK. In rheometry, viscosities of these samples were monitored at shear rate between 10.0 s^{-1} to 1,000.0 s^{-1}. The reason for that was there were quite lower determinants at high shear rate as illustrated in Figure 6.2. In addition, the measuring viscosity spectrum of the device was more reliable for viscosity below 5 mPa.s with absolute error approximately of 7% (see, Chapter 4).

However, the developed device could observed at maximum shear rate of 30.0 s^{-1}. This was limited by frame rate of the employed webcam. As a result, the cross over regime of shear rate was in comparison by both devices. For validation, the measured viscosity by our developed device was analysed through a regression analysis with those measured using the rheometer. This statistical analysis indicated the strength of relationship between our device and the rheometer. In the analysis, the result obtained by both devices were plotted against each other. Then, a linear regression was introduced to the plot for aiming a coefficient of determination (R-Squared). The result coefficients of the crossover shear rates were evaluated and depicted in Figure 6.90.

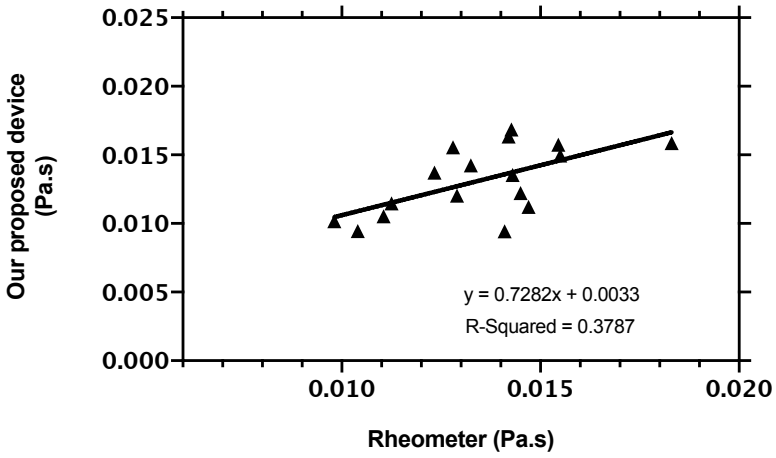

(a)

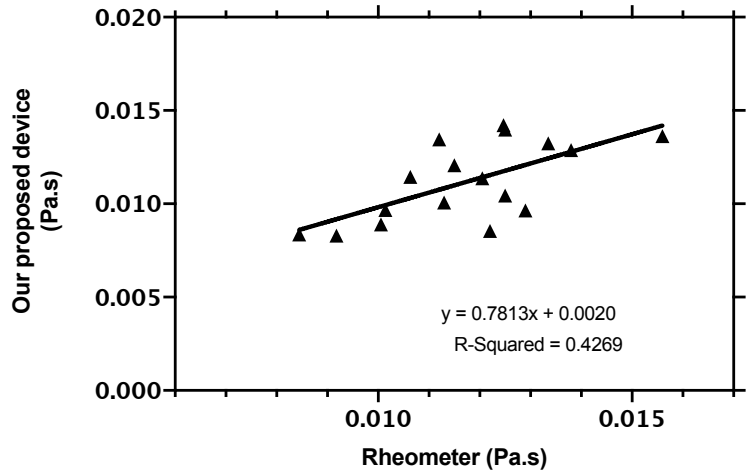

(b)

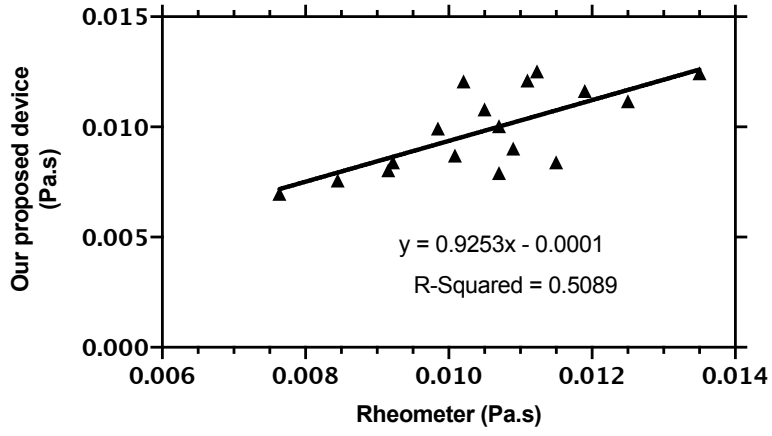

(c)

Figure 6.9. Regression plot of viscosities between the developed device and rheometer. The viscosities were obtained from measurement of fourteen blood samples at shear rate (a) 10.0 s^{-1}, (b) 15.8 s^{-1}, and (c) 25.1 s^{-1}.

The R-Squared is a statistical assessment indicates degree of relationship between x and y value [266]. When the R-Squared is 1, all of the variation in y value is accounted for by x value and none for 0. Figure 6.90 (a), the R-Squared revealed 37.76% of the variation of viscosities measured by the developed device was due to the variation of viscosities obtained from the rheometer. At this shear rate, the R-Squared showed the least among the crossover shear rates as illustration in Figure 6.90. Above all, all of statistical measures are listed in Table 6.1.

Table 6.1. Statistical measures of the correlation plots illustrated in Fig 6.90.

Shear rate	**Goodness of Fit**	
(s^{-1})	Regression model	R-Squared
10.0	$y = 0.7282x + 0.0033$	0.3787
15.8	$y = 0.7813x + 0.0020$	0.4269
25.1	$y = 0.9253x + 0.0001$	0.5089

All R-Squared listed in Table 6.1 indicated moderate relationship between developed device and rheometer. At shear rate of 25.1 s^{-1}, the R-Squared represented the highest value which is 0.5089. That is, 50.89% of variation of the viscosities measured by the developed device was accounted for by the measurement of the rheometer. Nevertheless, increasing of the sample size could achieve more reliable result.

C. Stroke

Stroke is a serious life-threatening neurological symptom which occurs when poor blood supply to part of the brain is obstructed [267]. Among stroke diseases, ischaemic stroke contributes 87% of admitted patients and it is a major case of stroke related to blood clot [268]. Elevation of fibrinogen levels, whole blood viscosity, and plasma

viscosity are major determinants related to various stroke events [269], [270]. High blood viscosity causes blood barely to flow and leads to a development of ischemic stroke.

In general, increasing of whole blood viscosity is mostly observed by a rheometer in the clinical study of stoke [269]–[272]. For instance, blood hyperviscosity of age-balanced 430 subjects were investigated by a rotational viscometer (Conteraves LS2) at 25°C [270]. These subjects were sub-divided into four groups which were 135 with acute stroke, 89 with ischaemic transient stroke, 115 recognised risk factors for stroke, and 91 healthy controls. According to the study, the viscosities of acute stroke, ischaemic stroke, and recognised risk factor for stroke were elevated compared to healthy subjects. In addition, the study reported plasma viscosities also increased in those subjects compared to healthy individuals. Besides, whole blood viscosity in stroke patient was also correlated to rigidity of RBCs. A study [273] showed the relationship of deformability of RBCs was remarkable decreased in stroke patient particularly in elderly. By indicating filterability of the whole blood, 53 patients and 23 healthy control subjects. Whole blood was filtered through a 5-μm polycarbonate filter, then, weight and assess filterability index according to the calculation in the study.

In this study, whole blood viscosities between healthy individuals and stroke patients were examined by our developed device. Blood samples of thirteen follow-up stroke patients and four healthy donors were provided by the Queen Elizabeth University Hospital, Glasgow. The aim of this study was to investigate alteration of viscosities between these two groups. Form the measurement, the mean and standard deviation of viscosities between two study groups is listed in Table 6.2

Table 6.2. Statistical descriptor of viscosity in healthy subjects and stroke patients. The measurement is conducted at shear rate of 25.1 s^{-1} and 20°C room temperature.

Study group	**Mean±SD** **Whole blood viscosity (mPa.s)**	**Sample size**
Control group (Healthy subjects)	6.67±1.54	4
Stroke patients	9.90±1.87	13

Evaluating a difference between means of two populations was done by parametric t-test because the sample size was small [274]. However, this statistical interference required a Gaussian distribution examination of the population. To examine the distribution, the obtained viscosities of both study groups were performed normality testing by using Shapiro-Wilk [275]. The normality verification was done by a statistics software (Prism 8) which produced a Q-Q plot for normality illustration of the test data. In this experiment, the viscosities of both groups were analysed at shear rate of 25.1 s^{-1}. This was because, the maximum value of R-squared between our developed device and the rheometer was yielded at that shear rate. As a result, the Q-Q plot of stroke patients and healthy subjects is shown in Figure 6.10.

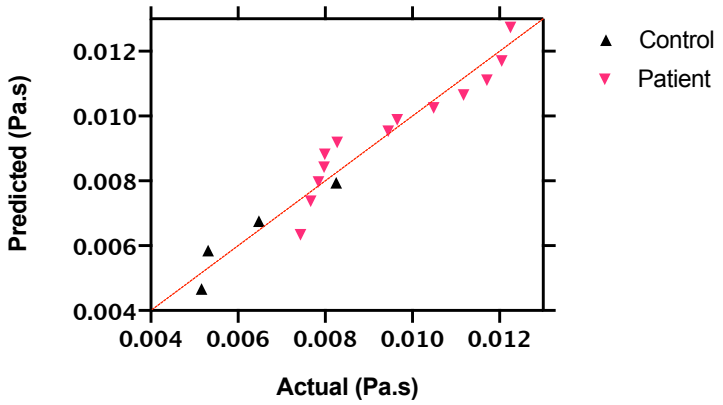

Figure 6.10. Q-Q plot of viscosities at 25.1 s^{-1} shear rate in healthy control and stroke patients populations. The pink upward triangles and black downward triangles represented the patients and healthy control. The red dashed line was responsible for the line slope of 1.

Figure 6.10 shows that both populations were passed the normality test with significantly level of 95%. This concluded that the data from both groups were in Gaussian distributions. For this reason, statistical interference analysis between both groups was performed using parametric t-test. Accordingly, the t-test result, which was obtained by using statistical analysis software (Prism 8), is listed in Table 6.3.

Table 6.3. t-test result between viscosities measured from healthy individual and stroke patients. The t-test was obtained by using a commercial software (Prism 8).

P value	**0.0070**
Significantly different ($P < 0.05$)?	Yes
One- or two-tailed P value?	Two-tailed

Results show, Table 6.3, that there was a significant difference between viscosity of healthy individual and stroke patients with confidential level of 99%. This preliminary result was in agreement with prior studies as discussed above.

6.6.2. Blood plasma

In this section, blood plasma was extracted from centrifugation of whole blood samples at 1.5 g for 5 min. After the first blood centrifugation, the supernatant part was drawn out, then recentrifuged for purification. The supernatant part was pipetted and dispensed into a sterilised Eppendorf tube for storage. To evaluate viscoelastic moduli, polystyrene beads particles were employed to the pre-processed plasma as tracer particles. Then, the movement of these particles were recorded to obtain their mean square displacement using DDA analysis. After that, the direct conversion method

was applied to the mean square displacement to evaluate viscoelastic moduli of the plasma which was shown in Figure 6.1.

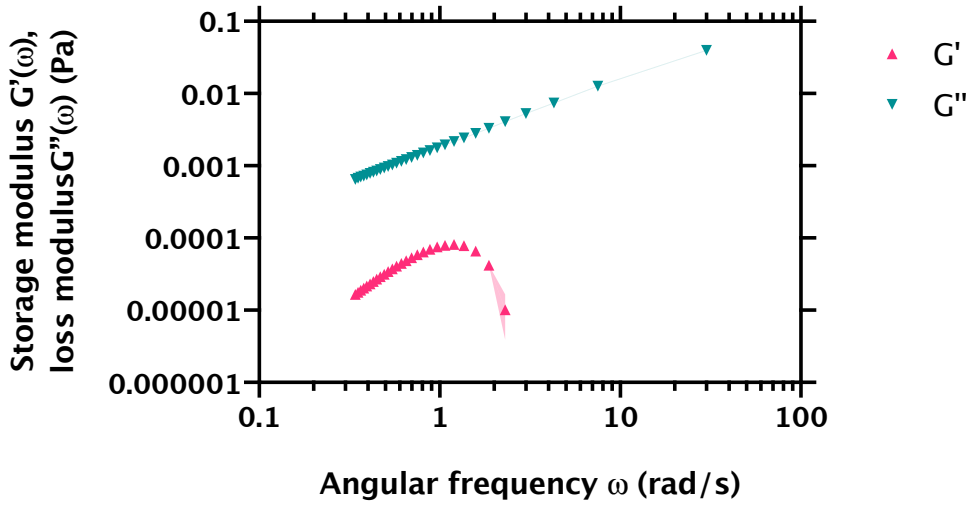

(a)

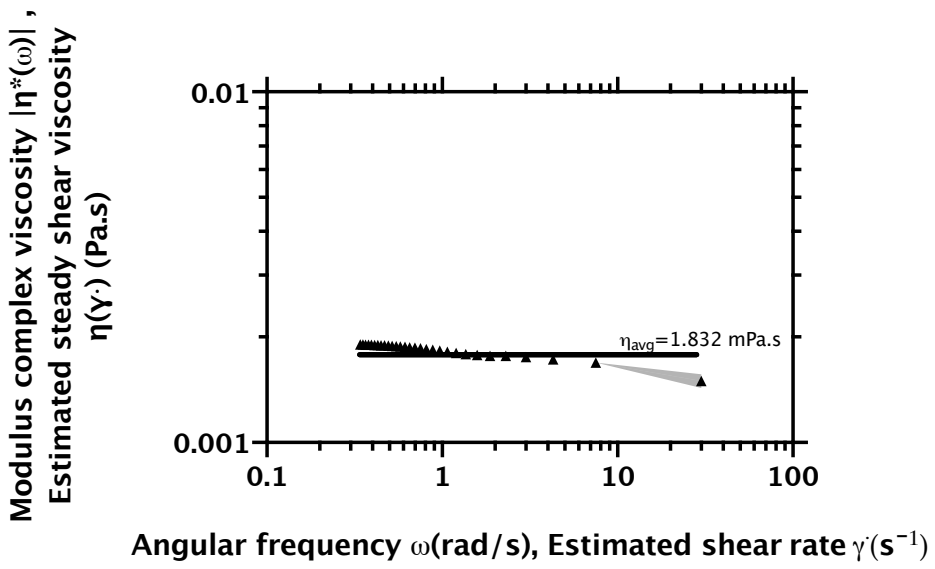

(b)

Figure 6.11. Rheological properties of human blood plasma from using 1.54 μm probe particles measured at $T = 20°C$. (a) A result viscoelasticity properties of human blood plasma. Green and pink triangles indicated the loss and storage moduli respectively. (b) the corresponding steady-shear viscosity (Cox-Merz rule) represented by the black triangles. The black line was the mean viscosity which was 1.83 mPa.s. The colour bands in (a) and (b) represented standard deviation from triplicated the measurements. It should be noted that standard deviation smaller than symbol size cannot be shown.

The result, Figure 6.11(a), viscoelastic properties exhibited both of viscous and elastic modulus. However, loss modulus was dramatically higher than storage modulus roughly 100 times higher. Apart from loss modulus, the result showed the elasticity term in the measurement at low frequency responses roughly from 0.3 to 1.1 rad/s. As a result, the corresponding steady-shear viscosity was slightly depended on shear rate as shown in Figure 6.11(b). In contrast to DI water, it exhibits only the loss modulus as illustrated in Figure 6.12.

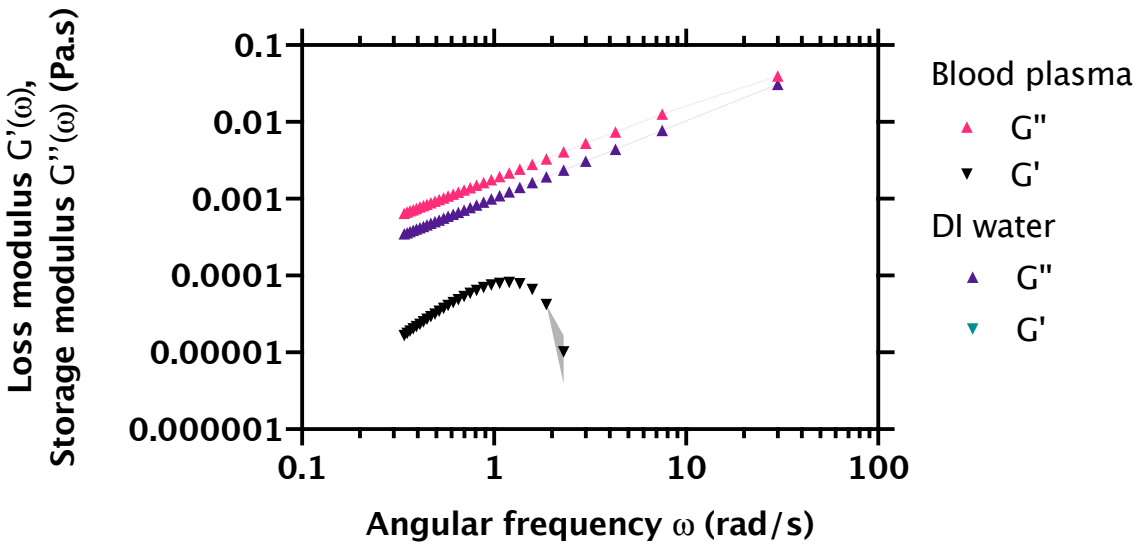

Figure 6.12. Triplication measurement of human blood plasma and DI water viscoelastic behaviours from using 1.54 μm probe particles at $T = 20°C$. Blue and violet dashed lines were responsible for loss and storage moduli of human blood plasma measurements respectively. A purple upward triangles indicated the loss modulus of the DI water. However the storage modulus cannot be displayed in the figure because they were all negatives as the DI is a Newtonian fluid. The colour bands represented the standard deviation of the measurements. It should be noted that standard deviation smaller than symbol size cannot be shown.

In general, blood plasma is considered as a Newtonian fluid. However, the obtained viscoelastic behaviour of the plasma revealed both of loss and storage moduli in this experiment. The existence of small storage modulus was an evidence that the plasma was a slightly non-Newtonian fluid which was reported in recent studies [211], [212].

In steady-shear viscosity, the result shown in Figure 6.11(b) was compared to a reference measurement of DI water as shown in Figure 6.12.

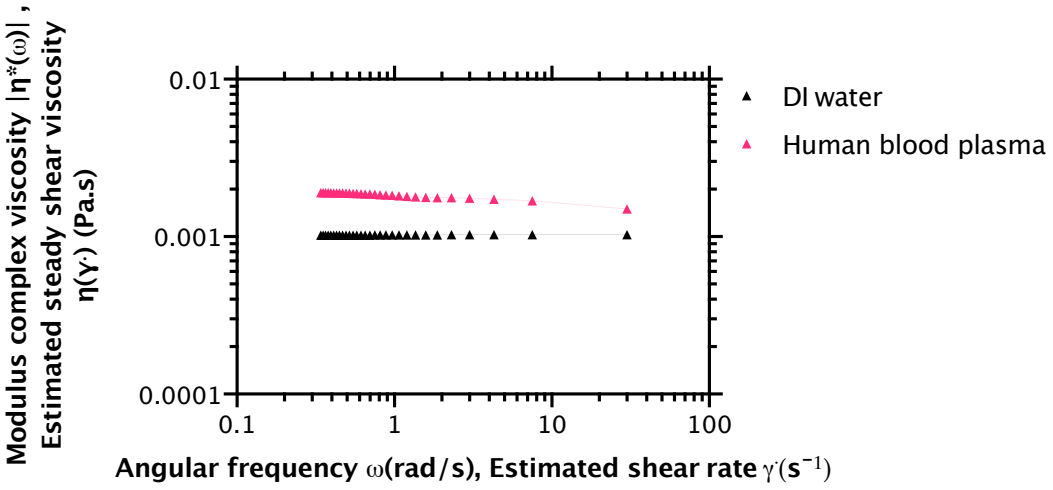

Figure 6.13. Shear viscosity of DI water and blood plasma using Cox-Merz rules. The pink upward triangles were the viscosity of the blood plasma whereas the black upward tringles indicated the average shear viscosity of DI water, and blood plasma at 20°C were 1.02 and 1.83 mPa.s respectively. The colour bands indicated the standard deviation from triplicate the measurements. It should be noted that standard deviation smaller than symbol size cannot be shown.

Figure 6.13 showed that the average viscosities of DI water and a blood plasma sample were 1.83 mPa.s and 1.02 mPa.s, respectively. In analogy to DI water, the viscosity of blood plasma was almost steady for the whole range of shear rate (0.2 s^{-1} to 30.0 s^{-1}). However, viscosity of blood plasma was decreased as an increment of shear rate from 0.2 s^{-1} to 1.0 s^{-1}. This was due to the existence of storage modulus (G') according to results shown in Fig 6.12. The experiment was repeated with the other human whole blood sample for verification, see Figure 6.14 for results.

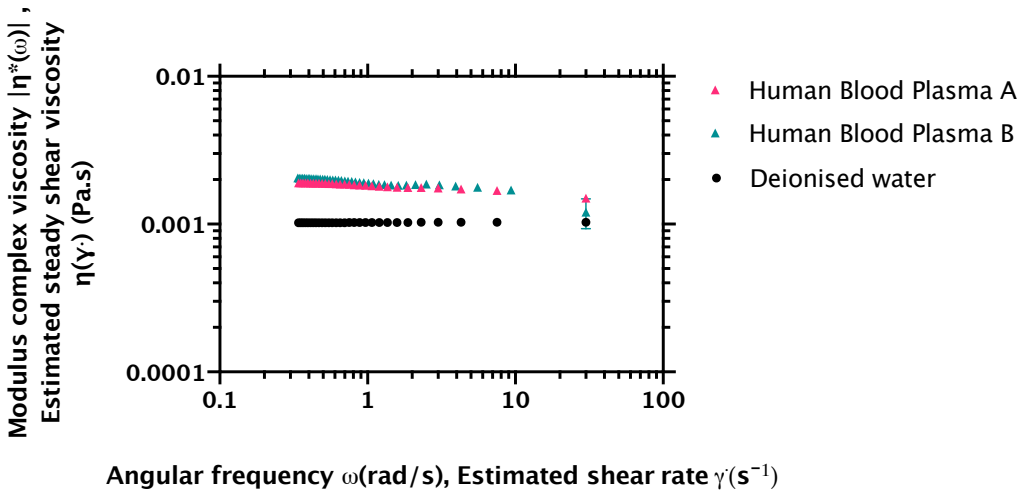

Figure 6.14. Steady-shear viscosities of two human blood plasma in comparison with steady-shear viscosity of deionised water. The plasma samples was obtained by centrifugation of two whole blood samples. human blood plasma represented by upward pink and green triangles for sample A (same as in Figure 6.13) and B respectively while the viscosity of water was represented by black dots.

6.6.3. Human whole saliva

This section presents a rheological study of human whole saliva using our developed device. In sample preparation, ~10 mL of saliva was obtained from a commercial available source (Bio IVT) which was collected from individual healthy donor. Because of the sample was opaque, the sample was centrifuged at 10,000 rpm for 15 min to settle particulates. Then, supernatant part was pipetted out and immediately dispensed into a sterilised Eppendorf tube for storage. Following this, a monodisperse polystyrene microparticles of 0.52 μm were employed in the tube as a tracer particles.

Finally, the tube was shaken by a vortex mixer to uniformly distribute the embedded microparticles prior to a measurement. To measure rheological moduli, an approximately of 6.0 μL human whole saliva was drawn up and dispensed into an in-house microchamber. Then, a coverslip was placed on top of sample. Next, edges of the coverslip were sealed to enclose and prevent the sample from evaporation. A video of image was collected by our developed device for 10 seconds. This corresponded to

measurements at shear rate from 0.1 s^{-1} to 30.0 s^{-1}. To minimise temperature fluctuation, this experiment was conducted in a controlled room temperature of 20°C. Subsequently, this recorded sequence was analysed using DDA analysis to retrieve mean square displacement of the tracer particles.

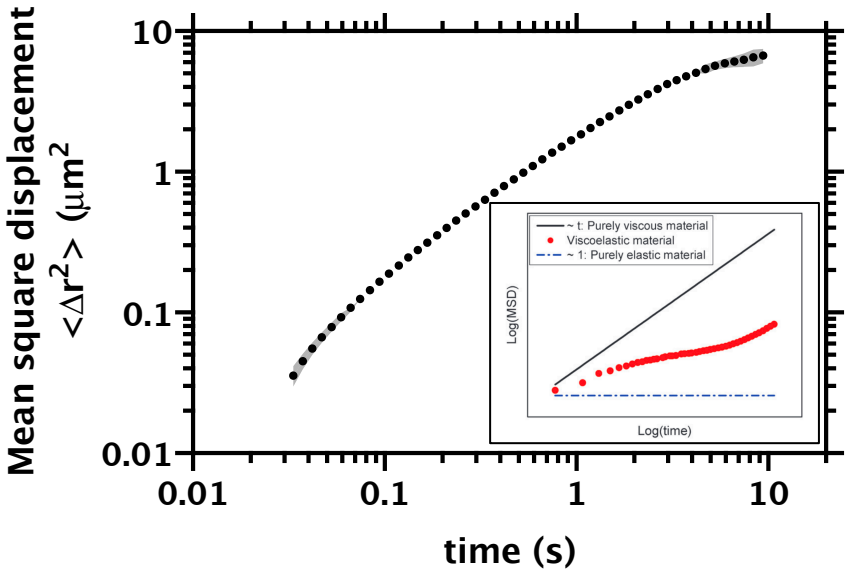

Figure 6.15. Log-log plot of retrieved mean square displacement as a function of time of embedded 0.52 μm Polystyrene microparticles in a human whole saliva sample. The black dots and the colour band represent mean of the mean square displacement and standard deviation of three-folded replication respectively. The inset (obtained from [276]) indicates mean square displacement behaviour as a function of time from three different materials - purely viscous (Newtonian fluid), purely elastic (solid materials), and viscoelastic material (non-Newtonian fluid).

Figure 6.2 shows that the measured mean square displacement grew non-linearly with time in the log-log plot. As a result, the observed saliva sample was considered as a non-Newtonian fluid from the experiment. For viscoelastic measurement, the direct conversion method (detailed in Chapter 2) was performed on the retrieved mean square displacement to evaluate viscoelastic moduli of the saliva. To achieve a reliable result, the above experiment was three-fold replicated. Accordingly, the mean and standard deviation of the moduli were obtained and are depicted in Figure 6.17.

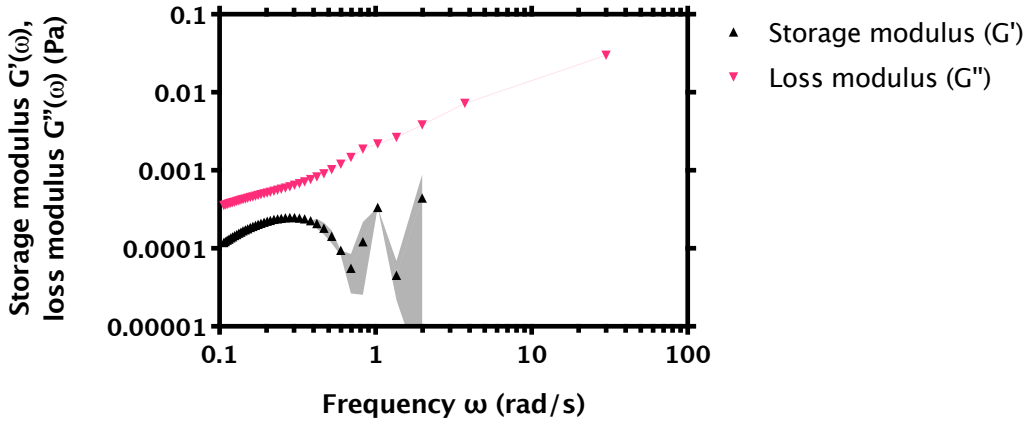

Figure 6.16. Viscoelastic moduli as a function of angular frequency omega of a human whole saliva sample. The measurement was conducted in a 20°C controlled room temperature by employing 0.52 μm polystyrene microparticles to probe the moduli. The black upward triangles showed the storage modulus while the pink downward triangles indicate the loss modulus of the saliva sample. Colour bands represent standard deviation from triplication of measurement.

From Figure 6.16, storage and loss moduli as a function of angular frequency of a human whole saliva were revealed by our developed device. Apparently, there was a constant grew of loss modulus from shear rate of 0.1 s^{-1} to 30.0 s^{-1}. By contrast, the storage modulus tended to rise along with shear rate from 0.1 s^{-1} to approximately 0.3 s^{-1}. After that, the modulus was fluctuated between shear rate of 0.3 s^{-1} to 30.0 s^{-1}. To obtain steady-shear viscosity, these moduli were converted to complex viscosity. Following this, the Cox-Merz rule was applied to the complex viscosity to evaluate corresponding steady-shear viscosity, see Figure 6.17.

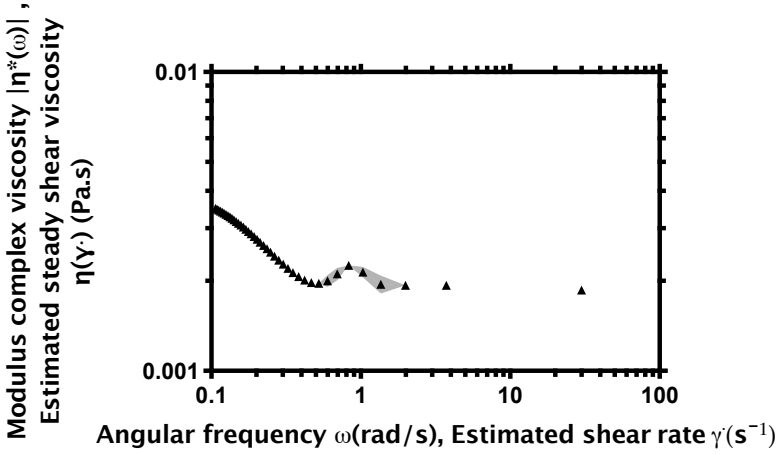

Figure 6.17. Steady-shear viscosity behaviours of human whole saliva obtained by our developed device at 20°C. The black upward triangles represented the mean viscosity. The colour band showed the standard deviation from three-fold replication of the measurement.

From Figure 6.17, the result steady-shear viscosity of the human whole saliva was shown a non-Newtonian fluid. As expected from literature [277]–[279], the viscosity exhibited shear-thinning behaviour since the viscosity decreased respect to an increment of shear-rate. However, the obtained viscosity showed a variation from shear rate of 0.4 s^{-1} to 2.0 s^{-1}. The result viscosity was also compared with deionised water, which represented a reference Newtonian fluid, see Figure 6.18.

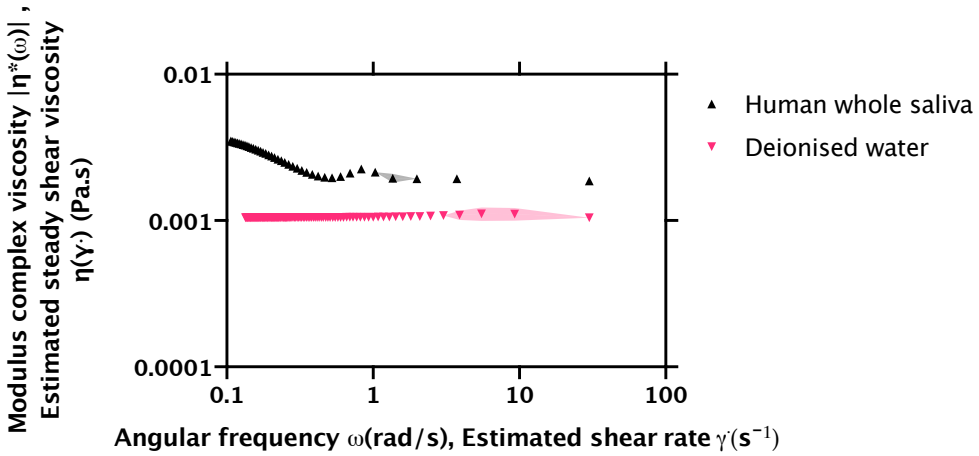

Figure 6.18. Comparison of the measured human whole saliva viscosity regarding to Figure 6.2 and deionised water probed using 0.52 μm polystyrene microparticles at 20 °C.

In fact, the saliva was composed of various components such as proteins and enzymes suspended in water. As a consequence, viscosity of saliva should be higher than viscosity of water.

From Figure 6.18, the measured saliva viscosity was greater than the deionised water for all measuring shear rate as expected. Nevertheless, there was a viscosity variation from shear rate of 0.4 s^{-1} which might relates to remaining small particulates in the collected supernatant of the saliva. Regarding to this, motion of such particulates also contributed to the measurement signal. However, these particulates could be removed by a filtration of the sample. To explain this, the particulates were filtered out using a membrane filter with 0.2 μm mesh size. This procedure ensured the particulates that larger than the resolution limit (0.35 μm/pixel) of our device were removed. Accordingly, only motion of the immersed tracer particles were recorded and processed.

In analogues to centrifuged saliva experiment, the 0.52 μm microparticles were employed in the filtered saliva as tracer particles. To visualize the result, the obtained steady-shear viscosity was plotted against the result shown in Figure 6.17 and depicted in Figure 6.19.

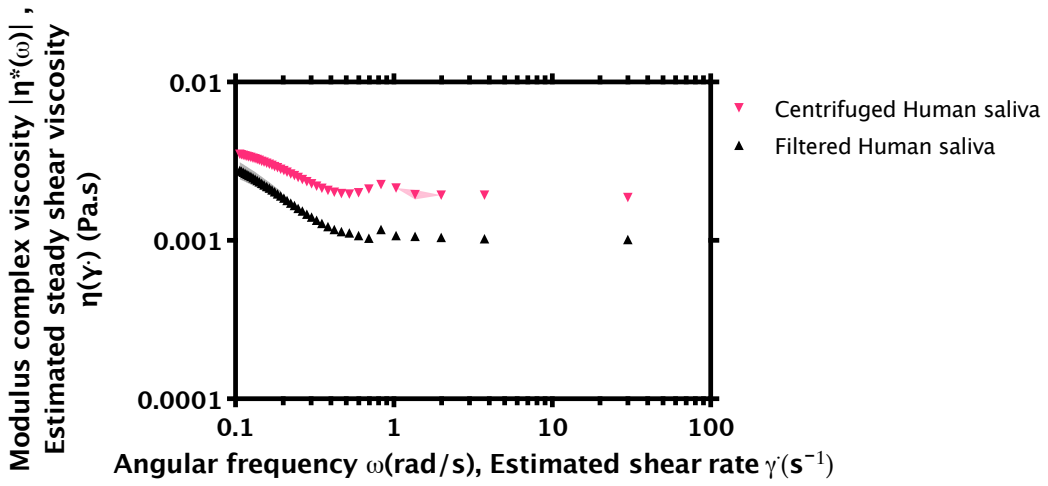

Figure 6.19. Viscosities as a function of shear rate of filtered and centrifuged human whole saliva. The measurement was done in a 20°C room temperature The black upward triangles indicated mean viscosity of a filtered saliva sample with mesh size of 0.2 μm. The pink downward triangles represented mean viscosity of a centrifuged saliva sample. Colour bands showed standard deviation of three-fold replication of the measurement.

Figure 6.19 depicts the measurement result of the steady-shear viscosities of a human saliva from two preparation methods which were centrifugation and membrane filtration. From the plot, the obtained viscosities of both saliva preparations were considerably declined from shear rate of 0.1 s^{-1} to 0.8 s^{-1}. However, the viscosity of filtered saliva was declined with a faster rate. Viscosities from both of saliva preparations fluctuated from shear rate from 0.8 s^{-1} to 1.0 s^{-1} and gradually dropped from shear rate of 1.0 s^{-1}. To summarise, filtration of saliva was negligibly influenced to the obtained viscosity variations, as seen in the plot. Instead, the viscosity was remarkably lowered compared to those prepared by centrifugation procedure. This rheological response might be caused by broken down of large proteins chains from using the filter [280], [281]. As a result, the tracer particles were “more free” to move, as seen from the results shown in Figure 6.20.

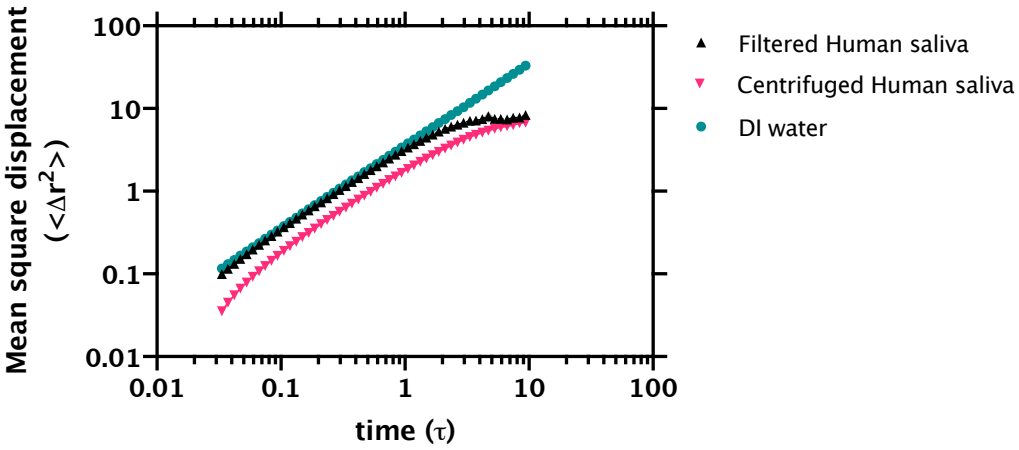

Figure 6.20. Mean square displacement of 0.52 μm tracer particles in a human whole saliva prepared using centrifugation at 10,000 rpm for 5 min and filtration by a membrane filter with mesh size of 0.20 μm. The black upward and pink downward triangles were average mean square displacement of the centrifuged and filtered saliva respectively. The green dots were average mean square displacement of 0.52 μm tracer particles in DI water. The error bars were standard deviation of three-folded replication of the measurement. The SD smaller than the symbol cannot be plotted by the software.

A. A model fitting for mean square displacement in saliva sample

In the direct conversion method, a mean square displacement of tracer particles was converted to viscoelastic moduli as mentioned in Chapter 2. Regarding to the reported works [70], [282], the direct conversion related to second-order differentiation of the mean square displacement :

$$G'(\omega) + iG''(\omega) = \frac{i\omega}{i\omega J_0 + \dot{J}(0) + \mathcal{F}[J_2(\omega)]} \tag{6.2}$$

where $J_2 = \ddot{J}(t)$ for $t > 0$, and is 0 for $t \leq 0$, $\ddot{J}(t)$ is second-order derivative of creep compliance $J(t)$, and $J(t) = \langle \Delta r^2(t) \rangle \cdot \frac{\pi a}{K_b T}$ [283], k_B is the Boltzmann's constant, T is the absolute temperature (K), a is the diameter of probe particles, J_0 represents the extrapolated creep compliance at $t = 0$, $\dot{J}(0)$ represents the gradient of creep

compliance at $t = 0$, $\mathcal{F}$ is the Fourier transform, i is the imaginary number, t indicates the measurement time, and ω is the angular frequency.

The second order derivative $\ddot{J}(t)$ is sensitive to noise [284]. Thus, fluctuation in viscoelastic moduli were unavoidably by using this approach. From the fact that steady-shear viscosity was estimated by performing the Cox-Merz rule on these moduli, this variation also exhibited in the obtained viscosity. A simple approach to this problem was to fit mean square displacement prior to the conversion. This procedure smoothened small deviation of mean square displacement. For saliva sample, a developed model fitting equation was introduced:

$$\langle \Delta r^2(t) \rangle = a(1 - e^{tb}) + c \tag{6.3}$$

where $\langle \Delta r^2(t) \rangle$ is the mean square displacement as a function of time t, whilst a, b, and c are the fitting parameters. The mean square displacement of the centrifuged saliva sample was fitted using Equation (6.3) and results are depicted in Figure 6.21.

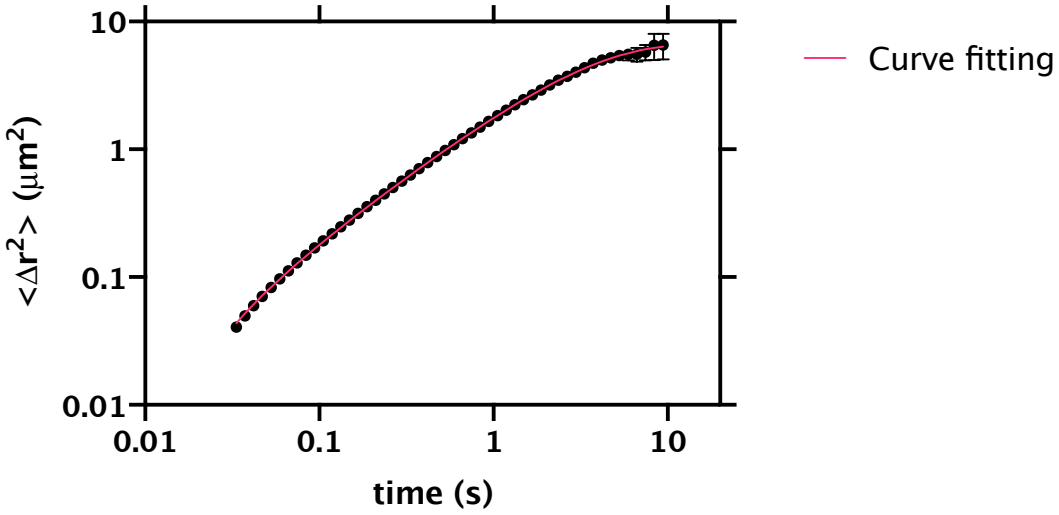

Figure 6.21. Mean square displacement of a centrifuged human saliva sample using probe particles of 0.52 μm. The original mean square displacement is indicated by black dots and fitted by the model Equation (6.3) and displayed by a red line.

From data depicted in Figure 6.21, a raw mean square displacement of 0.52 μm probes as a function of time was revealed. The model equation was fitted to the raw data with R-square of 1.00 and mean square error of 0.01. According to the plot, this fitted mean square displacement also smoothened the corresponding viscosity after the numerical conversion applied. The result conversion is shown in Figure 6.22.

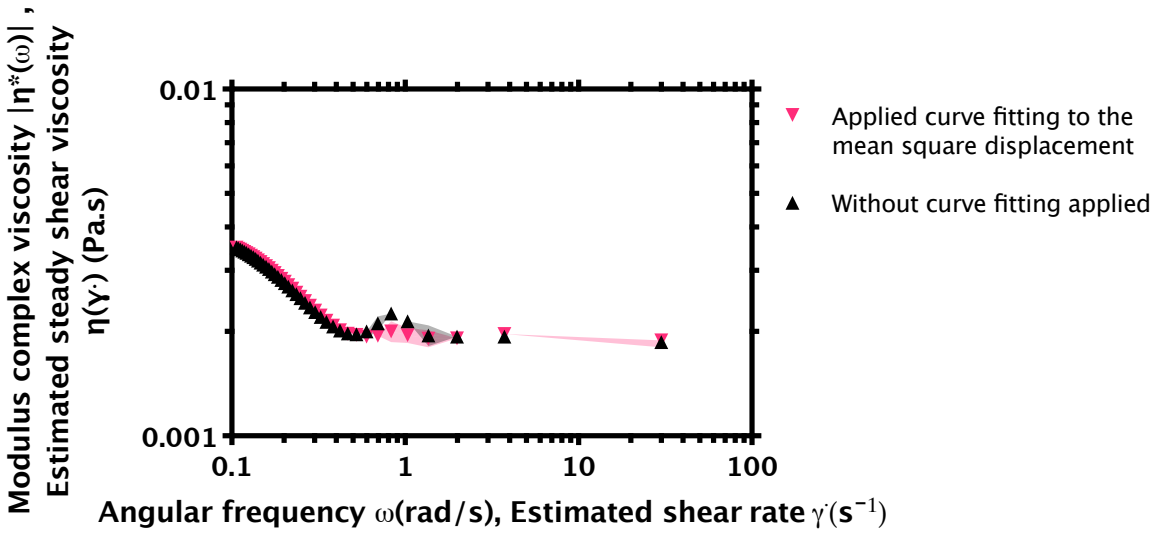

Figure 6.22. Viscosities of a centrifuged saliva sample obtained by conversions of a fitted mean square displacement using Equation (6.3) and raw mean square displacement. The black upward triangles are the viscosity obtained of raw mean square displacement. The pink downward triangles show the viscosity from fitted raw mean square displacement data. The colour bands indicate the error from triplicate the measurement.

The measured viscosities, Figure 6.22, showed shear thinning behaviours in both of raw and fitted mean square displacements. At low shear rate, the viscosities were rapidly declined to at around shear rate of 0.4 s^{-1}. Then, they reached a steady state from shear rate from 0.4 s^{-1}. Similarity, both of viscosity conversion from raw and fitted mean square displacement were in agreement from shear rates of 0.1 s^{-1} to 0.4 s^{-1}. Nevertheless, the viscosity of fitted mean square displacement showed a slight fluctuation from shear rates of 0.4 s^{-1} to 30.0 s^{-1}. The fitting function of mean square displacement produced less fluctuations of steady-shear viscosity after the conversion.

B. Experimental results with mean square displacement fitting

Achieving less noisy steady-shear viscosity could be performed by fitting mean square displacement as it was discussed in previous section. Thus, this section investigated steady-shear viscosity based on fitted mean square displacement of centrifuged and filtered saliva. To evaluate their viscosities, the mean square displacements from above Section were fitted to the fitting model using Equation (6.3). Then, their viscoelastic moduli were estimated by exploiting the direct conversion to the fitted mean square displacements. These viscoelastic moduli were converted to steady-shear viscosity via the Cox-Merz rule. For centrifuged saliva, the obtained viscoelastic moduli and the corresponding steady-shear viscosity is depicted in Figure 6.23.

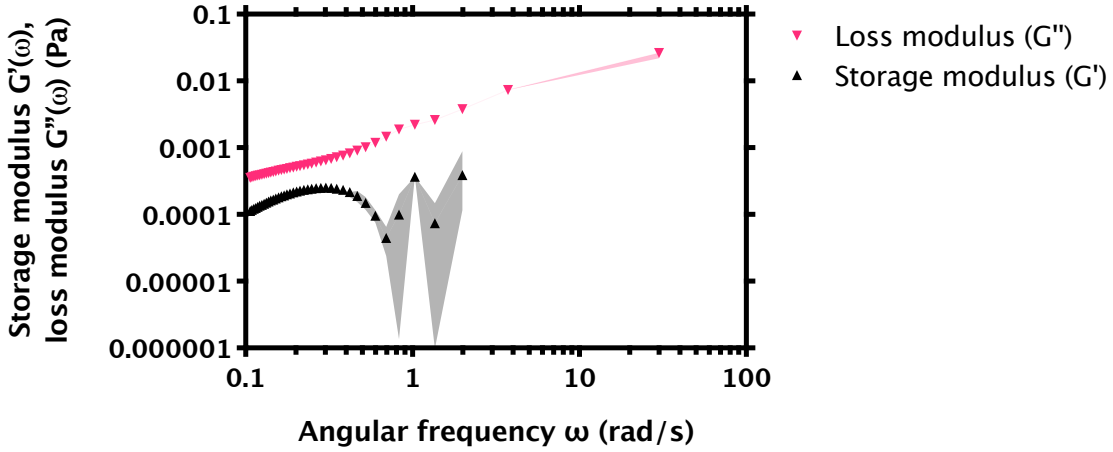

(a)

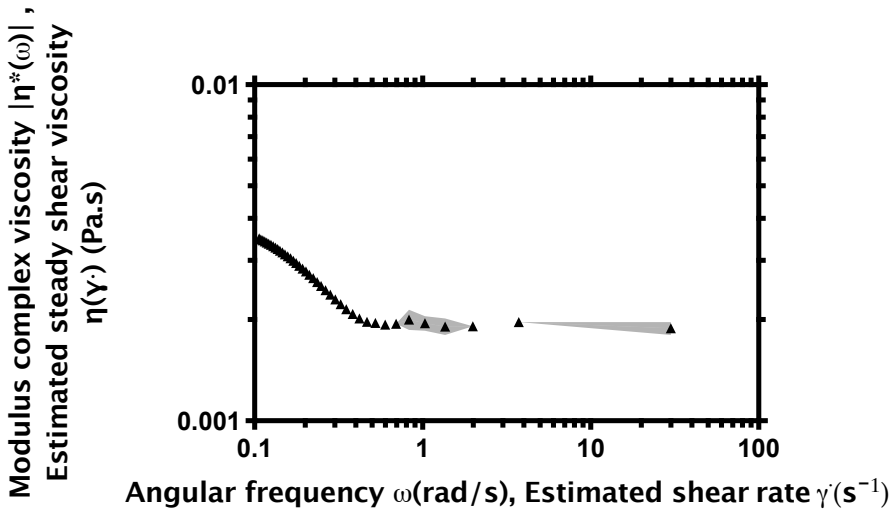

(b)

Figure 6.23. Measured rheological properties of centrifuged human saliva sample obtained by performing the direct conversion method to the fitted mean square displacement. (a) the measured viscoelastic behaviours are represented by storage (black upward triangles) and loss moduli (pink downward triangles); (b) the corresponding steady-shear viscosity by employing Cox-Merz rule to (a). Colours bands indicate the standard deviation from triplicate the measurement at 20 °C.

The above procedure was also performed with the centrifuged saliva. Then, both of steady-shear viscosities were calculated and depicted in Figure 6.24.

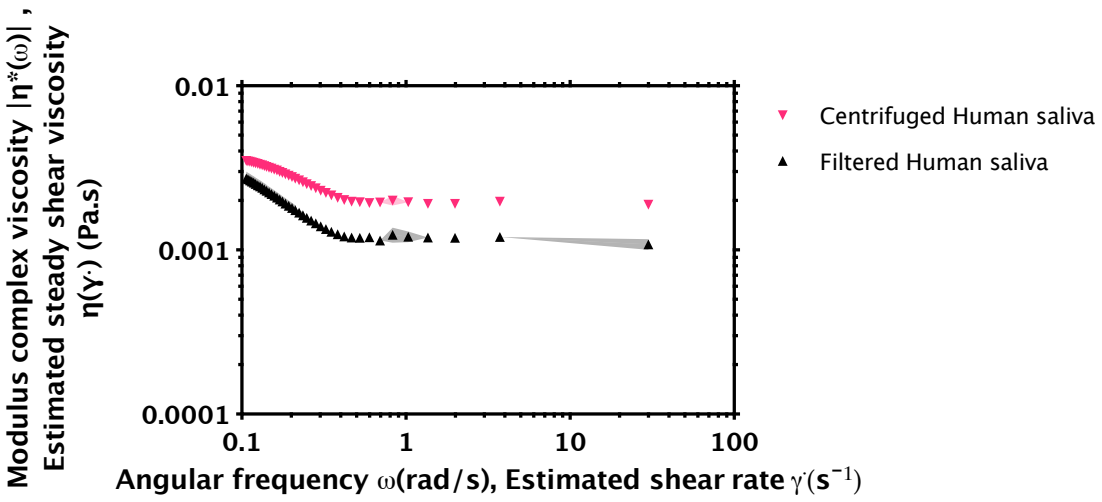

Figure 6.24. Viscosities of centrifuged saliva and filtered saliva after fitting their msd. The measurement is done by probing 0.52 μm polystyrene microparticles and at 20°C. Black upward triangles responsible for viscosity of centrifuged saliva. Pink downward triangles are the viscosity of filtered saliva. The colour bands show the standard deviation from triplicate the measurement.

From Figure 6.24, the obtained steady-shear viscosity of the centrifuged saliva was significantly levelled off from shear rate of 0.1 s^{-1} to 0.4 s^{-1}. The viscosity gradually declined from the shear rate of 0.2 s^{-1}. By analogy to the centrifuged saliva, the viscosity of the filtered saliva was in similar pattern. As opposed to the centrifuged saliva, the viscosity was remarkably lowered almost by between 2-3 fold.

6.7. Conclusions

This chapter demonstrated rheological characterisation of human biological fluids, which were blood plasma, whole blood and whole saliva, using the developed device. In blood plasma, which is typically regarded as a Newtonian fluid [211], [212], rheological investigation showed small elastic modulus at shear rates from 0.2 to 2.0 s^{-1}. This weak non-Newtonian characteristic was also recently found by recent studies [211], [212].

In human whole blood experiment, the developed device evaluated steady-shear viscosity of the blood in absence of probe particles and without blood dilution, as the RBCs were used as probe particles. In rheology measurement, the constitutive relation is derived for spherical particles. However, spheroid particle like RBCs can be estimated as a spherical particle for obtaining their MSD [285].

In fact, RBCs can aggregate together. As the RBCs aggregation proceeds, the average diffusion coefficient D decreases as the size of the aggregation increases by time. In addition, sedimentation of the aggregates becomes faster whereas the Brownian motion decreases [285]. As a result, these processes overestimate the viscosity measurement by the device particularly for long time measurement. To minimise these contributions, only 10.0 s of movement were analysed by the device.

The measured viscosity indicated a shear thinning behaviour in which the viscosity was remarkably decreased with increased of shear rate. This behaviour was in the same trend as the reference gold standard measurements although small sample volume of 6.0 μL was examined.

In performance evaluation, the developed device was compared to a rheometer (MCR302, Anton Paar GmbH) by measuring blood viscosity of 14 subjects. Measurements were performed with shear rates of 10.0 s^{-1}, 15.8 s^{-1}, and 25.1 s^{-1} in which they were the overlapped regime of both devices. Accordingly, correlation plots of viscosities at shear rate of 10.0 s^{-1}, 15.8 s^{-1}, and 25.1 s^{-1} evaluated R-Squared of 37.76%, 41.36% and 50.96% respectively. The limitation of this experiment was the developed device was relied on room temperature which was managed to 20°C. In addition, the maximum frame rate of camera (30 frame per second) was a restriction to access shear rate greater than 30.0 s^{-1}. To enable this, a high-speed camera was used for image acquisition in the device. In addition, further device modification is needed for enabling precisely temperature control of the sample to achieve more reliable result.

Furthermore, it should be noted that the length scale rheological characterisation of developed device lay on small length scales (micrometres) from passive microrheological measurement [225], [234], [236]. In contrast the reference rheometer has a length scale which is much larger (of the order of millimetres) [225], [234], [236], and as a result, this constrains validation with the different length scale systems.

Monitoring of blood viscosity undergoing storage was also analysed in this work. From the results, viscosity was seen to progressively increase at high shear rates. In contrast to low shear rate, viscosity rapidly declined in the first week and it then increased afterwards. As expected, this trend of viscosity was due to the loss of RBCs aggregability, followed by haemolysis as previously characterised [265].

The developed device was also demonstrated for investigating of whole blood viscosity in stroke patients and healthy individuals. Statistical analysis of interference between two groups were examined by t-test. At shear rate of 25.1 s^{-1}, the result indicated p-value of 0.0007 which infers the means between these two groups are different at confidential level of 99%. Thus, the device was able to differentiate two groups which could be used as a parameter for risk assessment of Stroke. However, a further study is necessary due to small sample sizes of both groups are examined in the test.

Despite whole blood and blood plasma viscosities, viscoelastic behaviours and viscosity of human saliva were also investigated by the developed device. A whole saliva sample revealed shear thinning behaviour according to the experiment. The finding was confirmed by several studies indicated the saliva exhibited lubrication function to oral surfaces [254], [255], [286], [287].

Chapter 7

Discussions, Conclusions, and Outlook

In this final chapter, the main findings of the experiments are described, summarised and discussed, together with the conclusions that can be drawn. In addition, suggestions over improvements and potential applications are gathered to expand and advance the approach for future work.

7.1. A portable DDM based device

In this thesis, a developed portable device was shown for quantitative measurements of rheological behaviour of biological fluids. This device was based on differential dynamic microscopy (DDM) which was able to perform light scattering experiments using image analysis. In general, the DDM is implemented using a standard light microscope with a white light illumination source. However, limitation of light source selection of the typical DDM brings difficulty to conduct experiments in some biological fluids. For example, visible light is mostly absorbed by human whole blood but near-infrared light. For this reason, an interchangeable fibre-coupled light source was employed for sample illumination of our developed device.

In comparison to mechanical rheometer, the developed device requires less than 10.0 μL of sample volume. In contrast to the developed device, the rheometer demands at least 1 mL of sample volume. In addition, the device is more sensitive to weak

responses due to microscale measurement by tracing movement of the embedded microparticles. Whereas, the mechanical rheometer provides average responses from millimetre length-scale measurement. However, measurement obtained using both approaches should follow similar trend.

In practice, the DDM acquires a sequence of images using a digital camera equipped with a standard light microscope. Then, image subtraction is applied to all the images in the sequence separated by a fixed lag time. This procedure has a notable benefit for eliminating a contribution of static signal in those images, i.e. container marks and dust particles. Following this, Fourier analysis is performed over the subtracted images to obtain a two-dimensional Fourier power spectrum. To simplify the analysis, the two-dimensional Fourier transform is reduced to one-dimension by radial averaging from its centre. This is due to the fact that the two-dimensional Fourier power spectrum is symmetrical. Indeed, this procedure achieves more reliable information from statistical averaging. However, the scattering around the centre may not yield a good statistic because of only fractional pixels are averaged. Finally, nonlinear fitting is applied to the power spectrum to obtain intermediate scattering function which is equivalent to the DLS experiment. By further processing, this function enables a key access to two complementary measurements which are those of particle sizing (Chapter 5) and rheological properties of a fluid (Chapter 6).

7.1.1. Time-stamp in image acquisition

As opposed to typical DDM, our developed device exploited a low-cost webcam (~£20) for data acquisition. Due to the webcam data transmission protocol, some images might be discarded during the data transmission because the images must be transferred in real-time. As a result, incorrect time information was recorded and leads to misinformation processed by typical DDM analysis (in Chapter 2). The reason for this was the typical DDM assumes a fixed lag-time (fixed frame rate) for all images

in the sequence. To tackle this problem, an image time-stamp procedure was implemented in this thesis to record actual time information of the acquired images. Accordingly, DDM precisely associates the actual time information into its calculation. Hence, this modification of DDM analysis tackled image discarding issue during the image transmission. As a result, the modification yields a more reliable result than the typical DDM procedure (section 3.3.1).

7.1.2. Evaluation of viscoelastic moduli

In rheological measurement, DDM has been demonstrated as a tool to characterise mechanical property of fluids by employing micro-size particles in a measuring fluid as tracer particles. These particles undergo Brownian motion due to random forces. Accordingly, DDM measures displacement of those particles to infer rheological properties based on passive rheology principle. A remarkable advantage of this principle is it does not require external force, therefore, this principle is simple to implement. As opposed to particle tracking microrheology, the displacement can be retrieved from intermediate scattering function without having a time-consuming and complicated tracking algorithm exploited. To obtain viscoelastic moduli, the displacement are usually converted using generalised Stokes-Einstein relation. However, this numerical conversion produces artefacts around high frequency (section 4.4.2). This is because, the generalised Stokes-Einstein relation has two-step numerical conversion. An alternative approach to tackle this issue is a direct conversion method. This approach directly converts mean square displacement to viscoelastic moduli. From this reason, the viscoelastic moduli are quantified using the direct conversion method throughout the study.

7.2. Particle size distribution

In this study, a numerical inversion method for obtaining particle size distribution was implemented for the developed DDM based device. By exploiting non-negative least square (NNLS), a particle size distribution of the suspension was measured (detailed in Chapter 2). In Chapter 5, demonstrations of the approach were carried out with various suspensions of colloidal particles. Apparently, the obtained particle size distribution was comparable to a standard dynamic light scattering (DLS) system. From the experiment, the obtained distribution shown a narrower distribution than that obtained from the DLS measurement. This was because, the developed device was able to collect scattered light from multiple angles from a single measurement. Whilst, the reference DLS could collect only a certain scattering angle. In addition, the obtained particle size distribution beyond the resolution limit of the device could be observed.

However, there was unexpected noise in the obtained distribution as the size of particles become smaller. The noise might be generated by electronic noise and heat of the camera. For mixtures of colloidal particles, larger particles were influenced more to the intensity in the distribution when particles populations were equalised (due to larger particles occupying more in pixel representations). Furthermore, the gap size between both populations was a major parameter that the developed device was able to differentiate. For single fold gap size, there was a crossover region between two population in the obtained particle size distribution. However, there was a negligible crossover region from more than twice gap size difference. The developed system distinguished two mixing populations with twice-size difference while the reference DLS system could not differentiate the populations.

7.3. Viscosity measurement of biological fluids

Majority rheological experiments of biological fluids are carried out particularly in steady-shear experiment. As opposed to steady-shear experiment, oscillatory-shear experiment can be observed by passive microrheology. As a result, complex viscosity can be obtained by the principle. However, the complex viscosity was converted to the corresponding steady-shear viscosity using an empirical relationship called Cox-Merz rule. Thus, steady-shear viscosity of sample fluids were obtained using the Cox-Merz relationship in this work.

Human saliva functioned as a protective material to oral surfaces. The primary rheology function of the saliva is lubrication and is reported as a shear thinning fluid. As expected, the obtained viscosity indicated a shear thinning behaviour.

However, viscosity measurement of the human whole saliva was not easy obtained, as the collected saliva was opaque by suspension of particulates. Accordingly, these particulates contributed significant influences to the signal measured by our developed device. Therefore, pre-processing of the saliva is necessary to eliminate such particulates. In this study, human whole saliva was pre-processed by two approaches which were centrifugation and filtration. In centrifugation, the saliva was centrifuged to settle the particulates and only the supernatant was reserved for the measurement. Moreover, the obtained supernatant was recentrifuged for purification.

In filtration, the saliva was pass through a membrane filter with mesh size of 0.2 μm. At this mesh size, particulates below the resolution limit of our developed system were removed. However, viscosity of the filtered saliva was lowered by the process, and the measured viscosity may not represent its actual value. This is because, the filter mesh

breaks apart protein chain structure of the saliva. Thus, particulates filtration of saliva should be avoided for rheological measurement.

In human blood plasma, the obtained result indicated steady-shear viscosity was dependent on applied shear rate. Precisely, it was slightly declined as an increasing of shear rate and behave like a shear thinning fluid. Similar to recent studies, plasma behaved as a viscoelastic material in extensional rheometry(studies also suggested that rotational rheometer cannot stretch the proteins in plasma effectively [288]).

For human whole blood experiments, near infrared light is employed for illumination due to the blood absorbs most of visible light. Only approximately 6.0 μL of sample volume was required to fill in an disposable in-house microchamber. This is much smaller compared to the sample volume required by a mechanical rheometer. Then, a coverslip was placed on top of the sample with nail polish to seal around the edge of the coverslip. This procedure prevented the sample being in contact with air and drying out.

In addition, the rheological measurement is not interfered by protein layers, as the blood has no direct contact with air. There are no tracer particles added since the RBCs are used as the tracer particles. The obtained steady-shear viscosity indicates the blood sample exhibits shear thinning behaviour which is consistent to the characteristic previously described [289], [290]. Furthermore, viscosity of blood storage was investigated for both of low and high shear rate. At low shear rate, viscosity of the blood rapidly declined and reached the lowest value after a week of storage. Subsequently, the viscosity considerably rose and reached the highest value on the last day of measurement, and observation that might be related to loss of aggregability of the RBCs during the first week of storage. For high shear rate, the viscosity was slightly declined for a week. Thereafter, it considerably increased, to reach the highest

value on the last day of measurement. As expected, this trend of viscosity was also found in the studies [291], [292].

The blood samples of 4 healthy individual and 13 strokes patients also investigated in this thesis. From determining viscosity of the whole blood samples, the developed device was also shown a moderate correlation when validated with a mechanical rheometer with R-squared of 50.89% at shear rate of 25.1 s^{-1}. This moderate correlation might be caused by the constraint of the measurement. First, the developed device cannot control the sample temperature. Second, the length scale of measurement were different in both devices which are micrometres in the developed device and millimetres in the mechanical rheometer. Third, the maximum viscosity that the developed device performed well roughly around 6.0 mPa.s (see Table 4.2). Nevertheless, the maximum viscosity was relatively low compared to the blood viscosity obtained by the rheometer in the experiment which was above 6.0 mPa.s. To overcome this problem, the blood could be either diluted by its plasma or measured at high shear rate. However, dilution of the blood sample nonlinearly decreases its viscosity. In addition, the diluted blood sample may lost the shear thinning characteristic and becomes a Newtonian fluid as in [293]. Thus, increasing of the frame rate of the camera used by the device to measure high shear rate measurement could be more practical approach to achieve more reliable result.

Statistical testing of the viscosity obtained by the developed device in healthy subjects and stroke patients were investigated. The result of a t-test shown that the viscosity of two group were different with p-value of 0.007, such that there was a significant difference between viscosity of healthy individual and stroke patients with confidential level of 99%. As expected, this preliminary result was in agreement with prior studies.

In conclusion, we shown that the developed DDM based device allowed for rheological studies of biological fluids particularly in Human body fluids. These fluids have not

yet studied using the DDM approach. In addition, the developed device uses an disposable microchamber that contains small sample volume of 6.0 μL, as might be required in point of care diagnostic settings. However, tracer particles that are moving proximity to surface of the microchamber slow down motion of the particles. This behaviour is due to hydrodynamic interaction from the presence of the surface causing Stokes drag force to increase. As a result, the viscosity measurement using the developed device could be overvalued. Nevertheless, the increase of Stokes drag force can be corrected by a factor given by Faxén correction [294] which is not implemented in this work.

7.4. Future work

Our developed device could be improved by using a temperature control unit for the fluid sample to ensure the fluid is equilibrated at the desired temperature. This would be of benefit for investigation of biological fluids at body temperature. In addition, the temperature control would minimise temperature influences by surrounding environment. However, the temperature control system must not consist of mechanical movement to avoid vibration to the whole device (image difference analysed by the DDA would produce unexpected movement signal caused by the movement). Employing a high frame rate camera to the developed device would also be a key improvement for investigating rheological responses at wider frequency range.

Another potential advancement of our device could be applicable for friction and lubrication study as known as tribology. By employing silica microspheres as tracer particles, these heavy particles would sediment on measuring surface and experience Brownian motion. As a result, mobility of the particles would be reflected by the roughness of the surface and hydrodynamic effect (see Appendix A).

Bibliography

[1] R. H. Ewoldt, M. T. Johnston, and L. M. Caretta, *Complex Fluids in Biological Systems*. Springer-Verlag New York, 2015. doi: 10.1007/978-1-4939-2065-5.

[2] L. Formaggia, A. Quarteroni, and A. Veneziani, *Cardiovascular Mathematics*, vol. 3, no. 1. Springer-Verlag Mailand, 2009. doi: 10.1007/978-88-470-1152-6.

[3] P. Connes, T. Alexy, J. Detterich, M. Romana, M.-D. Hardy-Dessources, and S. K. Ballas, 'The role of blood rheology in sickle cell disease', *YBLRE*, vol. 30, pp. 111–118, 2015, doi: 10.1016/j.blre.2015.08.005.

[4] D. A. Fedosov, W. Pan, B. Caswell, G. Gompper, and G. E. Karniadakis, 'Predicting human blood viscosity in silico'.

[5] P. F. Leblond, 'Hemorheology and blood diseases', in *Clinical Hemorheology: Applications in Cardiovascular and Hematological Disease, Diabetes, Surgery and Gynecology*, S. Chien, J. Dormandy, E. Ernst, and A. Matrai, Eds. Dordrecht: Springer Netherlands, 1987, pp. 227–254. doi: 10.1007/978-94-009-4285-1_8.

[6] W. H. Reinhart, 'Hemorheology: blood flow hematology', *Schweiz Med Wochenschr*, vol. 125, no. 9, pp. 387–395, Mar. 1995.

[7] P. Connes, T. Alexy, J. Detterich, M. Romana, M.-D. Hardy-Dessources, and S. K. Ballas, 'The role of blood rheology in sickle cell disease', 2015, doi: 10.1016/j.blre.2015.08.005.

[8] S. Chien, S. Usami, and J. F. Bertles, 'Abnormal rheology of oxygenated blood in sickle cell anemia.', *The Journal of clinical investigation*, vol. 49, no. 4, pp. 623–34, Apr. 1970, doi: 10.1172/JCI106273.

[9] Duncan W. Bruce Dermot O'Hare Richard I. Walton, *Multi Length-Scale Characterisation*. [Online]. Available: 10.1002/9781118683972

[10] G. A. M. Pop *et al.*, 'The clinical significance of whole blood viscosity in (cardio)vascular medicine.', *Netherlands heart journal : monthly journal of the Netherlands Society of Cardiology and the Netherlands Heart Foundation*, vol. 10, no. 12, pp. 512–516, Dec. 2002.

[11] E. Pretorius and D. B. Kell, 'Diagnostic morphology: biophysical indicators for iron-driven inflammatory diseases.', *Integr Biol (Camb)*, vol. 6, no. 5, pp. 486–510, May 2014, doi: 10.1039/c4ib00025k.

[12] K. S. Saladin, *Anatomy & Physiology: The Unity of Form and Function*. McGraw-Hill, 2010. [Online]. Available: https://books.google.co.th/books?id=BPVLAQAAIAAJ

[13] N. Beck, *Diagnostic Hematology*. Springer-Verlag London, 2009. doi: 10.1007/978-1-84800-295-1.

[14] R. Wang, L. Lei, S. Sridharan, Y. Wang, A. J. Levine, and G. Popescu, 'Dispersion relations of cytoskeleton dynamics', *Cell Health and Cytoskeleton*, vol. 8, pp. 1–7, 2016, doi: 10.2147/CHC.S62865.

[15] M. S. Amin *et al.*, 'Microrheology of red blood cell membranes using dynamic scattering microscopy', *Opt. Express*, vol. 15, no. 25, pp. 17001–17009, Dec. 2007, doi: 10.1364/OE.15.017001.

[16] P. Rodríguez-Sevilla, L. Labrador-Páez, and P. Haro-González, 'Upconverting materials for boosting the development of advanced optical microrheometric techniques', *Optical Materials*, vol. 84, pp. 514–523, 2018, doi: 10.1016/j.optmat.2018.07.058.

[17] V. Swaminathan, K. Mythreye, T. O'brien, A. Berchuck, G. C. Blobe, and R. Superfine, 'Mechanical stiffness grades metastatic potential in patient tumor cells and in cancer cell lines', doi: 10.1158/0008-5472.CAN-11-0247.

[18] J. Guck, R. Ananthakrishnan, H. Mahmood, T. J. Moon, C. C. Cunningham, and J. Käs, 'The Optical Stretcher: A Novel Laser Tool to Micromanipulate Cells', *Biophysical Journal*, vol. 81, no. 2, pp. 767–784, 2001, doi: https://doi.org/10.1016/S0006-3495(01)75740-2.

[19] P. Cicuta and A. M. Donald, 'Microrheology: a review of the method and applications', doi: 10.1039/b706004c.

[20] R. Kwok, 'Five hard truths for synthetic biology.', *Nature*, vol. 463, no. 7279, pp. 288–290, Jan. 2010, doi: 10.1038/463288a.

[21] D. Brutin and W. B. Zeid, 'Chapter 23 - Droplets of Biological Fluids', in *Droplet Wetting and Evaporation*, D. Brutin, Ed. Oxford: Academic Press, 2015, pp. 351–368. doi: 10.1016/B978-0-12-800722-8.00023-0.

[22] N. Wu and K. M. Schultz, 'Recent citations Microrheological characterization of covalent adaptable hydrogels for applications in oral delivery Accuracy improvement of centroid coordinates and particle identification in particle tracking technique Lester C. Geonzon and Shingo Matsukawa-On the Origin of Seemingly Non-Surface Active Particles Partitioning between Phase Separated Solutions of Incompatible Non-Adsorbing Polymers and', *Reports on Progress in Physics*, 2005, doi: 10.1088/0034-4885/68/3/R04.

[23] T. G. Mason, K. Ganesan, J. H. Van Zanten, D. Wirtz, and S. C. Kuo, *Particle Tracking Microrheology of Complex Fluids*, vol. 79, no. 17. American Physical Society, 1997, pp. 3282–3285. doi: 10.1103/PhysRevLett.79.3282.

[24] P. Edera, D. Bergamini, V. Trappe, F. Giavazzi, and R. Cerbino, 'Differential dynamic microscopy microrheology of soft materials: A tracking-free determination of the frequency-dependent loss and storage moduli', *Physical Review Materials*, vol. 1, no. 7, p. 073804, Dec. 2017, doi: 10.1103/PhysRevMaterials.1.073804.

[25] A. V Bayles, T. M. Squires, and M. E. Helgeson, 'Probe microrheology without particle tracking by differential dynamic microscopy', *Rheol Acta*, vol. 56, pp. 863–869, 2017, doi: 10.1007/s00397-017-1047-7.

[26] T. G. Mason' and D. A. Weitz', 'Optical Measurements of Frequency-Dependent Linear Viscoelastic Moduli of Complex Fluids', vol. 74, 1994.

[27] T. G. Mason, H. Gang, and D. A. Weitz, 'Rheology of complex fluids measured by dynamic light scattering', *Journal of Molecular Structure*, vol. 383, no. 1–3, pp. 81–90, 1996, doi: 10.1016/S0022-2860(96)09272-1.

[28] T. M. Squires and T. G. Mason, 'Fluid Mechanics of Microrheology', *Annu. Rev. Fluid Mech*, vol. 42, pp. 413–438, 2010, doi: 10.1146/annurev-fluid-121108-145608.

[29] J. Xu *et al.*, 'Compliance of actin filament networks measured by particle-tracking microrheology and diffusing wave spectroscopy', 1998.

[30] T. G. Mason, H. Gang, and D. A. Weitz, 'Diffusing-wave-spectroscopy measurements of viscoelasticity of complex fluids', 1997.

[31] T. G. Mason, A. Dhople, and D. Wirtz, 'Concentrated DNA rheology and microrheology', *Materials Research Society Symposium - Proceedings*, vol. 463, pp. 153–158, 1997, doi: 10.1557/proc-463-153.

[32] L. G. Rizzi and M. Tassieri, 'Microrheology of Biological Specimens', in *Encyclopedia of Analytical Chemistry*, Chichester, UK: John Wiley & Sons, Ltd, 2018, pp. 1–24. doi: 10.1002/9780470027318.a9419.

[33] M. Tassieri, *Microrheology with Optical Tweezers: Principles and Applications*. Jenny Stanford Publishing, 2016. [Online]. Available: https://books.google.co.th/books?id=TktnDwAAQBAJ

[34] T. G. Mason, 'Estimating the viscoelastic moduli of complex fluids using the generalized Stokes-Einstein equation', *Rheologica Acta*, vol. 39, no. 4, pp. 371–378, Aug. 2000, doi: 10.1007/s003970000094.

[35] R. Cerbino and V. Trappe, 'Differential Dynamic Microscopy: Probing Wave Vector Dependent Dynamics with a Microscope', doi: 10.1103/PhysRevLett.100.188102.

[36] F. Giavazzi, D. Brogioli, V. Trappe, T. Bellini, and R. Cerbino, 'Scattering information obtained by optical microscopy: Differential dynamic microscopy and beyond', *Phys. Rev. E*, vol. 80, no. 3, p. 31403, Sep. 2009, doi: 10.1103/PhysRevE.80.031403.

[37] M. S. Safari, M. A. Vorontsova, R. Poling-Skutvik, P. G. Vekilov, and J. C. Conrad, 'Differential dynamic microscopy of weakly scattering and polydisperse protein-rich clusters', *Phys. Rev. E*, vol. 92, no. 4, p. 42712, Oct. 2015, doi: 10.1103/PhysRevE.92.042712.

[38] D. Germain, M. Leocmach, and T. Gibaud, 'Differential dynamic microscopy to characterize Brownian motion and bacteria motility', *American Journal of Physics*, vol. 84, no. 3, pp. 202–210, 2016, doi: 10.1119/1.4939516.

[39] P. Edera, D. Bergamini, V. Trappe, F. Giavazzi, and R. Cerbino, 'Differential dynamic microscopy microrheology of soft materials: A tracking-free determination of the frequency-dependent loss and storage moduli', *PHYSICAL REVIEW MATERIALS*, vol. 1, p. 73804, 2017, doi: 10.1103/PhysRevMaterials.1.073804.

[40] A. V Bayles, · Todd, M. Squires, · Matthew, and E. Helgeson, 'Probe microrheology without particle tracking by differential dynamic microscopy', *Rheol Acta*, vol. 56, pp. 863–869, 2017, doi: 10.1007/s00397-017-1047-7.

[41] M. A. Escobedo-Sá *et al.*, 'Microliter viscometry using a bright-field microscope: g-DDM', *This journal is Cite this: Soft Matter*, vol. 14, p. 7016, 2018, doi: 10.1039/c8sm00784e.

[42] K. Breuer, Ed., *Microscale Diagnostic Techniques*, 1st ed. Springer-Verlag Berlin Heidelberg, 2005. doi: 10.1007/b137604.

[43] G. D. Jay, J. R. Torres, M. L. Warman, M. C. Laderer, and K. S. Breuer, 'The role of lubricin in the mechanical behavior of synovial fluid.', *Proc Natl Acad Sci U S A*, vol. 104, no. 15, pp. 6194–6199, Apr. 2007, doi: 10.1073/pnas.0608558104.

[44] E. Eiser, 'Dynamic Light Scattering', in *Multi Length-Scale Characterisation*, John Wiley & Sons, Ltd, 2014, pp. 233–282. doi: 10.1002/9781118683972.ch5.

[45] W. Liu, C. Wu, W. Liu, and C. Wu, 'Rheological Study of Soft Matters: A Review of Microrheology and Microrheometers', 2017, doi: 10.1002/macp.201700307.

[46] R. Pecora, B. J. Berne, *Dynamic Light Scattering: With Applications to Chemistry, Biology, and Physics*. Dover publication, 1976.

[47] R. Cerbino and P. Cicuta, *Perspective: Differential dynamic microscopy extracts multi-scale activity in complex fluids and biological systems*. American Institute of Physics Inc., 2017. [Online]. Available: https://doi.org/10.1063/1.5001027 http://aip.scitation.org/toc/jcp/147/11 https://aip.scitation.org/doi/am-pdf/10.1063/1.5001027?class=chorus+notVisible

[48] B. A. Krajina *et al.*, 'Dynamic Light Scattering Microrheology Reveals Multiscale Viscoelasticity of Polymer Gels and Precious Biological Materials', *ACS Cent. Sci.*, vol. 3, no. 12, pp. 1294–1303, Dec. 2017, doi: 10.1021/acscentsci.7b00449.

[49] E. Sarmiento-Gomez, D. Montalvan-Sorrosa, C. Garza, J. Mas-Oliva, and R. Castillo, 'Rheology and DWS microrheology of concentrated suspensions of the semiflexible filamentous fd virus', *The European Physical Journal E*, vol. 35, no. 5, p. 35, May 2012, doi: 10.1140/epje/i2012-12035-8.

[50] Z. Fahimi, F. J. Aangenendt, P. Voudouris, J. Mattsson, and H. M. Wyss, 'Diffusing-wave spectroscopy in a standard dynamic light scattering setup', doi: 10.1103/PhysRevE.96.062611.

[51] T. G. Mason ' and D. A. Weitz ', 'Optical Measurements of Frequency-Dependent Linear Viscoelastic Moduli of Complex Fluids', vol. 74, no. 7, 1995.

[52] D. A. Weitz, J. X. Zhu, D. J. Durian, and D. J. Pine, 'Principles and Applications of Diffusing-Wave Spectroscopy', in *Structure and Dynamics of Strongly Interacting Colloids and Supramolecular Aggregates in Solution*, S.-H. Chen, J. S. Huang, and P. Tartaglia, Eds. Dordrecht: Springer Netherlands, 1992, pp. 731–748. doi: 10.1007/978-94-011-2540-6_36.

[53] P. D. Kaplan, M. H. Kao, A. G. Yodh, and D. J. Pine, 'Geometric constraints for the design of diffusing-wave spectroscopy experiments.', *Appl Opt*, vol. 32, no. 21, pp. 3828–3836, Jul. 1993, doi: 10.1364/AO.32.003828.

[54] D. J. Pine, D. A. Weitz, J. X. Zhu, and E. Herbolzheimer, 'Diffusing-wave spectroscopy: dynamic light scattering in the multiple scattering limit', *J. Phys. France*, vol. 51, no. 18, pp. 2101–2127, 1990, doi: 10.1051/jphys:0199000510180210100.

[55] Y.-Q. Chen *et al.*, 'Microrheology of human synovial fluid of arthritis patients studied by diffusing wave spectroscopy.', *J Biophotonics*, vol. 5, no. 10, pp. 777–784, Oct. 2012, doi: 10.1002/jbio.201100128.

[56] J. W. Goodman, *Speckle Phenomena in Optics: Theory and Applications*. 2007.

[57] M. M. Tripathi, Z. Hajjarian, E. M. Van Cott, and S. K. Nadkarni, 'Assessing blood coagulation status with laser speckle rheology', *Biomedical Optics Express*, vol. 5, no. 3. pp. 817–831, Mar. 2014. doi: 10.1364/BOE.5.000817.

[58] M. M. Tripathi, Z. Hajjarian, E. M. Van Cott, and S. K. Nadkarni, *Assessing blood coagulation status with laser speckle rheology*, vol. 5. 2014. doi: 10.1364/BOE.5.000817.

[59] B. Fischer and V. Abetz, 'Determination of thermodynamic and structural quantities of polymers by scattering techniques', *Pure and Applied Chemistry*, vol. 90, no. 6, pp. 955–968, 2018, doi: 10.1515/pac-2017-1101.

[60] R. Dzakpasu and D. Axelrod, 'Dynamic Light Scattering Microscopy. A Novel Optical Technique to Image Submicroscopic Motions. II: Experimental Applications', *Biophysical Journal*, vol. 87, no. 2. pp. 1288–1297, Aug. 2004. doi: 10.1529/biophysj.104.041400.

[61] F. Giavazzi *et al.*, 'Viscoelasticity of nematic liquid crystals at a glance', *Soft Matter*, vol. 10, no. 22, pp. 3938–3949, 2014, doi: 10.1039/C4SM00145A.

[62] R. Cerbino and V. Trappe, 'Differential Dynamic Microscopy: Probing Wave Vector Dependent Dynamics with a Microscope', doi: 10.1103/PhysRevLett.100.188102.

[63] S. Amin, C. A. Rega, H. Jankevics, S. Amin, C. A. Rega, and · H Jankevics, 'Detection of viscoelasticity in aggregating dilute protein solutions through dynamic light scattering-based optical microrheology', *Rheol Acta*, vol. 51, pp. 329–342, 2012, doi: 10.1007/s00397-011-0606-6.

[64] E. M. Furst and T. M. Squires, *Microrheology*. OUP Oxford, 2017. [Online]. Available: https://books.google.co.th/books?id=R583DwAAQBAJ

[65] T. G. Mason, H. Gang, and D. A. Weitz, 'Rheology of complex fluids measured by dynamic light scattering', *Journal of Molecular Structure*, vol. 383, no. 1–3, pp. 81–90, 1996, doi: 10.1016/S0022-2860(96)09272-1.

[66] L. G. Wilson *et al.*, 'Differential Dynamic Microscopy of Bacterial Motility', *Phys. Rev. Lett.*, vol. 106, no. 1, p. 18101, Jan. 2011, doi: 10.1103/PhysRevLett.106.018101.

[67] A. V. Bayles *et al.*, 'Probe microrheology without particle tracking by differential dynamic microscopy', *Rheol Acta*, vol. 56, pp. 863–869, 2017, doi: 10.1007/s00397-017-1047-7.

[68] P. Edera, D. Bergamini, V. Trappe, F. Giavazzi, and R. Cerbino, 'Differential dynamic microscopy microrheology of soft materials: A tracking-free determination of the frequency-dependent loss and storage moduli', *PHYSICAL REVIEW MATERIALS*, vol. 1, no. 7, Dec. 2017, doi: 10.1103/PhysRevMaterials.1.073804.

[69] R. M. L. Evans, M. Tassieri, D. Auhl, and T. A. Waigh, 'Direct conversion of rheological compliance measurements into storage and loss moduli', doi: 10.1103/PhysRevE.80.012501.

[70] M. Tassieri, R. M. L. Evans, R. L. Warren, N. J. Bailey, and J. M. Cooper, 'Microrheology with optical tweezers: data analysis', *New J. Phys. New Journal of Physics New Journal of Physics*, vol. 14, no. 14, 2012.

[71] W. P. Cox and E. H. Merz, 'Correlation of dynamic and steady flow viscosities', *Journal of Polymer Science*, vol. 28, no. 118, pp. 619–622, 1958, doi: https://doi.org/10.1002/pol.1958.1202811812.

[72] M. A. Escobedo-Sá *et al.*, 'Microliter viscometry using a bright-field microscope: g-DDM', *This journal is Cite this: Soft Matter*, vol. 14, p. 7016, 2018, doi: 10.1039/c8sm00784e.

[73] G. Tomaiuolo, A. Carciati, S. Caserta, and S. Guido, 'Blood linear viscoelasticity by small amplitude oscillatory flow', *Rheologica Acta*, doi: 10.1007/s00397-015-0894-3.

[74] A. Fernandez-Nieves, A. M. Puertas, and N. Garti, *Fluids, Colloids and Soft Materials : An Introduction to Soft Matter Physics*. Hoboken, UNITED STATES: John Wiley & Sons, Incorporated, 2016. [Online]. Available: http://ebookcentral.proquest.com/lib/gla/detail.action?docID=4517563

[75] L. O. Figura and A. A. Teixeira, Eds., 'Rheological Properties', in *Food Physics: Physical Properties — Measurement and Applications*, Berlin, Heidelberg: Springer Berlin Heidelberg, 2007, pp. 117–206. doi: 10.1007/978-3-540-34194-9_4.

[76] H. A. Barnes, *A handbook of elementary rheology*. Aberystwyth: Univ. of Wales, Institute of Non-Newtonian Fluid Mechanics, 2000.

[77] K. S. Cho, *Viscoelasticity of Polymers*, vol. 241, no. Callen 1985. 2016. doi: 10.1007/978-94-017-7564-9.

[78] T. F. Tadros, *Rheology of Dispersions: Principles and Applications*. 2011. doi: 10.1002/9783527631568.

[79] T. G. Mezger, *The Rheology Handbook: For Users of Rotational and Oscillatory Rheometers*. Vincentz Network, 2006. [Online]. Available: https://books.google.co.th/books?id=N9Fdn0MEIDIC

[80] A. Ya. Malkin and A. I. Isayev, *Rheology : Concepts, Methods, and Applications*. Scarborough, UNITED STATES: ChemTec Publishing, 2017.

[Online]. Available:
http://ebookcentral.proquest.com/lib/gla/detail.action?docID=4787587

[81] D. Germain, M. Leocmach, and T. Gibaud, 'Differential dynamic microscopy to characterize Brownian motion and bacteria motility', *American Journal of Physics*, vol. 84, no. 3, pp. 202–210, 2016, doi: 10.1119/1.4939516.

[82] A. V Bayles, T. M. Squires, and M. E. Helgeson, 'Dark-field differential dynamic microscopy', *Soft Matter*, vol. 12, no. 8, pp. 2440–2452, 2016, doi: 10.1039/C5SM02576A.

[83] F. Croccolo, D. Brogioli, A. Vailati, M. Giglio, and D. S. Cannell, 'Use of dynamic schlieren interferometry to study fluctuations during free diffusion.', *Applied optics*, vol. 45, no. 10, pp. 2166–2173, Apr. 2006, doi: 10.1364/AO.45.002166.

[84] T. Butz, *Fourier Transformation for Pedestrians*. Springer Berlin Heidelberg, 2005. [Online]. Available: https://books.google.co.th/books?id=g1fDIvKq7S4C

[85] R. N. Zia, 'Active and Passive Microrheology: Theory and Simulation', vol. 50, no. 1, pp. 371–405, Jan. 2018.

[86] T. G. Mason, 'Estimating the viscoelastic moduli of complex fluids using the generalized Stokes-Einstein equation', *Rheologica Acta*, vol. 39, no. 4, pp. 371–378, Aug. 2000, doi: 10.1007/s003970000094.

[87] J. Mewis and N. J. Wagner, *Colloidal Suspension Rheology*. Cambridge University Press, 2011.

[88] T. F. Tadros, *Rheology of Dispersions: Principles and Applications*. doi: 10.1002/9783527631568.

[89] V. A. Martinez *et al.*, 'Differential Dynamic Microscopy: A High-Throughput Method for Characterizing the Motility of Microorganisms', *Biophysj*, vol. 103, pp. 1637–1647, 2012, doi: 10.1016/j.bpj.2012.08.045.

[90] J. Deodato, C. Jacob, K. He, S. T. Retterer, R. Krishnamoorti, and J. C. Conrad, 'Diffusive dynamics of nanoparticles in ultra-confined media †', 2015, doi: 10.1039/c5sm01437a.

[91] L. G. Wilson, W. C. K. Poon, L. G. Wilsonw, and W. C. K. Poon, 'Small-world rheology: an introduction to probe-based active microrheology', vol. 13, no. 22, May 2011, doi: 10.1039/c0cp01564d.

[92] M. E. Mackay, 'Rheological measurements on small samples', in *Rheological Measurement*, A. A. Collyer and D. W. Clegg, Eds. Dordrecht: Springer Netherlands, 1998, pp. 635–665. doi: 10.1007/978-94-011-4934-1_20.

[93] Y. Liu, N. Claes, B. Trepka, S. Bals, and P. R. Lang, 'Soft Matter A combined 3D and 2D light scattering study on aqueous colloidal model systems with tunable interactions A combined 3D and 2D light scattering study on aqueous colloidal model systems with tunable interactions', *Soft Matter*, vol. 12, p. 8485, 2016, doi: 10.1039/c6sm01376g.

[94] H. C. Berg, *Random Walks in Biology*, REV-Revised. Princeton University Press, 1993. doi: 10.2307/j.ctv7r40w6.

[95] P. Coussot, *Rheophysics*. Cham: Springer International Publishing, 2014. doi: 10.1007/978-3-319-06148-1.

[96] E. M. Terentjev and D. A. Weitz, *The Oxford Handbook of Soft Condensed Matter*. OUP Oxford, 2015. [Online]. Available: https://books.google.co.th/books?id=OFHCBwAAQBAJ

[97] R. Pecora, B. J. Berne, *Dynamic Light Scattering: With Applications to Chemistry, Biology, and Physics*. Dover publication, 1976.

[98] P. Edera, D. Bergamini, V. Trappe, F. Giavazzi, and R. Cerbino, 'Differential dynamic microscopy microrheology of soft materials: A tracking-free determination of the frequency-dependent loss and storage moduli', *PHYSICAL REVIEW MATERIALS*, vol. 1, 2017, doi: 10.1103/PhysRevMaterials.1.073804.

[99] P. S. Grassia, E. J. Hinch, and L. C. Nitsche, 'Computer simulations of Brownian motion of complex systems', *Journal of Fluid Mechanics*, vol. 282, pp. 373–403, 1995, doi: 10.1017/S0022112095000176.

[100] A. Rigato, A. Miyagi, S. Scheuring, and F. Rico, 'High-frequency microrheology reveals cytoskeleton dynamics in living cells', *Nature Physics*, vol. 13, no. 8, pp. 771–775, Aug. 2017, doi: 10.1038/nphys4104.

[101] L. Formaggia, A. Quarteroni, and A. Veneziani, *Cardiovascular Mathematics*, vol. 3. Springer-Verlag Mailand, 2009. doi: 10.1007/978-88-470-1152-6.

[102] T. Indei, J. D. Schieber, A. Córdoba, and E. Pilyugina, 'Treating inertia in passive microbead rheology', *Phys. Rev. E*, vol. 85, no. 2, p. 21504, Feb. 2012, doi: 10.1103/PhysRevE.85.021504.

[103] T. Yanagishima, D. Frenkel, J. Kotar, and E. Eiser, 'Real-time monitoring of complex moduli from micro-rheology', *Journal of Physics: Condensed Matter*, vol. 23, no. 19, p. 194118, Apr. 2011, doi: 10.1088/0953-8984/23/19/194118.

[104] B. M. Vyas, A. V. Orpe, M. Kaushal, and Y. M. Joshi, 'Passive microrheology in the effective time domain: analyzing time dependent colloidal dispersions', *Soft Matter*, vol. 12, no. 39, pp. 8167–8176, 2016, doi: 10.1039/C6SM00829A.

[105] W.P.Cox and E.H.Merz, 'Correlation of dynamic and steady flow viscosities', *Journal of Polymer Science*, vol. 28, no. 118, pp. 619–622, 1958.

[106] Z. Hajjarian and S. K. Nadkarni, 'Estimation of particle size variations for laser speckle rheology of materials', doi: 10.1364/OL.40.000764.

[107] G. Bryant, C. Abeynayake, and J. C. Thomas, 'Improved particle size distribution measurements using multiangle dynamic light scattering. 2. Refinements and applications', *Langmuir*, vol. 12, no. 26, pp. 6224–6228, 1996, doi: 10.1021/la960224o.

[108] R. Xu, *Particle Characterization: Light Scattering Methods*, vol. 1, no. 6. Springer Netherlands, 2007. doi: 10.1016/s1672-2515(07)60008-6.

[109] G. Bryant and J. C. Thomas, 'Improved particle size distribution measurements using multiangle dynamic light scattering', *Langmuir*, vol. 11, no. 7, pp. 2480–2485, 1995, doi: 10.1021/la00007a028.

[110] P. A. Hassan, S. Rana, and G. Verma, 'Making Sense of Brownian Motion: Colloid Characterization by Dynamic Light Scattering', doi: 10.1021/la501789z.

[111] J. Kim, S. Ahn, H. Lee, and M. Lee, 'Estimation of particle size distribution using photon autocorrelation function from dynamic light scattering considering unknown baseline', *OPTICS LETTERS*, vol. 38, no. 11, p. 1757, 2013, doi: 10.1364/OL.38.001757.

[112] K. Breuer, Ed., *Microscale Diagnostic Techniques*, 1st ed. Springer-Verlag Berlin Heidelberg, 2005. doi: 10.1007/b137604.

[113] M. S. Safari, R. Poling-Skutvik, P. G. Vekilov, and J. C. Conrad, 'Differential dynamic microscopy of bidisperse colloidal suspensions', *npj Microgravity*, vol. 321, 2017, doi: 10.1038/s41526-017-0027-7.

[114] S. Aime and L. Cipelletti, 'Probing shear-induced rearrangements in Fourier space. II. Differential dynamic microscopy', *Soft Matter*, vol. 15, no. 2, pp. 213–226, Jan. 2019, doi: 10.1039/C8SM01564C.

[115] R. Nixon-luke and G. Bryant, 'Differential dynamic microscopy to measure the translational diffusion coefficient of nanorods', 2020.

[116] A. Efimov, 'Spatial coherence at the output of multimode optical fibers', *Opt. Express*, vol. 22, no. 13, pp. 15577–15588, Jun. 2014, doi: 10.1364/OE.22.015577.

[117] D. Brogioli, A. Vailati, and M. Giglio, 'Dynamic heterodyne near field scattering', *Heterodyne speckle velocimetry Applied Physics Letters*, vol. 81, p. 110901, 2002, doi: 10.1063/1.5001027.

[118] E. Velichko, S. Makarov, E. Nepomnyashchaya, and G. Dong, 'Molecular Aggregation in Immune System Activation Studied by Dynamic Light Scattering', *Biology (Basel)*, vol. 9, no. 6, p. 123, Jun. 2020, doi: 10.3390/biology9060123.

[119] V. A. Martinez *et al.*, 'Differential Dynamic Microscopy: A High-Throughput Method for Characterizing the Motility of Microorganisms', *Biophysj*, vol. 103, pp. 1637–1647, 2012, doi: 10.1016/j.bpj.2012.08.045.

[120] L. Korson, W. Drost-Hansen, and F. J. Millero, 'Viscosity of water at various temperatures', *Journal of Physical Chemistry*, vol. 73, no. 1, pp. 34–39, 1969, doi: 10.1021/j100721a006.

[121] X. Bian, C. Kim, and G. E. Karniadakis, *111 years of Brownian motion*, vol. 12. 2016. doi: 10.1039/c6sm01153e.

[122] X. Chen *et al.*, 'Coaxial differential dynamic microscopy for measurement of Brownian motion in weak optical field', *Optics Express*, vol. 26, no. 24, p. 32083, Nov. 2018, doi: 10.1364/OE.26.032083.

[123] F. Giavazzi, P. Edera, P. J. Lu, and R. Cerbino, 'Image windowing mitigates edge effects in Differential Dynamic Microscopy', *The European Physical Journal E*, vol. 40, no. 11, p. 97, 2017, doi: 10.1140/epje/i2017-11587-3.

[124] R. G. Larson and R. G. Larson, *The Structure and Rheology of Complex Fluids*. OUP USA, 1999. [Online]. Available: https://books.google.co.uk/books?id=Vt9fw_pf1LUC

[125] J. Gavina, A. Furtado, J. Pereira, and J. Sousa, 'Indirect and direct temperature calibration methodology of a rheometer using a Newtonian reference material', *Journal of Physics: Conference Series*, vol. 1065, p. 042055, Aug. 2018, doi: 10.1088/1742-6596/1065/4/042055.

[126] P. Coussot, *Rheophysics*. Cham: Springer International Publishing, 2014. doi: 10.1007/978-3-319-06148-1.

[127] A. P. Deshpande, J. M. Krishnan, and S. Kumar, *Rheology of Complex Fluids*. Springer New York, 2010. [Online]. Available: https://books.google.co.th/books?id=iGQTp7v8OvQC

[128] T. A. Waigh and Thomas Andrew Waigh, 'Advances in the microrheology of complex fluids', *Reports on Progress in Physics*, vol. 79, no. 7, 2016, doi: 10.1088/0034-4885/79/7/074601.

[129] A. M. Puertas and T. Voigtmann, *Microrheology of colloidal systems*, vol. 26. Institute of Physics Publishing, 2014. doi: 10.1088/0953-8984/26/24/243101.

[130] I. Sriram, E. M. Furst, R. J. DePuit, and T. M. Squires, 'Small amplitude active oscillatory microrheology of a colloidal suspension', *Journal of Rheology*, vol. 53, no. 2, pp. 357–381, 2009, doi: 10.1122/1.3058438.

[131] D. Weihs, T. G. Mason, and M. A. Teitell, 'Bio-Microrheology: A Frontier in Microrheology', *Biophysical Journal*, vol. 91, no. 11, pp. 4296–4305, 2006, doi: https://doi.org/10.1529/biophysj.106.081109.

[132] P. Cicuta and A. M. Donald, 'Microrheology: a review of the method and applications', doi: 10.1039/b706004c.

[133] T. Savin and P. S. Doyle, 'Static and dynamic errors in particle tracking microrheology', *Biophysical Journal*, vol. 88, no. 1, pp. 623–638, 2005, doi: 10.1529/biophysj.104.042457.

[134] S. Thomas, R. Thomas, A. K. Zachariah, and R. Kumar, *Thermal and Rheological Measurement Techniques for Nanomaterials Characterization*. Elsevier Science, 2017. [Online]. Available: https://books.google.co.th/books?id=XYrCDQAAQBAJ

[135] M. S. Safari, M. A. Vorontsova, R. Poling-Skutvik, P. G. Vekilov, and J. C. Conrad, 'Differential dynamic microscopy of weakly scattering and polydisperse protein-rich clusters', *Phys. Rev. E*, vol. 92, no. 4, p. 42712, Oct. 2015, doi: 10.1103/PhysRevE.92.042712.

[136] A. V. Bayles, T. M. Squires, and M. E. Helgeson, 'Dark-field differential dynamic microscopy', *Soft Matter*, vol. 12, no. 8, pp. 2440–2452, 2016, doi: 10.1039/C5SM02576A.

[137] J. B. Segur and H. E. Oberstar, 'Viscosity of Glycerol and Its Aqueous Solutions', *Industrial & Engineering Chemistry*, vol. 43, no. 9, pp. 2117–2120, Sep. 1951, doi: 10.1021/ie50501a040.

[138] L. Korson, W. Drost-Hansen, and F. J. Millero, 'Viscosity of water at various temperatures', *Journal of Physical Chemistry*, vol. 73, no. 1, pp. 34–39, 1969, doi: 10.1021/j100721a006.

[139] M. A. Escobedo-Sá *et al.*, 'Microliter viscometry using a bright-field microscope: g-DDM', *This journal is Cite this: Soft Matter*, vol. 14, p. 7016, 2018, doi: 10.1039/c8sm00784e.

[140] J. B. Segur and H. E. Oderstar, 'Viscosity of Glycerol and Its Aqueous Solutions', *Industrial and Engineering Chemistry*, vol. 43, no. 9, pp. 2117–2120, Sep. 1951, doi: 10.1021/ie50501a040.

[141] R. Pecora, *Dynamic Light Scattering: Applications of Photon Correlation Spectroscopy*. 2008. doi: 10.1007/978-1-4020-4465-6_13.

[142] D. Leith, 'Drag on Nonspherical Objects', *Aerosol Science and Technology*, vol. 6, no. 2, pp. 153–161, 1987, doi: 10.1080/02786828708959128.

[143] M. Tassieri, M. L. Evans, R. L. Warren, N. J. Bailey, and J. M. Cooper, 'PAPER • OPEN ACCESS Microrheology with optical tweezers: data analysis', *New Journal of Physics*, vol. 14, p. 115032, 2012, doi: 10.1088/1367-2630/14/11/115032.

[144] B. S. Everitt and A. Skrondal, *The Cambridge Dictionary of Statistics*. Cambridge University Press, 2010. [Online]. Available: https://books.google.co.th/books?id=C98wSQAACAAJ

[145] D. M. Yu, G. L. Amidon, N. D. Weiner, and A. H. Goldberg, 'Viscoelastic properties of poly(ethylene oxide) solution.', *J Pharm Sci*, vol. 83, no. 10, pp. 1443–1449, Oct. 1994, doi: 10.1002/jps.2600831016.

[146] N. Shokeen, C. Issa, and A. Mukhopadhyay, 'Comparison of nanoparticle diffusion using fluorescence correlation spectroscopy and differential dynamic microscopy within concentrated polymer solutions', vol. 111, no. 26, p. 263703, Dec. 2017, doi: 10.1063/1.5016062.

[147] J. Lim, S. P. Yeap, H. X. Che, and S. C. Low, 'Characterization of magnetic nanoparticle by dynamic light scattering', *Nanoscale Research Letters*, vol. 8, no. 1, p. 381, Dec. 2013, doi: 10.1186/1556-276X-8-381.

[148] J. Stetefeld, S. A. Mckenna, and T. R. Patel, 'Dynamic light scattering: a practical guide and applications in biomedical sciences', doi: 10.1007/s12551-016-0218-6.

[149] F. Varenne, J. Botton, C. Merlet, M. Beck-Broichsitter, F.-X. Legrand, and C. Vauthier, 'Standardization and validation of a protocol of size measurements by dynamic light scattering for monodispersed stable nanomaterial characterization', *Colloids and Surfaces A: Physicochemical and Engineering Aspects*, vol. 486, pp. 124–138, 2015, doi: https://doi.org/10.1016/j.colsurfa.2015.08.043.

[150] K. Bai, G. V. Barnett, S. R. Kar, and T. K. Das, 'Interference from Proteins and Surfactants on Particle Size Distributions Measured by Nanoparticle Tracking Analysis (NTA).', *Pharm Res*, vol. 34, no. 4, pp. 800–808, Apr. 2017, doi: 10.1007/s11095-017-2109-3.

[151] D. E. Koppel, 'Analysis of Macromolecular Polydispersity in Intensity Correlation Spectroscopy: The Method of Cumulants', *The Journal of Chemical Physics*, vol. 57, no. 11, pp. 4814–4820, Dec. 1972, doi: 10.1063/1.1678153.

[152] B. J. Frisken, 'Revisiting the method of cumulants for the analysis of dynamic light-scattering data', 2001.

[153] J. Stetefeld, S. A. McKenna, and T. R. Patel, 'Dynamic light scattering: a practical guide and applications in biomedical sciences', *Biophysical Reviews*. 2016. doi: 10.1007/s12551-016-0218-6.

[154] A. G. Mailer, P. S. Clegg, and P. N. Pusey, 'Particle sizing by dynamic light scattering: non-linear cumulant analysis', *Journal of Physics: Condensed Matter*, vol. 27, no. 14, p. 145102, Apr. 2015, doi: 10.1088/0953-8984/27/14/145102.

[155] R. Cerbino and P. Cicuta, 'Perspective: Differential dynamic microscopy extracts multi-scale activity in complex fluids and biological systems Communication: Charge transfer dominates over proton transfer in the reaction of nitric acid with gas-phase hydrated electrons Perspective: Differential dynamic microscopy extracts multi-scale activity in complex fluids and biological systems', *The Journal of Chemical Physics The Journal of Chemical Physics The Journal of Chemical Physics The Journal of Chemical Physics*, vol. 147, no. 147, pp. 110901–91101, 2017, doi: 10.1063/1.5001027doi.org/10.1063/1.5001027.

[156] M. Danaei *et al.*, 'Impact of particle size and polydispersity index on the clinical applications of lipidic nanocarrier systems', *Pharmaceutics*, vol. 10, no. 2. MDPI AG, May 18, 2018. doi: 10.3390/pharmaceutics10020057.

[157] A. G. Mailer, P. S. Clegg, and P. N. Pusey, 'Particle sizing by dynamic light scattering: non-linear cumulant analysis', *Journal of Physics: Condensed Matter*, vol. 27, no. 14, p. 145102, Apr. 2015, doi: 10.1088/0953-8984/27/14/145102.

[158] H. Nomura and K. Katayama, 'Development of heterodyne detection of dynamic light scattering enhanced by the Talbot effect for the size measurement of nanoparticles.', *Anal Sci*, vol. 24, no. 4, pp. 459–462, Apr. 2008, doi: 10.2116/analsci.24.459.

[159] D. Magatti, M. D. Alaimo, M. A. C Potenza, F. Ferri, M. A. C. Potenza, and F. Ferri, 'Dynamic heterodyne near field scattering', vol. 92, no. 24, p. 241101, Jun. 2008, doi: 10.1063/1.2937841.

[160] A. Scotti *et al.*, 'The CONTIN algorithm and its application to determine the size distribution of microgel suspensions', *The Journal of Chemical Physics*, vol. 142, p. 234905, 2015, doi: 10.1063/1.4921686.

[161] R. Xu, *Light scattering: A review of particle characterization applications*, vol. 18. 2015, pp. 11–21. doi: 10.1016/j.partic.2014.05.002.

[162] T. Hiroi and M. Shibayama, 'Measurement of Particle Size Distribution in Turbid Solutions by Dynamic Light Scattering Microscopy', *J Vis Exp*, no. 119, p. 54885, Jan. 2017, doi: 10.3791/54885.

[163] F. Scheffold, A. Shalkevich, R. Vavrin, J. Crassous, and P. Schurtenberger, 'PCS Particle Sizing in Turbid Suspensions: Scope and Limitations', in *Particle Sizing and Characterization*, vol. 881, 0 vols, American Chemical Society, 2004, pp. 3–32. doi: 10.1021/bk-2004-0881.ch001.

[164] S. Marze, M. Choimet, and L. Foucat, 'In vitro digestion of emulsions: diffusion and particle size distribution using diffusing wave spectroscopy and diffusion using nuclear magnetic resonance', *Soft Matter*, vol. 8, no. 42, pp. 10994–11004, 2012, doi: 10.1039/C2SM26334C.

[165] F. Giavazzi and R. Cerbino, 'Digital Fourier microscopy for soft matter dynamics', *Journal of Optics (United Kingdom)*, vol. 16, no. 8, 2014, doi: 10.1088/2040-8978/16/8/083001.

[166] B. Lorber, F. Fischer, M. Bailly, H. Roy, and D. Kern, 'Protein analysis by dynamic light scattering: Methods and techniques for students', *Biochemistry and Molecular Biology Education*, vol. 40, no. 6, pp. 372–382, 2012, doi: https://doi.org/10.1002/bmb.20644.

[167] W. Anderson, D. Kozak, V. A. Coleman, Å. K. Jämting, and M. Trau, 'A comparative study of submicron particle sizing platforms: Accuracy, precision and resolution analysis of polydisperse particle size distributions', *Journal of Colloid and Interface Science*, vol. 405, pp. 322–330, 2013, doi: https://doi.org/10.1016/j.jcis.2013.02.030.

[168] K. Franks, V. Kestens, A. Braun, G. Roebben, and T. P. J. Linsinger, 'Non-equivalence of different evaluation algorithms to derive mean particle size from dynamic light scattering data', *Journal of Nanoparticle Research*, vol. 21, no. 9, p. 195, Aug. 2019, doi: 10.1007/s11051-019-4630-2.

[169] R. Finsy, N. de Jaeger, R. Sneyers, and E. Geladé, 'Particle Sizing by Photon Correlation Spectroscopy. Part III: Mono and bimodal distributions and data analysis', *Particle & Particle Systems Characterization*, vol. 9, no. 1-4, pp. 125–137, Jan. 1992, doi: 10.1002/ppsc.19920090117.

[170] W. Zhang *et al.*, 'Particle size distribution recovery in dynamic light scattering by optimized multi-parameter regularization based on the singular value distribution', *Powder Technology*, vol. 353, pp. 320–329, Jul. 2019, doi: 10.1016/j.powtec.2019.05.040.

[171] I. D. Morrison, E. F. Grabowski, and C. A. Herb, 'Improved Techniques for Particle Size Determination by Quasi-Elastic Light Scattering', 1985.

[172] Y. Luo and R. Duraiswami, 'EFFICIENT PARALLEL NON-NEGATIVE LEAST SQUARES ON MULTI-CORE ARCHITECTURES', *SIAM Journal on Scientific Computing*, vol. 33, pp. 2848–2863, 2011.

[173] M. W. Berry *et al.*, *High-Performance Scientific Computing: Algorithms and Applications*. Springer London, 2012. [Online]. Available: https://books.google.co.th/books?id=yVpYDkV-Zz4C

[174] C. L. Lawson and R. J. Hanson, *Solving Least Squares Problems*. Society for Industrial and Applied Mathematics, 1995. [Online]. Available: https://books.google.co.th/books?id=AEwDbHp50FgC

[175] M. Dessole, F. Marcuzzi, and M. Vianello, 'Accelerating the Lawson-Hanson NNLS solver for large-scale Tchakaloff regression designs', *Dolomites Research Notes on Approximation*, vol. 13, pp. 20–29, 2020.

[176] B. Garda and Z. Galias, 'Non-negative least squares and the Tikhonov regularization methods for coil design problems', in *2012 International Conference on Signals and Electronic Systems (ICSES)*, Sep. 2012, pp. 1–5. doi: 10.1109/ICSES.2012.6382220.

[177] M. Naiim, A. Boualem, C. Ferre, M. Jabloun, A. Jalocha, and P. Ravier, 'Multiangle dynamic light scattering for the improvement of multimodal particle size distribution measurements', *Soft Matter*, vol. 11, no. 1, pp. 28–32, 2015, doi: 10.1039/C4SM01995D.

[178] X. Zhu, J. Shen, W. Liu, X. Sun, and Y. Wang, 'Nonnegative least-squares truncated singular value decomposition to particle size distribution inversion from dynamic light scattering data', *Appl. Opt.*, vol. 49, no. 34, pp. 6591–6596, Dec. 2010, doi: 10.1364/AO.49.006591.

[179] X. Yuan, Z. Liu, Y. Wang, Y. Xu, W. Zhang, and T. Mu, 'The non-negative truncated singular value decomposition for adaptive sampling of particle size distribution in dynamic light scattering inversion', *Journal of Quantitative Spectroscopy and Radiative Transfer*, vol. 246, p. 106917, 2020, doi: https://doi.org/10.1016/j.jqsrt.2020.106917.

[180] R. R. Ansari and S. L. Nyeo, 'Submicron particle size distributions by dynamic light scattering with non-negative least-squares algorithm', *Chinese Journal of Physics*, vol. 50, no. 3, pp. 459–477, 2012.

[181] R. Bro and S. De Jong, 'A FAST NON-NEGATIVITY-CONSTRAINED LEAST SQUARES ALGORITHM', *Journal of Chemometrics*, vol. 11, pp. 393–401, 1997, doi: 10.1002/(SICI)1099-128X(199709/10)11:5<393::AID-CEM483>3.0.CO;2-L.

[182] 'ZETASIZER NANO Series'. https://www.malvernpanalytical.com/en/assets/MRK1839_tcm50-17228.pdf

[183] 'Microspheres & Particles Handling Guide', Mar. 16, 2019. http://www.polysciences.com/skin/frontend/default/polysciences/pdf/Microparticles%20Guide.pdf

[184] X. Liu, J. Shen, J. C. Thomas, S. Shi, X. Sun, and W. Liu, 'Multiangle dynamic light scattering analysis using angular intensity weighting determined by iterative recursion', *Appl. Opt.*, vol. 51, no. 7, pp. 846–854, Mar. 2012, doi: 10.1364/AO.51.000846.

[185] F. R. Hallett, 'Particle size analysis by dynamic light scattering', *Food Research International*, vol. 27, no. 2, pp. 195–198, 1994, doi: https://doi.org/10.1016/0963-9969(94)90162-7.

[186] A. M. Robertson, A. Sequeira, and M. V. Kameneva, 'Hemorheology'. [Online]. Available: https://fenix.tecnico.ulisboa.pt/downloadFile/1970943312265439/Hemorheology.pdf

[187] S. K. Hamlin and P. S. Benedik, 'Basic concepts of hemorheology in microvascular hemodynamics', *Critical care nursing clinics of North America*, vol. 26, no. 3, p. 337, 2014.

[188] A. S. Popel and P. C. Johnson, 'MICROCIRCULATION AND HEMORHEOLOGY', *Annu. Rev. Fluid Mech*, vol. 37, pp. 43–69, 2005, doi: 10.1146/annurev.fluid.37.042604.133933.

[189] O. K. Baskurt and H. J. Meiselman, 'Blood Rheology and Hemodynamics', *Seminars in Thrombosis and Hemostasis*, vol. 29, no. 5, pp. 435–450, 2003, doi: 10.1055/s-2003-44551.

[190] A. Sequeira, 'Hemorheology: Non-newtonian constitutive models for blood flow simulations', in *Lecture Notes in Mathematics*, vol. 2212, A. Farina, A. Mikelić, and F. Rosso, Eds. Cham: Springer International Publishing, 2018, pp. 1–44. doi: 10.1007/978-3-319-74796-5_1.

[191] D. Tahara, N. Oikawa, and R. Kurita, 'Mobility Enhancement of Red Blood Cells with Biopolymers', *J. Phys. Soc. Jpn.*, vol. 85, no. 3, p. 033801, Mar. 2016, doi: 10.7566/JPSJ.85.033801.

[192] V. N. Du Le and V. J. Srinivasan, 'Beyond diffuse correlations: deciphering random flow in time-of-flight resolved light dynamics.', *Opt Express*, vol. 28, no. 8, pp. 11191–11214, Apr. 2020, doi: 10.1364/OE.385202.

[193] J. R. Guzman-Sepulveda, R. Argueta-Morales, W. M. DeCampli, and A. Dogariu, 'Real-time intraoperative monitoring of blood coagulability via coherence-gated light scattering', *Nature Biomedical Engineering*, vol. 1, no. 2, p. 0028, Feb. 2017, doi: 10.1038/s41551-017-0028.

[194] C. Wagner, P. Steffen, and S. Svetina, 'Aggregation of red blood cells: From rouleaux to clot formation', *Comptes Rendus Physique*, vol. 14, no. 6, pp. 459–469, Jun. 2013, doi: 10.1016/j.crhy.2013.04.004.

[195] M. Hoore, F. Yaya, T. Podgorski, C. Wagner, G. Gompper, and D. A. Fedosov, 'Effect of spectrin network elasticity on the shapes of erythrocyte doublets', *Soft Matter*, vol. 14, no. 30, pp. 6278–6289, 2018, doi: 10.1039/C8SM00634B.

[196] M. Abbasi, A. Farutin, H. Ez-Zahraouy, A. Benyoussef, and C. Misbah, 'Erythrocyte-erythrocyte aggregation dynamics under shear flow', *Phys. Rev. Fluids*, vol. 6, no. 2, p. 023602, Feb. 2021, doi: 10.1103/PhysRevFluids.6.023602.

[197] M. M. Lee, P. B. Canham, and R. M. Barr, 'Adhesive interaction of erythrocytes in vitro in multiple myeloma.', *Microvasc Res*, vol. 40, no. 3, pp. 317–326, Nov. 1990, doi: 10.1016/0026-2862(90)90030-u.

[198] Kisung Lee *et al.*, 'Optical tweezers study of red blood cell aggregation and disaggregation in plasma and protein solutions', *Journal of Biomedical Optics*, vol. 21, no. 3, pp. 1–10, Mar. 2016, doi: 10.1117/1.JBO.21.3.035001.

[199] J. Stoltz and M. Donner, 'New trends in clinical hemorheology: an introduction to the concept of the hemorheological profile', *Schweizerische medizinische Wochenschrift. Supplementum*, vol. 43, p. 41—49, 1991.

[200] T. F. Tadros, *Rheology of Dispersions: Principles and Applications*. 2010. doi: 10.1002/9783527631568.

[201] Y. I. Cho, M. P. Mooney, and D. J. Cho, 'Hemorheological disorders in diabetes mellitus', 2008. doi: 10.1177/193229680800200622.

[202] L. Campo-Deaño, R. P. A. Dullens, D. G. A. L. Aarts, F. T. Pinho, and M. S. N. Oliveira, 'Viscoelasticity of blood and viscoelastic blood analogues for use in polydymethylsiloxane in vitro models of the circulatory system', *Biomicrofluidics*, vol. 7, no. 3, May 2013, doi: 10.1063/1.4804649.

[203] G. Tomaiuolo, A. Carciati, S. Caserta, and S. Guido, 'Blood linear viscoelasticity by small amplitude oscillatory flow', *Rheologica Acta*, doi: 10.1007/s00397-015-0894-3.

[204] U. Windberger, C. Pöschl, S. Peters, J. Huber, and R. Van Den Hoven, 'Measurement of whole blood of different mammalian species in the oscillating shear field: Influence of erythrocyte aggregation', in *Journal of Physics: Conference Series*, 2017, vol. 790, no. 1, p. 12035. doi: 10.1088/1742-6596/790/1/012035.

[205] P. C. Sousa, F. T. Pinho, M. A. Alves, and M. S. N. Oliveira, 'A review of hemorheology: Measuring techniques and recent advances', *Rheology Journal*, vol. 28, no. 1, pp. 1–22, 2016, doi: 10.1007/s13367-016-0001-z.

[206] C. J. Pipe and G. H. McKinley, 'Microfluidic rheometry', *Mechanics Research Communications*, vol. 36, no. 1, pp. 110–120, 2009, doi: https://doi.org/10.1016/j.mechrescom.2008.08.009.

[207] O. K. Baskurt *et al.*, 'New guidelines for hemorheological laboratory techniques *', *Clinical Hemorheology and Microcirculation*, vol. 42, pp. 75–97, 2009, doi: 10.3233/CH-2009-1202.

[208] S. Tripathi *et al.*, 'Passive blood plasma separation at the microscale: a review of design principles and microdevices Performance study of microfluidic devices for blood plasma separation—a designer's perspective Self-driven filter-based blood plasma separator microfluidic chip for point of care testing Hojjat Madadi, Jasmina Casals-Terré and Mahdi Mohammadi - Fundamentals and application of magnetic particles in cell isolation and enrichment: a review', [Online]. Available: http://iopscience.iop.org.ezproxy.lib.gla.ac.uk/article/10.1088/0960-1317/25/8/083001/pdf

[209] J. Mathew, P. Sankar, and M. Varacallo, 'Physiology, Blood Plasma.', in *StatPearls*, Treasure Island (FL): StatPearls Publishing, 2021.

[210] H. Oertel, *Biofluid Mechanics*, vol. 158. 2010. doi: 10.1007/978-1-4419-1564-1_12.

[211] G. P. Galdi, R. Rannacher, A. M. Robertson, and S. Turek, *Hemodynamical Flows*. Birkhäuser Basel, 2008. doi: 10.1007/978-3-7643-7806-6.

[212] M. Brust *et al.*, 'Rheology of human blood plasma: Viscoelastic versus Newtonian behavior', *Physical Review Letters*, vol. 110, no. 7, p. 078305, Feb. 2013, doi: 10.1103/PhysRevLett.110.078305.

[213] S. Varchanis, Y. Dimakopoulos, C. Wagner, and J. Tsamopoulos, 'How viscoelastic is human blood plasma?', *This journal is Cite this: Soft Matter*, vol. 14, p. 4238, 2018, doi: 10.1039/c8sm00061a.

[214] Y. Henon, G. J. Sheard, and A. Fouras, 'Erythrocyte deformation in a microfluidic cross-slot channel', *RSC Adv.*, vol. 4, no. 68, pp. 36079–36088, 2014, doi: 10.1039/C4RA04229H.

[215] H. Oertel, *Biofluid Mechanics*, vol. 158. 2010. doi: 10.1007/978-1-4419-1564-1_12.

[216] D. H. Boal, *Mechanics of the Cell*. Cambridge University Press, 2012.

[217] J. N. Thon and J. E. Italiano, 'Platelets: Production, Morphology and Ultrastructure', in *Antiplatelet Agents*, P. Gresele, G. V. R. Born, C. Patrono, and C. P. Page, Eds. Berlin, Heidelberg: Springer Berlin Heidelberg, 2012, pp. 3–22. doi: 10.1007/978-3-642-29423-5_1.

[218] A. J. Gale, 'Continuing education course #2: current understanding of hemostasis', *Toxicol Pathol*, vol. 39, no. 1, pp. 273–280, Jan. 2011, doi: 10.1177/0192623310389474.

[219] O. K. Baskurt, M. R. Hardeman, and M. W. Rampling, *Handbook of Hemorheology and Hemodynamics*. IOS Press, 2007. [Online]. Available: https://books.google.co.th/books?id=5fF6AFAsywMC

[220] W. H. REINHART and C. NAGY, 'Albumin affects erythrocyte aggregation and sedimentation', *European Journal of Clinical Investigation*, vol. 25, no. 7, pp. 523–528, Jul. 1995, doi: 10.1111/j.1365-2362.1995.tb01739.x.

[221] A. Q. Cowan, D. J. Cho, and R. S. Rosenson, 'Importance of Blood Rheology in the Pathophysiology of Atherothrombosis', doi: 10.1007/s10557-012-6402-4.

[222] O. K. Baskurt *et al.*, 'New guidelines for hemorheological laboratory techniques *', *Clinical Hemorheology and Microcirculation*, vol. 42, pp. 75–97, 2009, doi: 10.3233/CH-2009-1202.

[223] A. L. Copley, R. G. King, S. Chien, S. Usami, R. Skalak, and C. R. Huang, 'Microscopic observations of viscoelasticity of human blood in steady and oscillatory shear', *Biorheology*, vol. 12, no. 5, pp. 257–263, 1975, doi: 10.3233/BIR-1975-12501.

[224] P. Ruef, J. Gehm, L. Gehm, C. Felbinger, J. Pöschl, and N. Kuss, 'Determination of whole blood and plasma viscosity by means of flow curve analysis', *Gen. Physiol. Biophys*, vol. 33, pp. 285–293, 2014, doi: 10.4149/gpb_2014009.

[225] P. C. Sousa *et al.*, 'Shear viscosity and nonlinear behavior of whole blood under large amplitude oscillatory shear', *Biorheology*, vol. 50, no. 5–6, pp. 269–282, Jan. 2013, doi: 10.3233/BIR-130643.

[226] P. C. Sousa, F. T. Pinho, M. A. Alves, and M. S. N. Oliveira, 'A review of hemorheology: Measuring techniques and recent advances', *Rheology Journal*, vol. 28, no. 1, pp. 1–22, 2016, doi: 10.1007/s13367-016-0001-z.

[227] S. Rogers, 'Large amplitude oscillatory shear: Simple to describe, hard to interpret', *Citation: Physics Today*, vol. 71, p. 34, 2018, doi: 10.1063/PT.3.3971.

[228] J. M. Dealy, 'Official nomenclature for material functions describing the response of a viscoelastic fluid to various shearing and extensional deformations', *Citation: Journal of Rheology*, vol. 39, p. 253, 1995, doi: 10.1122/1.4765670.

[229] R. H. Ewoldt, M. T. Johnston, and L. M. Caretta, 'Experimental challenges of shear rheology: how to avoid bad data', doi: 10.1007/978-1-4939-2065-5_6.

[230] X.-B. Zhang *et al.*, 'Gravitational Sedimentation Induced Blood Delamination for Continuous Plasma Separation on a Microfluidics Chip', *Anal. Chem.*, vol. 84, no. 8, pp. 3780–3786, Apr. 2012, doi: 10.1021/ac3003616.

[231] A. Zhbanov and S. Yang, 'Effects of Aggregation on Blood Sedimentation and Conductivity', *PLoS One*, vol. 10, no. 6, pp. e0129337–e0129337, Jun. 2015, doi: 10.1371/journal.pone.0129337.

[232] A. Pribush, D. Meyerstein, and N. Meyerstein, 'The mechanism of erythrocyte sedimentation. Part 1: Channeling in sedimenting blood', *Colloids and Surfaces B: Biointerfaces*, vol. 75, no. 1, pp. 214–223, Jan. 2010, doi: 10.1016/j.colsurfb.2009.08.036.

[233] G. R. Cokelet, D. E. Brooks, R. Skalak, and M. Intaglietta, 'Blood Rheology Interpreted through the Flow Properties of the Red Cell', in *Microcirculation: Blood-Vessel Interactions Systems in Special Tissues 1*, J. Grayson and W. Zingg, Eds. Boston, MA: Springer US, 1976, pp. 9–76. doi: 10.1007/978-1-4613-4334-9_2.

[234] A. Jaishankar, V. Sharma, and G. H. McKinley, 'Interfacial viscoelasticity, yielding and creep ringing of globular protein–surfactant mixtures', *Soft Matter*, vol. 7, no. 17, p. 7623, Aug. 2011, doi: 10.1039/c1sm05399j.

[235] M. L. Gardel, M. T. Valentine, and D. A. Weitz, 'Microrheology', in *Microscale Diagnostic Techniques*, K. S. Breuer, Ed. Berlin, Heidelberg: Springer Berlin Heidelberg, 2005, pp. 1–49. doi: 10.1007/3-540-26449-3_1.

[236] G. Marin, 'Oscillatory Rheometry', in *Rheological Measurement*, A. A. Collyer and D. W. Clegg, Eds. Dordrecht: Springer Netherlands, 1993, pp. 297–343. doi: 10.1007/978-94-017-2898-0_10.

[237] F. Del Giudice, M. Tassieri, C. Oelschlaeger, and A. Q. Shen, 'When Microrheology, Bulk Rheology, and Microfluidics Meet: Broadband Rheology of Hydroxyethyl Cellulose Water Solutions', *Macromolecules*, vol. 50, no. 7, pp. 2951–2963, Apr. 2017, doi: 10.1021/acs.macromol.6b02727.

[238] S. Gupta, W. S. Wang, and S. A. Vanapalli, 'Microfluidic viscometers for shear rheology of complex fluids and biofluids', 1989, doi: 10.1063/1.4955123.

[239] A. Ostadfar, 'Chapter 1 - Fluid Mechanics and Biofluids Principles', in *Biofluid Mechanics*, A. Ostadfar, Ed. Academic Press, 2016, pp. 1–60. doi: 10.1016/B978-0-12-802408-9.00001-6.

[240] S. Oh, B. Kim, J. K. Lee, and S. Choi, '3D-printed capillary circuits for rapid, low-cost, portable analysis of blood viscosity', vol. 259, pp. 106–113, 2018, doi: 10.1016/j.snb.2017.12.025.

[241] B. J. Kim, S. Y. Lee, S. Jee, A. Atajanov, and S. Yang, 'Micro-Viscometer for Measuring Shear-Varying Blood Viscosity over a Wide-Ranging Shear Rate', 2017, doi: 10.3390/s17061442.

[242] Y. J. Kang and S. Yang, 'Integrated microfluidic viscometer equipped with fluid temperature controller for measurement of viscosity in complex fluids', *Microfluidics and Nanofluidics*, vol. 14, no. 3–4, pp. 657–668, Mar. 2013, doi: 10.1007/s10404-012-1085-5.

[243] T. M. Geislinger and T. Franke, 'Hydrodynamic lift of vesicles and red blood cells in flow — from Fåhræus & Lindqvist to microfluidic cell sorting', *Advances in Colloid and Interface Science*, vol. 208, pp. 161–176, Jun. 2014, doi: 10.1016/j.cis.2014.03.002.

[244] K. Sakai, T. Hirano, and M. Hosoda, 'Electromagnetically spinning sphere viscometer', *Applied Physics Express*, vol. 3, no. 1, 2010, doi: 10.1143/APEX.3.016602.

[245] K. Furukawa *et al.*, 'Measurement of human blood viscosity by an electromagnetic spinning sphere viscometer', *Journal of Medical Engineering and Technology*, vol. 40, no. 6, pp. 285–292, 2016, doi: 10.1080/03091902.2016.1181216.

[246] K. Fukunaga *et al.*, 'Blood viscometer applying electromagnetically spinning method', *Journal of Artificial Organs*, vol. 16, no. 3, pp. 359–367, 2013, doi: 10.1007/s10047-013-0707-3.

[247] D. Wirtz, 'Particle-tracking microrheology of living cells: Principles and applications', *Annual Review of Biophysics*, vol. 38, no. 1, pp. 301–326, Jun. 2009, doi: 10.1146/annurev.biophys.050708.133724.

[248] W.P.Cox and E.H.Merz, 'Correlation of dynamic and steady flow viscosities', *Journal of Polymer Science*, vol. 28, no. 118, pp. 619–622, 1958.

[249] L. Langstroth, 'BLOOD VISCOSITY : I. CONDITIONS AFFECTING THE VISCOSITY OF BLOOD AFTER WITHDRAWAL FROM THE BODY.', *The Journal of experimental medicine*, vol. 30, no. 6, pp. 597–606, Nov. 1919, doi: 10.1084/jem.30.6.597.

[250] J. A. McGlynn, N. Wu, and K. M. Schultz, 'Multiple particle tracking microrheological characterization: Fundamentals, emerging techniques and applications', *Journal of Applied Physics*, vol. 127, no. 20, p. 201101, May 2020, doi: 10.1063/5.0006122.

[251] K. A. Rose, M. Molaei, M. J. Boyle, D. Lee, J. C. Crocker, and R. J. Composto, 'Particle tracking of nanoparticles in soft matter', *Journal of Applied Physics*, vol. 127, no. 19, p. 191101, May 2020, doi: 10.1063/5.0003322.

[252] J. Chen, Z. Yin, Y. Tang, and T. Pan, 'Vis-NIR spectroscopy with moving-window PLS method applied to rapid analysis of whole blood viscosity', *Analytical and Bioanalytical Chemistry*, vol. 409, no. 10, pp. 2737–2745, 2017, doi: 10.1007/s00216-017-0218-9.

[253] F. Giavazzi and R. Cerbino, 'Digital Fourier microscopy for soft matter dynamics', *Journal of Optics (United Kingdom)*, vol. 16, no. 8, 2014, doi: 10.1088/2040-8978/16/8/083001.

[254] M. A. Escobedo-Sá, L. F. Rojas-Ochoa, M. Laurati, and S. U. Egelhaaf, 'Investigation of moderately turbid suspensions by heterodyne near field scattering', vol. 13, p. 5961, 2017, doi: 10.1039/c7sm00816c.

[255] J. H. H. H. Bongaerts, A. D. Rossetti, A. J. R. Stokes, D. Rossetti, and J. R. Stokes, 'The lubricating properties of human whole saliva', *Tribology Letters*, vol. 27, no. 3, pp. 277–287, 2007, doi: 10.1007/s11249-007-9232-y.

[256] D. Briedis, M. F. Moutrie, and R. T. Balmer, 'A study of the shear viscosity of human whole saliva', *Rheologica Acta*, vol. 19, no. 3, pp. 365–374, 1980, doi: 10.1007/BF01543149.

[257] D. C. Löfgren, 'International Journal of Oral and Dental Health The Challenge of Measuring Viscoelastic Properties of Human Whole Saliva to Fit Clinical Purpose', *Int J Oral Dent Health*, vol. 1, p. 4, 2015.

[258] C. S. Broberg *et al.*, 'Blood Viscosity and its Relationship to Iron Deficiency, Symptoms, and Exercise Capacity in Adults With Cyanotic Congenital Heart Disease', *Journal of the American College of Cardiology*, 2006, doi: 10.1016/j.jacc.2006.03.040.

[259] C. H. Lee, K. H. Jung, D. J. Cho, and S. K. Jeong, 'Effect of warfarin versus aspirin on blood viscosity in cardioembolic stroke with atrial fibrillation: A prospective clinical trial', *BMC Neurology*, vol. 19, no. 1, 2019, doi: 10.1186/s12883-019-1315-5.

[260] C. Trejo-Soto *et al.*, 'Front microrheology of the non-Newtonian behaviour of blood: scaling theory of erythrocyte aggregation by aging', *This journal is Cite this: Soft Matter*, vol. 13, p. 3042, 2017, doi: 10.1039/c6sm02412b.

[261] J. J. McNamara, D. Boatright, E. L. Burran, M. D. Molot, E. Summers, and J. F. Stremple, 'Changes in some physical properties of stored blood.', *Annals of surgery*, vol. 174, no. 1, pp. 58–60, 1971, doi: 10.1097/00000658-197107010-00010.

[262] A. R. Hradin, R. I. Weed, and C. F. Reed, 'Changes in Physical Properties of Stored Erthrocytes', *Transfusion*, vol. 9, no. 5, pp. 229–237, 1969, doi: 10.1111/j.1537-2995.1969.tb04929.x.

[263] J. R. Hess, 'Red cell changes during storage', *Transfusion and Apheresis Science*, 2010, doi: 10.1016/j.transci.2010.05.009.

[264] J. R. Hess, 'Red cell storage', *Journal of Proteomics*, vol. 73, no. 3, pp. 368–373, 2010, doi: 10.1016/j.jprot.2009.11.005.

[265] Z. Xu, Y. Zheng, X. Wang, N. Shehata, C. Wang, and Y. Sun, 'Stiffness increase of red blood cells during storage', *Microsystems & Nanoengineering*, vol. 4, no. 1, p. 17103, Feb. 2018, doi: 10.1038/micronano.2017.103.

[266] S. Henkelman, M. J. Dijkstra-Tiekstra, J. De Wildt-Eggen, R. Graaff, G. Rakhorst, and W. Van Oeveren, 'Is red blood cell rheology preserved during routine blood bank storage?', *Transfusion*, vol. 50, no. 4, pp. 941–948, 2010, doi: 10.1111/j.1537-2995.2009.02521.x.

[267] A. Colin Cameron and F. A. G. Windmeijer, 'An R-squared measure of goodness of fit for some common nonlinear regression models', *Journal of Econometrics*, vol. 77, no. 2, pp. 329–342, Apr. 1997, doi: 10.1016/S0304-4076(96)01818-0.

[268] Hademenos George J. and Massoud Tarik F., 'Biophysical Mechanisms of Stroke', *Stroke*, vol. 28, no. 10, pp. 2067–2077, Oct. 1997, doi: 10.1161/01.STR.28.10.2067.

[269] R. Wittenauer and L. Smith, 'Background Paper 6.6 Ischaemic and Haemorrhagic Stroke', 2012.

[270] S. H. Song, J. H. Kim, J. H. Lee, Y. M. Yun, D. H. Choi, and H. Y. Kim, 'Elevated blood viscosity is associated with cerebral small vessel disease in patients with acute ischemic stroke', *BMC Neurology*, vol. 17, no. 1, 2017, doi: 10.1186/s12883-017-0808-3.

[271] B. M. Coull *et al.*, 'Chronic blood hyperviscosity in subjects with acute stroke, transient ischemic attack, and risk factors for stroke.', *Stroke*, vol. 22, no. 2, pp. 162–8, Feb. 1991, doi: 10.1161/01.str.22.2.162.

[272] E. Ernst, A. Matrai, and M. Marshall, 'Blood rheology in patients with transient ischemic attacks', *Stroke*, vol. 19, no. 5, pp. 634–636, 1988, doi: 10.1161/01.STR.19.5.634.

[273] P. Kowal and A. Marcinkowska-Gapińska, 'Hemorheological changes dependent on the time from the onset of ischemic stroke', *Journal of the Neurological Sciences*, vol. 258, no. 1–2, pp. 132–136, Jul. 2007, doi: 10.1016/j.jns.2007.03.011.

[274] O. Elwan, S. Al-Ashmawy, S. El-Karaksy, and A. A. H. Hassan, 'Hemorheology, stroke and the elderly', *Journal of the Neurological Sciences*, vol. 101, no. 2, pp. 157–162, Feb. 1991, doi: 10.1016/0022-510X(91)90040-E.

[275] J.C.F. de Winter, 'Using the Student's "t"-Test with Extremely Small Sample Sizes', *PARE*, vol. 18, p. 12, 2013, doi: https://doi.org/10.7275/e4r6-dj05.

[276] A. Ghasemi and S. Zahediasl, 'Normality tests for statistical analysis: a guide for non-statisticians', *Int J Endocrinol Metab*, vol. 10, no. 2, pp. 486–489, 2012, doi: 10.5812/ijem.3505.

[277] A. Yao, M. Tassieri, M. Padgett, and J. Cooper, *Microrheology with optical tweezers*, vol. 9. Royal Society of Chemistry, 2009. doi: 10.1039/b907992k.

[278] M. S. Park, J. W. Chung, Y. K. Kim, S. C. Chung, and H. S. Kho, 'Viscosity and wettability of animal mucin solutions and human saliva', *Oral Diseases*, 2007, doi: 10.1111/j.1601-0825.2006.01263.x.

[279] S. J. Haward, J. A. Odell, M. Berry, and T. Hall, 'Extensional rheology of human saliva', *Rheologica Acta*, vol. 50, no. 11–12, pp. 869–879, 2011, doi: 10.1007/s00397-010-0494-1.

[280] M. S. Park, J. W. Chung, Y. K. Kim, S. C. Chung, and H. S. Kho, 'Viscosity and wettability of animal mucin solutions and human saliva', *Oral Diseases*, vol. 13, no. 2, pp. 181–186, Mar. 2007, doi: 10.1111/j.1601-0825.2006.01263.x.

[281] W. A. Van Der Reijden, E. C. I. Veerman, and A. V. Nieuw Amerongen, 'Shear rate dependent viscoelastic behavior of human glandular salivas', *Biorheology*, vol. 30, no. 2, pp. 141–152, 1993, doi: 10.3233/BIR-1993-30205.

[282] K. L. Helton and P. Yager, 'Interfacial instabilities affect microfluidic extraction of small molecules from non-Newtonian fluids', *Lab on a Chip*, vol. 7, no. 11, pp. 1581–1588, 2007, doi: 10.1039/b709585f.

[283] R. M. L. Evans, M. Tassieri, D. Auhl, and T. A. Waigh, 'Direct conversion of rheological compliance measurements into storage and loss moduli', *Physical Review E - Statistical, Nonlinear, and Soft Matter Physics*, vol. 80, no. 1, 2009, doi: 10.1103/PhysRevE.80.012501.

[284] T. A. Waigh, 'Advances in the microrheology of complex fluids', *Reports on Progress in Physics*, vol. 79, no. 7, 2016, doi: 10.1088/0034-4885/79/7/074601.

[285] M. K. Kwon, S. H. Lee, S. G. Lee, and K. S. Cho, 'Direct conversion of creep data to dynamic moduli', *Journal of Rheology*, vol. 60, no. 6, pp. 1181–1197, 2016, doi: 10.1122/1.4961484.

[286] I. Fine, A. Kaminsky, B. Kuznik, and L. Shenkman, 'A non-invasive method for the assessment of hemostasis in vivo by using dynamic light scattering', *Laser Physics*, vol. 22, no. 2, pp. 469–475, Feb. 2012, doi: 10.1134/S1054660X12020090.

[287] S. J. Haward, J. A. Odell, M. Berry, and T. Hall, 'Extensional rheology of human saliva', *Rheologica Acta*, vol. 50, no. 11–12, pp. 869–879, 2011, doi: 10.1007/s00397-010-0494-1.

[288] W. H. Schwarz, 'The Rheology of Saliva', *Journal of Dental Research*, vol. 66, no. 1_suppl, pp. 660–666, Feb. 1987, doi: 10.1177/00220345870660S109.

[289] S. Varchanis, Y. Dimakopoulos, C. Wagner, and J. Tsamopoulos, 'How viscoelastic is human blood plasma?', *This journal is Cite this: Soft Matter*, vol. 14, p. 4238, 2018, doi: 10.1039/c8sm00061a.

[290] C. S. Broberg *et al.*, 'Blood Viscosity and its Relationship to Iron Deficiency, Symptoms, and Exercise Capacity in Adults With Cyanotic Congenital Heart Disease', *Journal of the American College of Cardiology*, 2006, doi: 10.1016/j.jacc.2006.03.040.

[291] C. H. Lee, K. H. Jung, D. J. Cho, and S. K. Jeong, 'Effect of warfarin versus aspirin on blood viscosity in cardioembolic stroke with atrial fibrillation: A

prospective clinical trial', *BMC Neurology*, vol. 19, no. 1, 2019, doi: 10.1186/s12883-019-1315-5.

[292] S. Oh, B. Kim, J. K. Lee, and S. Choi, '3D-printed capillary circuits for rapid, low-cost, portable analysis of blood viscosity', vol. 259, pp. 106–113, 2018, doi: 10.1016/j.snb.2017.12.025.

[293] C. Trejo-Soto *et al.*, 'Front microrheology of the non-Newtonian behaviour of blood: scaling theory of erythrocyte aggregation by aging', *This journal is Cite this: Soft Matter*, vol. 13, p. 3042, 2017, doi: 10.1039/c6sm02412b.

[294] E. J. Lim, T. J. Ober, J. F. Edd, G. H. McKinley, and M. Toner, 'Visualization of microscale particle focusing in diluted and whole blood using particle trajectory analysis', *Lab Chip*, vol. 12, no. 12, pp. 2199–2210, 2012, doi: 10.1039/C2LC21100A.

[295] J. Leach *et al.*, 'Comparison of Faxén's correction for a microsphere translating or rotating near a surface', 2009, doi: 10.1103/PhysRevE.79.026301.

[296] B. H, 'The slow motion of a sphere through a viscous fluid towards a plane surface', *Chemical engineering science*, vol. 16, no. (3-4), pp. 242–251, 1961, doi: 10.1021/acs.analchem.6b04564.

Appendix A

Preliminary study of rheological behaviour on chemistry-modified surfaces

In this preliminary study, mobility of silica microparticles onto two surface chemistry-modified systems comprising hydrophilic and hydrophobic surfaces were observed. These two heterogeneous surface modifications indicate how the surface absorb or repel water. In hydrophilic, water tends to spread across the surface called wetting, as opposed to hydrophobic-treated surface, where water is repelled causing droplets to form.

To create a hydrophilic surface, a glass slide was sonicated in acetone for 10 mins. Then, the slide was washed with methanol and air dried. After that, the slide was plasma-treated with oxygen plasma asher for a few min to form hydrophilic surface.

To create a hydrophobic surface, this slide was immersed in a mixture of heptane and trichloro(1H,1H,2H,2H-perfluorooctyl)silane for 10 mins. Then, the slide was washed with clean, running water followed by air dried.

To obtain rheological measurement, aqueous solution of silica microparticles with diameter of 2.56 μm were added on surface-modified glass slide. Due to the fact that the particles were more dense than water, the particles settled on the surface of the surface-modified glass slide. Then, the movement of particles are recorded to further analysed with the DDA. From this analysis, the mean square displacement of the particles was obtained as regard to Figure A.1.

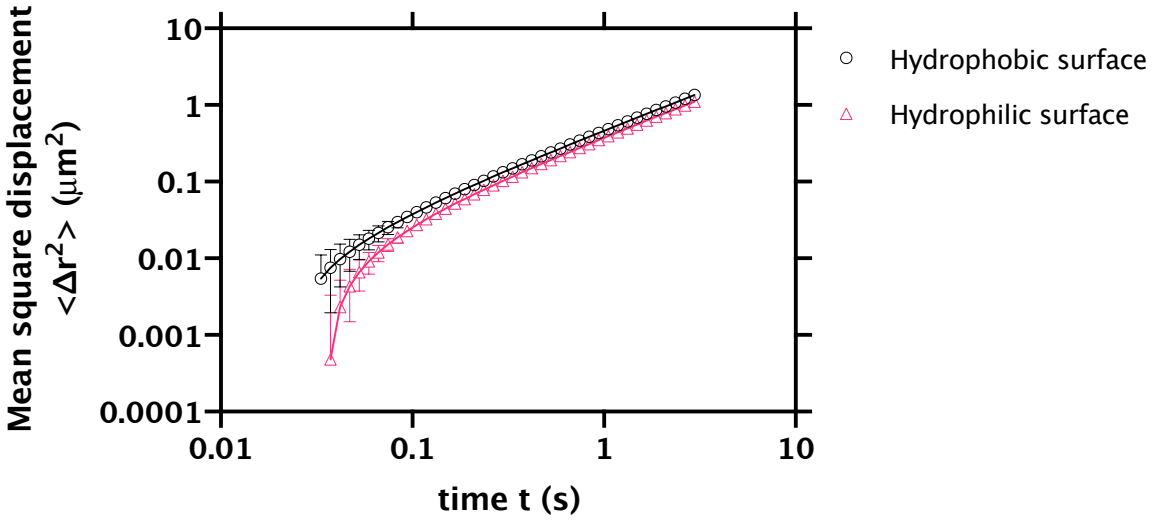

Figure A.1. Mean square displacement of 2.56 μm silica microparticles on hydrophilic (opened-circle symbol) and hydrophobic (upward-triangle symbol) surfaces.

Figure A.1 shows that the measured mean square displacement of hydrophobic-treated surface was slightly higher than hydrophilic-treated surface. That is, the microparticles can spread further after the surface was hydrophobic-treated. These mean square displacements were calculated to obtain viscoelastic moduli and steady-shear viscosity using the direct conversion method and Cox-Merz rule respectively, see Figure A.2.

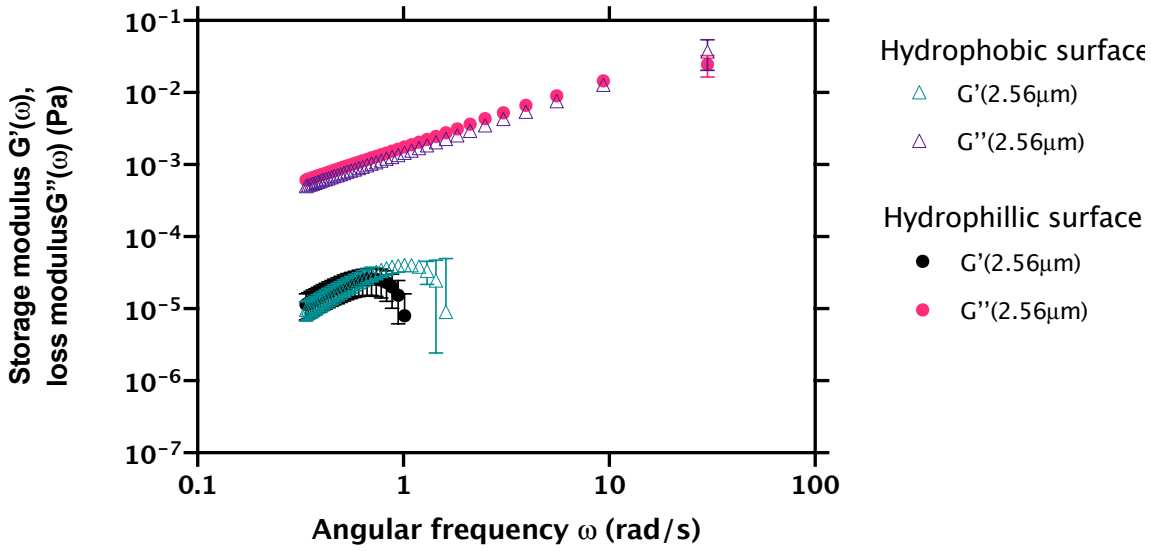

(a)

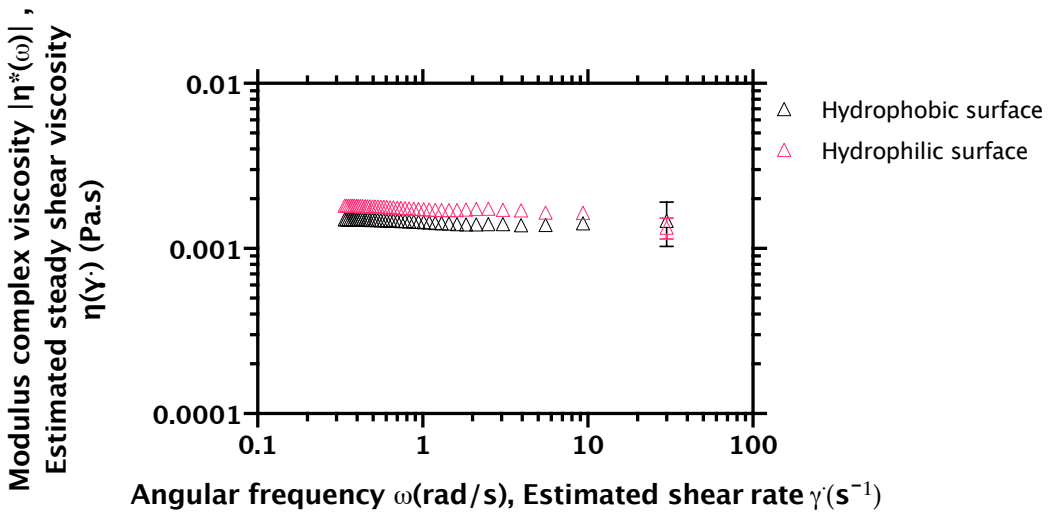

(b)

Figure A.2 Rheological study of surface modified glass slides using spherical silica microparticles with diameter of 2.56 μm. (a) Storage and loss moduli of hydrophobic (hollow symbols) and hydrophilic surfaces (solid symbols). (b) The corresponding steady-shear viscosity from performing Cox-Merz rule on (a).

From Figure A.2, viscoelastic moduli of water around chemical-treated surfaces of hydrophilic and hydrophobic were revealed. In Figure A.2(a), loss modulus of water on the hydrophilic-treated surface was higher than those obtained in hydrophobic surface. However, the storage moduli of water on these surface-modified glass slides were slightly different. As a result, the corresponding steady-shear viscosity of hydrophobic surface was slightly lowered than hydrophilic surface. The surface viscosities of hydrophobic and hydrophilic surface can be compared to water viscosity as shown in Figure A.3.

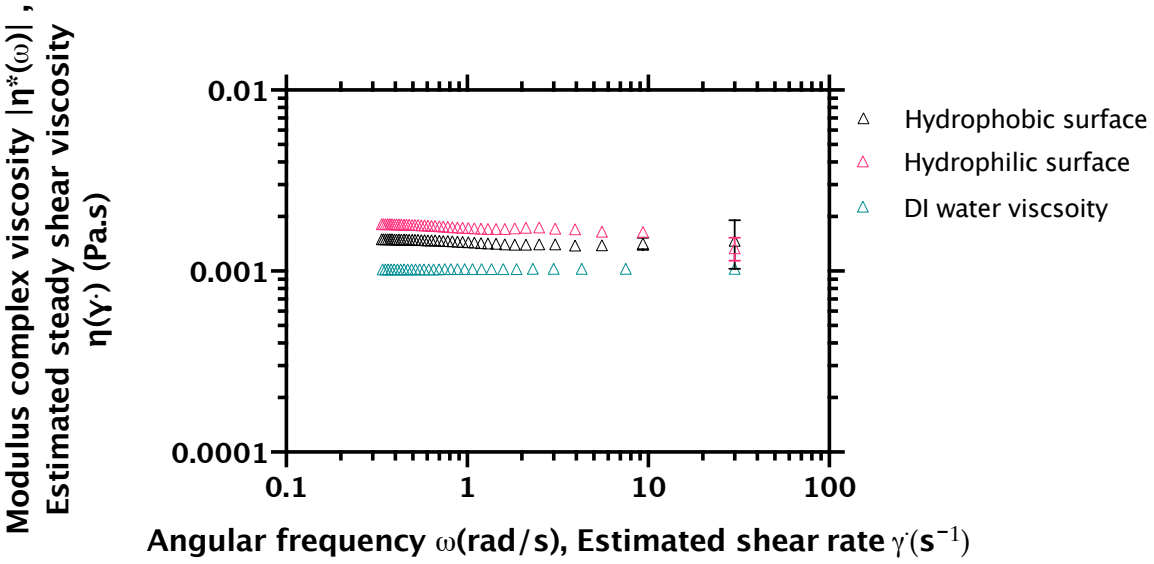

Figure A.3 Viscosity of deionised water and viscosity of deionised water on chemistry-modified surfaces at 20°C. The viscosities on the surface were obtained by using 2.56 μm silica microparticles whereas off-surface viscosity was obtained by exploiting 1.54 μm colloidal microparticles to probe.

It was apparent from Figure A.3 that viscosities of water on both of hydrophobic and hydrophilic surfaces were higher than off-surface viscosity. This might be related to surface roughness and emerging of hydrodynamic effect in close proximity of surface [296].

These preliminary results could be allow for surface investigation using our developed device. Hydrophobic-treated of glass surface elevated mobility of silica microparticles and a fall in the obtained loss modulus. Accordingly, the corresponding shear-viscosity of water on the surface was considerably fell off than the hydrophilic glass surface. However, these preliminary results only showed viscosity measurement characteristics of such chemistry-modified surfaces. A further improvement on the analysis could allow for obtaining the surface friction.